Convective assembly of nanoparticles into thin structured films

A DISSERTATION
SUBMITTED TO THE FACULTY OF THE GRADUATE SCHOOL
OF THE UNIVERSITY OF MINNESOTA
BY

Jun Alexander Lee

IN PARTIAL FULFILLMENT OF THE REQUIREMENTS
FOR THE DEGREE OF
DOCTOR OF PHILOSOPHY

Professor Michael Tsapatsis, Advisor

May 2010

Acknowledgements

For their direction and support of my studies at Minnesota, I am deeply indebted to my advisors, Professors Michael Tsapatsis and L. E. “Skip” Scriven. I cannot adequately express my gratitude for their guidance, patience, and example, which were generous in breadth and profound in extent; it is all the more regrettable that I cannot express my thanks personally to Skip. Piercingly critical and insightful powers of analysis, an uncanny ability to impart clarity (often in the mere minutes following endless days of my own attempts), meticulous yet judicious attention to detail, the general pursuit of excellence, and just plain *style* are but a few of their many qualities and philosophies that I have observed, come to admire, and aspire to make my own.

I am thankful for having had the opportunity to participate in the Coating Process Fundamentals Program, whose faculty and fellow members have all impressed me greatly. I thank professors Lorraine Francis and Satish Kumar—who are always gracious in their advising of all CPF students—for the many comments, observations, and suggestions they have given me. Wieslaw Suszynski has been a great help in getting my experiments started, and has been a wonderful friend (whose dinner parties and taste in liquor are exceptional).

I would like to acknowledge the staff of CEMS, whose often silent efforts ultimately keep things rolling. Thanks to the Industrial Partnership for Research in Interfacial and Materials Engineering for exposure to many excellent engineers (as well as funding), and the Materials Research Science and Engineering Center for the opportunity to explore the role of engineering in primary (K-12) education and giving me professional interests beyond research. Also through MRSEC, I had the privilege of working with a young researcher, Kayla Reibel from Trine University, whose summer work was instrumental in one of the chapters.

All of my peers from the Tsapatsis group and the CPFP, as well as my classmates, have offered me help in the lab, their thoughts on my work, and most importantly their friendships. As the group of people I ended up being immersed in almost every day of the last few years, they have truly been most influential during my graduate training and I thank them for their counsel and fellowship. Finally, I wish to express my thanks to all of my friends and family who have all in some way been a part of my experience.

Abstract

Convective nanoparticle film assembly is a simple process whereby particles from dilute liquid suspension assemble onto a substrate. Assembly occurs at the suspension-substrate-air contact line, where particles are carried toward it by convective currents set up in the meniscus region due to liquid evaporation. In the past, convectively assembled nanosphere films have been shown to be highly ordered (exhibiting colloidal crystallinity).

In this dissertation, convective assembly is initially explored as a potential method for the fabrication of "tiled" (highly ordered; uniformly oriented) nanocrystal films for application in zeolite membrane technology. It is found that films are generally assembled into jumbled multilayers, and that they are often nonuniform in coverage, sometimes leaving large areas of bare substrate in a banded pattern. Nevertheless, particles are shown quantitatively to be preferentially oriented, and some regions of the films do exhibit the desired "tiled" arrangement.

A convective assembly apparatus is introduced as an experimental platform for further investigation of the method as a practicable one for large-scale production of thin [monolayer] particle films in general, and zeolite membrane precursor films in particular. The performance of the apparatus and characteristics of the films are discussed in the context of a model silica nanosphere system. Monolayer film assembly turns out to be possible but difficult, with discrete banded film patterns being common in both sub-monolayer and super-monolayer films. The regularity and repeatability of these banded films are, however, very high.

The wavelength of the banded film patterns (specifically, the space between bands) are shown to be strongly dependent on particle size in sub-monolayer films. The relationship is investigated by experiment, and modeled using a simple geometric exclusion argument based on the liquid meniscus profile described by the Young-Laplace equation. The model implies that band wavelength should also be dependent on the thickness of the films (in super-monolayer films).

The geometric exclusion model makes unrealistic assumptions about the liquid meniscus during convective assembly, namely that the system is static. Thus, the final topic of this dissertation is to attempt an extension of the model by including liquid flow. This quantitatively refines the meniscus geometry, and allows a wider range of predictions of band spacing, although it seems to be far from the last word on modeling the banding phenomenon.

Table of Contents

List of Tables

List of Figures

Chapter 1

Introduction

This chapter briefly introduces the goals, challenges, phenomena, and methods that motivate the work presented in this dissertation. It is not meant to be a detailed discussion of the existing work and background; these are presented in the relevant context by chapter.

1.1 Colloidal films

This work concerns the production and characteristics of so-called colloidal films, or films comprising discrete solid particles in the size range of 1 nm $\sim$ 1 µm. Such films may also be referred to as particle or particulate films or coatings. The existence and formation of these films is inherently interesting from the point of view of the various phenomena behind self assembly/organization at large, and the films themselves have application (or potential application) in diverse fields. Among them are optics, photonics, chemical and biological sensors, colloidal lithography, and catalytic and/or separation membranes, the last being of immediate relevance.

In most of the aforementioned applications, functionality of the films derives from the structure of the constituent particles. For example, materials that are periodically organized at optical length scales, as in the case of close-packed spheres (illustrated in Figure 1.1), can in principle be exploited to modify and/or control photons for various applications due to their periodically alternating dielectric constant (refractive index). For their periodicity, such materials [actually

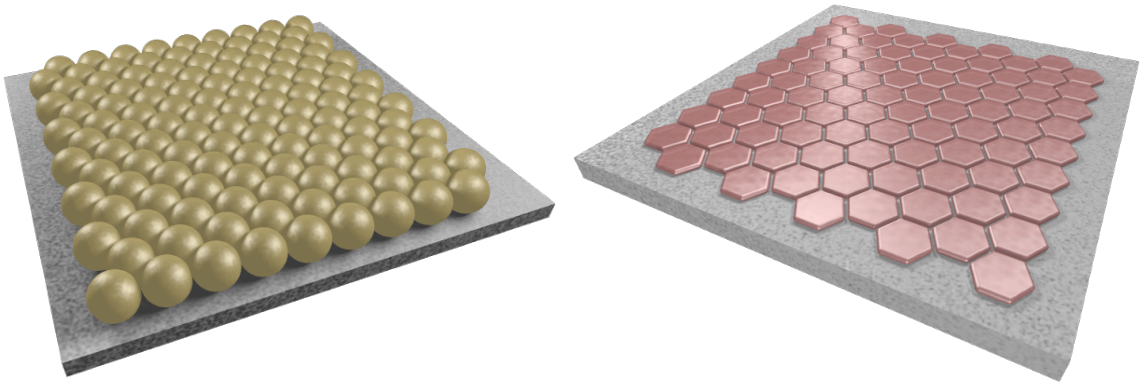

Figure 1.1: Cartoons representing interesting colloidal films. A single layer in an opaline film (left) and an idealized crystalline membrane precursor particle film (right).

their precursors] are often called colloidal crystals or more specifically opals, and various efforts have resulted in these types of films (see *e.g.* Norris *et al.*, 2004 for a short review).

The function-imparting structure need not be strictly crystalline. One strategy for reducing the glare on a reflective surface, for example, is to coat it with a porous or multiphase film of controlled thickness, a particle film being among the candidates (Hattori, 2001; Prevo *et al.*, 2005b). In this case, reduction in the reflectance is achieved by the [random] porous structure in the film whose constituent phases result in an effective refractive index that satisfies the relationship $n_c = (n_a n_s)^{1/2}$ where n_a and n_s are the refractive indices of the air and reflective surface, respectively (see *e.g.* Fowles, 1989).

Yet another kind of structural control concerns the orientation of constituent particles, in cases where the particles are anisometric or not spherical. Separation membranes based on the molecular sieving properties of zeolitic and other crystalline materials may rely on the orientational control of such particles in films. In these cases, the ultimate goal is to control the orientation of the underlying crystalline domains in the final membrane; oriented particle films can serve as a precursor to such membranes in a certain class of strategies (as illustrated in Figure 1.1). Because this particular application directly motivates this dissertation work, § 1.2 below is devoted to its introduction.

Having motivated the interest in colloidal films in general, it remains to briefly introduce the methods and phenomena surrounding their formation. The self assembly or organization

of particles into periodic structures has traditionally been studied in the context of thermodynamic equilibrium structures, such as discussed by Pieranski (1983) in terms of mutually repulsive spheres sedimenting in a liquid. However, recent studies have demonstrated that a process seemingly not related to equilibrium is capable of generating periodic colloidal structures. This process, often called convective assembly, has received much attention following the demonstration by Jiang *et al.* (1999) who produced opaline films with significantly lower crystalline defect densities than those previously produced by thermodynamically driven methods. The convective assembly mechanism is the basis of what follows, and so it is more carefully introduced in § 1.3 below.

Of course, many other methods for particle film deposition have been proposed and discussed, including electrostatic deposition (Boudreau *et al.*, 1999; Bertrand *et al.*, 2000; Hattori, 2001; Adamczyk, 2003), electrophoretic deposition (Fukada *et al.*, 2004; Ke *et al.*, 2001; Shan *et al.*, 2004), and Blodgett-Langmuir-like methods (Huang *et al.*, 2005; Picard, 1998). None of the phenomena relevant to these processes can be dismissed in the discussion of convectively assembled films, as they almost certainly play some role.

1.2 Crystalline membrane precursors

The fabrication of crystalline films is a significant challenge due to the brittle and directional nature of crystals in general. That is, crystals cannot be cast or extruded into film or membrane form in the way viscous materials such as polymer solutions or melts can be. Additionally, it is easy to imagine that the functionality of a crystalline film requires a high degree of alignment of its domains (the ideal case is a single crystalline film). This section will motivate in some detail a particular class of crystalline membranes, namely zeolite membranes, for application in chemical separations.

Zeolite membranes potentially provide a basis for inexpensive separation of chemicals via molecular sieving action (size-based transport discrimination). Molecular sieving is an attractive alternative to traditional separation methods like distillation (especially for close-boiling

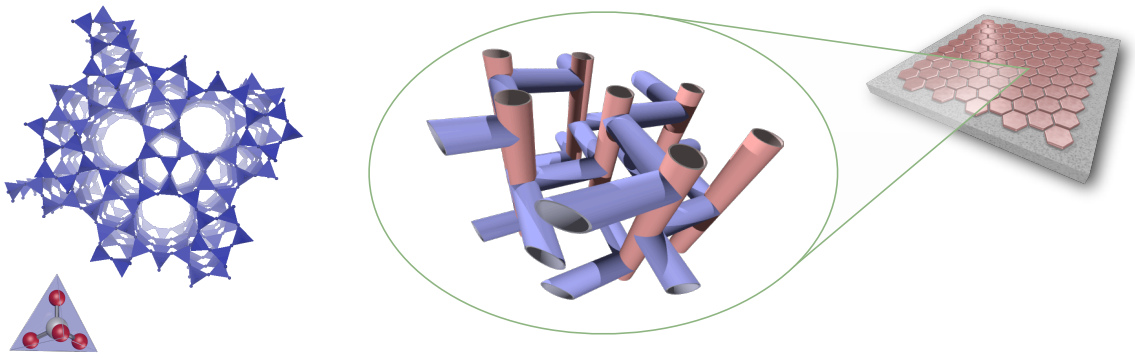

Figure 1.2: Structure of the FAU zeolite represented as SiO_4 or AlO_4 tetrahedra (left, tetrahedron illustrated in lower left). An idealized membrane precursor film comprising uniformly shaped zeolite ZSM-2 particles (right), where each particle has an underlying crystal structure that could impart separation selectivity to the membrane (the structure of MFI zeolite structure shown).

mixtures, as is common for isomeric separations), because of significantly lower energy requirements and potentially smaller equipment footprint requirements. Even as a marginal component in existing separation operations, the potential economic impact of zeolite membranes may be significant.

Zeolites, which are aluminosilicate crystals, can act as molecular sieves by virtue of their "open framework" structure, in contrast to dense crystals of similar composition such as quartz. The general zeolite structure can be constructed from SiO_4 and AlO_4 tetrahedra, and the resulting structures can form so-called "rings" or "pores" providing significant open volume in the crystalline network (see Figure 1.2). Such pores can be connected across unit cells in potentially interesting morphologies, giving rise to "channels" (see Figure 1.2) pervading the crystal structure. Because the material is crystalline, these channel/pore systems have strictly defined dimensions. In some zeolite structures, the channels can have dimensions comparable to the kinetic diameters of small molecules and have potential to discriminate between molecules based on size (sieve) to allow selective transport through it.

There are a limited number of zeolite structures available, but their lattice parameters can be altered (channel sizes tuned) to some extent by adjusting the ratio of aluminum to silicon in the composition, and/or changing the counter-ions that balance the negative charge on the framework aluminum. Matching any particular zeolite with any specific composition to a chem-

ical separation of interest is an open problem, and is beyond the scope of this work, although it is worth mentioning that one of the hurdles this area is the general inability to produce membranes for study in the first place!

This dissertation follows the body of work by Lovallo and Tsapatsis (1996a), who demonstrated a zeolite membrane fabrication route via the deposition of a so-called "seed layer" of crystal [nano]particles (*viz.* particle films as idealized in Figure 1.2), and the subsequent growth and intergrowth of these deposited crystals into a continuous film. This seeded membrane growth strategy can be considered as a response to the so-called *in situ* crystallization strategy (see *e.g.* Geus *et al.*, 1993; an extensive review has been provided by Bein, 1996), wherein the films are grown directly onto the substrate without the benefit of a seed layer. Such methods presented challenges not only regarding orientational control of the crystal domains, but also control of nucleation and growth to ensure the crystals formed on the substrate at all.

Boudreau and Tsapatsis (1997) later demonstrated that the orientation of the particles in this seed layer affects the consequent overall crystal orientation of the final membrane, and work by others since (*e.g.* Ha *et al.*, 2000) have focused on the fabrication of high quality seed layers. The polycrystalline membranes resulting from the secondary growth of such precursor films have been shown to possess preferential crystalline orientation and thus separation selectivity (see *e.g.* Lai *et al.*, 2003), and further advancements are under way. Introduction of the various methods for seed layer deposition is relegated to § 2.1.1.

1.3 Convective assembly

The convective assembly process examined in this dissertation is essentially the same as that responsible for the unsightly rings that may develop on the sides of a mug of coffee left out for too long, as in Figure 1.3a. According to the schematic in Figure 1.3b, the main zone of action in convective assembly is the meniscus region formed when the substrate is submersed in a suspension of the particles. For this meniscus to form, of course, the substrate must be well-wetted by the liquid component of the suspension.

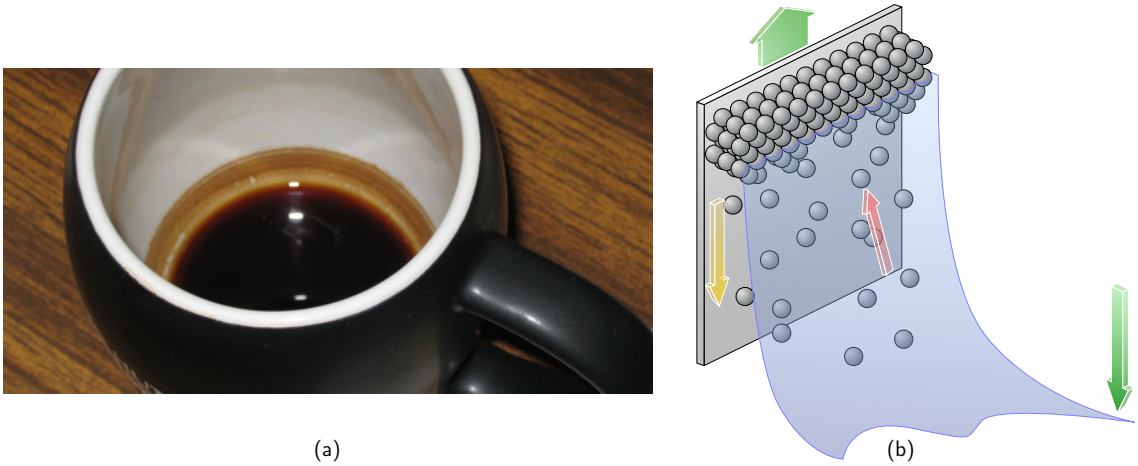

(a) (b)

Figure 1.3: Convective assembly is essentially the process that occurs during the deposit of coffee particles on the sides of an old coffee mug, as may reside on the desk of a graduate student (a). The schematic in (b) represents the general process of convective assembly, where arrows represent the most important rates: meniscus recession (green), particle flux (red), and film growth (gold).

When a particle film already exists (as it does in Figure 1.3b), a liquid-substrate-air contact line forms at the film's particle assembly front, and particles are carried from the bulk through the meniscus to this assembly front by convective currents that arise due to evaporation of the liquid in the meniscus region as well as the drying particle film.

The assembly of this particle film is advanced as the contact line is swept down the substrate by relative motion of the bulk liquid surface and the contact line, such as by action of substrate withdrawal; the particle film is coated onto the substrate by advancement of the film growth front at the contact line.

It is important to recognize that in the convective assembly regime, the rate of substrate withdrawal must not be so fast as to entrain a liquid film. This limit is dictated by the rate of liquid evaporation in addition to the fluid dynamics of entrainment coating. What is important here is that practically, any substrate withdrawal conducted during convective assembly should be on the order of the rate at which any entrainment film vanishes due to evaporation; one such rate would be the rate at which the bulk liquid surface of a contained liquid recedes due to evaporation of the contents alone, as for the case of the coffee in Figure 1.3a.

1.4 Dissertation outline

The remainder of this dissertation is divided into four topical chapters followed by a short epilogue. The chapters deal with demonstrating the application of controlled evaporation convective assembly phenomenon to zeolite nanoparticles (Chapter 2), developing a continuous mode controlled evaporation convective assembly apparatus (Chapter 3), and investigating the origins of the banded film morphology that are ubiquitous in particle films convectively assembled from dilute suspension (Chapters 4 and 5).

Chapter 2 motivates the investigation of convective assembly as a viable technique for fabricating zeolite membrane precursor particle films ("seed layers"), by demonstrating that zeolite nanoparticles can be preferentially oriented in convectively assembled films. The chapter opens with a review of zeolite synthesis and conventional seed layer deposition methods.

The experiments in Chapter 2 had been adapted from the work of Meng (2008), which precluded the possibility of operating in continuous mode (as would be desirable from a production standpoint). Another consequent drawback was the difficulty in controlling film thickness, especially in the case of ultra thin [monolayer] films. Thus, Chapter 3 describes the development of an apparatus for continuous mode controlled evaporation convective assembly. The chapter includes a review of the convective assembly literature as it is relevant to continuous operation, and a discussion of its application to zeolite membranes.

The discrete banded morphology of the films described in Chapter 3 as well as in the literature, warranted further investigation because its origins and formation have implications on the viability of convective assembly as a production-scale process for generating ultra thin particle films. Chapter 4 introduces a simple geometrically motivated model for describing the banding length scale of the discrete films as a function of constituent particle size.

The model described in Chapter 4 is based on the Young-Laplace equation, which governs the shape of a static liquid meniscus. Although this model qualitatively captured the behavior of the results, it is certainly not consistent with the premise behind convective assembly, namely that the liquid in the meniscus must be flowing. Chapter 5 attempts to extend the idea by allowing liquid flow to alter the meniscus profile.

Chapter 2

Preferentially oriented zeolite films

This chapter[†] presents a proof-of-concept for the application of convective assembly to the fabrication of particle films in the interest of zeolite membranes for chemical separations by molecular sieving; in other words the deposition of a crystal seed layer. Particles of the zeolite ZSM-2, which can be prepared as nominally hexagonal platelets, were coated onto flat and smooth glass substrates by a controlled evaporation (non-continuous) convective assembly technique to demonstrate the viability of the convective assembly technique for coating a continuous particle film with preferential particle orientation.

While preferential particle orientation out-of-plane was quantitatively demonstrated, preferential orientation in-the-plane was observed only partially. The uniformity of film thickness was shown to depend strongly on the coating process conditions, namely the particle concentration in the bulk coating suspension and the flow rate of the drying gas. Regions of particle monolayers were rare, but where present, particles did display preferential orientation in-the-plane of the film. This finding was the first documented demonstration of convective assembly applied to anisometric nanoparticles that resulted in particulate coatings with locally ordered microstructure, *i.e.*, colloidal crystallinity. A periodic film structure was observed also at a larger length-scale; this topic is discussed in detail in later chapters.

[†]based on published work (Lee *et al.*, 2006)

2.1 Background

From the introduction in § 1.2, the ideal characteristics for a particulate membrane-precursor film in the interest of zeolitic molecular sieve membranes are evident. First, the film should be of thin and uniform thickness in order that the secondary growth step does not add too much thickness in the course of filling the lateral gaps (preserve high permeance). Second, the particles in the film should be uniformly oriented in a certain direction to ensure proper molecular sieving action. Additionally, the hope is for the particles to arrange, if their geometry allows, in tiled manner to minimize the lateral gaps that need to be filled in by secondary growth.

2.1.1 Zeolite membrane precursor films

A recent review of zeolite membrane technology was given by Caro and Noack (2008). An earlier review by Bein (1996) describes synthesis techniques and applications of zeolite-containing films primarily focusing on *in situ* crystallization of pure zeolite films and composites containing discrete zeolite particles. Around that time, the seeded zeolite membrane growth method was introduced by Lovallo and Tsapatsis (1996b), and it was subsequently demonstrated that the uniformity of particle orientation in the seed layer improves the crystalline orientation in the final membrane (Boudreau and Tsapatsis, 1997).

Following these reports, the field has seen much activity in the generation of such membrane precursor films, that is uniformly (or preferentially) oriented zeolite particle films. The most successful demonstrations involved chemical anchoring of the zeolite particles to the supporting substrate (Ha *et al.*, 2000), and successful synthesis of functional zeolite membranes have since been reported (Lai *et al.*, 2003). While research in the field is active, attention devoted to the seeding step is still somewhat lacking.

One of the most successful methods reported in the literature for assembling close-packed zeolite monolayers with uniform orientation out-of-the-plane is by covalent linkages with the substrate. A fortunate result of these methods is a remarkable degree of close-packing, usually because of highly uniform particle orientations in-the-plane. Linkages as various as aminoalkylsylil and haloalkylsylil (Ha *et al.*, 2000; Choi *et al.*, 2000; Ha *et al.*, 2004), amines and epoxides

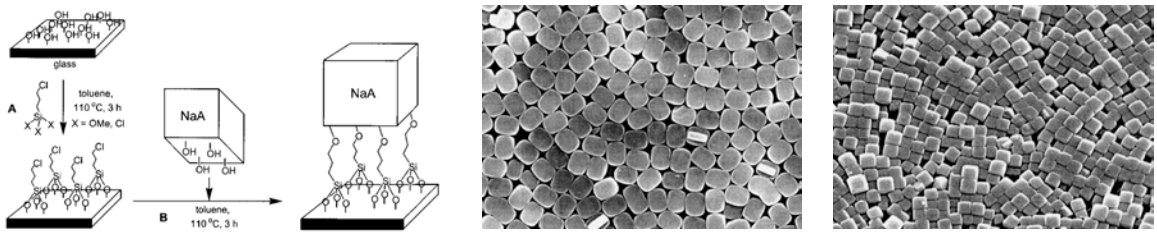

Figure 2.1: A schematic (left) and results (center, right) of the seed layer deposition method described by Ha *et al.* (2000) (originals cropped). Chloropropyl methoxysilanes are used as tethering agents to attach zeolites to the substrate. The methoxysilanes are condensed with the surface hydroxyls on the substrate, and the zeolites are subsequently introduced, whereupon the other end of the tethering agent covalently bond to the hydroxyls on the zeolite surface.

(Kulak *et al.*, 2000a), polyamines (dendritic and polymeric) (Kulak *et al.*, 2000b), diisocyanates (Chun *et al.*, 2002), and terephthaldicarboxaldehyde (Lee *et al.*, 2000) have been used.

Generally, the substrate, zeolite particles, or both are functionalized with a chemical linker and allowed to react in refluxing suspension, whereupon the zeolites bind to the substrate. The simpler of these methods are ones where only one linker compound reacts with both zeolite and substrate surfaces. In the method described by Ha *et al.* (2000), the substrate is functionalized by a halopropylsilyl compound and the zeolite is bound to these functional groups via their surface hydroxyl groups (see Figure 2.1).

The more complicated linker schemes involve functionalization of both the zeolite and substrate surfaces to strengthen the binding between them. It seems that there are more reactive groups on the surface of a functionalized zeolite or substrate than there are hydroxyl groups on the surface of an as-is zeolite or substrate surface. Consequently, bindings between two functionalized surfaces is stronger, but may require a third linking compound. For example, Choi *et al.* (2000) demonstrated that adding a fullerene between two aminoalkyl functional groups improved the binding strength between the zeolite and the substrate.

Although the chemically anchored seed layer deposition techniques have been successful in the laboratory, they all suffer from practical shortcomings. The condensation reactions are sensitive to moisture, and require completely dry environments to be carried out; the presence of water in the environment promotes the auto-condensation of the silyl groups, for example,

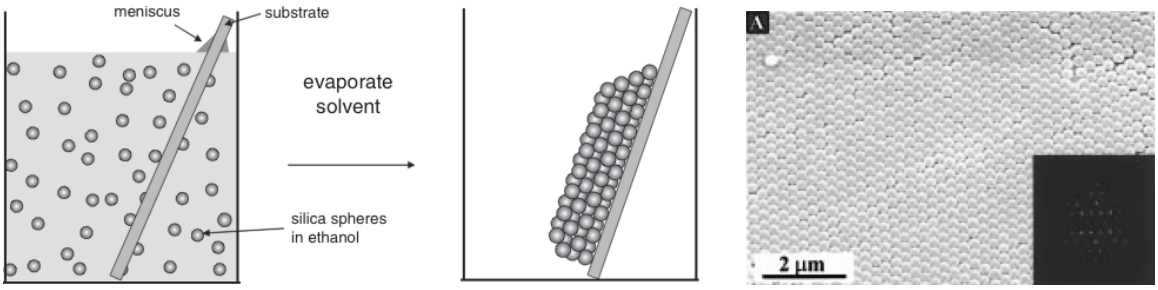

(a) Norris *et al.* (2004) (b) Jiang *et al.* (1999)

Figure 2.2: Method (a) as described by Norris *et al.* (2004) and results (b) of Jiang *et al.* (1999). Simple convective assembly produces high quality (highly ordered) colloidal crystals.

precluding the anchoring of the chemicals to the substrate. Such a dry environment is generally provided by carrying out the reaction in dry toluene, the use of which presents challenges from the environmental perspective. The process is also inherently batch-wise, so that scale-up opportunities are limited.

2.1.2 Convective assembly and related work

While the work of Boudreau *et al.* (1999) and predecessors did not focus on the method of zeolite particle seed layer deposition, a series of convergent studies was emerging concurrently in the fields of optical and other functional particle films (Dimitrov and Nagayama, 1996; Jiang *et al.*, 1999) that examined the methods and mechanics of particle deposition by convective assembly.

Of immediate relevance to this chapter is the work of Jiang *et al.* (1999), which demonstrated the fabrication of high quality opaline films (colloidal crystals comprising spherical particles). They showed that simply by placing a substrate into an alcohol suspension of silica spheres, the particles could be assemble at the contact line into a highly ordered opaline film (see Figure 2.2). Thick films could be produced by successive repetition of the deposition cycle. However, Jiang *et al.* (1999) had not attempted to make thin (monolayer) films.

Other works (Prevo and Velev, 2004; Meng *et al.*, 2006) have reported studies of convectively assembled colloidally crystalline structures (for example both of these works describe the crystal structure in film thickness transition regimes, *i.e.* from mono- to bilayer, bi- to trilayer, and so on). Whereas Prevo and Velev (2004) followed a method closely resembling that of Dimitrov and

Nagayama (1996) involving the action of substrate withdrawal (discussed in § 3.1.1), Meng *et al.* (2006) extended the method of Jiang *et al.* (1999) without forced substrate withdrawal. The adaptations made by Meng *et al.* (2006) include coating the films from aqueous suspension instead of alcohol, and also enhancing the evaporation of suspension liquid by introducing a laminar drying gas flow over the meniscus region. The latter probably also improved the degree of control and therefore consistency of the method (also see Meng, 2008).

In adapting the convective assembly method to zeolite particle films, an important question (beyond the issue of the general assembly mechanism) is the issue of ordering—what phenomena are responsible for the colloidal crystallization observed in the films? The most studied phenomena responsible for such spontaneous colloidal crystallization are due to thermodynamic equilibrium arguments (Pieranski, 1983), capillary forces (so-called immersion forces) during dry-out (Denkov *et al.*, 1992; Kralchevsky and Nagayama, 1994), and convective steering (Norris *et al.*, 2004; Gasperino *et al.*, 2008; Brewer *et al.*, 2008).

Briefly, the latter describes the arrival of new particles at the film growth front as being steered toward crystallographic positions by virtue of the distribution of the pores (particle-particle interstices) that develop as a result of the already-growing film. This mechanism is probably not as important to the growth of monolayer films because the assembly front does not have enough thickness to develop a network of pores.

Particle interactions due to electrostatic, electric double layer, van der Waals (collectively DLVO), and capillary immersion forces are, on the other hand, probably very important even for monolayer films. While the DLVO forces are important only in the suspension phase, Koh *et al.* (2008) suggest that the range of interaction among the particles (that is, the Debye length), should have an impact on the final quality of the colloidal crystal. The hypothesis rests on the premise that the particle film exists in a fully wet but colloidally crystalline state in a regime between convective assembly and subsequent dry-out (see Figure 2.3a)—a premise they have verified convincingly by light scattering experiments.

During dry-out, capillary forces from the curved liquid menisci bridging the particles exert lateral forces (Denkov *et al.*, 1992; Kralchevsky and Nagayama, 1994), promoting colloidal crys-

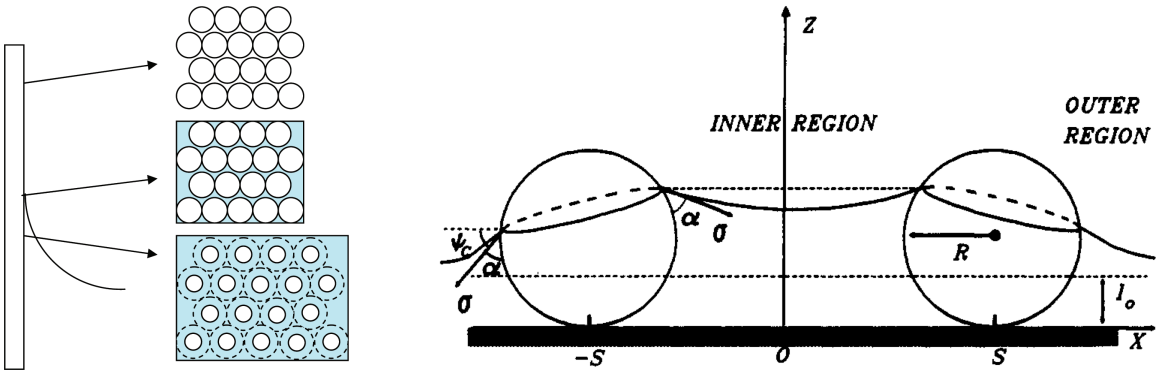

(a) Koh *et al.* (2008) (b) Denkov *et al.* (1992)

Figure 2.3: Two important forces in colloidal crystallization. DLVO forces influence colloidal crystallization in a wet state (a), and capillary immersion forces (b) influence the structure subsequent to drying by giving rise to net attractive potentials between particles.

tallization (see Figure 2.3b). Extended analyses for immersion forces among anisometric particles are also reported (Kralchevsky *et al.*, 2001; Loudet *et al.*, 2005), and such results are certainly relevant to the assembly of zeolite particles.

There are to date, however, no comprehensive models for the entire convective assembly process, nor a very large body of experimental work surrounding the convective assembly of anisometric particles, although several have appeared following the work presented in this chapter (Lee *et al.*, 2006), including the works of Hosein and Liddell (2007a,b). It should be noted that the major unresolved questions in convective assembly of thin films can largely be divided into this area of colloidal crystallization, and the related but more immediately problematic issue of assembly into uniformly thick films. This chapter focuses on the former and introduces the latter; subsequent chapters will address the issue of film uniformity in more detail.

2.2 Experimental methods

2.2.1 Synthesis of zeolite ZSM-2

Zeolite synthesis dates at least back to Bruce (1933) and traditionally involves the preparation of a slurry or gel containing silica, alumina, and a base (often serving also as a structure directing

agent), and subsequent crystallization under hydrothermal conditions. The resulting crystals tend to be large (too large for convective assembly) and generally unpredictable in morphology and size, as is the case in the first reported synthesis of zeolite ZSM-2 from slurry (Ciric, 1968) and subsequently from gel (Barrer and Sieber, 1977). More recent synthesis methods—aimed at producing small (micro- to nano-meter scale) zeolite particles—are generally carried out in aqueous solution, and the zeolite synthesis used in this work is based on such a recipe as described by Nikolakis *et al.* (2001), which was originally due to Schoeman *et al.* (1995).

The ingredients for ZSM-2 synthesis are given in Table 2.1. The recipe calls for the preparation of two separate clear aqueous solutions with the silica and alumina sources. The silica solution is prepared by dissolving TEOS in an aqueous LiOH/TMAOH solution, while the alumina solution is prepared by dissolving metallic aluminum in an aqueous TMAOH solution. Upon complete dissolution of the TEOS and aluminum (about a day), the solutions are filtered through .45 µm syringe filters to remove iron oxide particles (from impurities in the aluminum source), silica particles (from the TEOS source), dust, and other contaminants. The solutions are then combined slowly under vigorous stirring to a final composition of

$$6\ \mathrm{TMAOH} : 1.06\ \mathrm{LiOH} : 1.0\ \mathrm{Al} : 3.4\ \mathrm{SiO_2} : 315\ \mathrm{H_2O}$$

The resulting clear solution is transferred to a PTFE-lined stainless steel autoclave (47 mℓ capacity) and treated hydrothermally at 140 °C for 12 hours under quiescent conditions. Typical amounts for this synthesis route lead to a final solution volume of about 70 mℓ, split evenly into two autoclaves. Yields were not measured, but it is generally understood that aluminum is the limiting reactant, and the synthesis of ZSM-2 by this method often leads to significant formation of an undesired phase (which can be separated by centrifugation).

An alternative hydrothermal synthesis recipe reported by Covarrubias *et al.* (2008) produces ZSM-2 particles of comparable size and somewhat diminished aspect ratio. This recipe is attractive because it can be carried out at a milder temperature of 90 °C, requiring only a a sturdy teflon-lined polypropylene bottle with a tight lid, as opposed to the bulky stainless steel autoclave. The recipe requires a slightly longer hydrothermal treatment time of 20 hours. The batch

Table 2.1: Chemicals used in zeolite ZSM-2 synthesis

Chemical name	Abbrv.	Source	Form
DI water	H_2O	in-house	distilled and deionized
tetramethylammonium hydroxide	TMAOH	Aldrich	25 wt% in water
tetraethylorthosilicate	TEOS	Aldirch	98 wt% in water
lithium hydroxide	LiOH	Aldrich	98 wt% pellets
aluminum	Al	Aldrich	99.99 wt% flakes

sizes were kept at about 70 mℓ, similarly to the previously described method.

Following hydrothermal treatment, the synthesis mixture was cooled to room temperature by contacting the reaction vessel with tap water. The synthesis mixture typically showed signs of sedimentation (by visual inspection of an opaque bottom layer and clear top layer) and was homogenized by agitation prior to post-treatment. Post-treatment of the sysnthesis involved removal of residual reactants by centrifugation washing until the pH was lowered from 14+ to about 8 (requiring about $7 \sim 9$ cycles of 15 min. each at 12000 rpm). The crystals were stored at close to the synthesis concentration of about 4 wt% solids, and diluted to an appropriate concentration with DI water directly prior to film coating experiments.

2.2.2 Film coating method

The specific method of convective assembly used in the following work has been described in detail by Meng (2008), but the salient points are described here. The method is an improvement over that of Jiang *et al.* (1999) in that evaporation of the solvent is enhanced by a drying gas flow delivered by a slot die, also ensuring uniform gas flow rate and therefore uniform evaporation characteristics across the substrate. However, as the method was designed specifically for *in situ* visualization by video microscopy, it did not allow for controlled substrate withdrawal for thickness control.

The films were assembled directly onto the slanted wall of a container such as the one shown in Figure 2.4. The experiment is so designed to allow direct observation *in situ* by a video microscope positioned directly behind the substrate. The substrate, which must also be removable to allow for subsequent characterization, is a glass coverslip (for microscopy slide preparation)

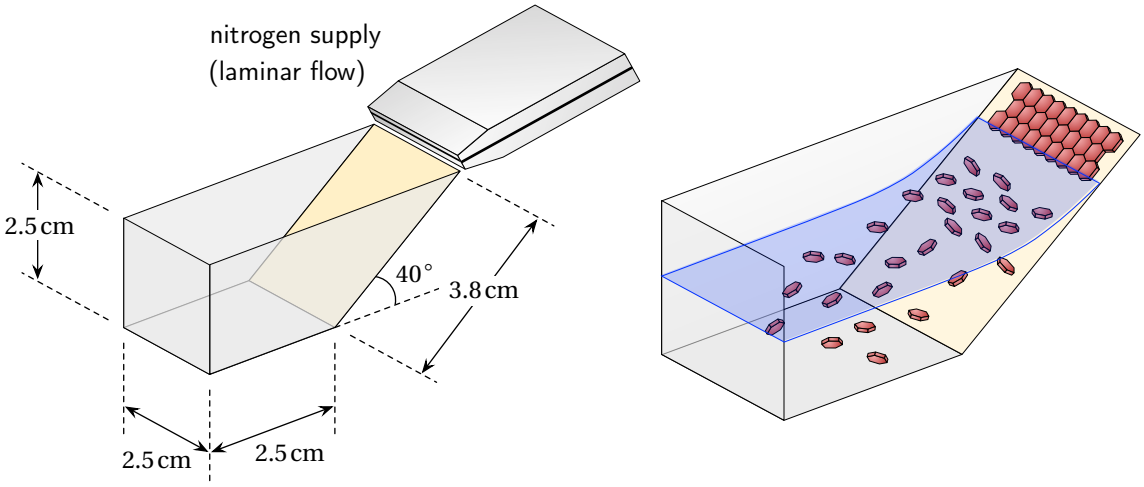

Figure 2.4: Convective assembly apparatus designed for batch coating. The slot die delivers a controlled laminar sheet of gas to enhance the solvent evaporation.

mounted onto the main container with molten paraffin wax. The substrate and cell walls were cleaned by a hydrofluoric acid (HF) soak for 2 minutes followed by thorough rinsing with DI water. The HF soak serves to dissolve the surface and expose a layer of freshly cleaved silica, which is extremely hydrophilic (ultra low contact angles with water).

The film assembly proceeds as described generally in § 1.3, wherein particles convect toward the contact line due to evaporation of the solvent. In the case of the experiments described here, the suspension evaporation also causes recession of the total bath level (this action is equivalent to substrate withdrawal), ultimately causing the contact line to sweep down the substrate to advance the film assembly. Thus, it should be noted that strictly, the process is not steady; the relative position of the drying gas flow to the assembly front changes as assembly proceeds. Furthermore, the bulk concentration may change significantly with time, and in general the film thickness may also change with the implication that the linear growth rate of the assembling film will change. Some of these issues will be explored in later chapters.

The particle suspension was prepared in DI water with concentration ranging from 0.002 % to 0.05 % by weight. These correspond to about $8 \sim 200 \times 10^{12}$ particles/mℓ. For reference, a particle concentration of 0.002 % is sufficient to hypothetically coat the entire vessel with a continuous 100-layer of particles assuming close-packed tiled layers.

Nitrogen (zero grade) was used as the drying gas, and in a typical experiment was delivered at about $1000 \sim 2000\,\mathrm{m}\ell/\mathrm{min}$. Through a 1 inch wide slit, this corresponds to about $6 \sim 13\,\mathrm{cm}^3/\mathrm{s/cm}$. This drying enhancement corresponded to a bulk surface recession rate of about $0.5\,\mathrm{cm/hr}$ (or about $1.4\,\mu\mathrm{m/s}$) in the direction parallel to the substrate.

For comparison, the chemical anchoring method was applied to the ZSM-2 particles (Appendix A.I); results were not promising. Also, experiments in which the substrate's electrical charge was reversed are described in Appendix A.II.

2.3 Results and analysis

2.3.1 Characterization of particles

Following zeolite synthesis, the ZSM-2 phase was confirmed by powder x-ray diffractometry (XRD) on a Siemens D5005 (line collimated, Cu-Kα source) in $\theta/2\theta$ reflection geometry. The nanoparticles were directly observed by scanning electron microscopy (SEM) in either a JEOL-6500 FEG or JEOL-6700 FEG (secondary electron collection at working distances $4 \sim 8\,\mathrm{mm}$ and 5 kV accelerating voltage) to confirm the target crystal morphology of hexagonal platelets with size ranging from 100 nm to 200 nm in the longest dimension (breadth) and 30 nm in the smallest dimension (thickness). In general, samples for SEM were platinum coated to reduce charging; nominal Pt coating thicknesses were $20 \sim 50\,\text{Å}$. Representative characterizations are given in Figure 2.5.

Both of these methods are also applicable to the characterization of the films; SEM provides direct visual characterization, while XRD can provide quantitative information about the particle orientation out-of-the-plane (see § 2.3.4). Because the indexing of the XRD pattern will be important for the discussion of quantifying out-of-plane particle orientation, it is reproduced in Table 2.2 from the original patent describing its synthesis (Ciric, 1968). Details of the crystal structure are discussed by Treacy *et al.* (1996) and is summarized in Figure 2.6.

Briefly, the zeolite ZSM-2 is belongs to to a class of faujasite-like zeolites in which the FAU and EMT isomorphs coexist in various fractions with various domain contiguities. According to Treacy *et al.* (1996), the FAU and EMT structures can be imagined as being built from different stackings of

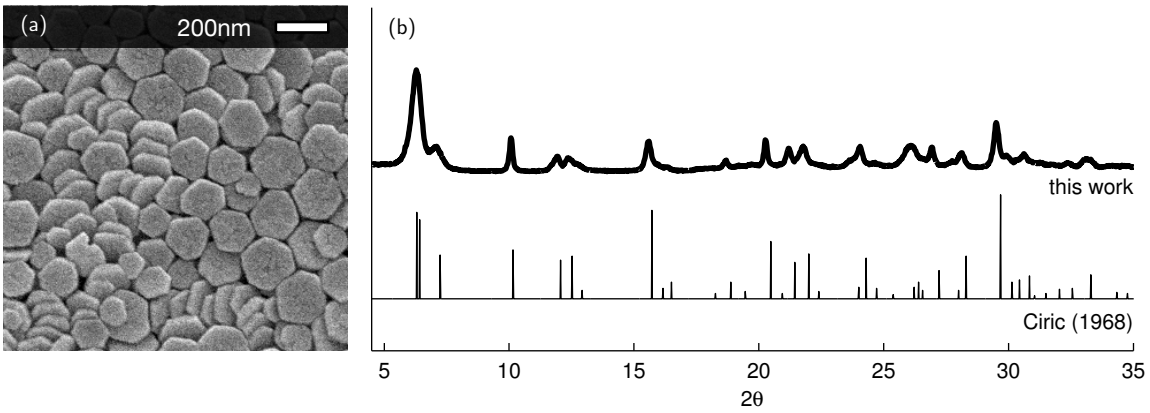

Figure 2.5: Typical synthesis results for ZSM-2. The SEM image in (a) demonstrates hexagonal platelet morphology, while the powder XRD pattern in (b) confirms the ZSM-2 crystal phase; the peaks are in the correct positions, and broadening suggest low crystallinity and/or small crystalline domains.

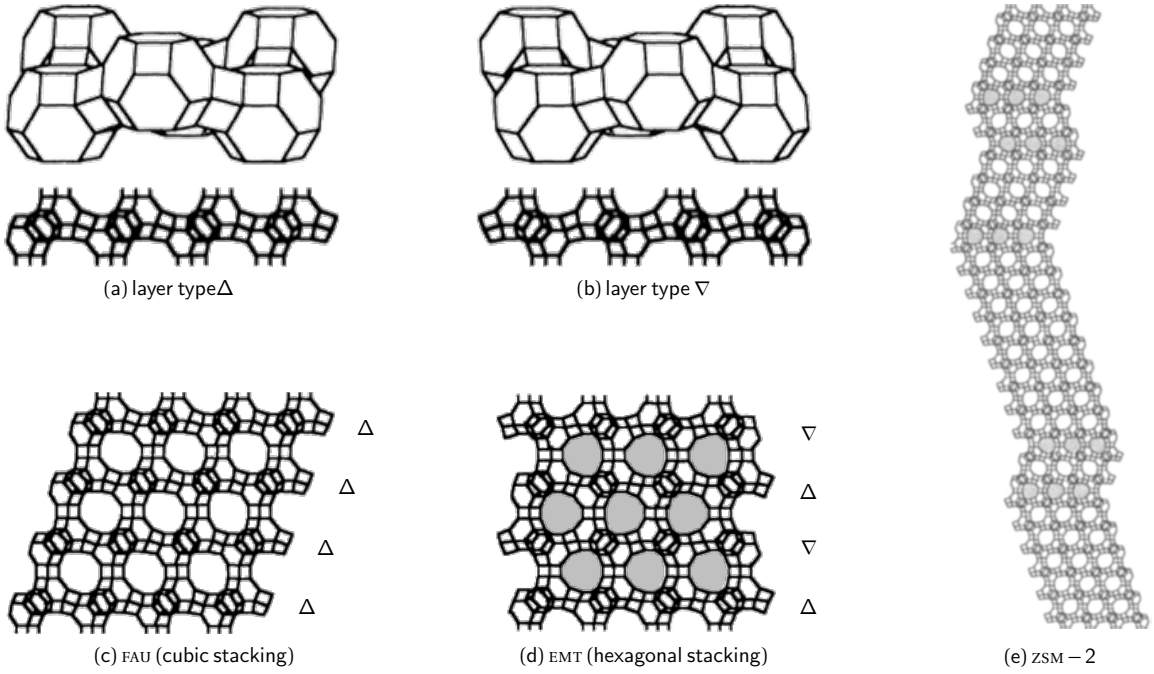

Figure 2.6: The structure of ZSM-2 is predominantly of the FAU structure type with a low probability of EMT intergrowth. Both the FAU and EMT structure types are built from the two layer types Δ (a) and ∇ (b). The FAU structure results when the crystal is built solely of either type Δ or ∇ layers, while the EMT structure results when the crystal is built from alternating layers of Δ and ∇. ZSM-2 is a class of so-called faujasite-like crystals in which the structure is predominantly composed of FAU layer stackings, interspersed with short-lived EMT stackings. Images are adapted from Treacy *et al.* (1996).

Table 2.2: The XRD pattern for zeolite ZSM-2 as indexed by Ciric (1968)

2θ	hkl or (h,k,l)	$100I/I_0$	d-spacing (Å)	2θ	hkl or (h,k,l)	$100I/I_0$	d-spacing (Å)
6.30	002	83	14.00	26.21	652	11	3.40
6.42	200	76	13.80	26.40	218	16	3.38
7.24	210	42	12.20	26.56	733	8	3.36
10.17	310	47	8.70	27.21	653; 308	27	3.28
12.05	321	37	7.34	28.00	715; 555	8	3.19
12.52	004	41	7.07	28.30	527	41	3.15
12.92	400	8	6.85	29.69	753	100	3.01
15.73	005	85	5.63	30.14	920; 760	16	2.97
16.16	500; 430	10	5.48	30.45	726	18	2.94
16.50	510; 501; 431	16	5.37	30.84	850	22	2.90
18.27	440; 225	5	4.86	31.04	930	3	2.88
18.89	006; 530	16	4.70	31.51	852	5	2.84
19.47	600	7	4.56	32.04	904	9	2.79
20.48	602	55	4.34	32.56	816; 746	10	2.75
20.95	335	5	4.24	33.30	(3,0,10)	23	2.69
21.44	425	35	4.14	34.34	952	6	2.61
22.00	631	43	4.04	34.75	(10,2,3)	5	2.58
22.40	107	7	3.97	35.30	(10,4,0); 916	3	2.54
24.00	227	11	3.71	36.35	(2,2,11)	12	2.47
24.30	642	39	3.66	36.95	719; 559	3	2.43
24.72	535	10	3.60	38.41	(0,0,12)	10	2.34
25.38	650	4	3.51				

the same constituent (111) layers designated Δ and ∇ (see Figure 2.6a,b), where ∇ is related to Δ by a mirror operation perpendicular to (111). An FAU structure results when the crystal consists of purely Δ layers (or purely ∇ layers), while an EMT structure results when the crystal consists of alternating layers of Δ and ∇ (see Figure 2.6c,d). The structure of ZSM-2 is characterized by a low probability that any FAU stack is followed by an EMT (long contiguous series of FAU stackings), and a low probability that any EMT stacking is followed by another EMT stacking (short contiguous series of EMT stackings) as illustrated in Figure 2.6e. Thus, ZSM-2 can be considered as having a predominantly FAU structure, although it is not clear how this interpretation of the structure relates to the physical morphology of the individual particles.

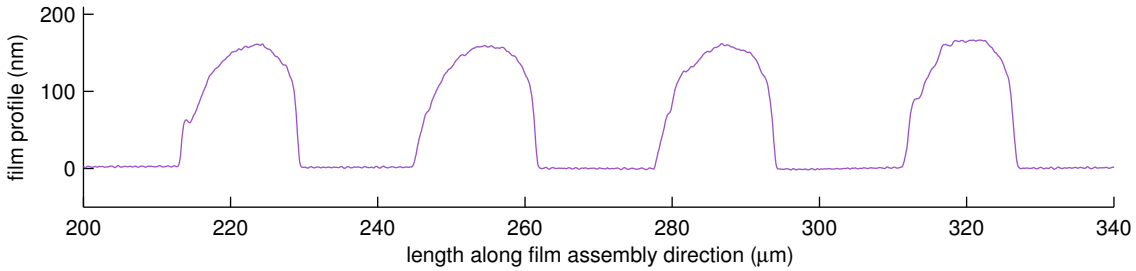

Figure 2.7: A thickness profile (line-scan) of a convectively assembled ZSM-2 film. The scan is oriented so that left corresponds to the top of the film, *i.e.* the leading edge of assembly. Films apparently start thin and grow in thickness. The termination of the film is more abrupt than its buildup. For reference, the ZSM-2 particle is about 30 nm thick and about 200 nm wide.

2.3.2 Film morphology

The resulting final ZSM-2 films generally have a discrete banded morphology, where the bands build up gradually in thickness before abruptly terminating, as shown by a profile scan in Figure 2.7 (taken by a Tencor P-10 contact profilometer).

As the experimental series shown in Figure 2.8 suggests, the films are progressively more "complete" as the bulk particle concentration is increased, all other conditions being the same. Without quantitative information about the thickness of the films, it is not strictly possible to claim that higher bulk particle concentrations lead to increased particle coverage, however such a result would be consistent with the mechanics of convective assembly.

The film assembled from the 0.05 wt% suspension was thick and continuous (without void bands), so that no images were available for inclusion in Figure 2.8. Thus, the film thickness (and continuity) can be controlled in a convective assembly process by adjusting the bulk particle concentration (this had been demonstrated many times over in the literature for thick multilayer films). Chapter 3 will discuss the role of substrate withdrawal as an additional method to control film thickness.

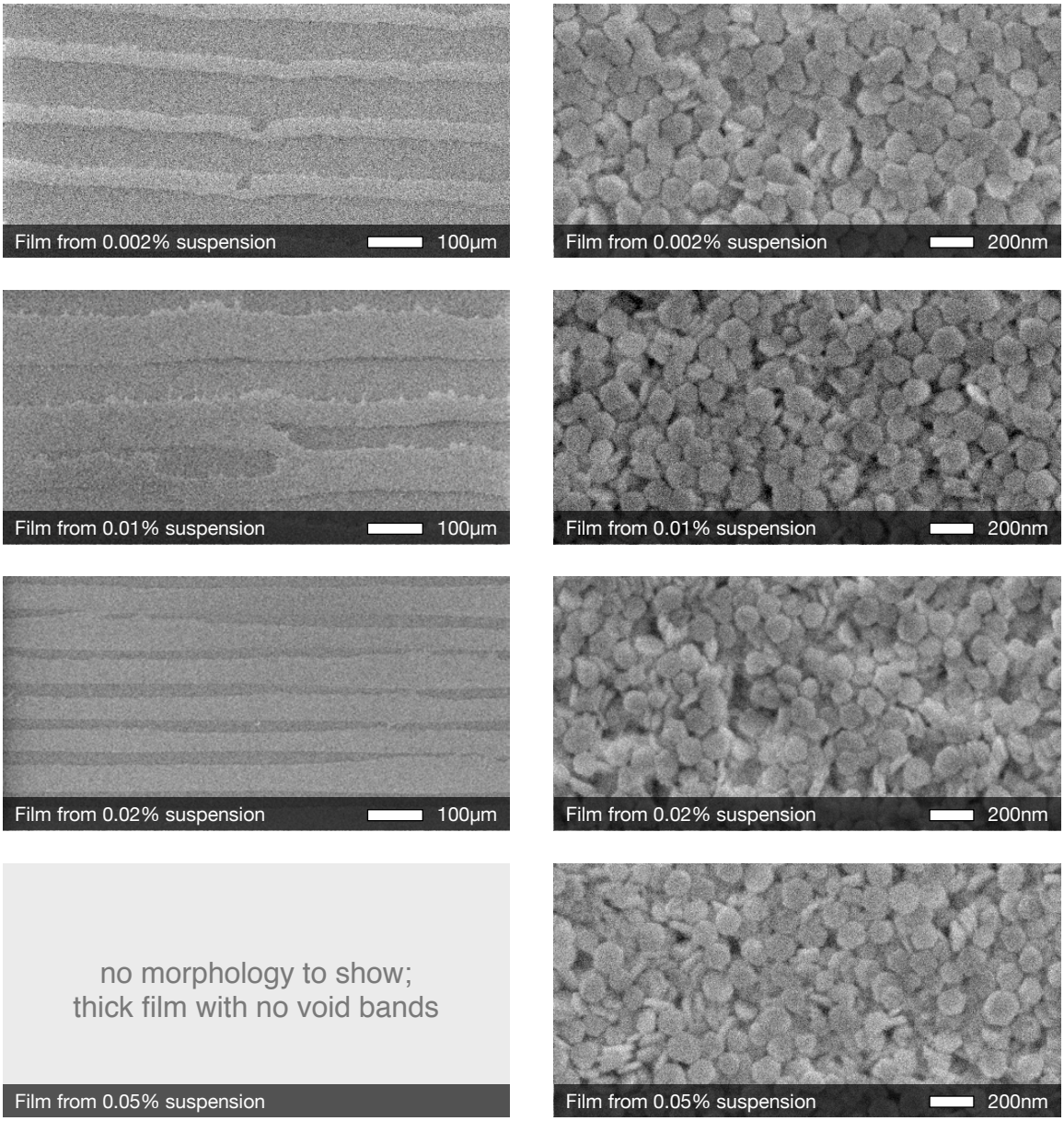

Figure 2.8: Films of ZSM-2 by convective assembly. Images on the left show low magnification, while images on the right show a close up of the particles.

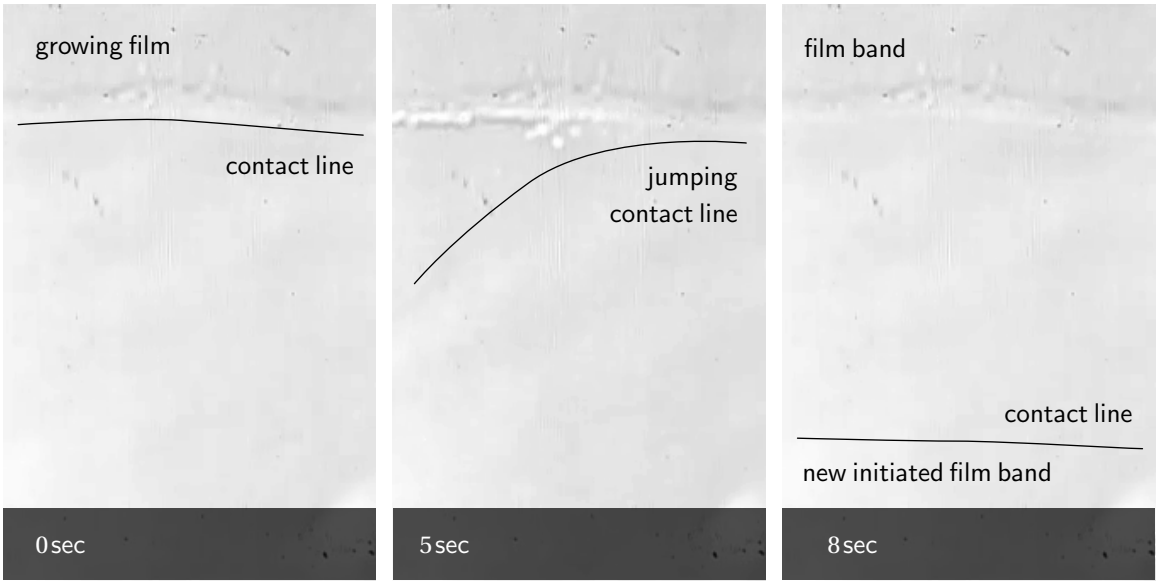

Figure 2.9: Video microscopy of ZSM-2 convective assembly during banded morphology development. At time 0 sec, the film is assembling. The contact line is visible as the film assembly front. At time 5 sec, the contact line is in the process of jumping off the assembly front; the right half visible in the frame is still attached to the assembly front, while the left half has partially jumped. At time 8 sec, the contact line has separated completely from the film (within field of view of the frame), leaving behind a band of particles. The contact line has taken a new position below the band, and has initiated the growth of a new film.

2.3.3 *In situ* observation by video microscopy

The formation of the discrete banded morphology was captured by video microscopy of the coating process. The contact line, visible as a front toward which the particles move, periodically jumps off the growing deposit and starts a new deposition cycle farther down the substrate (see Figure 2.9). Adachi *et al.* (1995) describe this phenomenon as "stick-and-slip" of the contact line, governed by a balance between the increasing component of surface tension in the receding direction at the pinned contact line and some slipping yield force due to viscous effects (see § 4.1). A more detailed exploration of this phenomenon, particularly from the point of view of the final banded morphology, is the subject of Chapters 4 and 5.

2.3.4 Particle orientation out-of-plane

The particles in the film exhibit preferential orientation out-of-the-plane of the film, as demonstrated by XRD in Figure 2.10. Some SEM images of the films are shown in Figure 2.8. While the

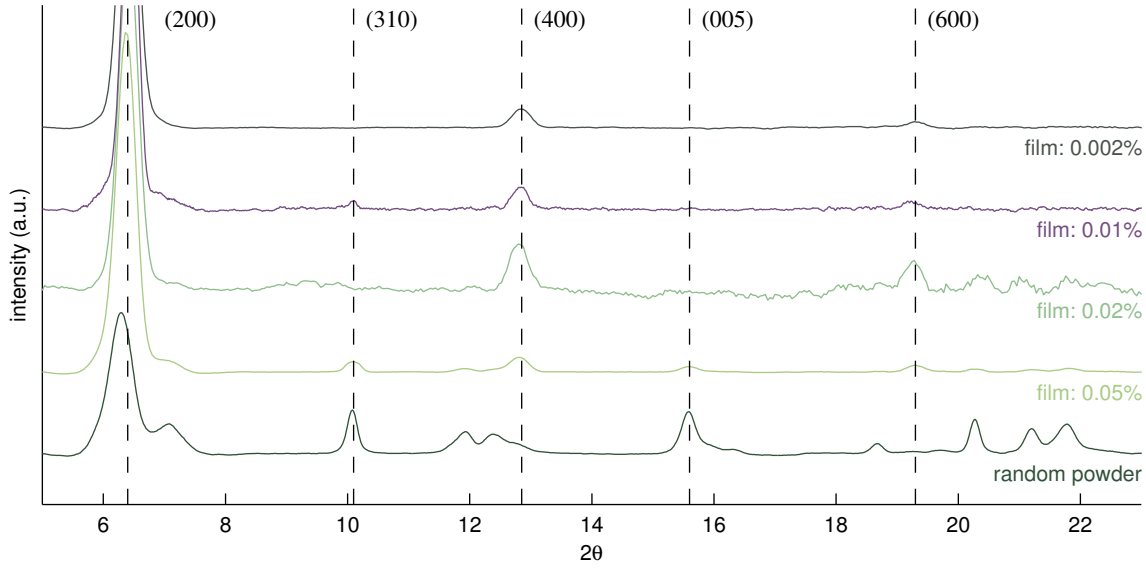

Figure 2.10: XRD patterns for ZSM-2 films compared to that of random ZSM-2 powder. Absence of certain peaks in the patterns for films indicates that the crystal domains, and thereby the particles, are preferentially oriented with the basal plane parallel to the substrate.

images do not particularly suggest preferential orientation of the particles, the XRD patterns in Figure 2.10 show quantitatively that they are in fact preferentially oriented with the particles "lying flat against the substrate".

The random powder pattern in Figure 2.10 corresponds to a sample in which particles are [uniformly] randomly oriented; in other words a sample in which all possible particle orientations are present [presumably with equal likelihood]. It is clear that the XRD patterns for the films lack certain peaks corresponding to certain crystal (particle) orientations. The surviving peaks are indexed as (h00), which come from the Bragg planes parallel to the basal dimension of the particle (for details about ZSM-2 crystallography see Ciric, 1968 and Treacy *et al.*, 1996). Taken together with the fact that scattering radiation was collected with respect to the substrate surface, dominance of the (h00) peaks in the scattering signal suggests that the basal planes of the crystals [particles] were aligned parallel to the substrate surface—particles were preferentially lying flat against the substrate.

In the thick continuous film (0.05 wt% suspension), some peaks other than the (h00) survive, notably the (310) and (005) peaks as highlighted in Figure 2.10. The relative peak intensities of

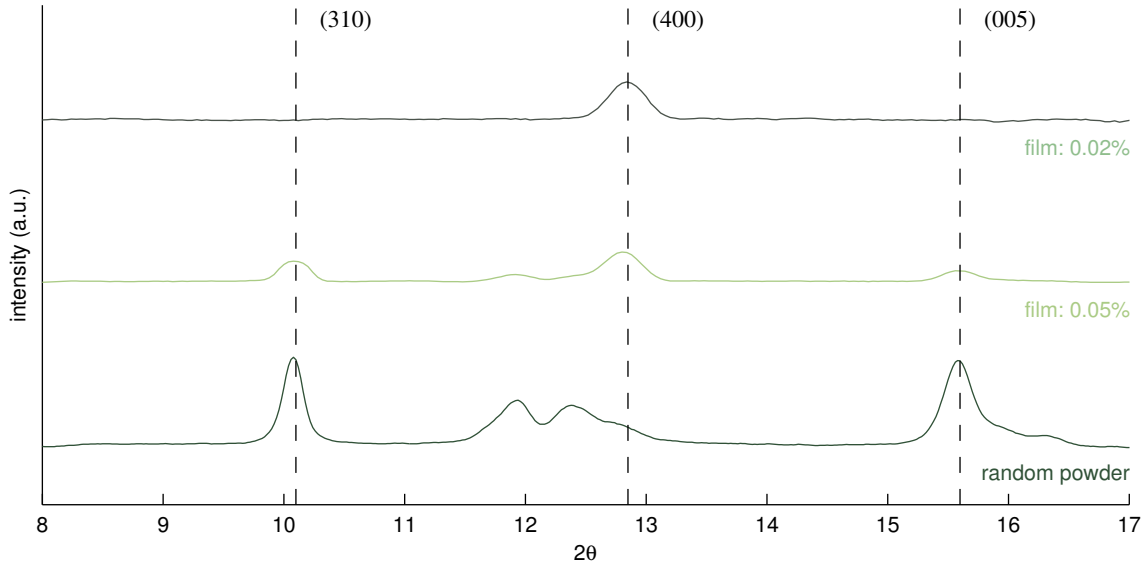

Figure 2.11: A comparison of the relative intensities of the peaks from scattering planes with disparate orientations. The inverted relative intensities from the (400) and (005) suggest preferential orientation of the scattering planes, and ultimately the particles themselves.

the (400) and (005)—actually, any of the other peaks from non-basal scattering planes—in the film versus in the random powder patterns can be compared to evaluate the claim that particles are preferentially oriented in these films. As Figure 2.11 shows, a random powder scatters more intensely from the (005) plane ($2\theta = 15.6°$) than from the (400) plane ($2\theta = 10.17°$) whereas the film scatters more intensely from the (400) plane.

Because the random powder sample and the film contain particles from the same synthesis batch, it can be claimed with some confidence that the particles in the films are preferentially oriented despite the presence of XRD peaks from non-basal scattering planes. Conversely, the thinnest films (films from more dilute suspensions) appear to be *more* preferentially oriented than the thickest film, as their XRD patterns are completely lacking the non-basal peaks.

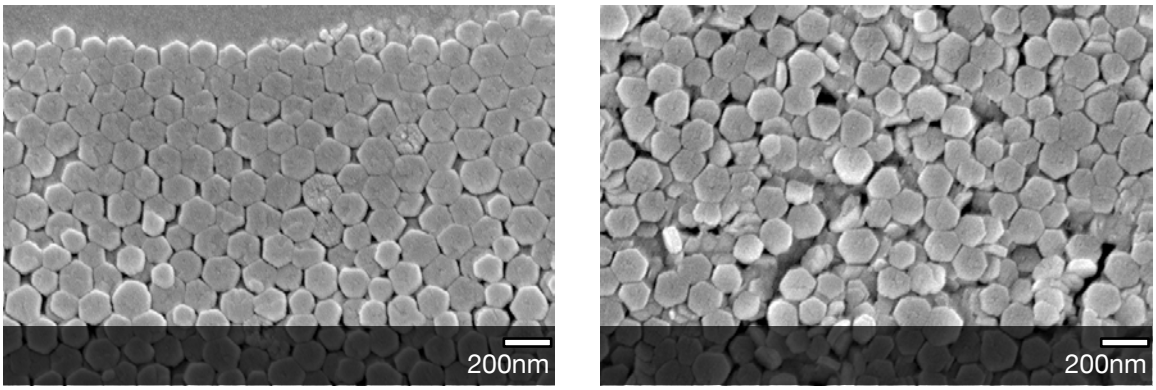

(a) monolayer region (b) multilayer region

Figure 2.12: Films start in monolayer and grow in thickness, as shown in Figure 2.7. The monolayer region seem to be in a tiled arrangement with preferential orientation (a), and the thicker region lose some of this orientational preference (b), although the films are shown quantitatively to be preferentially oriented out-of-plane.

2.3.5 Particle orientation in-the-plane

Recall that the bands in Figure 2.7 suggest a gradual increase in film thickness from the leading edge of each band and a sharp decrease at the trailing edge. In fact, direct imaging by SEM shows that at the "beginning" of any given band, *i.e.* its leading edge, the film is limited to a monolayer (Figure 2.12a). In a representative SEM image (Figure 2.12b) of the "interior" of any given band (where it is thicker), particles appear jumbled.

Remarkably, particles in the monolayer region seem to be oriented preferentially in-the-plane of the film in a "tiled" arrangement owing to the hexagonal shape of the particles. This structure is ideal for applications in zeolite membrane precursors (see § 1.2), but unfortunately does not seem to persist; the film grows in thickness beyond that of a monolayer, and the particles lose the tiled arrangement (although particles still seem to prefer an out-of-the-plane orientation where particles' bases are parallel to the substrate according to XRD).

An attempt to quantify the in-plane preferential orientation can be made by examining (1) the misalignment of nearest-neighbor particles and (2) the degree of symmetry of each particle. These were determine by analysis of several SEM images like the one shown in Figure 2.12a.

First, the misalignment of neighboring particles can be quantified by considering the difference between the angles $\varphi_{i,j}$ of the main diagonals of the hexagons defined by the outline of each

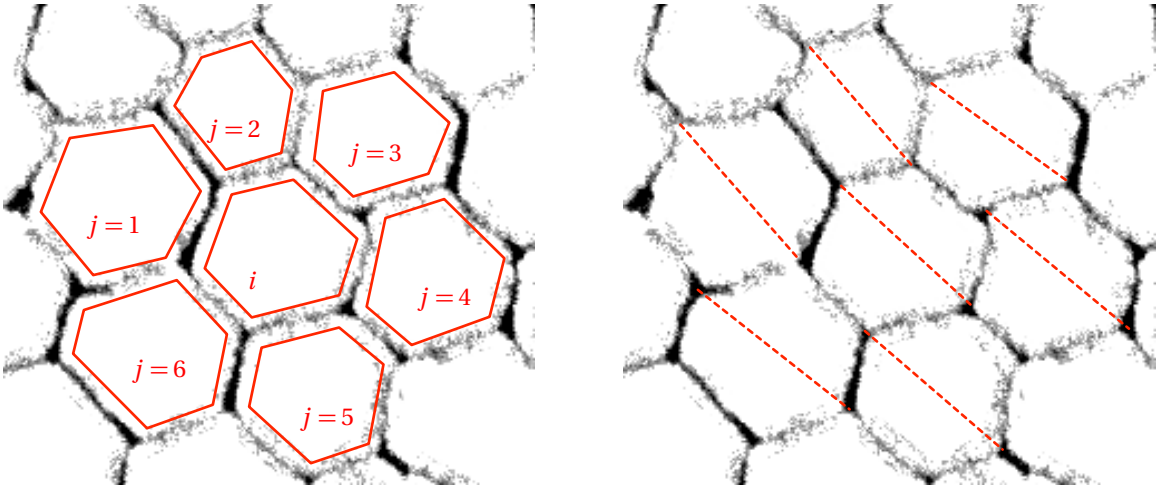

Figure 2.13: The image analysis technique used to quantify preferential in-plane orientation. The diagonals of each particle are compared. Which diagonal to use is determined randomly for each image.

particle i (of n total particles in the image) and its nearest neighbors $j = \{1, 2, ..., 6\}$ (Figure 2.13). For each particle in an image, 6 angles can be measured so that the sample size of the distribution is $6n$. As indicated in Figure 2.13, the choice of which diagonal to use was determined "by eye", which almost always is the choice that minimizes $\varphi_{i,j}$. An example measurement is shown in Figure 2.14a.

Evidently, the maximum allowed misalignment is $\varphi_{i,j} = \pm 30°$ to either side of the diagonal of i, because any greater misalignment can be considered as a smaller misalignment with respect to a different diagonal of i (again, providing a practical guideline for determining which diagonal to compare). The results are summarized in Figure 2.15, and show that $\varphi_{i,j}$ is distributed normally, and as determined by least squares fit, is centered on $-0.2°$ with a standard deviation of $7.3°$ (the probability density decays essentially to 0 within $\pm 30°$). This result is consistent with the interpretation that the particles are indeed preferentially oriented, with any deviation being random. It should be noted that this measure is an ensemble of local measures, rather than a global measure; it could not capture a situation, for example, where the particle orientation gradually twists over large distances.

From the SEM images, it is also clear that the particles have imperfect shapes; their deviation from equilateral hexagons has an obvious influence on the degree to which it is possible for the

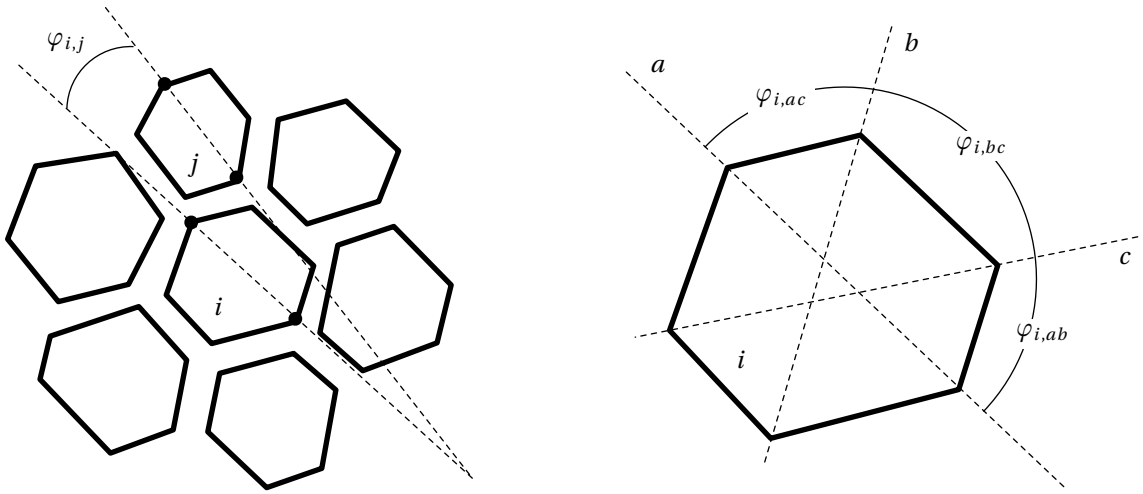

(a) nearest neighbor misalignment (b) self misalignment

Figure 2.14: Examples of measurements to quantify in-plane orientation. Nearest neighbor misalignment (a) and self-misalignment, or degree of symmetry (b).

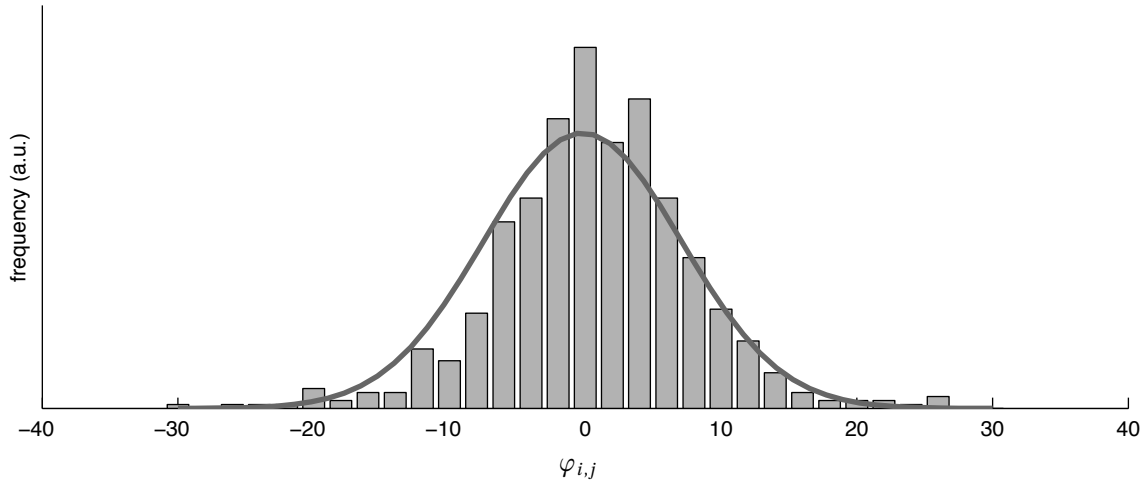

Figure 2.15: Nearest neighbor misalignment is normally distributed, centered on -0.2° with standard deviation 7.3° (best fit curve superimposed). These results are consistent with the claim that particles are preferentially oriented in-plane. The data were collected from a sample of 100 particles for 600 total measurements.

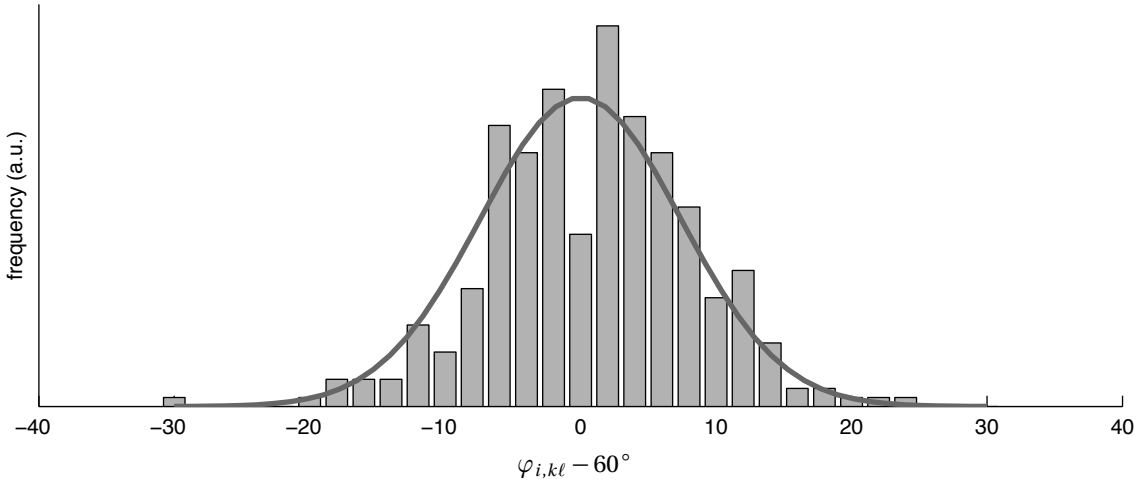

Figure 2.16: The particles' internal degrees of misalignment is normally distributed, centered on $0°$ with standard deviation of $7.4°$ (best fit curve superimposed). The data were collected from a sample of 100 particles for 300 total measurements.

particles to arrange themselves in a tiled manner. Therefore, it seems the results in Figure 2.15 should be considered with some idea of how much the particle shapes deviate from equilateral hexagonal, which can be thought of as a degree of "internal" misalignment of a particle's own diagonals. Specifically, the i-th particle can be characterized by three angles, $\varphi_{i,ab}$, $\varphi_{i,bc}$, and $\varphi_{i,ac}$ between its main diagonals (see Figure 2.14b); the remaining complimentary angles are not independent and so we only consider three. Then the degree of a particle's internal misalignment can be defined as the deviation of these angles from $60°$, *viz.* the quantity $\varphi_{i,k\ell} - 60°$.

The results, summarized in Figure 2.16, show that the distribution of $\varphi_{i,k\ell} - 60°$ is also normal and centered on $0°$ (this must always be true due to the nature of the measure) with a standard deviation of $7.4°$. Interestingly, the widths of the distributions in Figures 2.15 and 2.16 are similar, perhaps suggesting that the degree of preferential orientation in-the-plane is limited only by the imperfection of the particle morphology, where size dispersity (not considered in this analysis) would certainly have an added adverse effect on the arrangement.

2.4 Concluding remarks

In summary, this chapter explored the potential of evaporation assisted convective assembly to produce particulate films with regions of highly ordered microstructure from suspensions of hexagonal nanoparticles. Films start out thin, and generally grow thicker (and more jumbled) as the film assembly proceeds. When the bulk particle suspension is comparatively dilute, the film abruptly ends, giving way to a region of bare substrate. A new film develops yet farther down the substrate, and goes through the same cycle. The result is a banded film morphology that nominally spans the entire breadth of the substrate; to give a better idea of the scope, the image in Figure 2.17 shows a larger field of view than previously shown.

All convectively assembled films display preferential particle orientation out-of-the-plane of the film (evidenced by XRD). At the leading edge of the films (or of each of the bands), the particles are in monolayer, lying flat against the substrate. They are also preferentially oriented in-the-plane of the film in a tiled arrangement. Further, these tiled regions nominally span the entire width of the bands (see Figure 2.17). This remarkable order, though short-lived, is a promising feature of the coating process, potentially useful as precursors to ultra-thin selective membranes. The degree of preferential orientation seems to be determined by the imperfection in each particle's shape. As films develop in thickness, the particles lose preferential orientation in-the-plane and become jumbled, but seem to retain preferential orientation out-of-plane.

It remains to explore the possibility for scale-up, which begs a continuous mode of operation such as those reported by Dimitrov and Nagayama (1996) and Prevo and Velev (2004). A description of such a technique and the development of the associated apparatus is the subject of the next chapter.

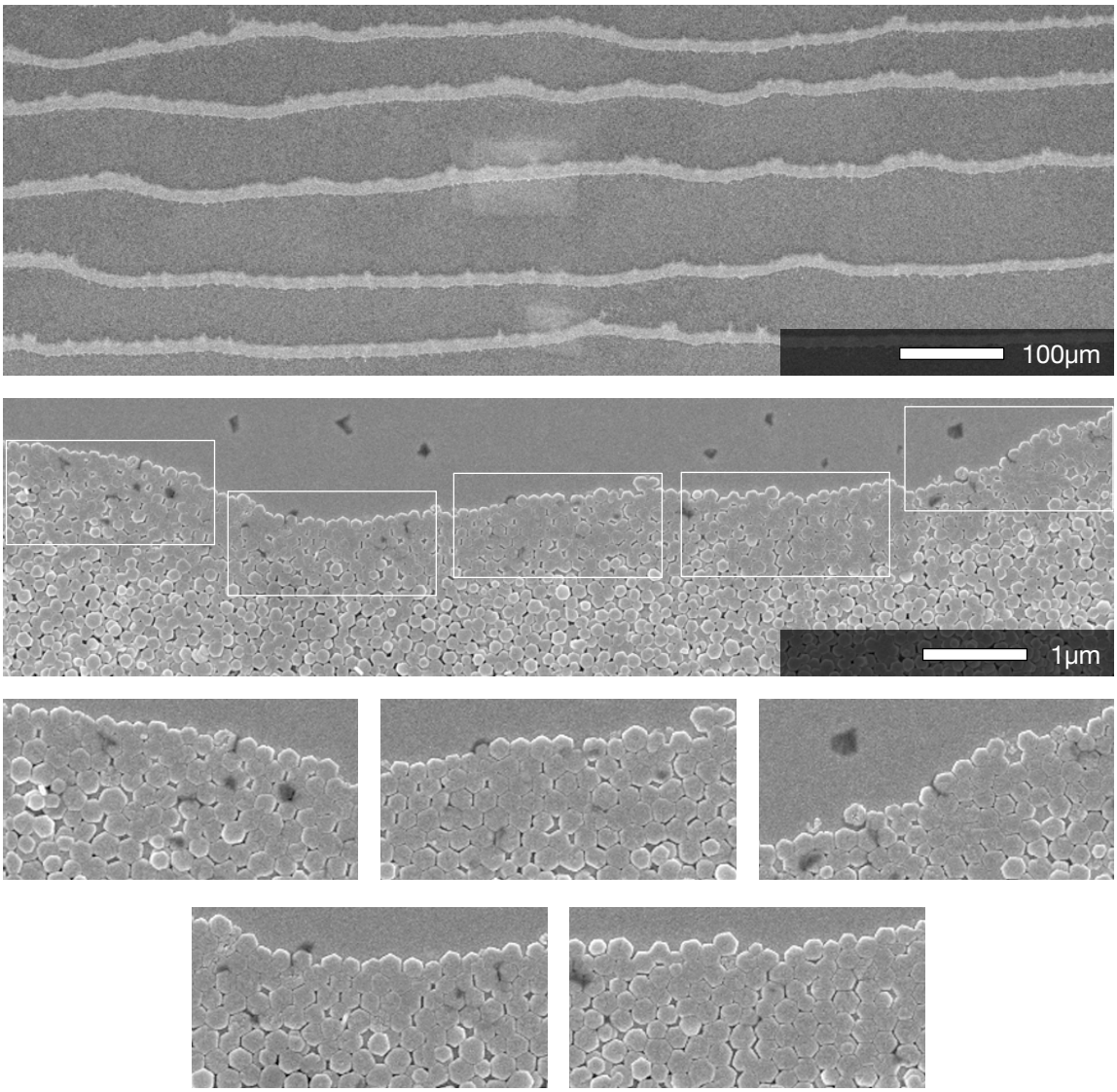

Figure 2.17: Additional SEM images of the convectively assembled ZSM-2 films. The top image demonstrates the regularity of the observed bands, while the image below shows the leading edge of a typical band. The outlined regions are reproduced at the bottom.

Chapter 3

Continuous convective assembly

It was demonstrated in Chapter 2 that convective assembly could produce particle films with preferential orientation, such as would be useful in the fabrication of crystalline membranes. It was noted that the method described lacked a key feature for film thickness control and process scale-up, namely a system for controlled substrate withdrawal. This chapter describes the development and use of a convective assembly apparatus that incorporates both controlled evaporation based on the work of Meng (2008) as well as the idea of continuous mode operation by substrate withdrawal based primarily on the work of Dimitrov and Nagayama (1996) and other subsequent works.

Some of the nanoparticle film assembly work presented in this chapter[¶] is the result of a collaboration with Dr. Mark A. Snyder concerning the assembly of films comprising so-called Lysine-Silica nanoparticles (see § 3.3). Specifically, the apparatus was demonstrated to be capable of producing nearly continuous monolayer films (as well as multilayer films) of the nanoparticles by adjusting the substrate withdrawal speed. These films also exhibited colloidal crystallinity (at least on the surface). The chapter includes some brief descriptions of experiments with zeolite particles, and closes with a discussion of recommendations for further investigation of convective assembly phenomena as well as further development of the convective assembly method and apparatus.

[¶] based partially on published work (Snyder *et al.*, 2007)

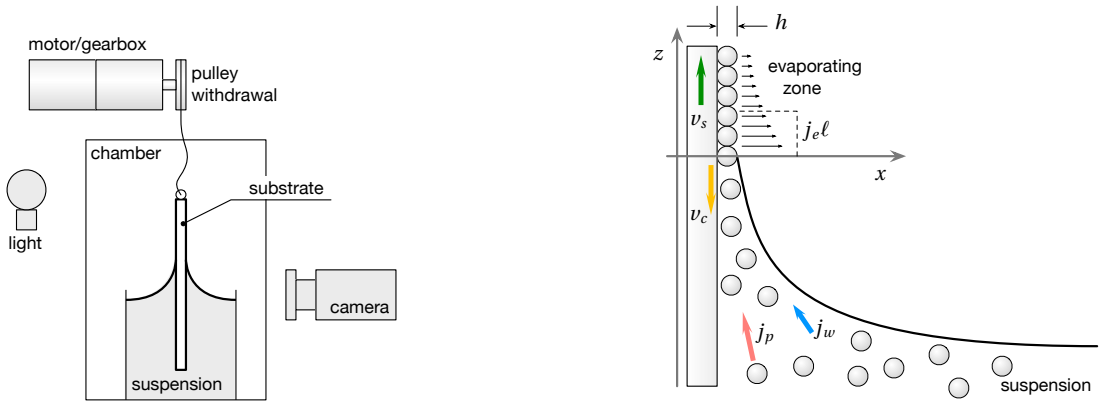

(a) Experimental configuration (b) Process schematic

Figure 3.1: Schemata of Dimitrov and Nagayama (1996) (re-created) describing the experimental configuration (a) and the convective assembly process (b).

3.1 Background

3.1.1 Continuous convective assembly

Dimitrov and Nagayama (1996, 1995), demonstrated that withdrawal assisted convective assembly could achieve monolayer particle films when the substrate withdrawal speed was adjusted to balance the linear growth rate of the film. Although their experiment resembles dip coating (see Figure 3.1a), it is important to note that a fluid mechanical analysis of the entrained liquid film (such as the well-known analysis of Landau and Levich, 1942) is generally not the appropriate framework for describing the resulting particle film thickness, although this relationship is sometimes invoked (see *e.g.* Ghosh *et al.*, 2007). The reason that such analyses are inappropriate is that substrate withdrawal speeds in a typical convective assembly experiment are too slow for liquid film entrainment (a condition supported by direct video microscopy observation of convective assembly to a film growth front, described for example in § 2.3.3).

According to Dimitrov and Nagayama (1996), the convective assembly process, assumed to be at a steady state, is schematized by Figure 3.1b where the rates of film growth v_c and substrate withdrawal (dipping speed) v_s are equal. Clearly, the rate v_c depends upon the particle flux at the growth front j_p and the current film thickness h. The particle flux depends in turn on the

liquid flux j_w, which is assumed to be effected solely by the evaporation of liquid from the region indicated. This total evaporation is assumed to be captured by the product $j_e \ell$, which represent a linear evaporation rate j_e of the liquid and some "effective evaporation length" ℓ.

Specifically, given some *current* film thickness $h = k\,d$ (where k denotes the number of layers and d is the size of each particle), Dimitrov and Nagayama (1996) formulated an expression for the rate of particle film growth *in the direction of substrate withdrawal*

$$v_c^{(k)} = \frac{\Theta \ell}{0.605} \frac{j_e \varphi}{k d (1-\varphi)} \tag{3.1}$$

where 0.605 represents the densely-packed packing fraction of spheres, and φ is the bulk particle concentration. The idea is that as long as the substrate is being withdrawn at a rate v_s equal to the rate of film growth, the parameters on the right hand side of Equation 3.1 should not change, and the process would yield a complete k-layered film. In other words, the continuous k-layer film assembly is described by $v_s = v_c^{(k)}$.

Indeed, Dimitrov and Nagayama (1996) were able to show that by monitoring the film assembly with a camera (see Figure 3.1a) and accordingly adjusting the substrate withdrawal speed v_s *in situ*, they could produce continuous monolayers and bilayers.

3.1.2 Experimental considerations

In the mode described above, convective assembly requires certain material property conditions to be met, many of which were summarized by Dimitrov and Nagayama (1996). These are not true restrictions, but rather conditions that may significantly affect the process.

Wettable substrate

First, we note that all of the convective assembly discussed up to this point have occurred in a wedge-shaped meniscus. In other words, the film substrate must be well-wettable by the suspending liquid (small contact angle). In many convective assembly works in the literature, and

all of the works in this dissertation, the substrate had a silica surface (glass or silicon with oxide layer) and the suspending liquid was water. Under typical conditions (clean glass and pure water), the contact angle between water and glass can be quite small.

However, it is expected that any substrate/liquid pair with low contact angle should be suitable for the mode of convective assembly described here, as long as the liquid is reasonably volatile. Any further issues are expected to be purely practical ones, for example availability, toxicity, chemical reactivity, and so on. For comparison, experiments conducted with relatively hydrophobic substrates (silicon wafer; $\theta_s > 30°$) and aqueous suspensions yielded no films.

Particle stability

Particles must be stable in several senses. Obviously, they should be solid and stable to dissolution or fusing. For the vertically oriented substrate configuration, another consideration is stability against sedimentation. A reasonable rule of thumb is that for latex particles, sedimentation becomes problematic above $D = 1\,\mu\text{m}$ (Dimitrov and Nagayama, 1996) while experience from this dissertation work suggests silica particles with $D = 500\,\text{nm}$ tend to sediment visibly within a day. For neutrally buoyant particles, size is obviously less of an issue.

It is worth noting that for positively buoyant particles, the film assembly process essentially becomes a Blodgett-Langmuir process, where assembly considerations are relegated to the thermodynamics at the liquid-air interface, although instabilities and other issues of film-transfer have led to interesting observations (Huang *et al.*, 2005).

Particle-particle repulsion

Particles must also be stable against aggregation in the bulk liquid, especially for the assembly of thin, densely packed films. For the aqueous zeolite and silica systems, this issue is implicit; silicious surfaces in water over a large range of pH—especially at mild (pH ≈ 7) conditions—carry a negative surface charge due to partial ionization of the exposed hydroxyl groups. This surface charge leads to the buildup of excess charges in the water "atmosphere" surrounding the particle (the electric double-layer), which ultimately contribute to a repulsive potential between any two

particles. The well-known DLVO theory attempts a comprehensive description of inter-particle interactions due to this and other potential fields (*e.g.* van der Waals).

Substrate-particle repulsion

Related to this requirement of mutually repulsive particles is the requirement that particles are stable to adsorption on the substrate (and for practical reasons, they should not adsorb to the container walls either). Again for the experiments described so far, the substrate was generally silicious, so that it carried a like charge as the particle in the suspending liquid (see Appendix A.II for discussion on adsorbing particles, as well as the work of Ray *et al.*, 2005). Briefly, adsorbing particles tend to stick to the substrate and lose the mobility necessary to reorganize into close-packed structures, and tend to have a sparse final structure.

3.2 Description of apparatus

As described at the outset of this chapter, the natural continuation of research in the vein of convective assembly for practical applications is the merging of controlled substrate withdrawal with controlled drying. While the former is necessary in principle to control the film thickness/morphology, the latter is crucial in ensuring uniform and steady evaporation and hence particle assembly. A series of additional (more practical) concerns have shaped the development of the controlled evaporation continuous convective assembly apparatus, described below. Technical drawings complete with dimensions are given in Appendix B.I.

3.2.1 Suspension bath

The method described here relies on the supply of particles from a bath of suspension, out of which substrate is withdrawn (much like in a dip coating configuration). This is in contrast to, for example, supplying the suspension locally in a pre-metered fashion (akin to slot coating). Such a pre-metered system would require much more process control than the simple bath system, which at this stage of research was deemed as probably more trouble than it is worth.

One important consideration is to have a large enough bath volume so as to eliminate sensitivity to (1) diminishing particle concentrations during assembly, as well as (2) the bulk suspension liquid level; in other words to ensure operation as close to steady as possible. At the same time, large quantities of material are often not available due to synthesis constraints, so that some kind of compromise is required.

Another consideration is to achieve the "free meniscus" condition, or that the wall of the bath container facing the coated surface of the substrate should be sufficiently far away that the meniscus decays to a practically "flat" profile. There are two arguments for this design, related to the consistency and constancy of the meniscus region across and within experiments. The surface profile of a confined meniscus would be quite sensitive to minor differences in conditions; not knowing anything about the sensitivity of the convective assembly to the meniscus profile, it is desirable to remove this uncertainty. Furthermore, the free meniscus configuration is less sensitive to the depletion of total suspension volume (related to the earlier point). Specifically, a large exposed surface means that the liquid level should not change significantly as a function of the depleted liquid volume (although the desirability of this condition is eliminated for a confined pre-metered suspension feed).

To establish a consistent bulk liquid level across experiments, a line was scored along the inside perimeter of the container. This line additionally kept the liquid pinned at the proper level and prevented the undesired climbing of the liquid too far up the container walls (simply a practical concern). When the liquid was being loaded into the bath, the amount was deemed to be proper when the liquid was visually observed to make an apparent contact angle of 90° with the walls as it pinned to the scored line.

The bath container shown in Figure 3.2 (where one of the "side" walls is removed for illustrative purposes; the substrate is also shown) attempts to address these considerations. The bath extends far away from the substrate surface to ensure a free meniscus geometry (and also to allow for the drying gas delivery assembly described in § 3.2.3), and the "L"-shape profile of the bath limits the total volume without sacrificing the large surface.

During operation, the bath is completely covered by the drying gas delivery assembly (see

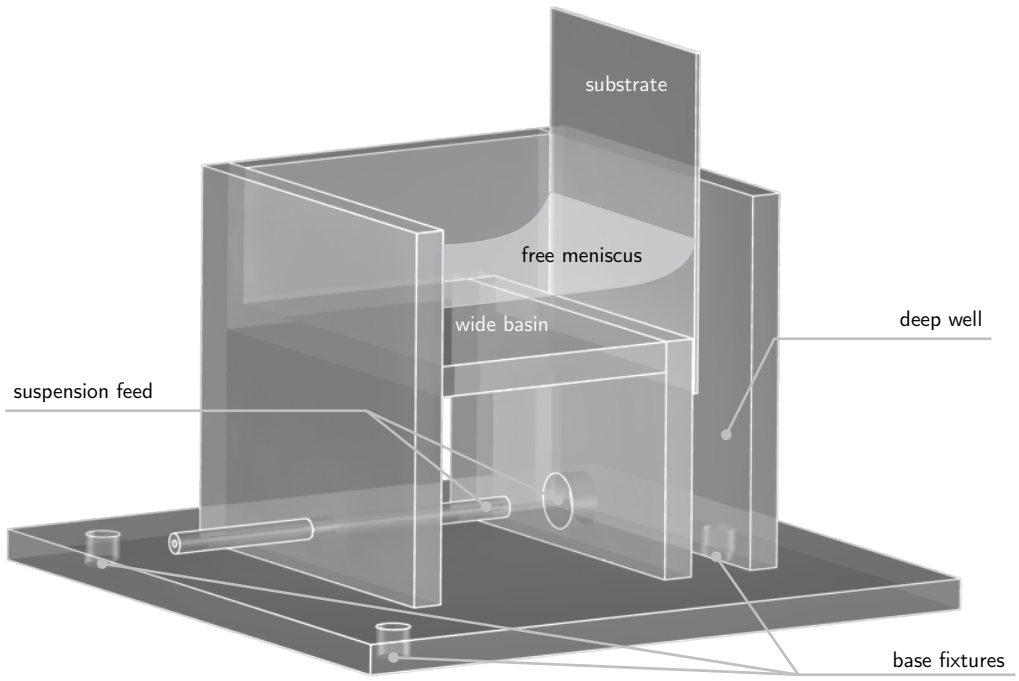

Figure 3.2: Schematic of the suspension bath container. A wide basin ensures a free meniscus configuration, which combined with sufficient total volume, is insensitive to liquid depletion. The bath volume is kept minimal by creating an "L"-shaped container forming a deep well where the substrate is submersed. The base is fixed at three locations to allow for adjustable tilt.

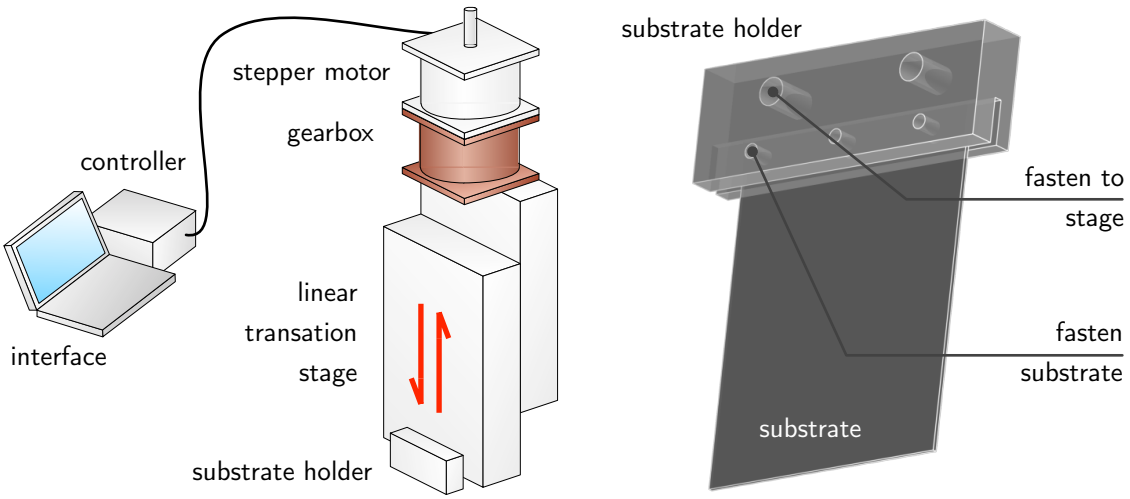

(a) Substrate withdrawal drivechain (b) Substrate holder

Figure 3.3: (a) Schematic of the substrate withdrawal drive chain. Substrate withdrawal is effected by a computer controlled stepper motor driving a linear translation stage via a reducing gearbox. (b) Substrate holder and substrate. The substrate is accommodated by the slit in the holder, and is held in place by nylon machine screws. The holder itself is fastened directly to the linear translation stage by machine screws.

§ 3.2.3); suspension could not simply be poured in from the top, so a feed port was added near the bottom of the bath (NPT fixture to teflon tube to disposable syringe). Ideally, the feed port would have been positioned so that all of the suspension may be drained (and the "shelf" region of the bath would be slanted to prevent residual suspension in the basin), however the design depicted in Figure 3.2 serves all practical purposes. The bath container itself is fixed onto a translating stage by three threaded posts, allowing for adjustable tilt in all directions—a necessary feature for alignment (see § 3.2.4).

3.2.2 Substrate withdrawal

Substrate withdrawal was effected through a drive chain consisting of a computer controlled stepper motor (Parker Compumotor, S/SX 51-57), a gearbox (Bayside, NS23-100; 1:100 ratio), and a worm-gear driven linear translation stage (Tusk Direct, L-BX series) as shown in Figure 3.3a.

The stepper motor's range of rotational speed (drive speed ω) is $0 \sim 25$ rev/s at a step resolution of 50,800 steps/rev. This drive speed is reduced by a 1:100 ratio gearbox to achieve a fi-

nal substrate withdrawal speed applicable to the convective assembly at reasonable motor drive rates ($> 0.1\,\text{rev/s}$). The worm gear driven linear translation stage has a range of about 5.8 cm at 0.254 cm/rev. Thus, the relationship between the substrate withdrawal speed v_s and the motor drive speed can be summarized as

$$v_s = \omega\,\text{rev/s} \times \frac{1}{100} \times \frac{0.254\,\text{cm}}{\text{rev}} \tag{3.2}$$

$$= 9.144\omega\,\frac{\text{cm}}{\text{hr}} \tag{3.3}$$

$$= 25.4\omega\,\frac{\mu\text{m}}{\text{s}} \tag{3.4}$$

Typical motor drive rates were in the range of $0.1 \sim 1.2\,\text{rev/s}$, to give substrate withdrawal speeds in the approximate range $0.9 \sim 11.0\,\text{cm/hr}$ or about $2.5 \sim 30\,\mu\text{m/s}$. The motor step resolution was sufficiently high to ensure "smooth" motion relative to particle sizes; the substrate motion resolution δ_{v_s} assuming a perfect gearbox (no play) gives

$$\delta_{v_s} = \frac{1}{100} \times \frac{\text{rev}}{50,800\,\text{steps}} \times \frac{0.254\,\text{cm}}{\text{rev}} \times \frac{10,000,000\,\text{nm}}{1\,\text{cm}} \tag{3.5}$$

$$= 0.5\,\frac{\text{nm}}{\text{step}} \tag{3.6}$$

One limitation of this system, however, is that the motor control is an open loop so that the set point withdrawal speed is at best a nominal one. In practice, effects from possible set point errors could not be discerned, although any such errors were not quantitatively characterized.

The substrate was attached to the linear translation stage with a substrate-holder of custom design (shown in Figure 3.3b), where the substrate is held in a slit by several nylon screws. The material, shape, and tightness of the screws are important when the substrate material is fragile, as was often the case for the experiments described in the following chapters.

3.2.3 Controlled drying

In the convective assembly experiments of § 2.2.2, controlled evaporation was effected by delivering a gas sheet over the suspension surface as depicted in Figure 2.4 (on p. 16). From the figure,

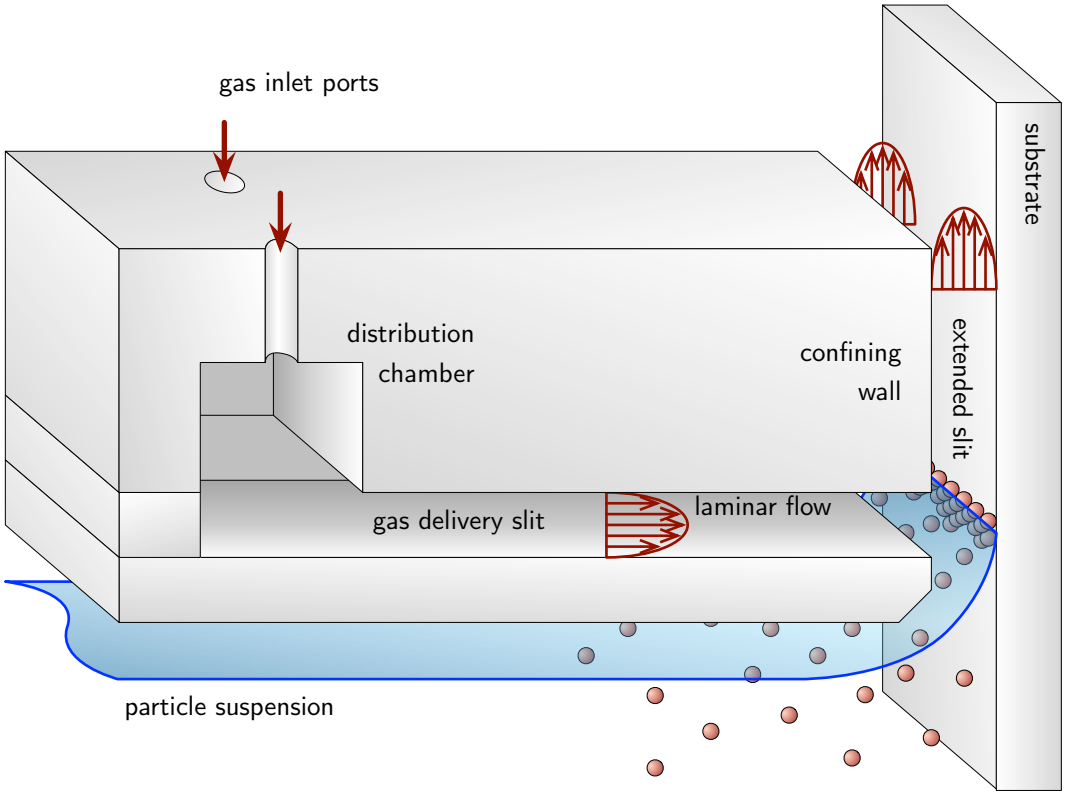

Figure 3.4: Schematic (not to scale) of controlled drying strategy. The gas is delivered through a slit in laminar flow (backed by a distribution chamber to flatten the depth-wise pressure/flow rate profile) and aimed at the liquid meniscus. The slit is continued along the substrate direction by a confining wall in an attempt to prolong the region of laminar flow.

it is evident that although the gas is delivered initially as a sheet via the slit assembly, the exit is quite unconfined and therefore uncontrolled. Moreover, it is aimed toward the bulk, rather than the meniscus at which the assembly is occurring; this is because the apparatus was originally designed to expedite the bulk liquid evaporation (bulk liquid level recession rate) rather than to control evaporation characteristics near the contact line.

The adaptation of this *enhanced* drying into *controlled* drying in the context of the continuous convective assembly apparatus is described here. A descriptive schematic is given in Figure 3.4, where the slit dimensions are exaggerated to emphasize the principle. As the figure indicates, the gas sheet is aimed more directly to the meniscus region, where evaporation is surely most important to convective assembly; in fact, Dimitrov and Nagayama (1996) had pro-

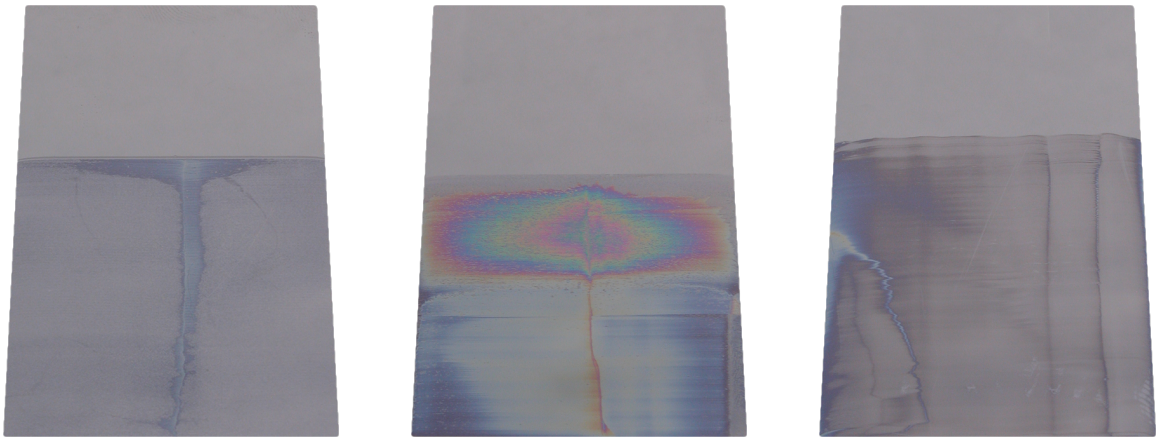

(a) (b) (c)

Figure 3.5: Film uniformity depends strongly on drying gas uniformity and hence design of the drying gas delivery apparatus. Film (a) resulted from nonuniform drying gas delivery due to the lack of a gas distribution chamber; the drying gas flow was stronger near the middle of the coating, where it is thicker as indicated by the color. Film (b) resulted when the drying gas delivery was additionally non-uniform in the coating direction due to a non-uniform width in the extended slit; the film thickness apparently changes from top to bottom as indicated by the coloration. Film (c) resulted from an obstruction in the path of the drying gas (probably a liquid droplet that invaded into the drying gas delivery slit).

posed that liquid evaporation should be restricted to the contact line region to avoid aggregation of particles at the bulk surface (as in skinning).

The gas flow within the delivery slit is nominally laminar, and even as the gas leaves the slit and contacts the liquid meniscus surface, an attempt is made to maintain laminar flow in the gas by continuing its confinement along the substrate direction with a confining wall (see Figure 3.4). Thus, there are two critical aspects to the apparatus's gas delivery portion.

One aspect is the design of the delivery slit and the distribution chamber, and the other is the extended slit region (in the direction of the substrate). The importance of these aspects is exemplified in Figures 3.5a and 3.5b, respectively showing films resulting from a poorly designed distribution chamber and a non-uniform extended slit (due to an alignment problem). The film exemplified in Figure 3.5c, made when the gas delivery was obstructed somewhere along the slit (probably by a droplet of the liquid suspension), further impresses the importance of controlled gas delivery and drying conditions.

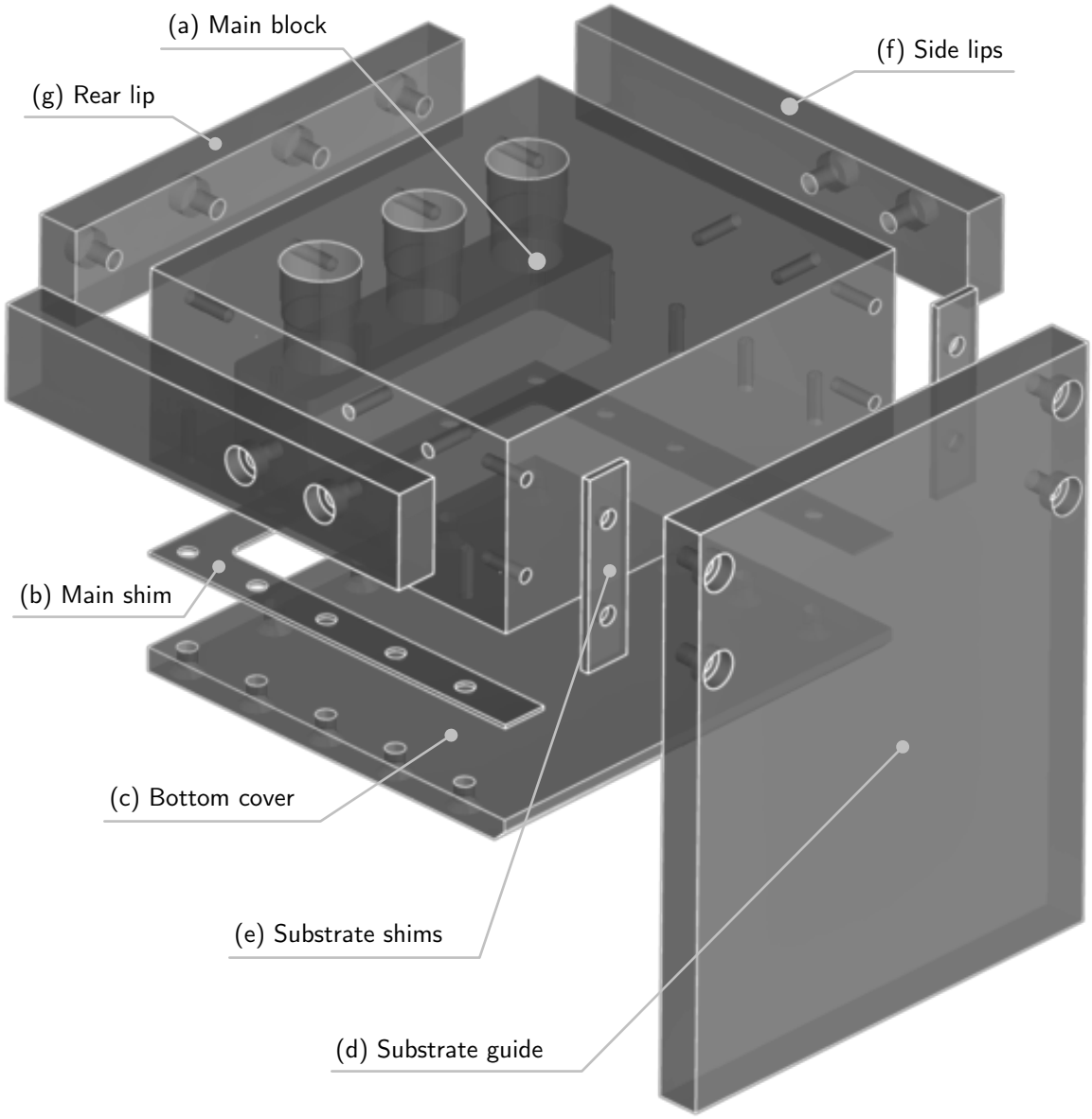

Figure 3.6: Exploded view of the drying gas delivery apparatus. The distribution chamber is contained in the main block (a); the drying gas delivery slit is made up of the main block (a) and bottom cover (b) separated by the main shim (c); the shim thickness sets the slit width. The substrate is properly aligned by positioning it flush with the substrate guide (d), and is held at the appropriate distance from the drying gas delivery slit outlet by the substrate shims (e). The side (f) and rear (g) lips are used to rest the apparatus on the suspension bath (Figure 3.2).

Gas delivery slit and distribution chamber

A comprehensive list of parts composing the controlled evaporation apparatus is given in Figure 3.6. Items (a)-(c) constitute the gas delivery slit and distribution chamber. The main block and bottom cover sandwich the main shim to form a gas delivery slit of precisely uniform width. The main shim is swappable to allow for adjustable slit width, bearing in mind that the gas flow is intended to be laminar. Detailed drawings of the parts are given in Appendix B.I.

To supply the drying gas to the delivery slit, the main block accommodates three gas feed ports (1/8″ NPT) that open up into the distribution chamber. The delivery slit must be long/thin, and/or the distribution chamber must be large enough, to ensure a uniform gas flow profile along the width of the substrate. These dimensions must be decided with an eye toward practicality, such as the economy of size, and in order to mitigate the damage of these limitations, the gas feed ports should be placed in optimal positions (details in Appendix B.II). The feed is supplied directly from a gas cylinder with pressure regulator (set to ~ 15 psi) through a flow controller (Key Instruments, MR3A07BVBN).

Extended slit region

The main block has a significant height in order to possess enough area for the confining wall (see Figure 3.4) that is meant to form, along with a substrate guide (item (d) in Figure 3.6), the extended slit for continuing controlled gas flow after contact with the meniscus. The extended slit width should be the same as the main delivery slit, and is determined by the difference of the substrate shim thicknesses (items (e) in Figure 3.6) and the thickness of the substrate itself.

Because the slit dimensions are generally thin, the alignment of the substrate becomes critical; minor misalignments of the substrate with respect to the slit can have significant consequences in terms of the slit width uniformity, the results of which are exemplified in Figure 3.5b. To facilitate the proper alignment, the substrate guide item (d) in Figure 3.6) is designed to be large and flat so that the relatively easier task of ensuring flush contact between the substrate and substrate guide would ensure a uniform extended slit (§ 3.2.4 describes the details of alignment).

Miscellaneous design considerations

Clearly, both the main shim and substrate shims can be replaced to adjust the gas delivery slit width, as well as accommodate substrates of varying thickness. As a practical matter, a substrate that is thick in comparison to the slit width can be problematic for the distribution of the gas flow as it travels along the substrate; especially for narrow substrates, more gas may be diverted toward to edges of the substrate, significantly widening the edge effects. Thus, the substrate should fill as much of the width of the apparatus as possible, or the shims should be made wider to effectively reduce the width of the apparatus.

The gas delivery assembly completely covers the bath container. One reason is to minimize liquid loss to evaporation, but another more important reason is to force the gas to exit via the extended slit: because of the desirability of a thin gas delivery slit, any other escape route for the gas is likely to offer less resistance than the slit. The "lips" (items (f) and (g) in Figure 3.6) serve to prop the gas delivery assembly atop the bath container to seal it (though not in a strict sense).

The bottom cover (item (c) in Figure 3.6) can be somewhat of a tricky issue. Referring back to the schematic in Figure 3.4, it is apparent that the meniscus must climb sufficiently high onto the substrate in order for a significant portion of it to be exposed to the gas sheet. A typical capillary rise for clean aqueous suspensions on a clean silica surface is on the order of 3 mm, so that the bottom cover must be quite thin, especially considering the additional gap needed between it and the free bulk surface of the liquid. The bevel indicated on the bottom cover in Figure 3.4 is to give the meniscus some clearance.

A practical problem with the thinness requirement of the bottom cover is the potential for deformation in the case where the material is flexible. For example, since all machining is susceptible to precision errors, the bores in the bottom cover and main block (for the fixture screws) may not properly align, leading to a stress on the screws and the parts. This stress could cause the bottom cover to bow so that it pinches the gas delivery slit in either direction, adversely affecting the uniformity of gas delivery along the slit width.

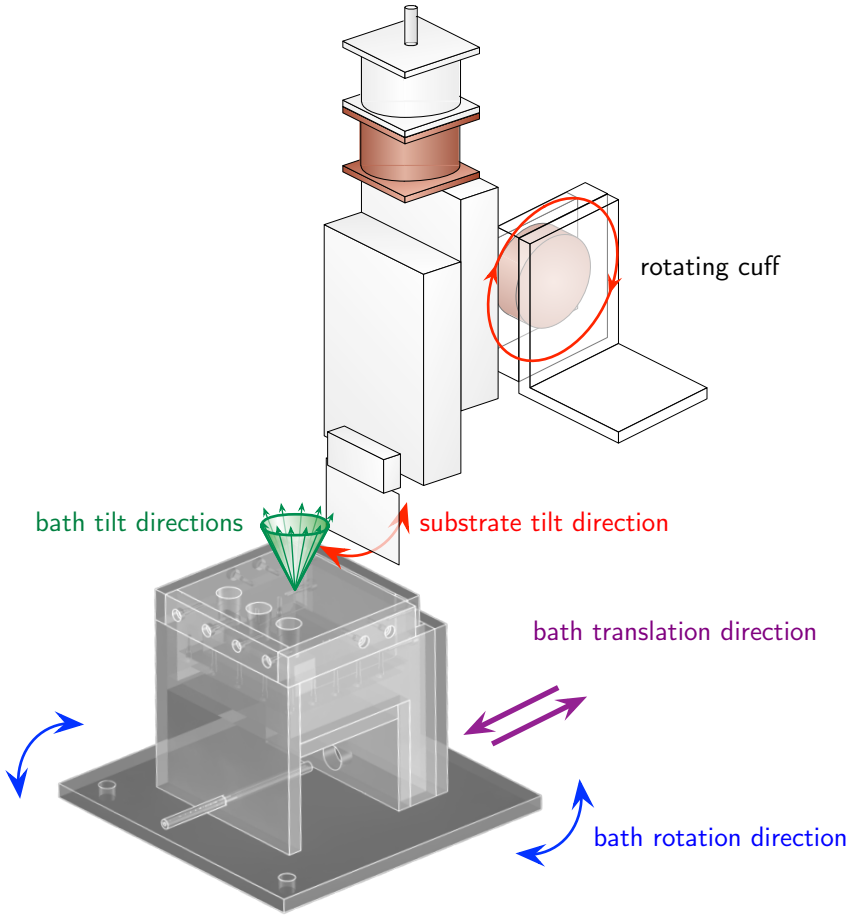

Figure 3.7: The adjustable components of the apparatus during alignment. All of these degrees of freedom serve to align the substrate precisely flush with the substrate guide (of the gas delivery assembly). Thus flushness ensures the proper formation of the extended gas slit between the gas delivery assembly and the substrate.

3.2.4 Overall alignment

As mentioned, alignment of the substrate with respect to the gas delivery assembly can be critical for the outcome of the experiment. Any misalignment can adversely affect the uniformity of the extended gas flow slit along the substrate, leading to film defects like the one shown in Figure 3.5b. Thus, the apparatus design must incorporate several adjustable elements for alignment, which must be performed before every experiment because the entire apparatus is usually taken apart between experiments for cleaning (especially in cases where the coating suspension is to be changed).

The built-in degrees of freedom are summarized in Figure 3.7. The entire bath container/gas delivery assembly can tilt (in the direction indicated by the cone) by virtue of the three-stud fixture scheme described in the previous section. This tilt is important for aligning the substrate relative to the gas delivery assembly. It is also able to rotate to a limited extent in the direction indicated by the arrows because of the over-size bores in the bath container base. The translation in the direction toward and away from the substrate are enabled by a sliding stage on which the entire apparatus is fixed. Of course, a better solution for the tilt and rotation are to employ similar opto-mechanical mounting stages.

The angle of the substrate itself can also be adjusted by the rotating cuff (shown in Figure 3.7) on which the linear translation stage is mounted. This adjustable angle was originally intended for exploring the effects of substrate angle (which ultimately affects the meniscus configuration) on convectively assembled films (recall the slanted substrates in the experiments of Chapter 2). In the end, this parameter was left unexplored for this dissertation. However, the added adjustability did facilitate the alignment of the substrate with the bath container/gas delivery assembly.

3.2.5 Materials of construction

For the purposes of alignment and observing the bulk liquid level, the bath container should be transparent. The material of choice in this particular design was scratch-resistant polycarbonate, which could be sealed together by dissolution with dichloromethane. For aqueous experiments, chemical stability is not an issue. However, polycarbonate (especially at the seams of the container) is vulnerable to ethanol. During experiments in which particle suspensions had significant ethanol content, the seams of the bath were quickly destroyed, resulting in leaks. Obviously, organic solvents are not ideal for use in plastic bath containers.

The gas delivery assembly does not need to be transparent, so balancing chemical resistivity with ease of machining led to the choice of acetal polymer (trade name Delrin) for most of the parts. However, the bottom cover is required to be rigid despite being thin, and Delrin is not rigid enough at the designed thickness. Several versions of Delrin bottom covers were machined, but they always bowed when fixed to the main block, resulting in a pinched gas delivery slit.

Ultimately, the part was machined from aluminum, which is soft enough to work easily but hard enough to withstand deformation under the working conditions.

The shims were cut out of metal shim stock, where consideration was not for the material performance but rather for availability and machinability. Though plastic shim stock would have been ideal for chemical resistivity, metal sheets were much more convenient for precision machining, especially given the possibility of making several versions with varying thicknesses. The metal parts (the bottom cover and all shims) suffered some oxidation due to the humid environment, but this seemed not to pose major problems as long as the assembly was periodically disassembled and cleaned.

3.3 Lysine-Silica particle films

The convective assembly device and associated coating technique were demonstrated using a model nanoparticle system described by Davis *et al.* (2006), which served to refine the convective assembly technique and apparatus by providing particles of reliably consistent characteristics and sizes with relative ease. The particle system was additionally interesting because of the apparently high quality of colloidal crystal formation. Much of the work in this section was also reported in Snyder *et al.* (2007).

3.3.1 Preparation and characterization of Lysine-Silica nanoparticles

Lysine-silica (Lys-Sil) nanoparticles were prepared by extending the recipe described by Davis *et al.* (2006). The synthesis starts with the hydrolysis of tetraethyl orthosilicate (TEOS; 98 %, Aldrich) in an aqueous solution of L-lysine (Sigma-Aldrich) at 60 °C under vigorous mixing for 20 hours. A typical synthesis mixture totaled about 90 mℓ with molar composition

60 TEOS : x lysine : 9500 H_2O : 240 ethanol

where the lysine component was between $x = 1.7$ and 5.4 ($25 \sim 85$ % solubility in pure water).

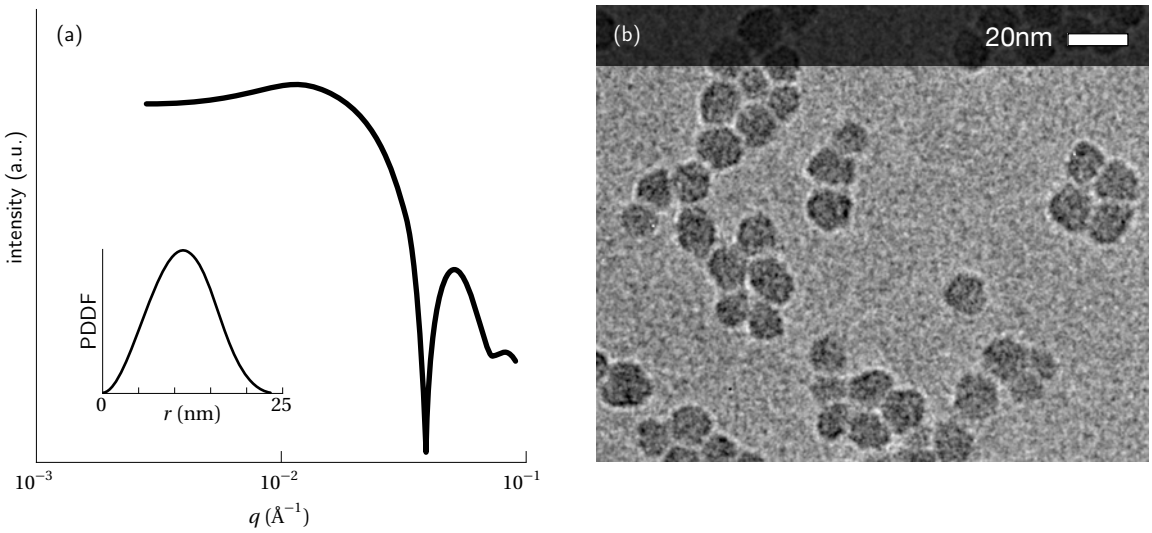

Figure 3.8: Characterization of a typical batch of LYS-SIL particles. The sharp peaks in the de-smeared SAXS pattern (a) indicates high degree of size monodispersity (inset shows the intra-particle pairwise distance distribution function; particles are about 25 nm in diameter). A direct observation [of a different batch] is made by TEM (b) where it is evident that particle shapes deviate somewhat from truly spherical.

Following this initial hydrolysis, the mixture was heated to 100 °C and hydrothermally aged for an additional 20 hours. This synthesis procedure yields approximately 1 vol% particles with size varying from $10 \sim 20$ nm. Average particle diameters were measured primarily by small angle x-ray scattering (SAXS), although dynamic light scattering (DLS) is also a reliable technique with particles about 20 nm or larger in diameter. Particles were quantitatively shown to be highly monodisperse in size by the presence of distinct higher order peaks in the [desmeared] SAXS scattering patterns (Figure 3.8a); such sharp peaks were not observed for the particles synthesized without aging at high temperature (*i.e.* by the original method of Davis *et al.*, 2006). Though SAXS indicated a high degree of monodispersity, transmission electron microscopy (TEM) images of isolated particles betray globular geometries with imperfect sphericity (Figure 3.8b).

As described by Snyder *et al.* (2007), the aged LYS-SIL particles tend to spontaneously crystallize into highly ordered and closed-packed structures, owing in part to the high degree of size monodispersity, although the exact origins of crystallization are admittedly unknown. The colloidally crystalline arrangement is observed in both [cryogenically] vitrified thin films of aqueous suspensions (Figure 3.9) and monoliths formed by evaporative drying of the aqueous suspen-

sions (solids collected from a dried cup-full of suspension; Figure 3.10).

3.3.2 Convective assembly of Lysine-Silica films: experimental protocol

The simplicity of the LYS-SIL particle system both in terms of composition and synthesis, along with the highly monodisperse nature of the particles and their propensity to crystallize, presented us with a model system useful for both evaluating the controlled evaporation continuous convective assembly apparatus, and characterizing the resulting particle films.

The films were coated onto either glass cover slides (2×3 in; Brain Research Laboratories) or silicon wafers cut down to size. Glass substrates were cleaned by a 1 minute soak in 2 % hydrofluoric acid (HF) followed by rigorous rinsing with distilled de-ionized (DI) water. Silicon substrates had to be first cut down to size: wafers were scored and broken, and the edges along the breaks were sanded smooth. The cut and sanded wafers were soaked in an HF solution to remove the extant oxide layer, and treated in piranha solution for 15 min (to eliminate organic residues and re-form a fresh oxide layer) followed by a triple rinse in DI water. Silicon wafer treatment was conducted in the controlled environment of a wafer processing bay at the university's nanofabrication center because large amounts of HF and piranha solution can be dangerous.

Following DI water rinse, the substrates were stored partially wet in an upright position, taking care to prevent contact of the substrate surface with any potential source of contaminants. Especially avoided was contact with hands (gloved or ungloved), which would leave a trace of enough oil to adversely affect the wetting of the substrate. Immediately prior to the experiment, before submersing into the bath (by inverse action of the withdrawal mechanism), the substrate was transferred to the holder with plastic tweezers and rinsed thoroughly again with DI water. To avoid water droplets plugging up the gas delivery system, the substrates had to be dried before being plunged into the slit; drying was achieved by a diverted stream of the drying gas.

In virtually all cases, zero-grade nitrogen was used for the drying gas. It was used directly from the gas cylinder without any thermal treatment or mixing with any other gases. A fine mesh hydrophilic (0.2 µm GHP) syringe filter was placed in-line directly before the drying gas distribution chamber to catch any potential particulates and organic droplets, although it was

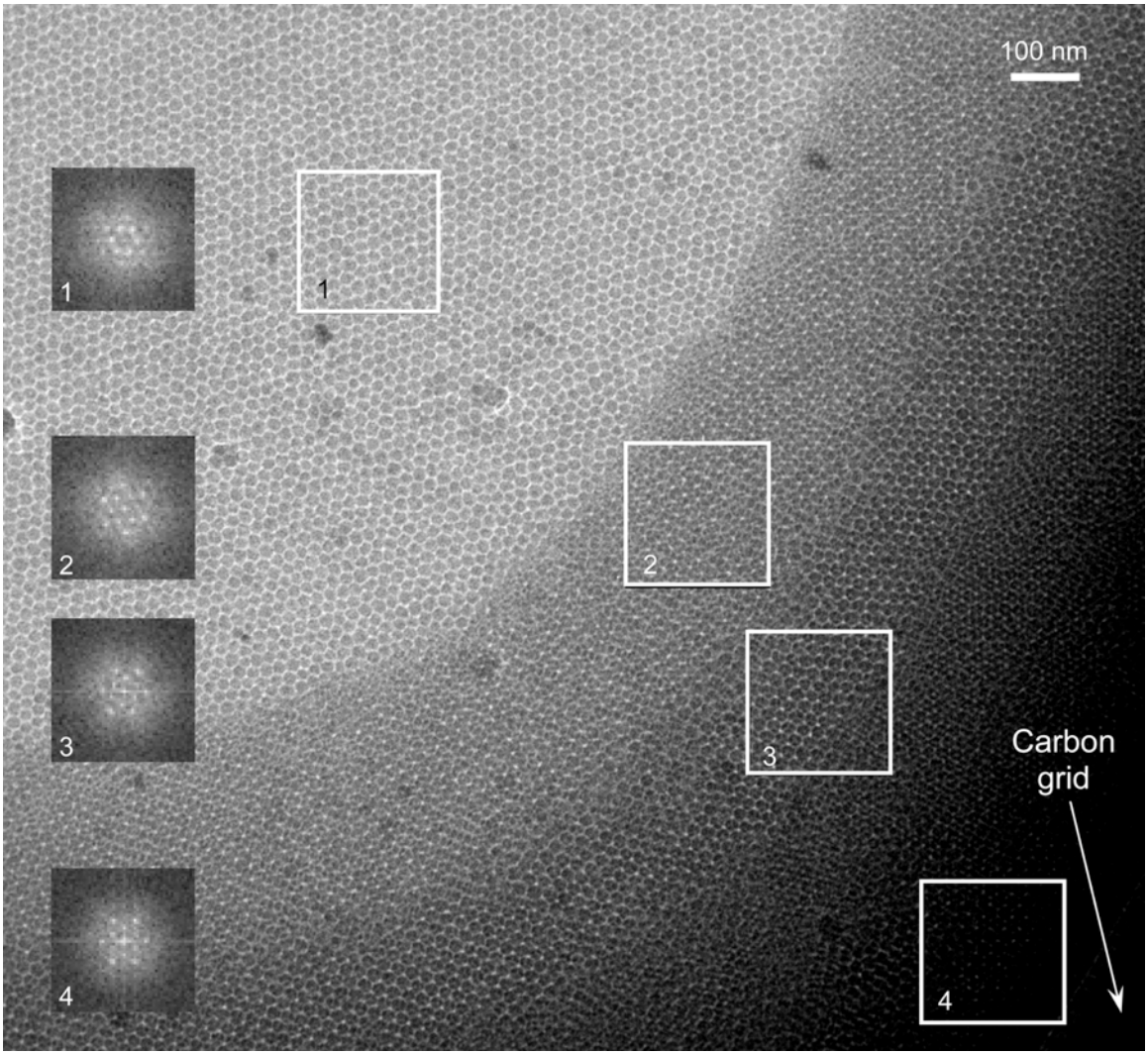

Figure 3.9: Vitrified aqueous sols of Lys-Sil on a TEM grid show signs of spontaneous colloidal crystallization of the particles in the vicinity of the TEM grid supports. The particle layer thickness gradient (manifesting as the darkness gradient in the image) ostensibly follows the liquid film profile that bridges the TEM grid supports. Insets (left) show finite Fourier transforms of the areas indicated by the outlines; these emulated "diffraction" patterns are characterized by distinct spots indicating hexagonal close-packing (in 2-D).

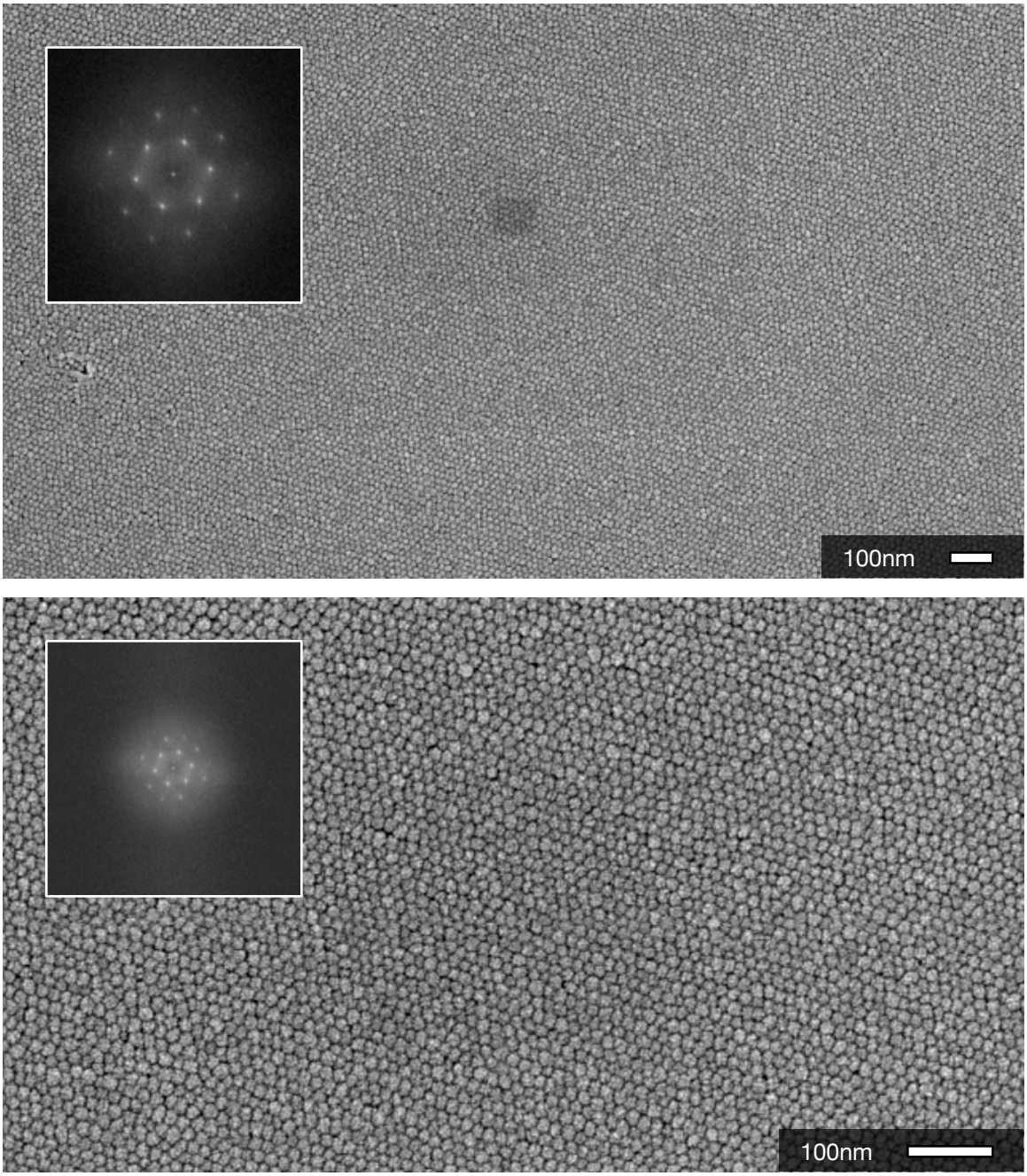

Figure 3.10: A monolith of LYS-SIL formed by evaporation of an aqueous LYS-SIL sol in a cup. Top and bottom images show different magnifications of different regions. Inset finite Fourier transforms of the entire images show distinct spots, indicating hexagonal close-packing (in 2-D).

probably superfluous. Drying gas was supplied at $1.5 \sim 5\,\mathrm{cm}^3/\mathrm{s/cm}$ (corresponding to Reynolds numbers about $35 \sim 110$ in the slit) across the 5 cm width of the device/substrate for a total of $7.5 \sim 25\,\mathrm{cm}^3/\mathrm{s}$ (all converted to STP).

The particle suspensions were kept at bulk concentrations between 0.05 and 0.5 wt%, corresponding to about $0.02 \sim 0.25$ vol%. Substrate withdrawal speeds were in the range $5 \sim 50\,\mu\mathrm{m/s}$.

From the mechanism of convective assembly presented in this dissertation, particularly the discussion by Dimitrov and Nagayama (1996) given in § 3.1.1, a reasonable [however incomplete] description of the continuous convective assembly process can be summarized:

For a bulk suspension particle volume fraction and a certain liquid evaporation rate, some rate of particle flux to the assembly front is set up. The linear film growth rate is determined by this particle flux and the current film thickness at the assembly front. The film growth rate (and indirectly the film thickness) is mediated by the substrate withdrawal rate.

Specifically, it follows that given some reference substrate withdrawal speed v_s^{ref}—say, that satisfies the k-layer steady state assembly condition in Equation 3.1 (Dimitrov and Nagayama, 1996)—any *slower* substrate withdrawal rate should lead to films with *more* particles while *faster* substrate withdrawal rates should lead to films with *fewer* particles. This is also verified in numerous forms by several independent works concerning similar processes (see *e.g.*, Zhou and Zhao, 2004 and Prevo *et al.*, 2005a).

3.3.3 Colloidally crystalline multilayers

The first LYS-SIL film exemplified in Snyder *et al.* (2007) is the continuous multilayered film. This film was coated from a suspension with about 1 wt% particles at 55 µm/s. Images of this film are shown in Figure 3.11 both from the top and the side at a fracture. The inset finite Fourier transform (FFT) shows 6 smeared spots, indicating medium-range hexagonal crystalline order in the particles (smearing of the spots and the absence of higher order spots betrays that the colloidal crystallinity of the film is not as long-ranged as that of the non-film assemblies shown in Figure 3.10); the image itself shows "micro crevices" that seem to disrupt the colloidal crystallinity.

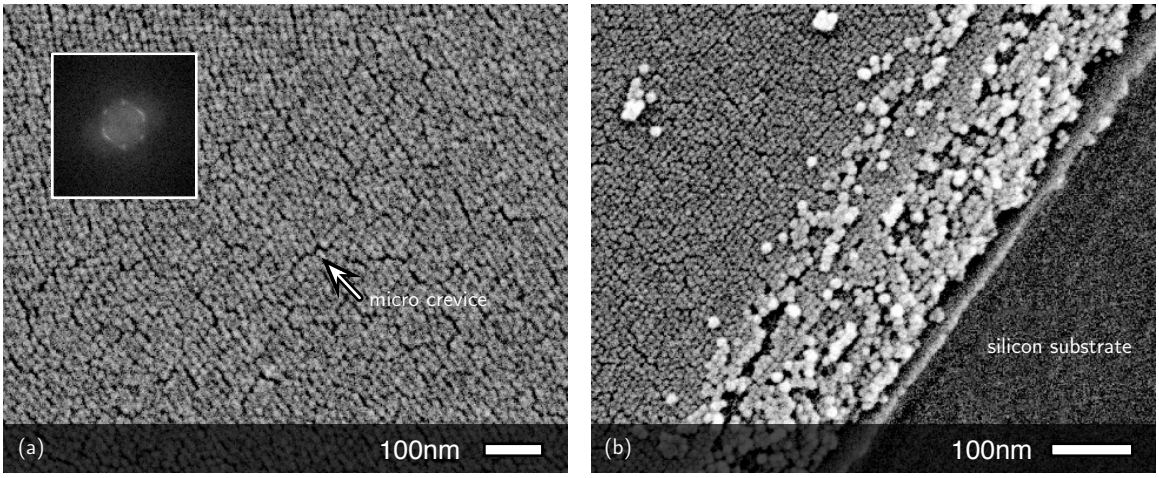

Figure 3.11: Convectively assembled multilayer LYS-SIL film. The SEM image on the left (a) shows the film from the top, while the image on the right (b) shows a cross-section of the film along a broken edge (the edge of the silicon wafer is indicated).

Thus, while the particles clearly have potential for crystallizing into highly ordered structures, some mechanism during convective assembly seems to disrupt that potential, if only to a limited extent. The cross-section in Figure 3.10 further demonstrates that the particles are densely packed in the lower layers, although the image cannot verify any claims about the crystallinity within those layers (FFT of the images can only characterize the visible surface). Evidence of crystallinity in the lower layers of thicker films is shown in Figure A.8 (in Appendix A.III).

Some further experiments and potentially useful notes for extending these results to study both the crystallinity (microstructural quality) of the films and film cracking (macroscopic quality; thickness control) are presented in Appendices A.III through A.V.

3.3.4 Nearly continuous monolayers

The premise of the apparatus introduced in this chapter was that fine thickness control should be achievable by adjusting the substrate withdrawal rate (given a set of other parameters). Indeed, Dimitrov and Nagayama (1996) had shown that *in situ* adjustments of the substrate withdrawal rate could lead to continuous monolayer films. By effecting well-controlled drying (for uniformity and constancy), it was hoped that continuous monolayer films could be achieved without interactive adjustments.

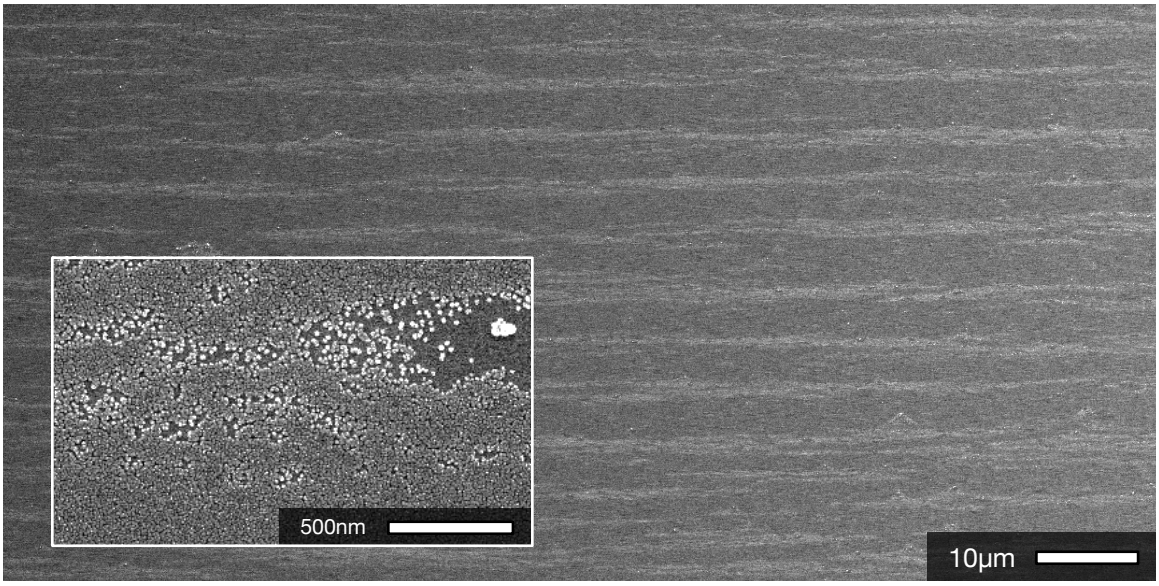

Figure 3.12: Nearly complete LYS-SIL monolayer film. Highlighted regions indicate sparsely-packed particles while the darker background indicates close-packed particles (see inset).

We have been successful in coating nearly complete monolayer films with the LYS-SIL particle system (images shown in Figures 3.12 to 3.14) by retroactively adjusting the substrate withdrawal speed across separate experiments at fixed suspension particle concentration and drying gas flow rate (Snyder *et al.*, 2007). The film in Figure 3.12 is characterized by dark background (close-packed film) highlighted by light streaks (loosely-packed film; see inset).

The film in Figure 3.13, on the other hand, is highlighted by dark strips discernible from the otherwise featureless image. The dark regions turn out to be bare regions on the substrate (devoid of even loosely packed particles), while the lighter region indicates close-packed monolayer (see inset of Figure 3.14), which is shown to exhibit short-range colloidal crystallinity (inset FFT). Another noteworthy feature of the film in Figure 3.14 is the indication of a mono- to bi- layer transition, visible above the bare region as a slight highlight. The fact that the bilayer transition immediately precedes the void strip in Figure 3.14 is suggestive that such transitions accompany all of the voids. A profile scan (Figure 3.15a) shows that in fact, bilayer transitions occur even more frequently than the voids.

The apparent periodicity of the bilayer locations is reminiscent of the banding phenomenon

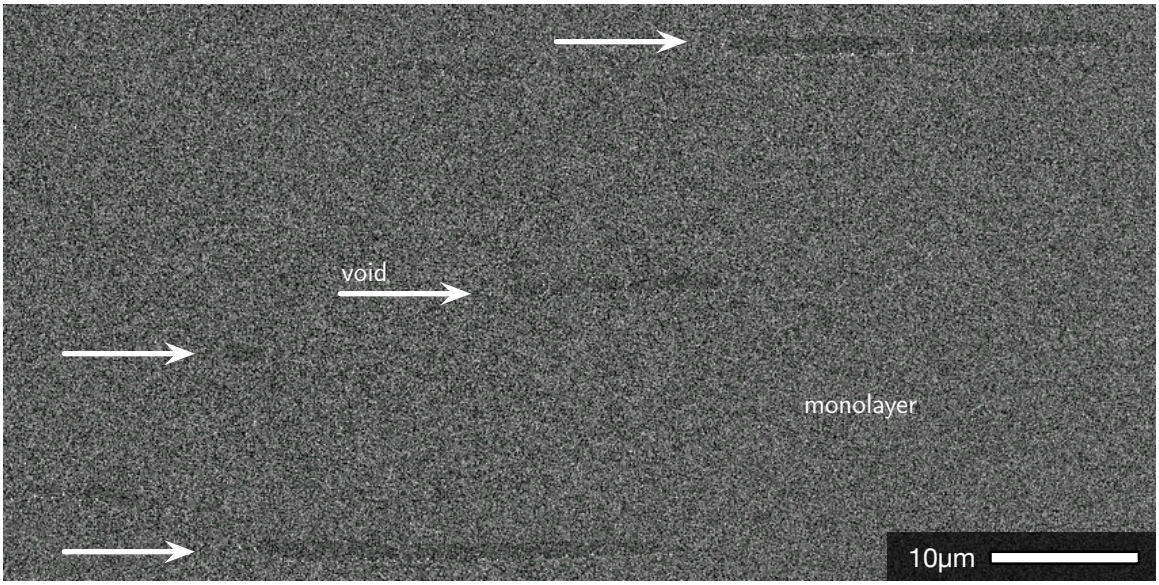

Figure 3.13: Nearly complete LYS-SIL monolayer film. Defects (in the form of voids, or bare substrate) are evident as dark strips in the otherwise featureless image.

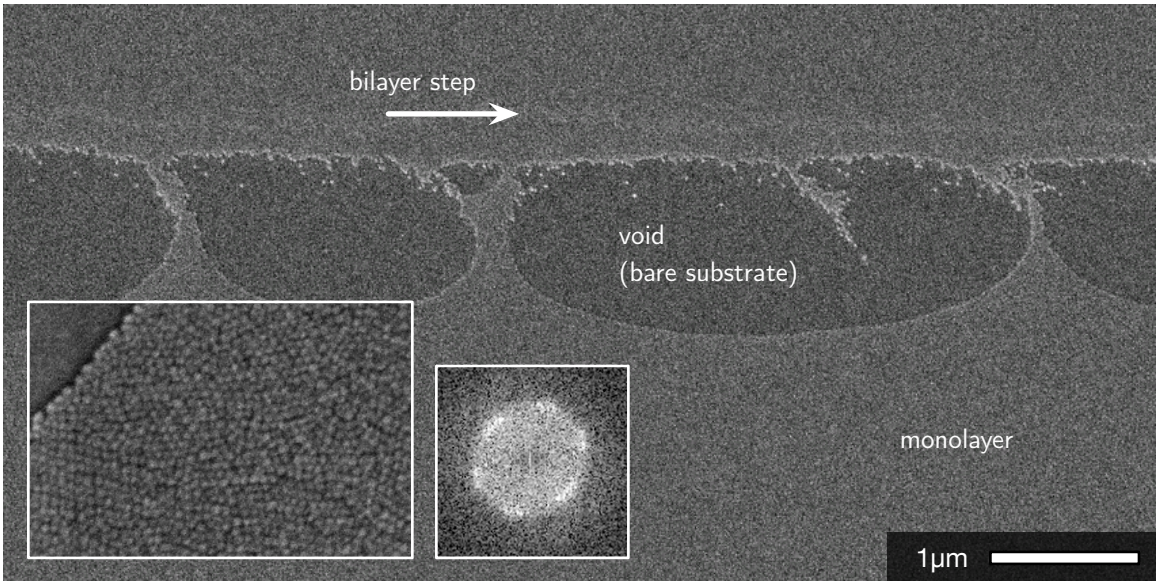

Figure 3.14: Higher magnification SEM images of the nearly complete LYS-SIL monolayer film (Figure 3.13) at a void region. A subtle highlight above the void indicates the presence of a step-change in film thickness (from monolayer to bilayer). The left inset shows resolution of individual particles. The right inset shows the FFT of a monolayer region, indicating short-range hexagonal order (colloidal crystallinity).

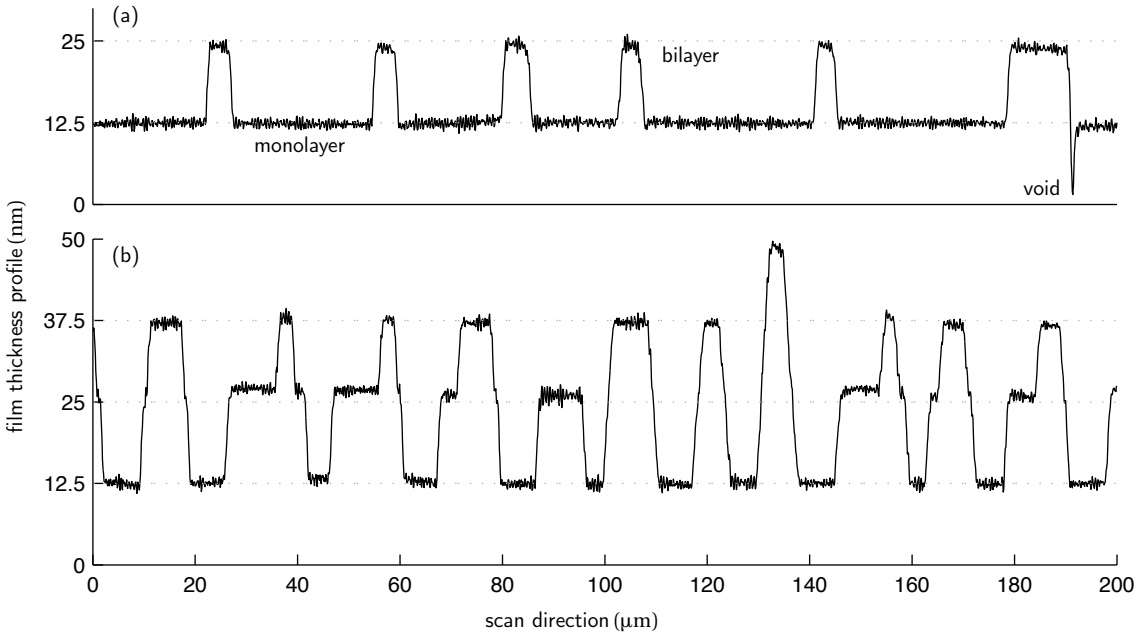

Figure 3.15: Thickness profile scan of a near monolayer (a) and "continuous multilayer" film (b). Particles are independently determined to be about 12 nm in diameter, corresponding well to the apparent steps in the profiles. The nearly monolayer film has periodic void and bilayer defects. The multilayer film shows no voids, but multilayers up to at least 4-layers.

observed in § 2.3.2 with the ZSM-2 films. A profile scan of a "continuous multilayer" LYS-SIL film ("continuous" in the sense of being completely covered), reveals that the film suffers modulations in its thickness, resulting again in a banded pattern (Figure 3.15b).

3.3.5 Banded films

As indicated in Figure 3.15b and reiterated in Figure 3.16, films generally do not have an integral number of complete layers; rather, they have a banded profile. Further, the periodicity seems quite regular and the results are easily reproducible, implying that there may be some avenues of systematic study of these films. Before we discuss these, however, it is worth mentioning that we have observed several other kinds of patterned films (see Appendix A.V), which were not very regular or reproducible, but nevertheless quite interesting.

Although the profiles in Figure 3.15 suggest periodicity, they do not possess quantitatively measurable regularity. It was found, though, that sub-monolayer bands—*i.e.* banded films with

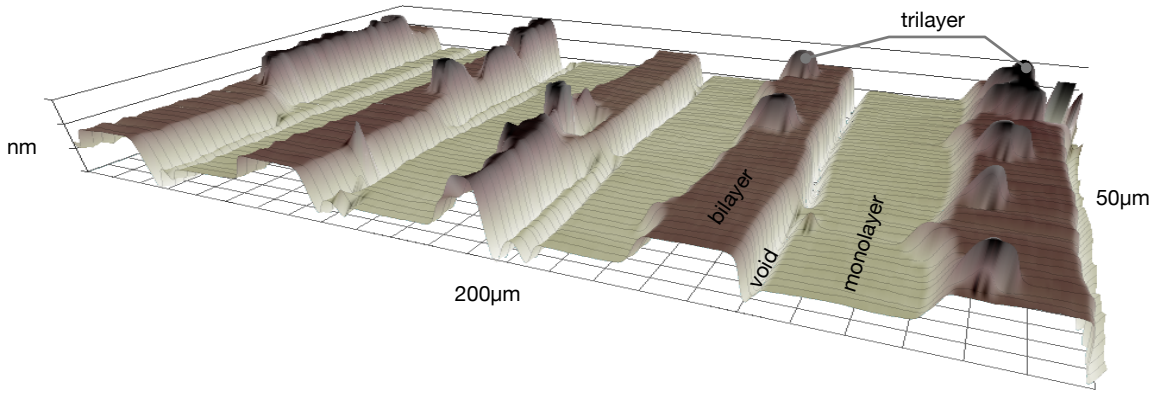

Figure 3.16: Areal profile scan of a multilayered LYS-SIL film. This multilayer film *does* possess void regions (indicated) and up to 3-layers of particle film.

alternating bands of bare substrate and *strictly monolayer* regions—do possess striking regularity as demonstrated in Figure 3.17. Such monolayer banded films can easily and reproducibly be assembled by operating in a substrate withdrawal speed regime that is higher than the speed $v_c^{(1)}$ necessary to assemble a complete monolayer (see Equation 3.1 on p. 33).

Specifically, the film shown in Figure 3.17 is part of an experimental series in which the substrate withdrawal speed was varied between 5 and 50 μm/s, spanning both the [banded] multilayer and banded monolayer regimes. Increasing withdrawal speed allows fewer particles to assemble into the films. Accordingly, the experiments summarized in Figure 3.18 shows (as the substrate withdrawal is increased) transitions from a [banded] multilayer to a near-monolayer (the film shown in Figure 3.14), and further transitions to banded monolayers.

In Figure 3.18, film (f) is the same near-monolayer film that was shown in Figures 3.13 and 3.14. Consistent with expectations, there are fewer particles assembled in film (b), for which the drying gas flow rate—and therefore the evaporation-induced convection and particle flux—was reduced. Films (a) and (e) were coated at low enough substrate withdrawal speeds that multiple layers could assemble, although the images still hint a banded structure (albeit on larger length scales). A caveat, probably due to experimental variability, is that the films (b) and (c) are inconsistent with the expectation that film (c) ought to contain fewer particles.

Overall, the results in Figure 3.18 confirm the role of substrate withdrawal in controlling the average film thickness, namely that fast withdrawal speeds lead to thinner films due to a compe-

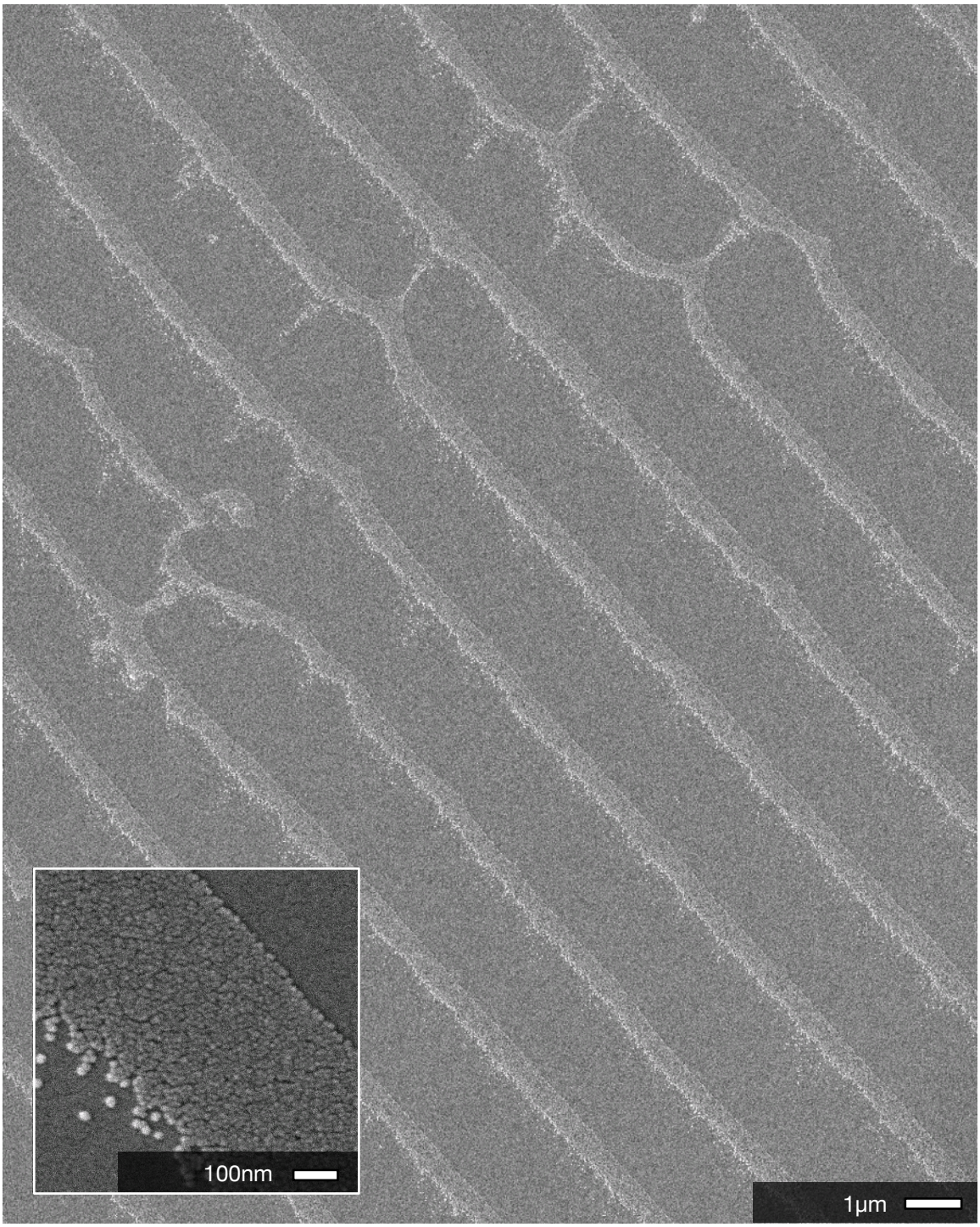

Figure 3.17: Banded monolayer film from LYS-SIL. Inset shows that each band is a close-packed monolayer (short-range colloidal crystallinity).

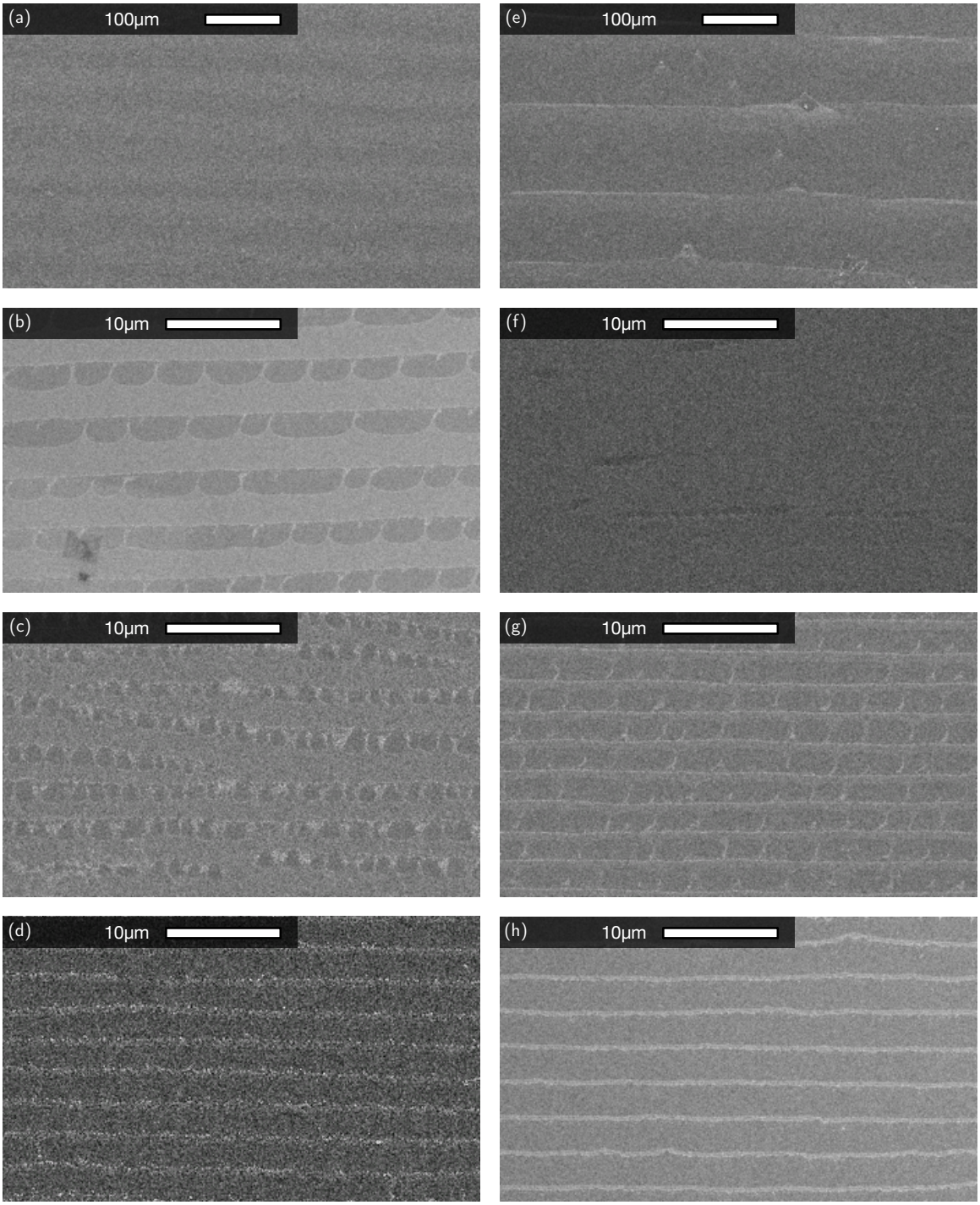

Figure 3.18: Banded monolayer films of Lys-Sil at varying drying gas flow rates and substrate withdrawal speeds. Left and right: $1.6\,\mathrm{cm}^3/\mathrm{s}/\mathrm{cm}$ and $4.8\,\mathrm{cm}^3/\mathrm{s}/\mathrm{cm}$ drying gas. From top to bottom: 5, 15, 27.5, and $50\,\mu\mathrm{m}/\mathrm{s}$ substrate withdrawal.

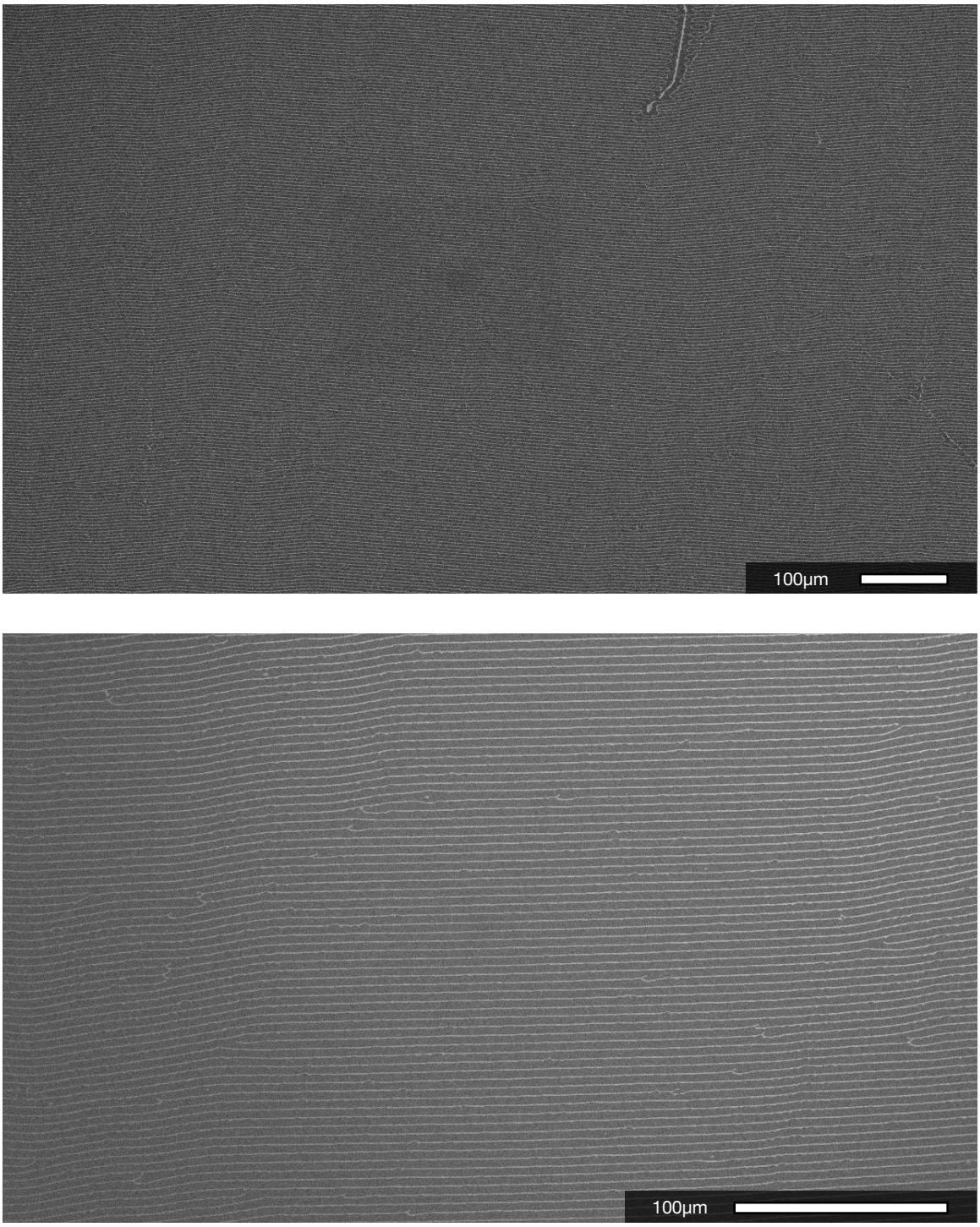

Figure 3.19: Low magnification SEM images of monolayered bands show very high degree of regularity over long ranges. The imaged regions are, however, scarred by occaisional defects.

tition between contact line advancement and particle flux to the contact line. In the case of sub-monolayer films, this thinning manifests as the formation of discretely patterned films characterized by banding, in which monolayer bands of decreasing width (width increasing withdrawal speed) are separated by void bands of similar widths.

The interesting result here is that in sub-monolayer films, the particles tend to arrange in a surprisingly regular banded arrangement, similarly to the multilayer banded films observed in both the LYS-SIL and the previously described ZSM-2 system (though the latter results from a non-continuous mode of operation; see Chapter 2). To better illustrate this regularity over long ranges, Figure 3.19 shows some SEM images at the lower limit of magnification. The nature of this banding phenomenon is further examined in Chapters 4 and 5.

3.4 Zeolite films

Let us now recall that the original motivation for opening the investigation into convective assembly, specifically its refinement described in this chapter, was part of an effort to provide a fabrication route for zeolite particle films (with potential application as precursors to continuous pure zeolite membranes). The LYS-SIL particle system described in § 3.3 presented us with a nice model system to test and refine the convective assembly method and apparatus. Admittedly, the focus of the remaining chapters of this dissertation are dedicated to the examination of the banded morphology of convectively assembled films, regardless of their constituent particles. The following section can be considered a brief digression from this vein, in which some experiments concerning zeolite applications are described.

3.4.1 Films of ZSM-2

From the results of Dimitrov and Nagayama (1996) and the work presented in § 3.3, it seems that monolayer films can be coated at an appropriate substrate withdrawal speed given some bulk suspension particle concentration and a drying gas flow rate. Without modeling the actual particle flux with respect to convective assembly process conditions (such as described by Dimitrov and Nagayama, 1996), one can anticipate that the appropriate speed can be determined by

successive experiments at varying substrate withdrawal speeds with retrospective adjustment, based on the relative particle coverages achieved in each experiment. This idea led to the nearly complete monolayer LYS-SIL films described in § 3.3.

Similarly, a series of experiments with the zeolite ZSM-2 were conducted, in which films were assembled from a 0.1 wt% suspension at a constant drying gas flow rate of 4.8 $cm^3/s/cm$ and varied substrate withdrawal speeds. According to lessons of § 3.3, such experiments could help us to empirically approach the monolayer assembly speed ($v_s \rightarrow v_c^{(1)}$). The first half of the series ran from $v_s = 5$ to 25.4 µm/s (Figure 3.20).

Experiments in this series were carried out from the same suspension (no replenishment), which is increasingly diluted as more and more experiments are carried out and the particle supply is depleted . The order of experiments (b, e, a, c, d) may explain the inconsistent result that the film in Figure 3.20d has seemingly fewer particles than the film in Figure 3.20e. Nevertheless, the close-up image in Figure 3.20f indicates a multilayer in the band, suggesting that substrate speeds need to be further increased to approach $v_c^{(1)}$.

In a new experimental series (same conditions), the substrate withdrawal speeds were further increased. The results are summarized in Figure 3.21, in which the film morphology transitions from multilayered bands to islands. The islands do not appear to contain enough particles for a hypothetical complete monolayer, and the transition occurs apparently without going through a complete or nearly complete monolayer morphology. Thus, it unfortunately appears that some aspect of the ZSM-2 system impedes the assembly of continuous monolayers, especially in which all particles lie flat in a tiled arrangement (a desirable characteristic for zeolite membrane applications).

The silver lining is that, as with the thick multilayer ZSM-2 films in Chapter 2, the particle orientation in the thick ZSM-2 films described here are shown quantitatively to be preferentially oriented out-of-plane of the film, in an orientation parallel to the substrate surface (see Figure 3.22).

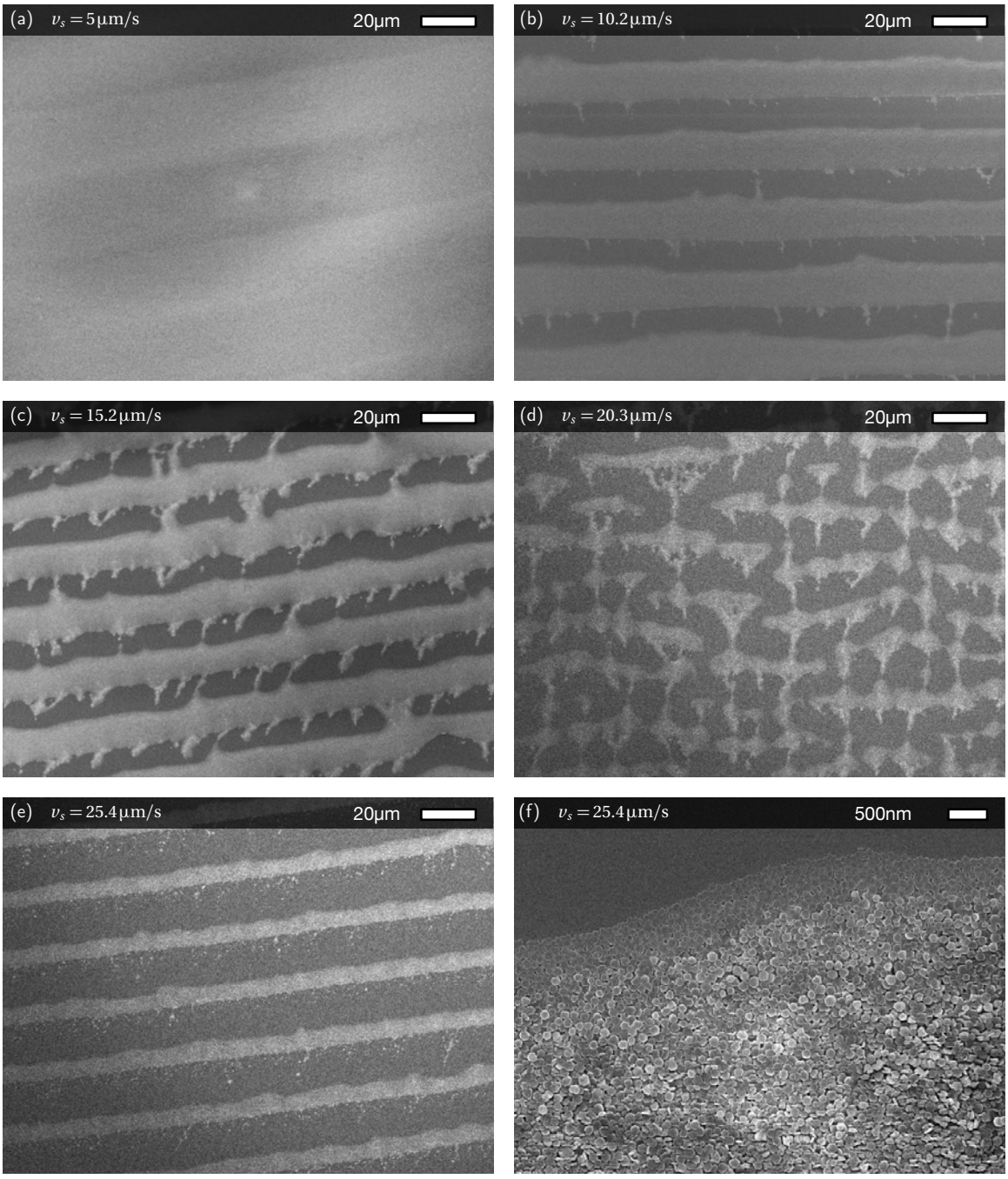

Figure 3.20: Substrate withdrawal speed variation for convective assembly of ZSM-2 films. Images (a)-(e) show films assembled at increasing speeds. Film morphologies transition from a wavy multilayer (a) to multilayered bands. Image (f) shows about 70% of a single band in (e), reflecting the same trends described for banded ZSM-2 films in Chapter 2.

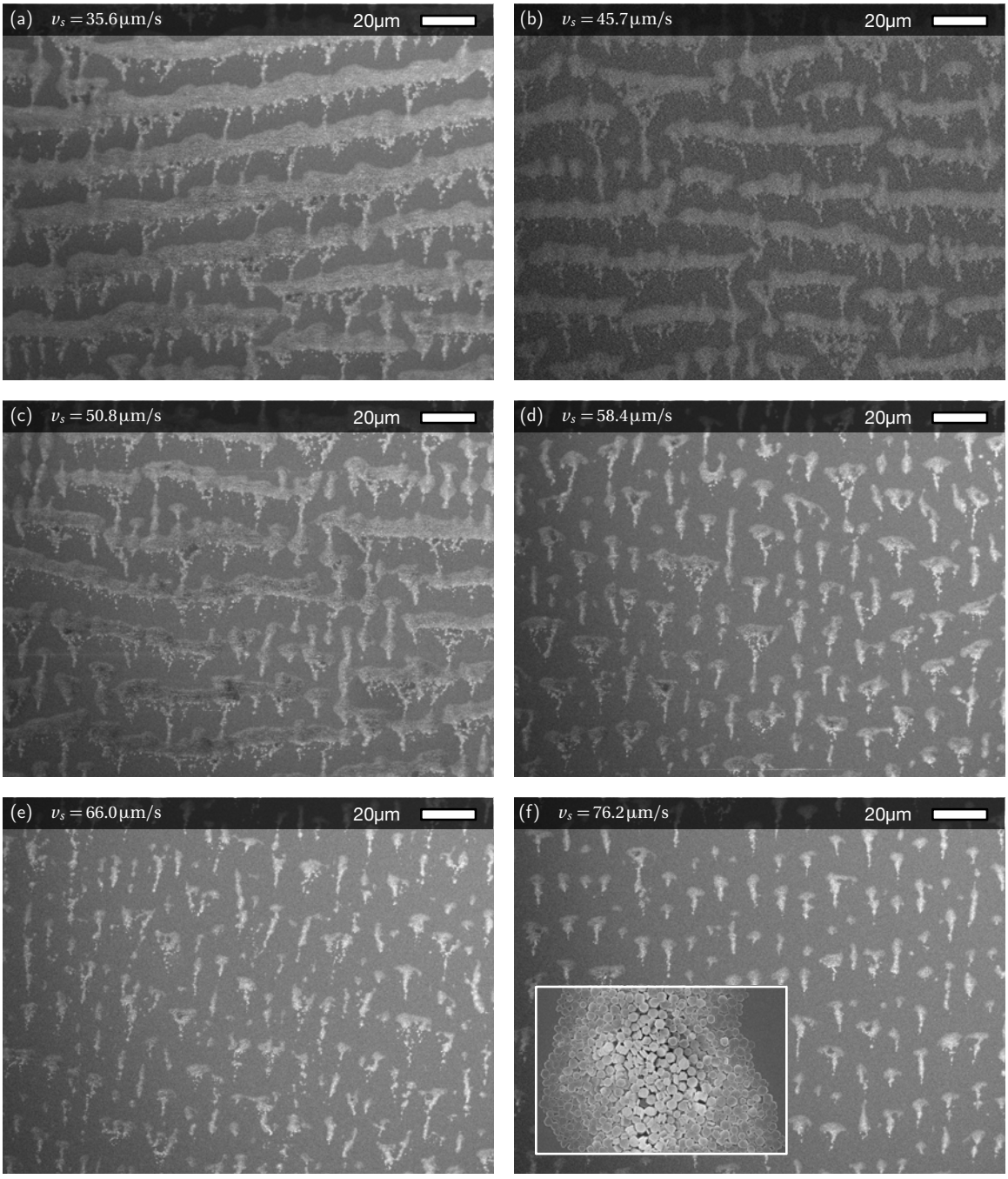

Figure 3.21: Substrate withdrawal speed variation for convective assembly of ZSM-2 films. Images (a)-(f) show films assembled at increasing speeds. The film morphology transitions from mutilayered bands to islands. Inset in (f) shows a close up of an island.

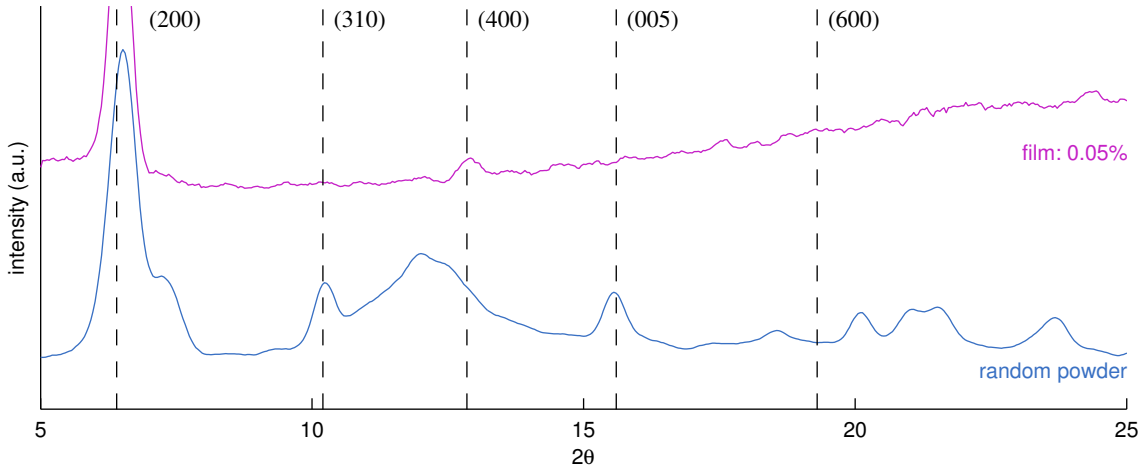

Figure 3.22: Thick multilayer films of ZSM-2 by continuous convective assembly with controlled evaporation are preferentially oriented, as evidenced by the presence only of (h00) Bragg peaks.

Discussion and analysis

One might cautiously speculate that the particle shape is responsible for this inability, in light of Equation 3.1 combined with the transition within a band from the "tiled" to "jumbled" morphology. Recall that in Equation 3.1, the linear film assembly rate v_c is related to the current film thickness kd (the particle film thickness at the assembly front) by

$$v_c \propto \frac{1}{kd} \tag{3.7}$$

According to this relation, the linear film growth rate is quite sensitive to perturbations in the growing film thickness for small k (monolayers, bilayers, and so on). For example, the film growth rate will drop by a factor of 2 during a monolayer to bilayer transition, while it would only drop by a factor of 11/10 (10%) during a 10- to 11-layer transition.

In general, we may consider only the effective film thickness $h \equiv kd$, which is relevant in cases where films do not necessarily take thicknesses that are integral multiples of the constituent particle diameters, *i.e.*, when particle sizes cannot be summarily characterized by their diameter (non-spherical) as is the case for ZSM-2 particles. One can imagine that as soon as a significant number of the particles in the developing film take an orientation not lying flat,

the effective film thickness can increase by a factor of as much as 5 if the particles are standing straight up, for example.

The initiation of film assembly occurs in a sharp meniscus wedge so that the first particles are ostensibly confined geometrically by the meniscus profile. On the other hand, once a film is initiated, the film thickness at the contact line will limit this confinement effect; as soon as a significant number of ZSM-2 particles take a non-flat orientation, the film thickness increases, and some consequences can be imagined. The incoming particles should no longer prefer the flat orientation, because there is less confinement. Therefore the "size" of the incoming particle cannot be characterized solely by its thickness, which is only appropriate when the film is understood to be composed of all particles lying completely flat; rather, the particle size must be considered as some other "characteristic dimension" of the anisometric particle (some average size, or perhaps the largest dimension). As a result, the notion of "the speed at which a monolayer is formed" may need to be revised.

In other words, it is possible that the only "monolayer" of ZSM-2 that can be assembled is the monolayer of a "jumbled heap" of ZSM-2 whose film thickness is some "effective particle size" that is not the particle thickness. With this interpretation, the "thick" bands may in fact be submonolayer bands, and it was a mistake to explore higher substrate withdrawal speeds in search of a tiled ZSM-2 monolayer. One observation consistent with this speculation is given in the film profile scan of Figure 2.7 (p. 20), in which the film thickness in the "multilayer" build-up never exceeded the maximum dimension of a single particle.

However, this is not a strong argument, and the reasoning remains speculative at best. Unfortunately, the experiment was not followed up in detail, and no definitive conclusions could be drawn in terms of the possibility of using convective assembly for the fabrication of ZSM-2 monolayers, despite the promising results of Chapter 2. We may note, though, that the same morphological feature of the leading edge monolayer region ("tiles"; see Figure 3.20f) was preserved in the continuous mode operation of convective assembly.

3.4.2 Films of other zeolites and crystals

The following concerns the application of the current method to coating films of various other zeolite particles. The first part very briefly describes convectively assembled films of larger zeolite particles. The second and third parts describe recent attempts at applying the method to immediate membrane fabrication goals.

Films of zeolites LTL and MFI

The zeolite with structure MFI is the recipient of intense study in the zeolite separation field, due to its ease of synthesis and promising separation properties (see *e.g.* Lai *et al.*, 2003). Traditional MFI synthesis routes result in particles with a "pill box" shape—essentially a low-aspect platelet—conducive to preferentially oriented films. It would thus seem that experiments with MFI are an obvious opportunity for comparison with other zeolite seed layer fabrication methods. The zeolite LTL (Lee *et al.*, 2005; Lovallo and Tsapatsis, 1996a) can be prepared as rod-like particles of varying aspect ratio, and while this zeolite is not as heavily studied for membrane applications, the rod-like morphology is nevertheless interesting and worth exploring.

Traditional particle syntheses of zeolites with both the MFI and LTL structures result in rather large particles, with sizes on the order of 1 µm. Because these are moderately dense (silicious) materials, particles in this size regime sediment rapidly; this presents a practical challenge for the convective assembly method described in this dissertation, which must oppose gravity.

Nevertheless, a few experiments were carried out in attempts to assemble MFI and LTL particle films. The results are shown in Figures 3.23 and 3.24, where it is apparent that these films too take a banded [sub-monolayer] morphology. The morphologies are banded despite high bulk suspension concentrations (~ 0.2 wt%) because convective [upward] fluxes of the heavy particles are inhibited due to their negative buoyancy.

Limited attempts were made to assemble more continuous (higher coverage) films of the MFI particles by using slower substrate withdrawal, and the results are shown in Figure 3.25. Coverage was indeed increases as expected, but it is evident in these films that particles become "jumbled

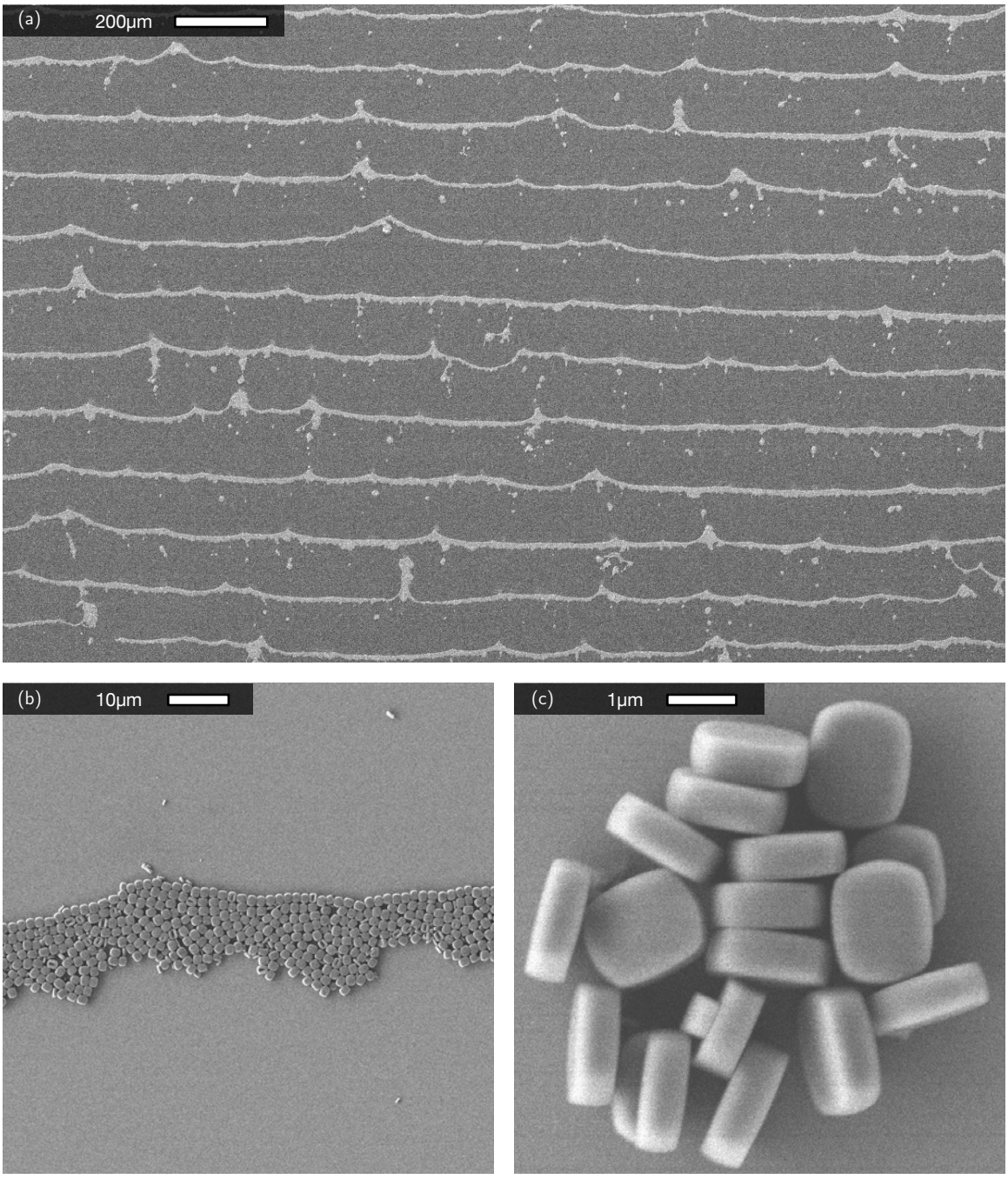

Figure 3.23: Films of MFI are banded (a). Films were coated from 0.2 wt% suspensions at 25.4 μm/s and 1.6 $cm^3/s/cm$ drying gas flow. Panels (b) and (c) show higher magnification SEM images.

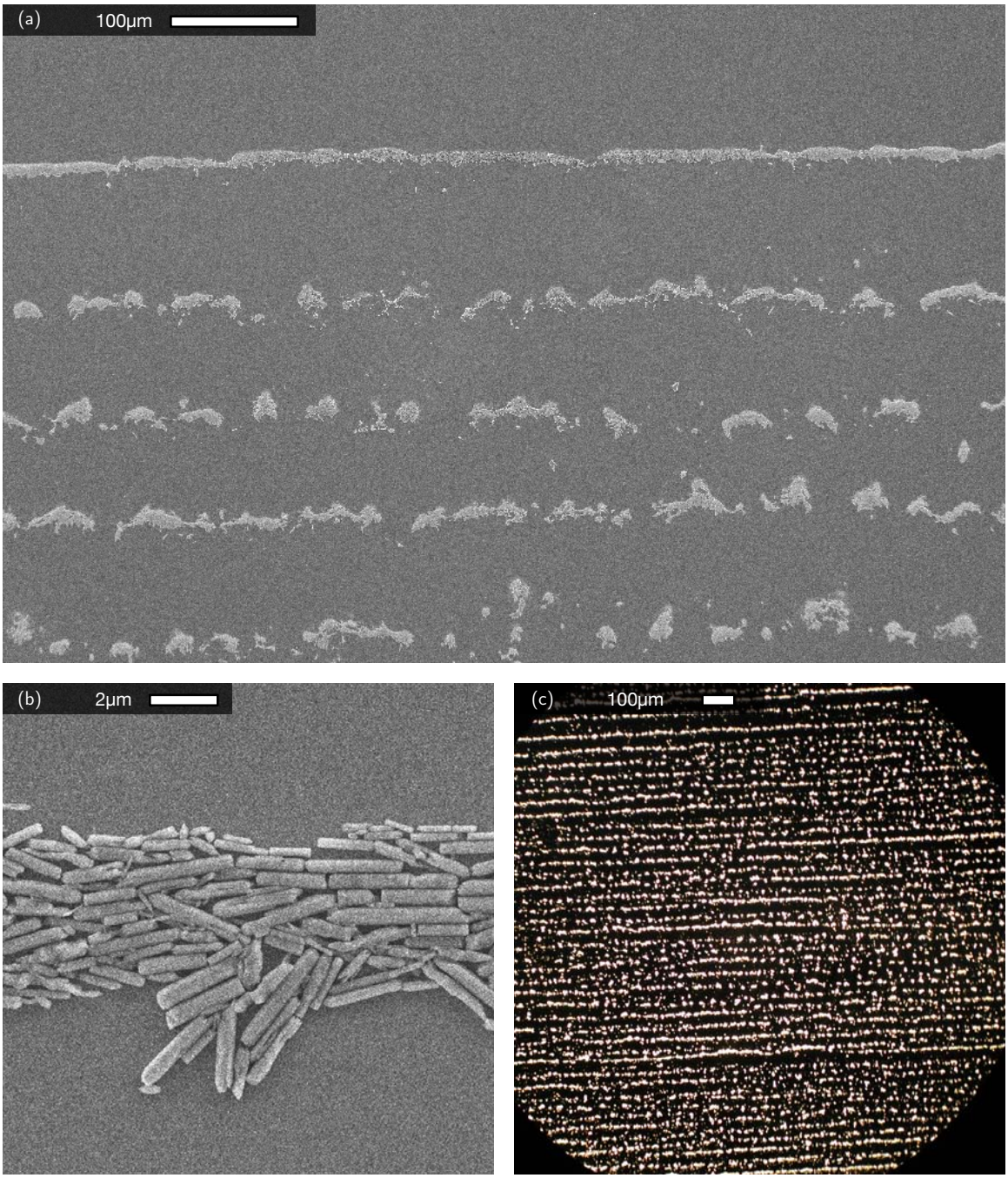

Figure 3.24: Films of LTL are banded (a). Films were coated from $0.16\,\mathrm{wt\%}$ suspensions at $5\,\mu\mathrm{m/s}$ and $4.8\,\mathrm{cm^3/s/cm}$ drying gas flow. Panel (b) shows a higher magnification SEM image. Panel (c) shows a dark field light microscope image (for lower magnification for a wider view of the bands). Bright regions indicate the presence of particles.

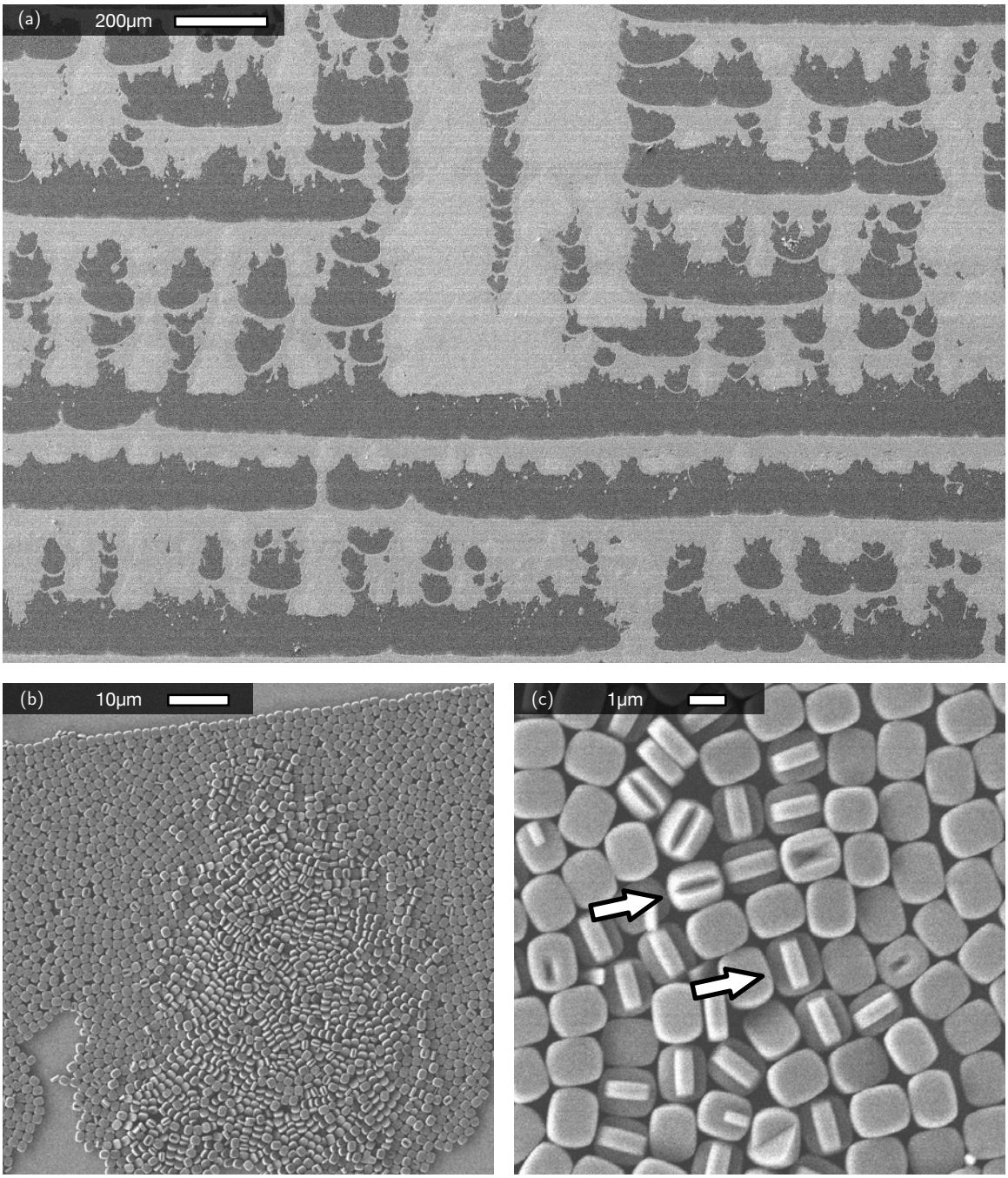

Figure 3.25: Films of MFI at slower substrate withdrawal still show signs of banding, but have higher coverage (a). Films were coated from $0.2\,\mathrm{wt\%}$ suspensions at $5\,\mu\mathrm{m/s}$ and $1.6\,\mathrm{cm^3/s/cm}$ drying gas flow. Panel (b) shows that interior regions of bands are jumbled, as in the case of ZSM-2 films. Panel (c) shows a higher magnification, where twinned particles are highlighted.

heaps" similarly to the ZSM-2 films described earlier. The problem is exacerbated by the significant presence of so-called "twinned" particles—two platelets inter-grow to form a particle best described as an "x"-shaped prism—whose effective size is larger than that of normal particles.

Films of nano-MFI

As noted above, the MFI particles by traditional synthesis routes tend to be too large for the convective assembly method described here, although they have been successfully incorporated into other membrane precursor deposition schemes (Lee *et al.*, 2000; Lai *et al.*, 2003). Recent advances in nanoscopic MFI particle synthesis in confined spaces (Yoo *et al.*, 2008) have re-opened the investigation of convective assembly as a potentially viable route to membrane precursor film assembly, although the original motivation for developing nano-MFI particles was for the eventual fabrication of much thinner membranes for increased fluxes.

The nano-MFI particles are in many ways analogous to the LYS-SIL particles (silicious, approximately spherical globular particles with diameter $\sim 20\,\text{nm}$), and our expectation was that assembly conditions would be similar to those for LYS-SIL. Unfortunately, at the time of these experiments, nano-MFI synthesis yields were prohibitively low and therefore obtaining enough suspension for convective assembly experiments was difficult. The film in Figure 3.26 was coated onto a glass slide exactly following the method for near-monolayer LYS-SIL films.

Nano-MFI films seem to be "messier" than their LYS-SIL counterparts, but the reason for this is not clear, and further experiments could not be conducted due to the above limitations. We tentatively speculate that other chemicals in the suspension necessary for the preparation of nano-MFI (which is significantly more complicated than the preparation of either LYS-SIL or traditional MFI particles) may act as surfactants, for example, introducing unwanted Marangoni effects to disrupt the film assembly.

Noting that the nano-MFI particles are globular, any resultant films are bound to be randomly oriented. The crystallographic orientation of the films could not, however, be quantified by XRD due to a lack of signal (undetectable scattering intensity). This could be due to either or both of the effects of the ultra thin nature of the film and low crystallinity of each particle; both lead to

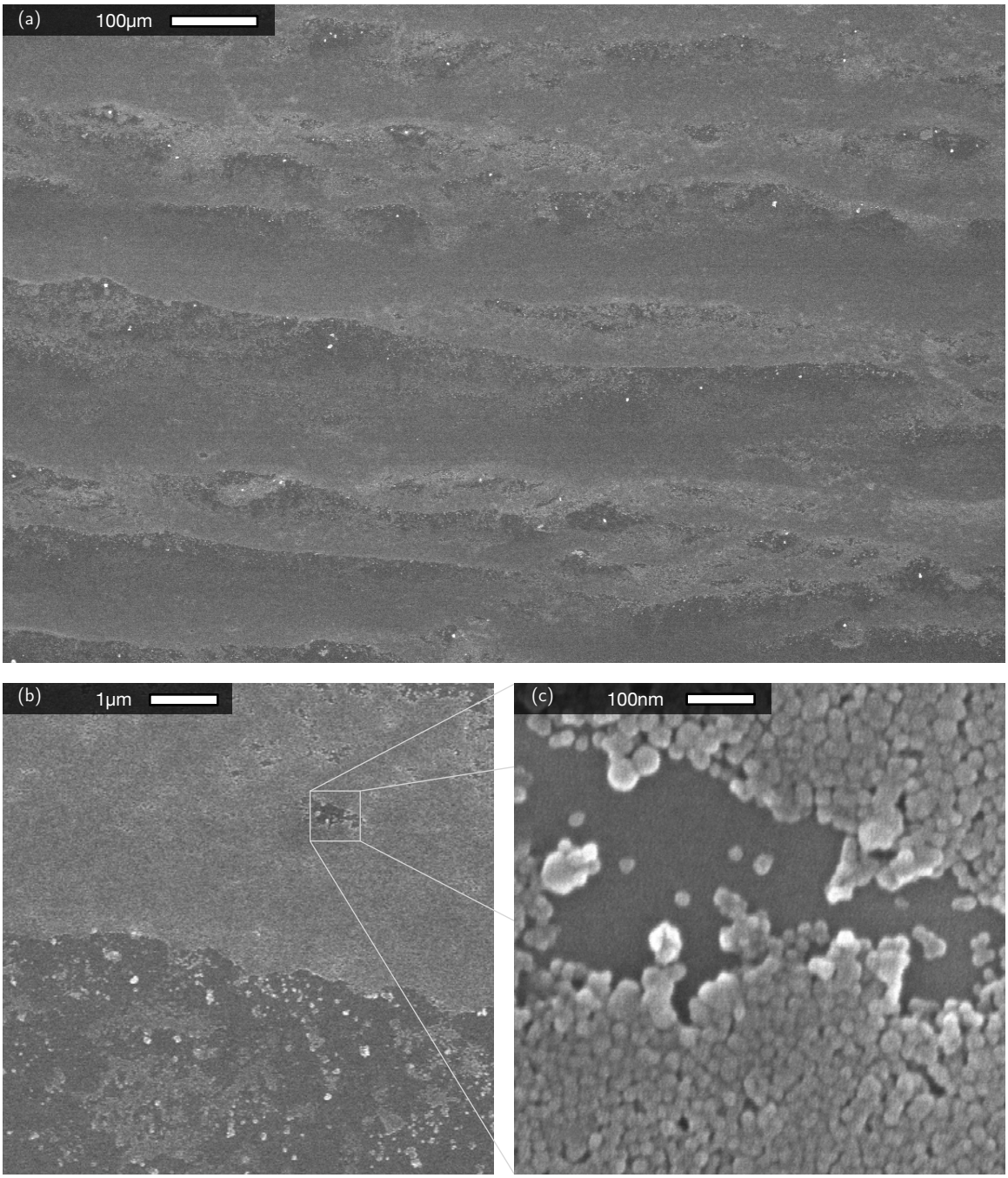

Figure 3.26: Convectively assembled nano-MFI particles. The film appears to be at least a bilayer (c) with patches of voids. The void and film regions do not appear as regular as for LYS-SIL films.

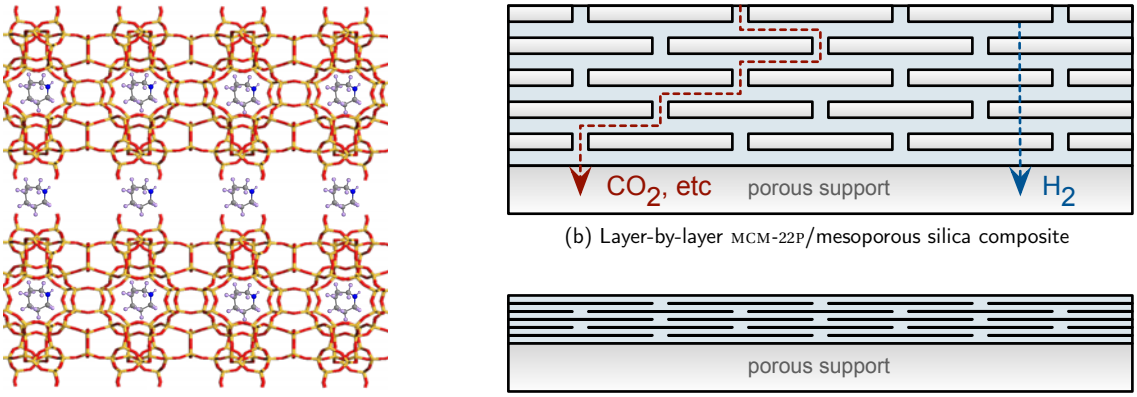

(a) Stick model of MCM-22P

(b) Layer-by-layer MCM-22P/mesoporous silica composite

(c) Nanosheet [composite] film

Figure 3.27: Schematics of the material MCM-22P (a) and the stacked nanosheet arrangement for potential in molecular sieving membranes (b, c). The MCM-22P crystal is made up of aluminosilicate sheets held together by hydrogen bonding of surface groups with the organic structure directing agent. Composite MCM-22P/mesoporous silica membranes (b) have exhibited H_2/N_2 separation selectivity. Using exfoliated nanosheets instead of MCM-22P particles may increase selectivity and/or flux by increasing the tortuosity in the nanosheet interstices and/or decreasing the film thickness.

insufficient sample of scattering planes. Powder XRD experiments of the particles did, however, confirm the MFI crystallographic structure, where peaks were somewhat broadened (not shown) due to the small sizes of the crystalline domains.

A more recent investigation into the growth of nanoscopic MFI synthesis (Yoo *et al.*, 2009) describes the development of facets on the particles. This line of work suggests the potential for oriented films from well-developed nano-MFI, either by convective assembly or another method. Currently, however, such goals are elusive due to synthesis limitations.

Films of crystalline nanosheets from MCM-22P

The results of experiments with ZSM-2 (see § 2.3.4 and § 3.4.1) force us to recognize that, with the current method, assembling monolayers of tiled plate-like particles is a difficult endeavor at best. However, multilayers with complete coverage (albeit with the possibility of banded thickness profiles) can be assembled easily. Furthermore, such films are quantitatively shown to be preferentially oriented (with respect to crystallography), despite their physically jumbled appearance in the SEM. Multilayered films then, seem to be a worthwhile application goal.

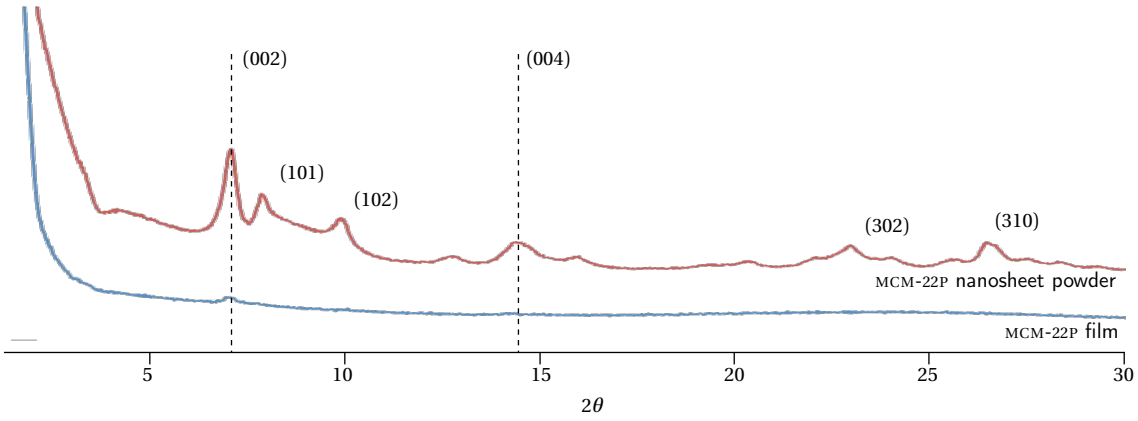

Figure 3.28: Comparison of the MCM-22P nanosheet powder and film XRD patterns. The results are not conclusive; there are not enough peaks to compare relative intensities to quantitatively determine the orientation of particles.

Recent work in the group (Maheshwari *et al.*, 2010) describes the preparation of a flake-like material (super high aspect plates; nanosheets) by delamination of the zeolite precursor material MCM-22P, following the report of a similar material designated ITQ-2 (Corma *et al.*, 1999). The new nanosheet materials described by Maheshwari *et al.* (2010) retain their crystallinity better than ITQ-2, and are speculated to have potential for separation applications (in addition to the catalytic potential originally described) in membranes with a "stacked interlaced sheets" configuration (see Figure 3.27). Briefly, each sheet's crystalline microstructure retains the pores necessary for molecular sieving action, and a stacked sheets configuration would form a tortuous path for molecules that cannot transport across the sheets, thus giving rise to separation potential.

An example of a convectively assembled MCM-22P nanosheet film is given in Figure 3.29. Cursory examination reveals no features on a long length scale (b), suggesting thickness and microstructural uniformity. A close-up view (c) of the surface indicates that the nanosheets are randomly oriented. The arrangement is elucidated in the cross-sectional image in (a). Evidently, the nanosheets do not spontaneously orient in the desired stacked sheet configuration, although such films are easily assembled. An XRD pattern of the nanosheet film in comparison with the nanosheet powder is given in Figure 3.28, but the results are not very telling (and should not be considered too seriously) because of a lack of peaks to compare.

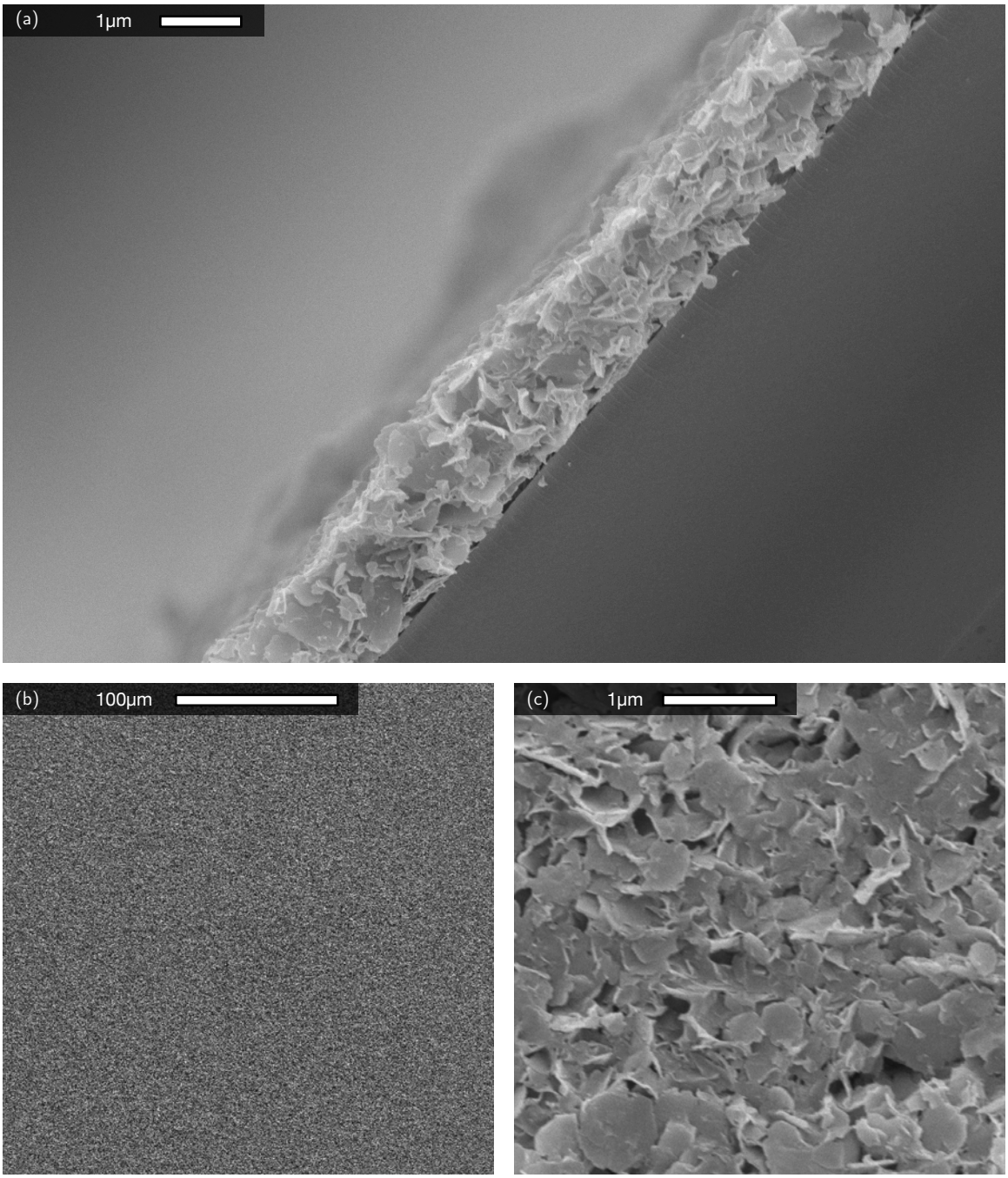

Figure 3.29: Multilayered nanosheet film. The nanosheets are prepared by delaminating particles of the zeolite precursor material MCM-22P. The low magnification view in (b) is featureless, suggests uniformity over long ranges. A high magnification image of the surface in (c) shows the nanosheets in a somewhat disordered state (not preferentially oriented in stacked sheets). The cross sectional image in (a) shows the interior of the film.

3.5 Concluding remarks

3.5.1 Chapter summary

This chapter began by describing an apparatus for continuous mode convective assembly with controlled drying. The apparatus extended the continuous convective assembly method first described by Dimitrov and Nagayama (1996) with a modified version of controlled drying inspired by Meng (2008).

The chapter continued to introduce a model particle system, and developed a procedure for the prototypical convective assembly experiment. It was shown that the microstructure of the films can be characterized as colloidally crystalline. Furthermore, the morphology and thickness of LYS-SIL (spherical silica nanoparticles) films are a function of the substrate withdrawal speed at a given bulk suspension concentration and drying gas flow rate. In particular, near monolayer films can be made by achieving the appropriate substrate withdrawal speed. Films can be made thicker by decreasing this speed, while increasing this speed leads to sub-monolayer films characterized by a regular banding pattern.

In fact, banded films are shown to be the most general type of result; thickness profile scans of multilayer films show reasonably periodic thickness modulations. Other patterned films have been documented in Appendix A.V, but were not discussed in the main text. (The banding phenomenon will be further explored in the following chapters.)

The chapter detoured with a discussion of convectively assembled zeolite particle films, starting with ZSM-2. Evidently, the method is ill-suited for assembling particles in the completely "tiled" monolayer arrangement suggested in the results of Chapter 2. On the other hand, multilayer films with preferentially oriented particles (at least out-of-plane of the film) were shown to be relatively easy to assemble. Experiments with some other types of particles were also briefly described in this section, addressing interesting applications in the zeolite membrane field.

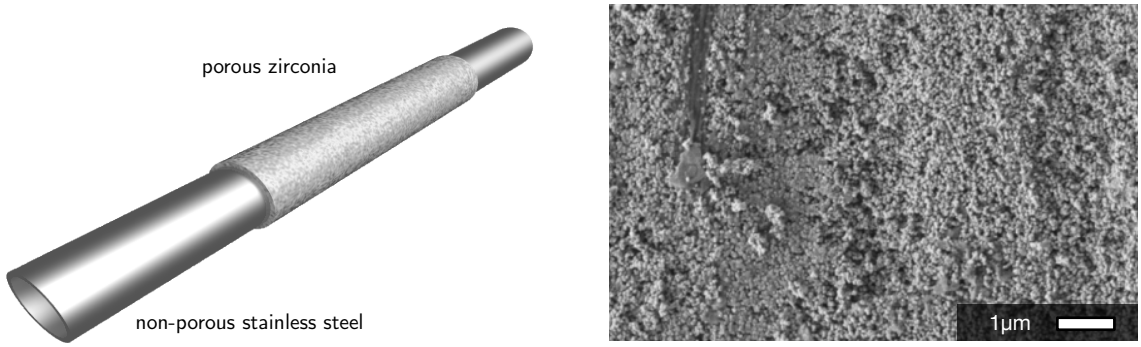

Figure 3.30: Tubular porous supports for gas separation membranes. The functional separating membrane would be supported on the porous region, while the non-porous region serves to couple the membrane to the process line. The SEM image on the right shows the rough surface of the porous zirconia region.

3.5.2 Further development of convective assembly

The apparatus described in this chapter was meant as a investigative tool, although the process and operation were designed to be adaptable for industrial relevance. This section briefly lays out some potential extensions of this work if it were to be pursued.

Adapting for tubular substrates

Practical, *i.e.* industrially relevant, application of zeolite-based membrane technology requires the membrane to be in a form amenable to operation; in other words, any method for fabricating zeolite membranes must be adaptable to being supported on tubular substrates (see Figure 3.30), not just flat ones as described in the scope of this dissertation.

The cartoon of a stainless steel/zirconia tubular support shown in Figure 3.30 has a porous middle for gas permeability (to support the actual separation membrane) and non-porous ends for coupling to the gas flow line. Several veins of work are investigating the fabrication of zeolite membranes by various methods on these supports (Choi *et al.*, 2009; Maheshwari *et al.*, 2010). Adaptation of the convective assembly method described in this dissertation to tubular supports would require some design adaptations of the apparatus. A proposed rough schematic is shown in Figure 3.31.

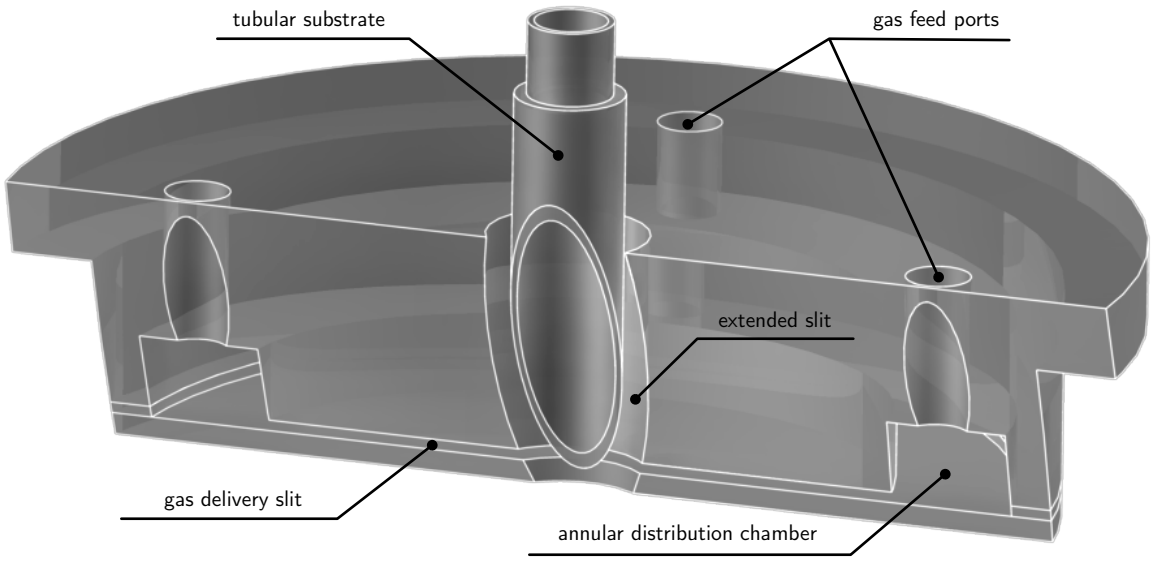

Figure 3.31: Proposed apparatus for tubular substrates.

The gas delivery along the substrate would be annular; in some sense this eases machining demands for the apparatus, as a simple smooth bore would serve the purpose. However, alignment may become more complicated, because the substrate cannot be aligned against anything, such as the substrate guide (see Figure 3.6). The distribution chamber can be prepared as an annular slot in the main block, and the main shim can be prepared as a ring. However, since the delivery slit will be disc-like in shape, the gas will be compressed as it travels from the distribution chamber to the outlet bore; the effects of this geometry on performance is unclear, and the issue may require further investigation.

Nanoscopic films on rough substrates

Another technical issue surrounding the stainless steel/zirconia substrate is the roughness of the porous zirconia (see Figure 3.30). Especially for small nanoparticles, this roughness may be detrimental to the formation of uniformly thin films. One possible solution to this problem is suggested by the assembly of colloidally crystalline films of spherical particles. For example, successive films of spherical ceramic particles (perhaps even silica) of diminishing size can be

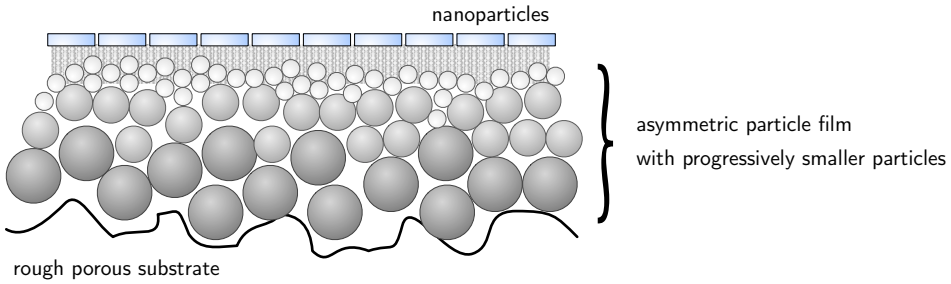

Figure 3.32: Proposed solution to priming a rough substrate for nanoparticle film assembly: asymmetric particulate primer film with progressively smaller particles will preserve porosity while providing a smoother surface.

assembled onto the zirconia support, providing successively smoother surfaces while retaining the porosity necessary for efficient gas permeation (see Figure 3.32).

The porosity itself may present challenges to the convective assembly process, as well as opportunities for exploiting other flow-related phenomena (imagine the filtration phenomenon across the porous membrane support).

True continuous operation

In principle, the current suspension bath design does not allow for a truly continuous operation; both the suspension concentration and total suspension volume are continually diminishing as the film assembly progresses. Furthermore, unacceptable concentration gradients may develop locally to the meniscus.

These issues may be mitigated by introducing continuous stirring and replenishment of the bath from an external supply. An obvious improvement would be to localize the availability of suspension by confining the suspension to a small bead on the substrate with a controlled feed arrangement, analogous to a transformation from dip coating to slot coating described in Kistler and Schweizer (1997).

One severe technical challenge in developing such a process is that in a vertical configuration with a well-wetting substrate and slow withdrawal speeds, the supplied liquid suspension will be sure to run down the substrate ("flood" upstream) rather than form a meniscus downstream. In other words, the analog between continuous convective assembly and liquid coating processes becomes much more strenuous under the necessary operating conditions.

Experimental parameters

As certainly as the liquid properties are important in liquid coating processes, they are important in convective assembly (although liquid property effects are not systematically studied in this dissertation). Specifically, the following properties should be important in the context of convective assembly based on the principles believed to be at play (these can still be examined using the flat substrate apparatus).

Liquid density, relative to that of the particle, affects the gravitational stability of the suspension. One might consider pursuing liquids with higher volatilities to promote more rapid convection. The surface tension of the liquid may be important insofar as it affects (in combination with the substrate-liquid-air contact angle) the meniscus geometry; it may as well potentially affect the final inter-particle structure in the film by virtue of capillary immersion forces. The polarity of the liquid molecules themselves (the electronic environment local to the particle surfaces) may be of interest in investigating the effects of inter-particle forces during assembly.

For example, one might propose to repeat many of the experiments described here with alcoholic suspensions (with light alcohols like ethanol or propanol). Other than having precedent (*e.g.* Jiang *et al.*, 1999), such experiments would have value in terms of definitely affecting most of the material properties discussed above (limiting the scope to light alcohols should keep the process more or less environmentally benign). The suspensions can be purely alcoholic or in aqueous mixture. It can be anticipated, though, that mixtures (especially with water) will create as many (or more) adverse influences than positive ones; assembly dynamics may be affected by potential Marangoni flows in the meniscus region owing to gradients in composition—and therefore surface tension—set up by differential volatilities of the mixture components.

Another obvious avenue of investigation would be the conditions regarding the various aspects of the drying gas. These include temperature, "humidity," and mode of delivery. These may include parameters such as flow rate and slit geometry, which may in turn affect the turbulence and inertia. The former may enhance drying but reduce uniformity, while the latter may have implications on the geometry of the meniscus on which the gas impinges.

Along with the suspension liquid properties, the drying gas conditions are certain to affect the liquid convection, and therefore particle flux. A critical unanswered question is whether assembly rate has important consequences for the final film morphology and structure. Specifically, one might consider the competition between the particle's inertia and colloidal forces, for example. In other words, is there a tradeoff between rapidity of assembly and the quality of the film (in the case of colloidal crystals)?

Moving forward with continuous convective assembly with controlled drying

These and many other experimental parameters remain interesting avenues for further study. Any such pursuits should be guided by the need for "industrializing" the process and methodology, and the need for addressing some of this work's shortcomings that are evidenced by the limitations in achieving desirable particle film qualities. On the other hand, some promising results have also come out of this work, the deeper origins of which remain unclear. Further investigations of the experimental parameters, concurrently with the development of theoretical descriptions of the process, are surely required to better understand the phenomena behind the development of favorable film qualities and improving the conditions that promote them.

3.5.3 Remarks on banded film morphologies

Having developed, demonstrated, and discussed further development of an improved convective assembly methodology and apparatus, I would now like to redirect attention to the exploration of one specific property of convectively assembled films. The most persistent and noteworthy result pervading all of the experiments discussed so far is the banded film morphology. These bands result regardless of the particle shapes and sizes, and occur in both sub-monolayer and super-monolayer films.

In the context of zeolite membrane precursor films and colloidally crystalline monolayers, the development of the banded pattern during convective assembly is problematic. Although it seems that monolayers of spherical particles can be assembled under the right conditions, the set of such "right conditions" seem to be characterized by a *point* in parameter-space, rather

than as a *window*, thus making it difficult to justify the process as viable for rapid mass production. Furthermore, experiments with anisometric (high aspect) particles seem to indicate that complete monolayers in a "tiled" arrangement are unobtainable.

On the other hand, banded films are relatively easy to assemble, as they occupy everywhere else in the parameter-space (except the extreme ones that lead to the relatively exotic patterns described in Appendix A.V), and their regularity suggests that some explicable phenomenon governs their formation. In fact, several reports concerning the banding phenomenon had existed (Adachi *et al.*, 2006; Abkarian *et al.*, 2004; Masuda *et al.*, 2004) or were appearing concurrently to the work described here (Ray *et al.*, 2005; Ghosh *et al.*, 2007; Watanabe *et al.*, 2009), variously attempting to model the appearance of the bands.

Still, no definitive and comprehensive explanation has yet been put forth, and so the remaining chapters of this dissertation are dedicated to the investigation of the banding phenomenon, particularly in the case of sub-monolayer coverage where each particle band is limited to a monolayer thickness.

Chapter 4

Banded monolayers: a static model

Nanoparticle films that are convectively assembled on smooth substrates from dilute suspension are known to have discrete film morphologies, as described in § 2.3.2, § 3.3.5, and numerous works in the literature, notably Adachi *et al.* (1995), Masuda *et al.* (2004), and Ghosh *et al.* (2007). Specifically, the film morphology is characterized by alternating bands of densely packed particles and bands of bare substrate.

Convective assembly is a frontal film growth process that occurs at the three-phase contact line formed by the substrate, the suspension in which it is submersed, and the surrounding air. The bands are parallel to this contact line, and can be either monolayered or multilayered. Monolayer bands result whenever the substrate is withdrawn from the suspension at a rate too high for particles to assemble into a continuous film. One noteworthy feature of such monolayer banded films is that the length scale of the bands (that is, the spacing between the bands) are strongly dependent on the constituent particle size.

In this chapter[‡], I propose a simple geometric exclusion argument to qualitatively explain this dependence by using the Young-Laplace equation to model the meniscus profile. The model is compared against experimentally made banded films with systematically varied particle sizes (silica; 20 nm to 500 nm diameter). The model predicts increasing inter-band spacings with larger particle sizes, in qualitative agreement with the experimentally observed trend. The model

[‡]based on published work (Lee *et al.*, 2009)

also correctly predicts (qualitatively) that films made up of multilayered bands have higher inter-band spacings than their submonolayer counterparts—this was demonstrated independently by Watanabe *et al.* (2009) with better experimental evidence but similar arguments.

4.1 Background

Stick-slip motion of the contact line

To the author's knowledge, the earliest relevant description of the banded film morphology resulting from convective assembly was given by Adachi *et al.* (1995), who addressed the formation of bands resulting from the convective assembly toward the contact line of a drying sessile drop of suspension; in other words the convective assembly occurred toward a nominally circular contact line to produce concentric bands of particle film on a flat substrate. Like the mechanism described in § 2.3.3, the process observed by Adachi *et al.* (1995) was characterized by a stick-slip motion of the contact line during assembly, wherein the assembly front periodically shifted due to the abrupt detachment of the contact line.

Adachi *et al.* (1995) described this motion by constructing the Newton's law of motion for the sessile drop radius, where the force was equated to a sum of the surface tension forces at the contact line and a so-called "friction force" that arises from viscous forces. When the flow rate is related back to the drop radius using various physical arguments, the resulting equation has a periodic solution that is shown to correspond to the observed contact line motion after fitting a few parameters.

Regimes in withdrawal velocities (banded films by dip coating)

Several subsequent works have described the spontaneous development of banded morphologies in convective assembly where the geometry more closely resembles the methods described in this dissertation, namely in a vertical orientation with a linear contact line. In continuously assembled films reported by Ghosh *et al.* (2007), the band widths and spacings were related to the substrate withdrawal speeds. Specifically, three distinct substrate withdrawal speed regimes

were described in relation to a "transition" speed U_T, beyond which a liquid film is entrained; no theoretical origins were described. These regimes are discussed in the context of dip-coating, so that substrate withdrawal speeds were associated with entrained liquid film thicknesses via the famous relationship due to Landau and Levich (1942):

$$h \propto \left(\frac{\sigma}{\rho g}\right)^{1/2} \left(\frac{\mu U}{\sigma}\right)^{2/3} \tag{4.1}$$

where h is the liquid film thickness, U is the substrate withdrawal speed, g is the acceleration due to gravity, and σ, ρ, and μ are respective the bulk liquid surface tension, bulk liquid density, and bulk liquid viscosity.

The mechanisms in all regimes, namely $U < U_T$, $U > U_T$, and $U >> U_T$ proposed by Ghosh *et al.* (2007) presuppose the entrainment of this liquid film, and explain the morphological characteristics of the resulting films (namely band width and spacing) in terms of the relative thickness of this film with respect to the particle size, specifically the time available for band formation based on arguments using the liquid evaporation rate, particle size, entrained film thickness, and substrate withdrawal speed.

Contact angles and meniscus configurations

Convectively assembled banded films can also be coated onto the inner walls of capillary tubes, as demonstrated by Abkarian *et al.* (2004). In this case, the contact line forms as a circle instead of a line. Moreover, owing to the confinement of the capillary tube, evaporation characteristics near the contact line are certainly changed as the contact line position changes along the length of the tube. Nevertheless, the principle mechanism of convective assembly remains unchanged.

In their report, Abkarian *et al.* (2004) put forth an explanation for the banding behavior by considering the disparate equilibrium contact angle of the suspending liquid (ethanol) on the capillary walls (glass) versus the particles (polystyrene). Because water on the less-wettable polystyrene film has a larger contact angle, the total curvature in the meniscus is smaller, so that the capillary rise (the level of the liquid in the capillary tube) is lower (c.f. the Young-Laplace

equation). The spaces between the particle bands are thus explained by the jumping of the capillary rise due to changes in the equilibrium contact angle when the particle film is present.

A closer look at this analysis seems to reveal an apparent inconsistency in the reasoning: if the meniscus hanging on a polystyrene surface suddenly transitioned to a glass surface (regardless of the origins behind this event, which are anyway not considered here), the meniscus should be pushed back *up* the capillary due to the increased curvature, not pushed *down* the capillary, as would separate the assembling bands. Nevertheless, the phenomenon of equilibrium contact angles of heterogeneous surfaces is certainly important.

Similarly, Ray *et al.* (2005) examined the bands resulting from convective assembly in the context of the geometry of the meniscus wedge that forms as it hangs off of the developing film. Specifically, they attributed the banding wavelength to the space available in the meniscus wedge for the next particle band to develop. The experiments described in their work involved particles and substrate that were oppositely charged, so that the convective assembly mechanism was certainly affected by electrostatic deposition, which was not active in any of the other works described above, nor the main experiments in this dissertation.

Ray *et al.* (2005) also claimed that the Coulombic attraction was critical to the formation of regularly spaced bands, citing the work of Adachi *et al.* (1995) as producing bands with comparatively irregular spacings. However, recent work has shown that Coulombic attraction is not necessary for the formation of regularly spaced bands (Masuda *et al.*, 2004; Ghosh *et al.*, 2007; Lee *et al.*, 2009; Watanabe *et al.*, 2009).

Other works of interest

Although not directly relevant to this chapter, there are several other works reporting the convective assembly of banded films. Many of them deal with convective assembly of particles onto topographically or chemically *pre-patterned* surfaces, for example by Fan and Stebe (2004), Gleiche *et al.* (2000), Malaquin *et al.* (2007), Xia *et al.* (2007), Zheng *et al.* (2002), Lallet and Olivi-Tran (2006), and Karakurt *et al.* (2006). It may be worth re-emphasizing that the banded films

under consideration in this dissertation, in contrast, are formed on smooth and unpatterned substrates.

Another interesting report by Huang *et al.* (2005) describes the formation of *vertically* oriented bands (stripes) during a Blodgett-Langmuir type deposition. Similar striped films can be made by the convective assembly method of Chapter 3 (see Appendix A.V), although the phenomenon was not pursued in detail.

4.2 A static meniscus model for monolayer bands

4.2.1 Overview of band formation by convective assembly

To briefly reiterate the salient points in § 1.3, convective assembly relies on the rapid evaporation of solvent near the substrate-suspension contact line to drive particle convection toward the growing film (see Figure 4.1a). In the sense that film entrainment must be avoided, the evaporation is rapid compared to substrate withdrawal speed. Thus, in the prediction of final film thickness, a fluid mechanical analysis of liquid film coating is not appropriate; rather, the relevant competition is between the rates of particle arrival and contact line recession (*i.e.* substrate withdrawal speed) rather than the capillary, viscous, and gravity forces.

Slow substrate withdrawal speeds allow more particles to arrive at the contact line (resulting in thicker films) whereas fast substrate speeds allow fewer particles to arrive to the contact line so that film growth cannot keep up; the relationship between substrate speed and resulting film thickness has been established to be roughly inverse (Dimitrov and Nagayama, 1996; Zhou and Zhao, 2004; Jiang *et al.*, 1999; Gu *et al.*, 2002). Bulk particle concentration is also a key parameter for tuning film thickness at given process conditions. Thus, it is possible to obtain monolayer films by convective assembly when the linear film growth rate (determined by the bulk particle concentration, evaporation rate, and growing film thickness) is matched exactly by the substrate withdrawal speed (Dimitrov and Nagayama, 1996).

In this near-monolayer regime, increasing the substrate speed will not lead to uniformly thinner films because particles are discrete entities; rather, films will become more sparse, lead-

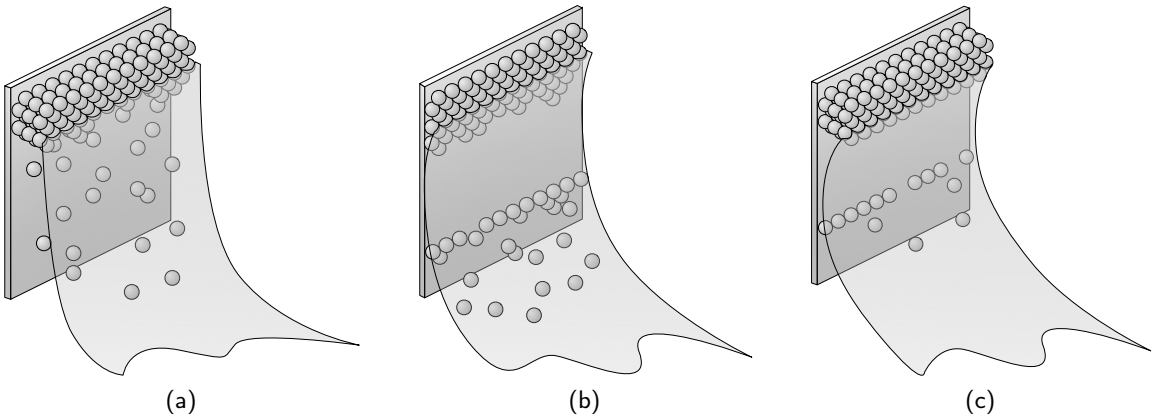

Figure 4.1: Schematic for banding mechanism in convective assembly. Film thickness is generally determined by the competition between substrate withdrawal speed and particle arrival, *i.e.* linear film growth rate (a). At "fast" substrate speeds, particles do not have enough time to assemble into a continuous film and the film will be characterized by bare regions (b). At "slow" substrate speeds, multilayers may build up forcing the process into a situation where withdrawal speed is again too fast for the assembly of a complete multilayer, possibly resulting again in bare regions (c).

ing to discrete morphologies (corroborated in Prevo *et al.*, 2007). Figure 4.1b shows a one-dimensional (with depth-wise symmetry) implication of this idea, graphically predicting the banded monolayer film morphology: if the substrate speed is much faster than the growth rate of the particle film, the meniscus may begin to stretch and choke off the convective supply of particles, thus resulting in bands of bare substrate.

On the other hand, slowing down the substrate speed arbitrarily will not necessarily result in a thicker continuous film. At decreased substrate speeds, particles will have too much time to assemble and may build up multiple layers; however, if the substrate speed is not exactly slow enough to match the *linear* growth rate of this thicker film, the process is pushed back into the same operating regime as before, again implying the stretching and choking of the meniscus to result in multilayer banding (as in Figure 4.1c), or more generally modulations in the film thickness (also observed in experiment; see § 3.3.3).

The morphologies suggested in Figures 4.1b and 4.1c are indeed realized experimentally for both the monolayered (Lee *et al.*, 2009) and multilayered (Ghosh *et al.*, 2007; Masuda *et al.*, 2004; Watanabe *et al.*, 2009) bands, where bands of densely packed particles are separated by bands of bare substrate. Systematic variation of the substrate speed in the near monolayer regime illus-

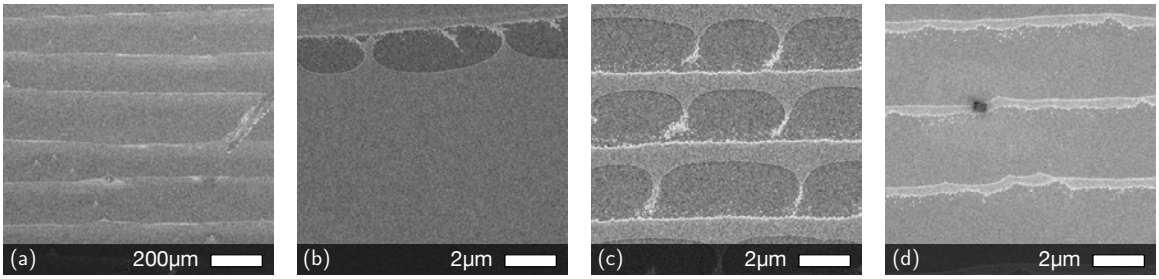

Figure 4.2: Band morphology with respect to substrate withdrawal speed. The speeds for (a–d) are 2, 6, 11, and 20 cm hr^{-1}, respectively. For (b–d), darker regions are bare substrate while lighter regions are densely packed monolayer, while for (a), the contrast represents different multilayer thicknesses. The result in (b) is the reference velocity for which the film is in monolayer (with occasional defects like the one shown). At higher velocities (c, d), fewer and fewer particles compose the film because as film growth cannot keep up with the substrate withdrawal; these films have a banded monolayer structure. At lower velocities (a), films have a banded multilayer structure.

trates the progression of morphologies from multilayered bands to continuous monolayer films to monolayered bands (Figure 4.2; see also § 3.3.5). Thus, the continuous monolayer film can be thought of as a special case of the more general discrete banded film, where depending on the relative process rates, particle bands can be either monolayered or multilayered. The regularity of banding in the experiment suggests that the phenomenon is predictable.

Although the schematics in Figure 4.1 make intuitive use of the meniscus shape to express the general banded films resulting from convective assembly, a quantitative description of the meniscus can be developed. A side view of the meniscus configuration in Figure 4.1b shows the stretched liquid meniscus hanging from the band of particles, touching the substrate, and allowing a new band of particles to form in the wedge formed with the meniscus (Figure 4.3). The modeled inter-band spacing λ will be taken as the center-to-center distance of the last and first particles in the top and bottom bands, respectively, separated by a static meniscus whose profile is governed by the Young-Laplace equation.

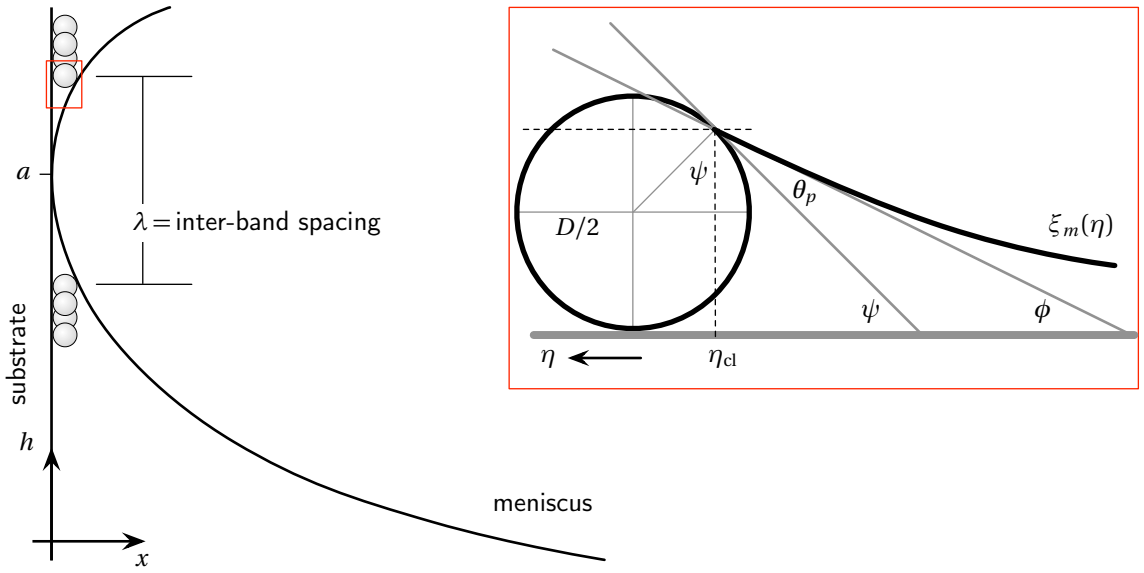

Figure 4.3: Schematic of the proposed model. Particles are wedged between a stretched static liquid meniscus. The inter-band spacing is the center-to-center distance between these particles. The horizontal dimension is x ($x = 0$ gives the surface of the substrate) and the vertical dimension is h ($h = 0$ gives the surface level of the bulk liquid). The height a where the meniscus is tangent to the substrate is the capillary length given in Equation 4.3. Inset: detailed description of the upper particle for use in constructing the model (see § 4.2.2).

Table 4.1: List of symbols used in this chapter

symbol	scaled	meaning
x	ξ	horizontal dimension
h	η	vertical dimension
ρ		density
g		acceleration due to gravity
σ		surface tension (of liquid)
a		capillary length
θ_s		contact angle between a liquid and a substrate
θ_p		contact angle between a liquid and a particle
ψ		angle between the substrate and line tangent to the particle-liquid contact line
φ		angle between the substrate and meniscus inclination at particle-liquid contact line
	D	particle diameter
	$\xi_m(\eta)$	position of a liquid meniscus
	η_{cl}	vertical position of a particle-liquid contact line
	η_{pc}	vertical position of a particle's center

4.2.2 Model based on the Young-Laplace equation

Static meniscus equation

The shape of a static liquid meniscus is governed by the Young-Laplace equation, which states that the capillary pressure jump across the surface of a curved meniscus must balance the hydrostatic pressure there

$$\sigma \frac{\mathrm{d}^2 h}{\mathrm{d}x^2}\left[1+\left(\frac{\mathrm{d}h}{\mathrm{d}x}\right)^2\right]^{-\frac{3}{2}} = (\rho_{\text{liquid}} - \rho_{\text{air}})g\,h \tag{4.2}$$

where ρ are densities, g is the acceleration due to gravity, and σ is the liquid surface tension. The only relevant length scale in the system is the capillary length a defined by

$$a = \sqrt{\frac{2\sigma}{(\rho_{\text{liquid}} - \rho_{\text{air}})g}} \tag{4.3}$$

and so the spatial variables can be scaled according to

$$\xi = x/a \tag{4.4}$$

$$\eta = h/a \tag{4.5}$$

The scaled spatial variables can then be used to express Equation 4.2 in dimensionless form

$$\frac{\mathrm{d}^2 \eta}{\mathrm{d}\xi^2}\left[1+\left(\frac{\mathrm{d}\eta}{\mathrm{d}\xi}\right)^2\right]^{-\frac{3}{2}} = 2\eta \tag{4.6}$$

The relevant boundary conditions for a liquid meniscus on a flat substrate are

$$\left.\frac{\mathrm{d}\eta}{\mathrm{d}\xi}\right|_{\xi\to\infty} = 0 \tag{4.7}$$

$$\left.\frac{\mathrm{d}\eta}{\mathrm{d}\xi}\right|_{\xi=0} = -\cot\theta \tag{4.8}$$

The first states that the interface is flat far from the substrate and the second describes the contact angle θ_s with the substrate. Using these conditions, Equation 4.6 can be solved for the meniscus profile

$$\xi_m(\eta) = \frac{1}{2\sqrt{2}} \ln\left(\frac{\sqrt{2}+\sqrt{2-\eta^2}}{\sqrt{2}-\sqrt{2-\eta^2}}\right) - \sqrt{2-\eta^2} + \sqrt{1+\sin\theta_s} - \frac{1}{2\sqrt{2}} \ln\left(\frac{\sqrt{2}+\sqrt{1+\sin\theta_s}}{\sqrt{2}-\sqrt{1+\sin\theta_s}}\right) \tag{4.9}$$

We note that the situation illustrated in Figure 4.2 calls for a zero contact angle ($\theta = 0$), and restrict ourselves to this contact angle (until § 4.4). A convenient intermediate result for the determination of inter-band spacing is the expression for the meniscus inclination

$$\frac{\mathrm{d}\xi_m}{\mathrm{d}\eta} = \frac{\eta^2-1}{\eta\sqrt{2-\eta^2}} \tag{4.10}$$

Modeling the inter-band spacing

The proposed model for predicting inter-band spacing λ is graphically represented in Figure 4.3; a meniscus (2D; trivial direction along breadth of the substrate) hangs off of the last particle in the upper band of particles, intersects the substrate at a tangent, and the first particle in the bottom band is touches the meniscus at a tangent. Therefore, λ is modeled by solving for the positions of these two particles along the η-dimension, subject to certain contact conditions.

As the inset in Figure 4.3 shows, it makes sense that the contact condition on the top particle should be a prescribed contact angle θ_p. For the bottom particle, the prescribed contact angle condition does not make sense because a finite contact angle would require it to "jut out of the meniscus". We choose, rather a tangency condition, which describes an "incipient collision" of the particle with the meniscus.

The particle positions are determined relative to the meniscus position, which is fixed (the meniscus that intersects the substrate at a tangent). They are most readily defined by the position of intersection with the meniscus, namely $(\eta_{\mathrm{cl}}, \xi_{\mathrm{cl}})$. However, since one of the contact conditions is a contact angle θ_p, it is more convenient to replace the ξ-wise position by the angular variable ψ (see Figure 4.3), which is just the particle's tangent at the contact line. In terms

of η_{cl} and ψ, the contact line position condition can be written

$$\xi_m(\eta_{\mathrm{cl}}) = \frac{D}{2} + \frac{D}{2}\cos\psi \tag{4.11}$$

where D is the dimensionless particle diameter (scaled by a). The contact angle condition can be expressed in terms of the meniscus inclination φ, defined as

$$\tan\varphi = \left.\frac{\mathrm{d}\xi_m(\eta)}{\mathrm{d}\eta}\right|_{\eta_{\mathrm{cl}}} \tag{4.12}$$

by equating it to the difference of the particle tangent at the contact line and the contact angle ($\varphi = \psi - \theta_p$) so that

$$\tan\left(\psi - \theta_p\right) = \left.\frac{\mathrm{d}\xi_m(\eta)}{\mathrm{d}\eta}\right|_{\eta_{\mathrm{cl}}} \tag{4.13}$$

Thus the particle's position can be obtained by simultaneously solving equations 4.11 and 4.13 using a numerical method. Evidently, these equations describe *both* the upper and the lower wedged particles, and so have at least two real solutions: the positions of the upper and lower particles. Either can be specified by appropriately choosing the initial guess used for the solution of the equations. For each particle, the particle's center position will finally be given by

$$\eta_{\mathrm{pc}} = \eta_{\mathrm{cl}} + \frac{D}{2}\sin\psi \tag{4.14}$$

and the inter-band spacing λ, which we defined as the center-to-center distance between the wedged particles is

$$\lambda = \eta_{\mathrm{pc,top}} - \eta_{\mathrm{pc,bottom}} \tag{4.15}$$

In summary, this proposed model predicts as a function of particle diameter D the inter-band spacing λ, which represents the distance (along the substrate) separating two particles wedged into the converging segments of a meniscus that is tangent to the substrate.

4.3 Experimental

Inter-band spacings predicted by the proposed model were compared to experimentally observed banded films. In the experiments, particle size was varied systematically, and process parameters were chosen to yield sub-monolayer films—banded films in which bands were strictly limited to monolayer thicknesses. This section details the experimental procedures.

4.3.1 Preparation of silica particles

Silica spheres $D = 80\,\text{nm}$ and smaller were synthesized according to the amino-acid hydrolysis methods described independently by Yokoi *et al.* (2006) and Davis *et al.* (2006) and subsequently extended by Hartlen *et al.* (2008). For 20 nm particles, the synthesis was carried out as described in § 3.3.1 according to Davis *et al.* (2006). For particles between 20 nm and 80 nm (inclusive), the method of Hartlen *et al.* (2008) allowed more rapid synthesis. Larger particles required a modified (seeded) version (Hartlen *et al.*, 2008) of the well-known Stöber and Fink's (1968) method.

Briefly, the method described by Hartlen *et al.* (2008) uses arginine instead of lysine as the basic amino acid. Additionally, TEOS is hydrolyzed (60 °C) at the interface of a cyclohexane phase (containing the TEOS) and an aqueous phase (the arginine solution); although not stated, this strategy may have been adopted to control the rate of hydrolysis and suppress nucleation (resulting in the bigger particles). The hydrolysis was carried out under stirring, but at a speed low enough to barely perturb the cyclohexane/water phase interface. A typical batch totaled 90 mℓ with molar composition

62 TEOS : 1.3 arginine : 9500 water : 104 cyclohexane

The seeded Stöber synthesis was carried out by dispersing these primary particles in a solution of water, ethanol, and ammonia, and subsequently adding TEOS at a controlled rate of about 1 mℓ/hr (by syringe pump), under vigorous stirring at room temperature.

Particles synthesized by either amino-acid synthesis method were unwashed, and were diluted to final concentration without consideration for pH; the post-synthesis mixtures in these

Table 4.2: Physical and chemical properties of the particles and coating suspensions

batch id	D (nm)	pH	c μS/cm	ζ-potential (mV)	σ (dyn/cm)
lyssil k026	20	7.4	23.8	-45	68.4
argsil 004.b	50	7.8	15.5	-21	70.1
argsil 003.c	80	6.7	8.6	-34	67.0
argsil 003.c.st004	160	8.6	51.2	-95	64.0
argsil 003.c.st002	230	8.5	32.4	-84	54.6
argsil 003.c.st001	300	8.3	27.5	-102	71.4
argsil 003.c.st007	360	9.0	99.7	-90	71.3

reactions are relatively clean, *i.e.* mostly water, and close to neutral in pH. The Stöber particles required washing by repeated centrifugation due to extremely high pH and significant ethanol content. The characteristics of the final particles are given in Table 4.2.

The most relevant quantity measured in each sample is the surface tension σ, upon which the model quantitatively depends. The suspensions all have bulk surface tensions (as measured by a Wilhelmy plate apparatus, Krüss K10) very close to that of pure DI water (72 dyn/cm); this is an indication that the suspensions were relatively "clean".

It should be noted that although Table 4.2 lists ζ-potential data (Brookhaven Instruments Corporation ZetaPALS), the model described here does not consider the colloidal interactions between particles. The ζ-potential values are simply intended to demonstrate that the particles should behave qualitatively the same; that is mutually repulsive, and repulsive with respect to the substrate. Combined with the pH values, the measured ζ-potential values suggest that the suspensions are of relatively low ionic strength.

4.3.2 Convective assembly of banded monolayers

All films were assembled according to the methods described in Chapter 3. Glass cover slides (2×3 in., Brain Research Laboratories) were used as substrates. These were cleaned immediately prior to coating by a 1 minute hydrofluoric acid (2 %) soak followed by rinsing with copious DI water. The drying nitrogen gas flow rate was fixed at 4.6 $\mathrm{cm}^3/\mathrm{s/cm}$ (Re = 110). Typical bulk suspension particle concentrations were $0.05\sim0.5$ wt% depending on the particle size.

Because the model is not dynamic, it does not allow prediction of the process conditions for which resulting films will have the desired monolayered banded structure. Therefore, process conditions were chosen empirically. For small particles (where gravitational settling was not an issue), the results were reasonably consistent across particle sizes by setting constant the bulk particle concentration (by weight) and coating parameters (substrate withdrawal speed and drying gas flow rate). All substrate withdrawal speeds were between 2 and 12 cm/hr ($5 \sim 30\,\mu$m/s).

Varying the substrate speeds did not affect the band spacings in any systematic way. For larger particles where gravitational settling became problematic, bulk particle concentration was increased until the desired film morphology was obtained at similar coating parameters. Some representative SEM (JEOL-6500, JEOL-6700) images of the resulting monolayered bands are shown in Figures 4.4 to 4.7.

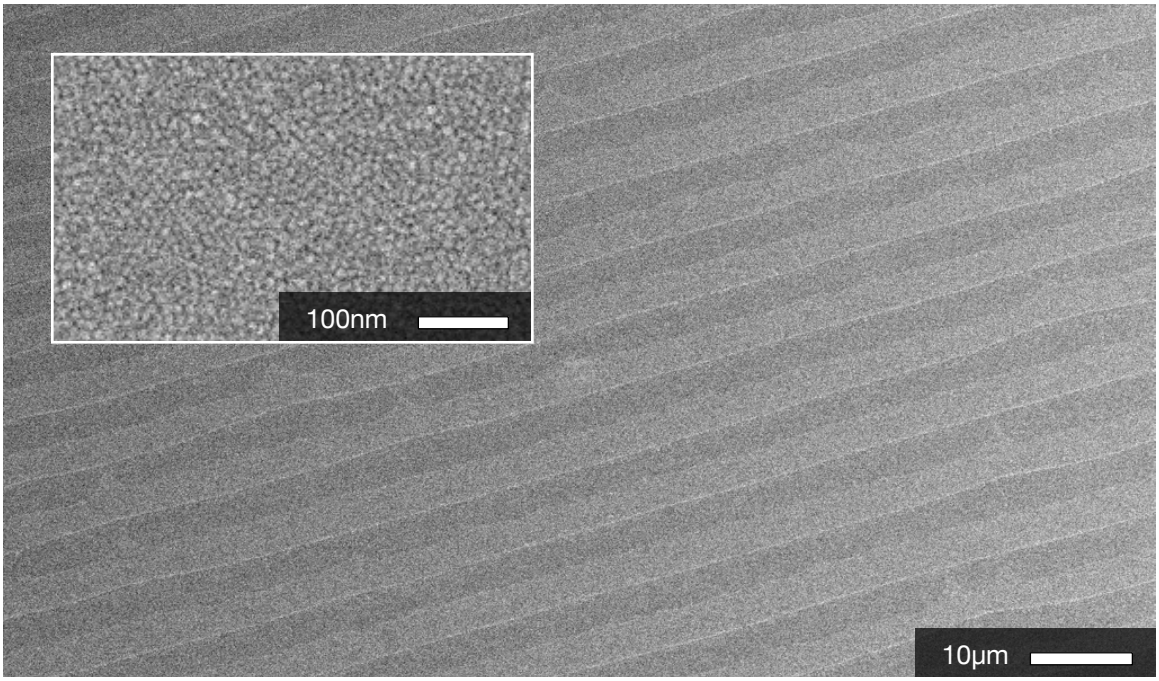

Figure 4.4: Convectively assembled monolayer band: 20 nm

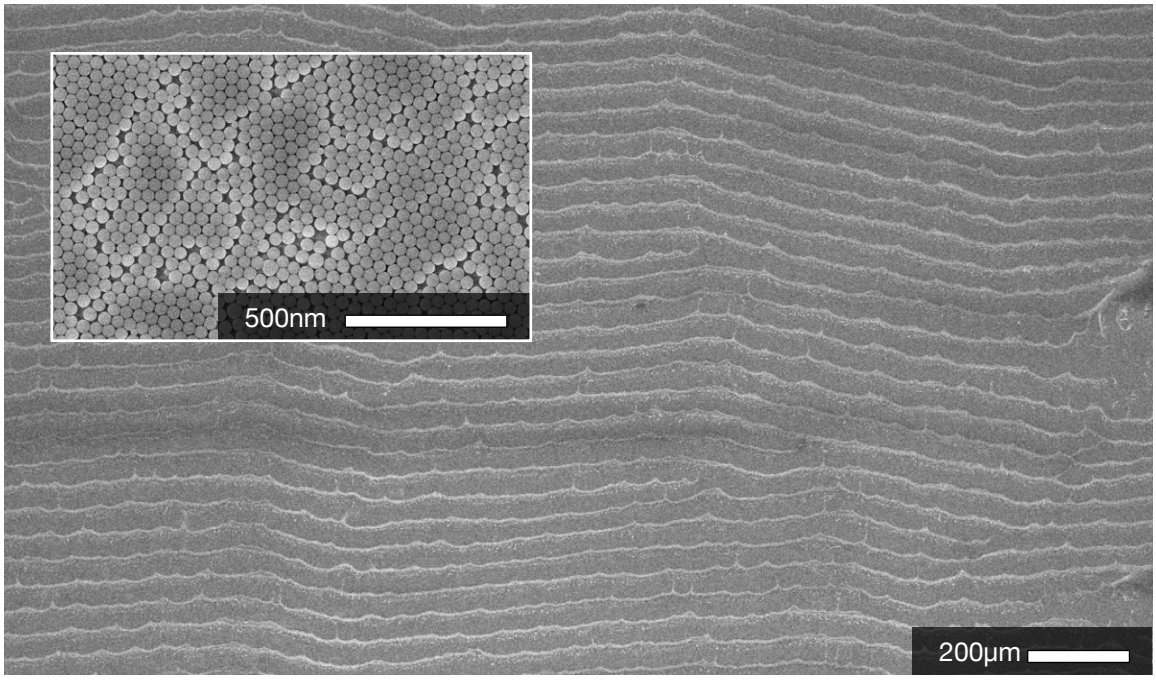

Figure 4.5: Convectively assembled monolayer band: 160 nm

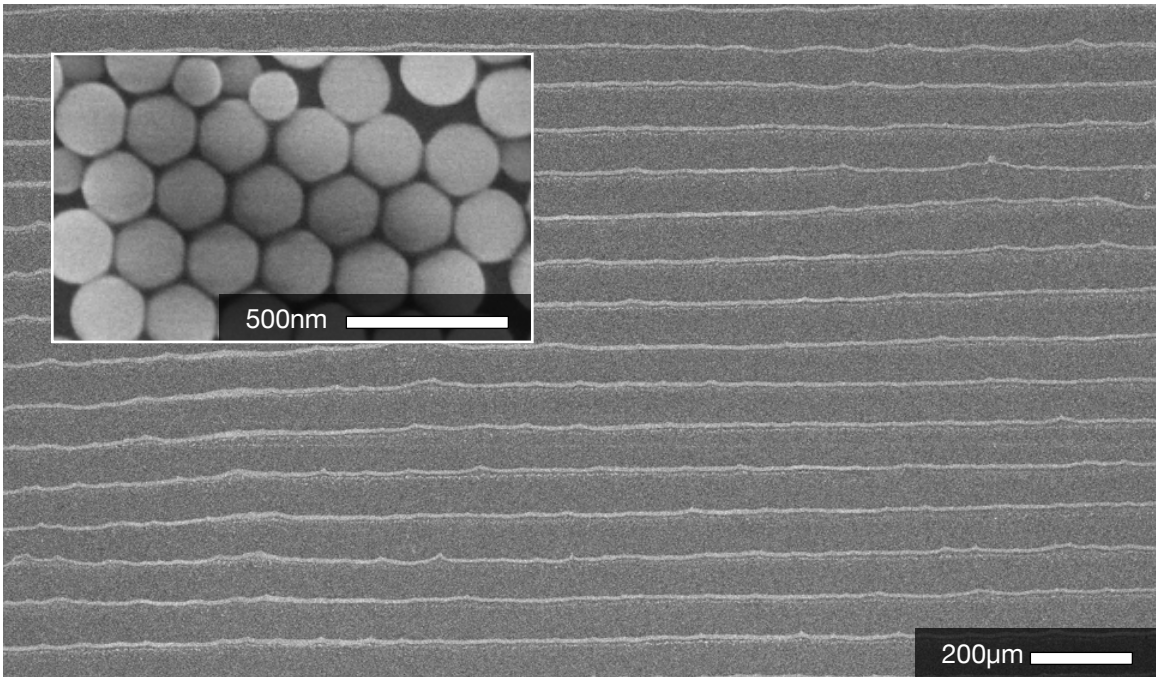

Figure 4.6: Convectively assembled monolayer band: 230 nm

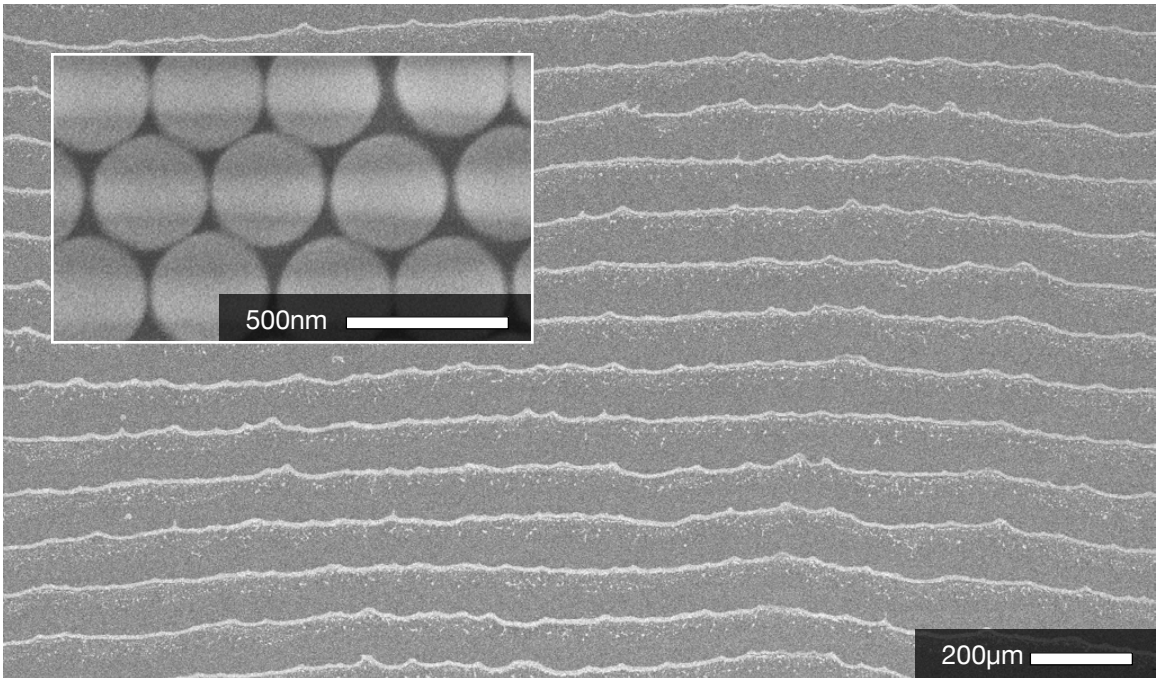

Figure 4.7: Convectively assembled monolayer band: 360 nm

4.3.3 Inter-band spacing measurements

The inter-band spacings were measured by SEM image analysis; while profilometric measurements may seem more appropriate, such data were generally too noisy (small features) and too time-consuming to collect, especially considering the trustworthiness of the results.

Images were analyzed according to a custom-made algorithm (see Appendix C). The process is briefly described below. Because particle-rich regions (bands) appear brighter in the SEM images, the luminance values in the image can be translated to topography (at least for monolayer bands). Images were thresholded following minor contrast and brightness adjustments and smoothing (naïve noise reduction), so that the topography could be described in binary terms; band regions (monolayers) could be treated as "1" and void regions as "0". Ideal bands would be strictly parallel and straight, and the band spacings could be quantified by taking the "profile scan" perpendicular to the banding direction and analyzing the lengths of the trough regions.

The real bands are neither strictly parallel nor straight, and furthermore the images were not necessarily oriented perpendicular to the bands. Thus, multiple parallel "profile scans" were taken for statistics, and the scans were re-taken at series of angles. The "true" inter-band spacings were taken to be those at the angle for which measured average trough length was minimized (as this would be a measure of the scans being as close to perpendicular to the bands as possible). For images where this algorithm did not work well, the spacings were collected manually by drawing and measuring the length of lines drawn in the void bands (locally perpendicular to the band) at many locations.

The inter-band spacing data so-collected for all experiments are plotted in Figure 4.8, along with the prediction made by the model described in § 4.2.2. The prediction is for a zero contact angle between the upper particle and the meniscus surface ($\theta_p = 0$), and a value of capillary length a corresponding to that of pure water ($\sigma = 72\,\mathrm{dyn/cm}$, $\rho = 1000\,\mathrm{kg/m^3}$). As Figure 4.8 shows, variation of the substrate withdrawal speed (data point symbols) did not systematically affect the measured inter-band spacings in the resulting films, nor were the effects significant compared to the effect of particle size.

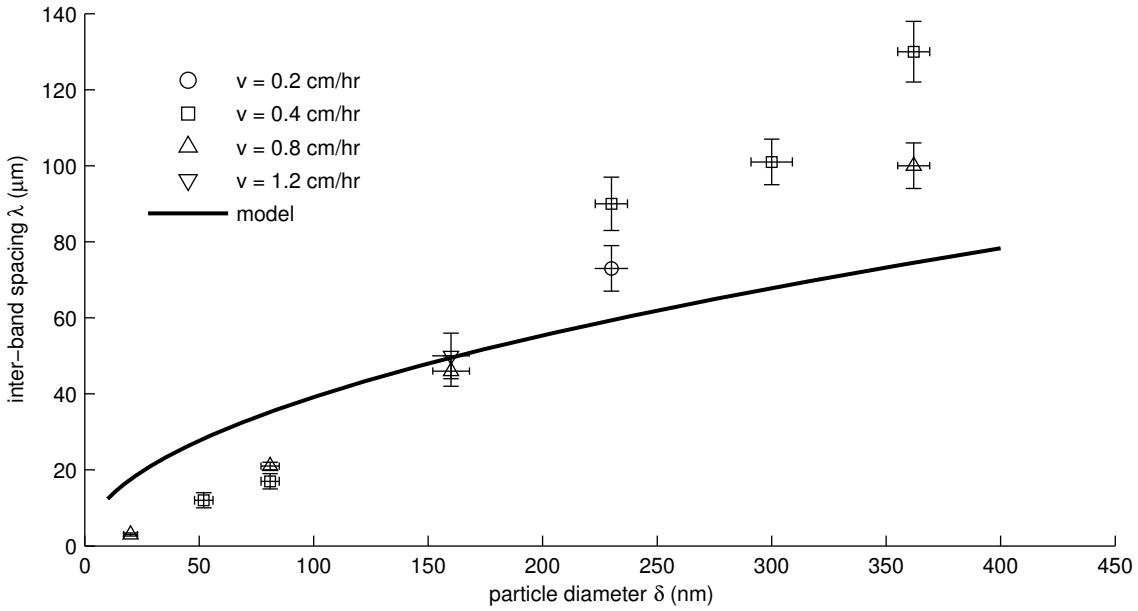

Figure 4.8: Inter-band spacing of banded monolayer films against particle diameter, at various substrate withdrawal speeds (symbols). The solid line is the predicted inter-band spacing for a zero contact angle between particles and the meniscus surface assuming pure water ($\sigma = 72\,\mathrm{dyn/cm}$, $\rho = 1000\,\mathrm{kg/m^3}$).

4.4 Parametric variations

The model described in § 4.2.2 seems to over-predict inter-band spacings for small particles and under-predict them for larger particles. A parametric study on the most relevant parameters, namely the liquid's bulk surface tensions σ and its contact angle with the particle θ_p, shows that neither parameter can quantitatively improve the predictions. Their effects are discussed below.

The predicted λ decrease with decreasing σ between 40 dyn/cm and 72 dyn/cm (Figure 4.9), which are reasonable bounds for water (tap water has a surface tension of about 55 dyn/cm, compared to 72 dyn/cm for pure water). The decreased surface tension manifests as a diminished value of the capillary length a—the length-scale of the meniscus—so that predicted λ are shorter (the meniscus itself is "compressed").

Another available parameter in the model is the contact angle θ_p between the liquid and the spherical particle. As θ_p increases (the particle becomes less wettable), the predicted λ decrease (Figure 4.10). This is due to a shortening of the upper meniscus wedge region (component of λ

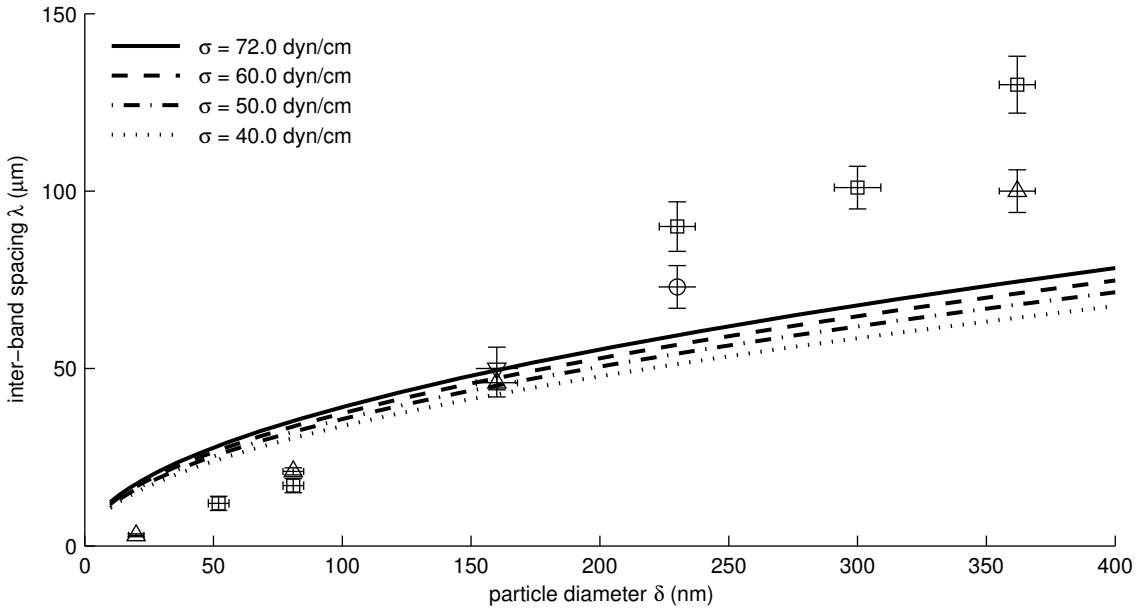

Figure 4.9: Inter-band spacings predicted by the static model for varying liquid surface tensions σ.

from the contact line on the upper particle to the intersection between the meniscus and substrate) when the liquid-particle contact line is allowed to be finite. The effect is small, and is only exaggerated in Figure 4.10 using contact angles up to 80°, which is unreasonably large for a silica surface and water.

So far, the model considered only the situation of a meniscus that intersects the substrate at a tangent, and sensitivity to the available parameters has been shown to be much weaker than the experimental variation itself. The model could be modified to allow for a finite contact angle of the liquid with the *substrate* θ_s, in addition to that with the particle θ_p. However, such an extension requires some tweaking of the definition of the predicted inter-band spacing. In the new definition, the two wedge sections of the meniscus must be considered separately: the top wedge is considered at "incipient breakage" as the meniscus is stretched, while the bottom wedge is that for the meniscus "after breakage", as it takes up a new equilibrium contact position defined by the contact angle θ_s (see Figure 4.11).

Specifically, the treatment of the upper particle will be the same; the contact angle with the particle θ_P will be enforced, but the meniscus profile must be the one that intersects the sub-

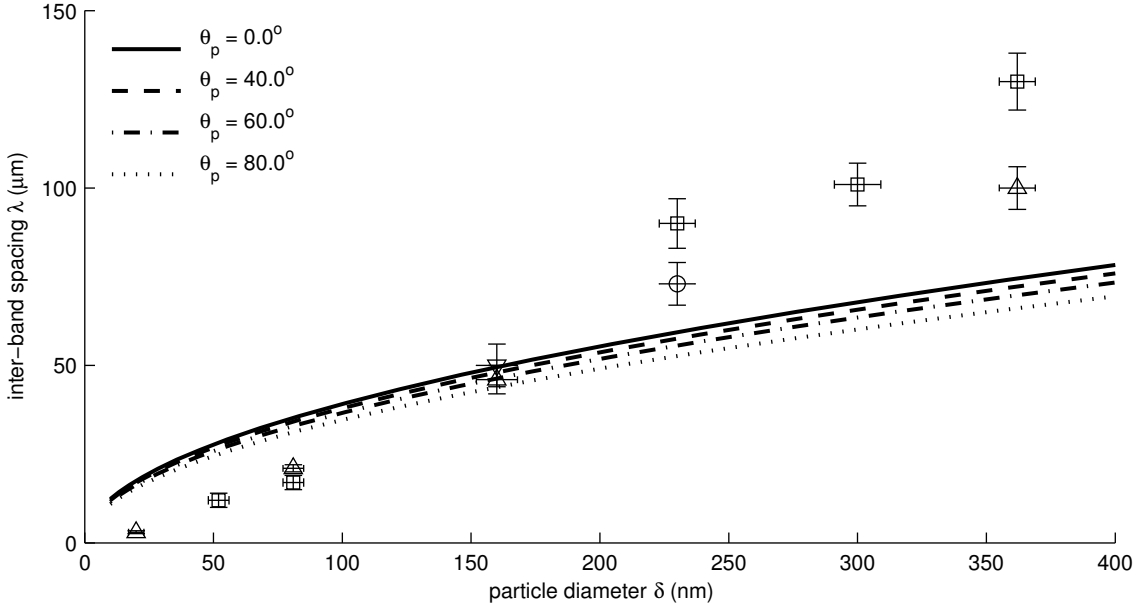

Figure 4.10: Inter-band spacings predicted by the static model for varying liquid-particle contact angles θ_p.

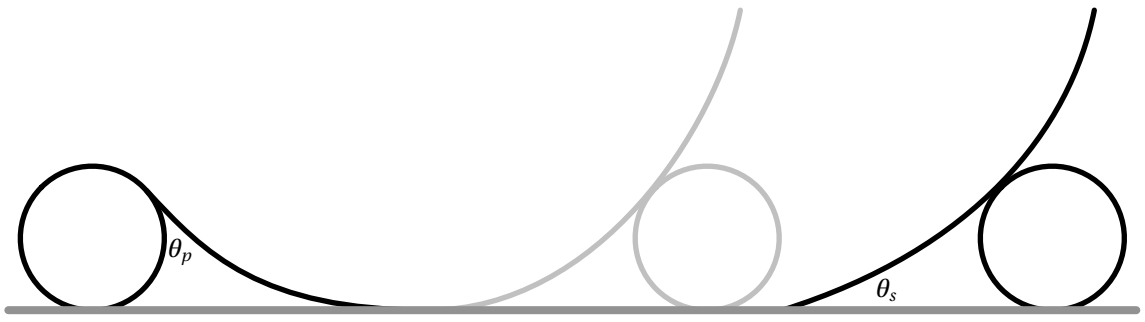

Figure 4.11: Static model for inter-band spacing with consideration for liquid-substrate contact angle. A finite contact angle θ_s after a meniscus "breakage" implies an equilibrium capillary rise smaller than for zero-contact angle, and the predicted inter-band spacing λ will consequently be larger.

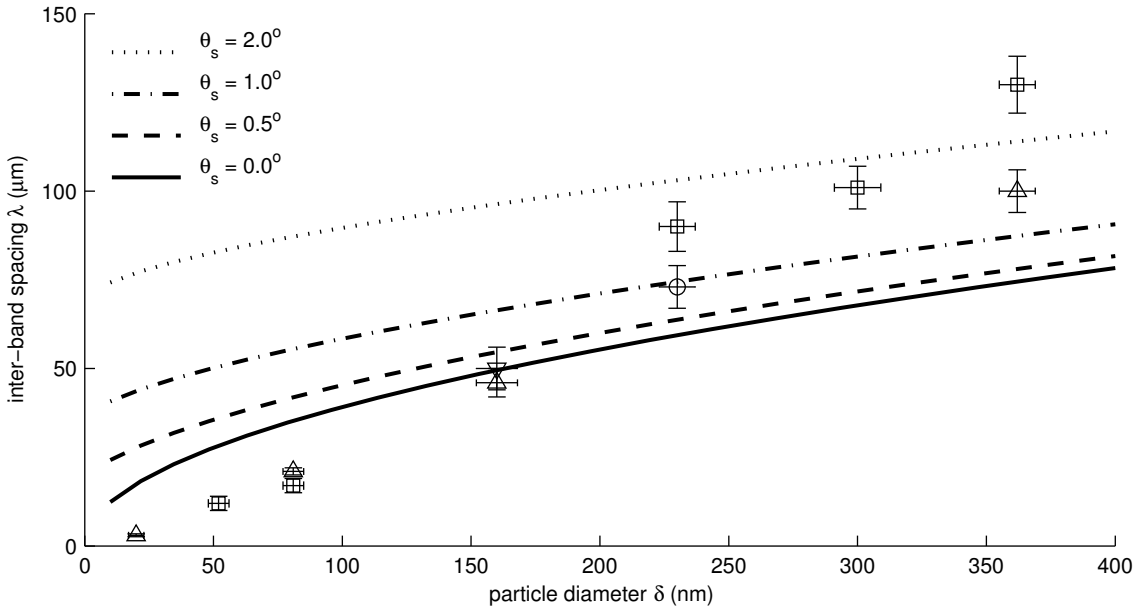

Figure 4.12: Inter-band spacings predicted by the static model for varying liquid-substrate contact angles θ_s.

strate a tangent ($\theta_s = 0$) because it does not make sense to consider a contact angle on the upper wedge. The bottom wedge will be considered using $\theta_p = 0$ for the same reason discussed in § 4.2.2, but the meniscus with which the bottom particle intersects will be the meniscus that makes a contact angle θ_s with the substrate. The situation described here is shown schematically in Figure 4.11. The finite contact angle implies a diminished equilibrium capillary rise, resulting in extra space between the upper and lower wedged particles. This is quantitatively shown in Figure 4.12, where it is evident that the predicted λ are accordingly shifted up.

4.5 Inter-band spacings in multilayered banded films

The initial premise—that larger particle sizes lead to larger spacings between monolayer bands—has the additional implication that inter-band spacing is dependent on the thickness of the preceding particle band, as suggested schematically in Figure 4.1c. Thus, inter-band spacing should be larger for multilayered bands than for monolayered bands, given a particle size. Although the experimental series described here did not result in well-formed multilayer bands, evidence in

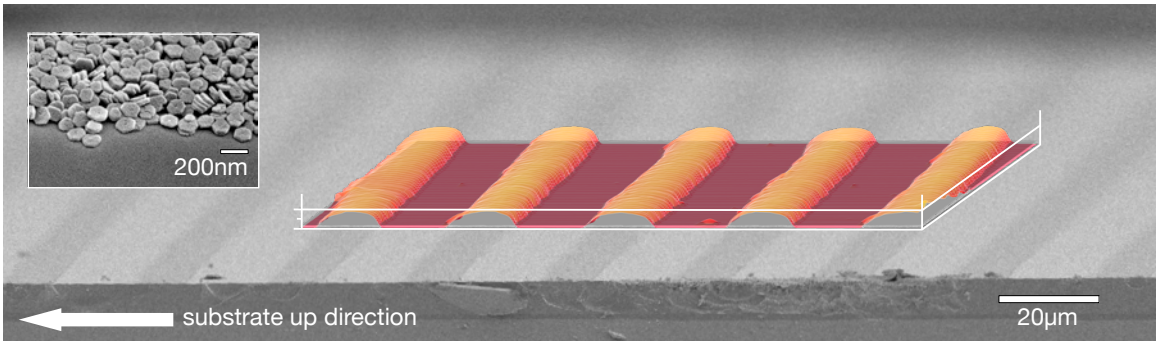

Figure 4.13: Cross sectional SEM image of a banded multilayer ZSM-2 film. A profilometric scan is superimposed onto the image. The inset SEM image shows a trailing edge of on of the bands. Bands are about 180 nm thick at their crest, and are spaced about 20 μm apart.

the literature (Masuda *et al.*, 2004; Watanabe *et al.*, 2009) suggest that such morphologies are indeed possible. In fact, Watanabe *et al.* (2009) reported a model similar to the one presented here, and applied it to the prediction of inter-band spacings in multilayered films.

Recalling that the ZSM-2 films described in both Chapters 2 and 3 exhibited a banded multilayer morphology, we can re-examine the results in the context of the static meniscus profile model for inter-band spacing. A typical banded ZSM-2 film is shown in Figure 4.13 (on a silicon wafer); the inset SEM image of a band's trailing edge and the superposed profilometric scan confirm that the the bands are multilayered.

As described in Chapters 2 and 3, particles at the leading edges of new bands lie flat. Therefore, the short dimension of the particles (about 40 nm) can be considered the particle size *in the context of the lower wedge of the meniscus*. Profilometry indicates the bands are about 180 nm thick at their crest, and this value can be considered the particle size *in the context of the upper meniscus wedge*. Using these values as the diameters of the circular particles, the value of surface tension for pure water, and stipulating zero contact angles $\theta_s = \theta_p = 0$, the model predicts inter-band spacings of $\lambda = 39\,\mu\text{m}$, while the experimentally measured spacings are about 20 μm. With a slightly modified model abandoning the circular particle shape in favor of corners and altering the situation with the incoming particle (see Figure 4.14), the prediction becomes a somewhat closer $\lambda = 25\,\mu\text{m}$.

Without making any quantitative claims, we note that the measured inter-band spacing in

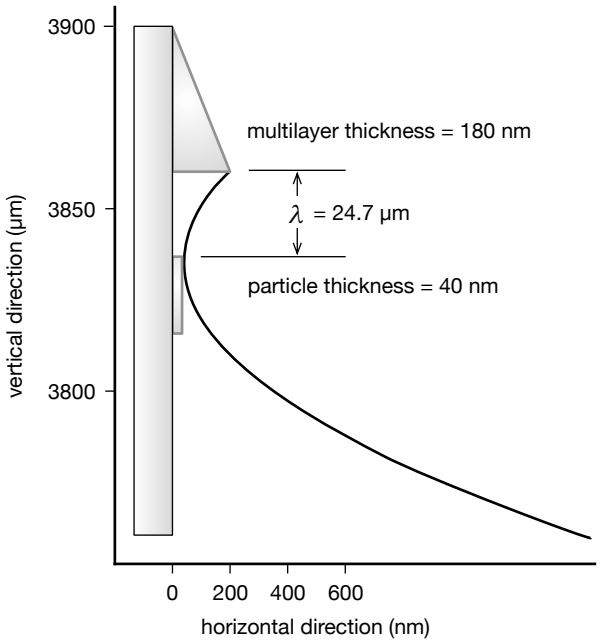

Figure 4.14: Modified model of the inter-band spacing in multilayered ZSM-2 films. The meniscus does not touch the substrate; rather, the contact line condition at the upper particle is changed to a corner so that a contact angle cannot be specified. This allows for solution of a meniscus profile parameterized by its minimum approach to the substrate. Using the particle size (thickness in the case of ZSM-2) as this minimum approach, a slightly more realistic model can be constructed, in which λ is determined by the distance between the upper particle deposit and the particle that is sandwiched between the meniscus and the substrate.

the multilayered ZSM-2 films are within order of magnitude with the predictions made by the static meniscus model and its variants. Furthermore, multilayered banded films made with the lysine-silica spheres (20 μm), though ill-defined, were observed to have a banded morphology with wavelength much larger than would be predicted for the particle size using this model (see Figure 4.2a). This latter point is also demonstrated by Watanabe *et al.* (2009).

4.6 Concluding remarks

Although it is well known that convective assembly from dilute suspension generally result in banded film morphologies (either monolayered or multilayered), there does not seem to be a complete understanding of the underlying mechanism despite various attempts in the literature. This chapter described a systematic study of the dependence of inter-band spacing (in strictly monolayered banded films) on particle size, and a simple geometrical model based on the stretched static meniscus profile prescribed by the Young-Laplace equation. The model was shown to qualitatively capture the dependence of inter-band spacings on the constituent particle diameters, namely that larger particles assemble into banded with larger spacings.

Although dynamic considerations are certainly at play, the weak dependence of measured inter-band spacings with substrate withdrawal velocity (as long as they all result in monolayered banded morphologies) suggests that dynamics are not as important as the geometric constraint when predicting the inter-band spacings. The model further predicts that multilayered banded films should have larger spacings than a monolayered banded film (with the same constituent particle diameter). This was verified qualitatively for films from silica spheres and one ZSM-2 film, while a contemporaneous report by Watanabe *et al.* (2009) further corroborates the idea with films from spherical particle.

The model could be extended to include other forces that would alter the meniscus profile, for example molecular forces (which may be important for the very small particles) and viscous forces arising due to liquid flow within the meniscus (which would become increasingly important as the drying rate is increased, effecting stronger liquid flow). Such extensions, however,

would still not address the dynamic nature of the real process, which might manifest as the interplay between arriving particles and the dynamics of meniscus stricture (due to a combination of substrate withdrawal and film growth), for example. Nevertheless, a study of the meniscus profile with finite flow is presented in the following chapter.

Chapter 5

Banded monolayers: a kinematic model

The previous chapter introduced the idea of relating the inter-band spacing in convectively assembled films to the minimum distance between two particles wedged in, and separated by, a completely "choked" static meniscus. While the choked static meniscus model is unrealistic in its disregard for liquid flow (which is ultimately responsible for the particle convection), the concept seemed to reasonably fit the observations. This chapter takes the model one more step by allowing for the effects of liquid flow using the thin film approximation, and modeling the incoming particle as a smooth hump on the substrate.

Liquid flow alters the meniscus profile by introducing viscous terms to the Young-Laplace pressure balance equation, and thus requires finite clearance between the meniscus surface and the substrate (including the hump). At the contact line, the meniscus must be separated from the substrate, and a convenient assumption is that the meniscus is pinned at an already-extant film assembly front; this film is about one particle diameter thick in the case of monolayer bands. The inter-band spacings in the films can then be related to the position of this substrate hump relative to the contact line.

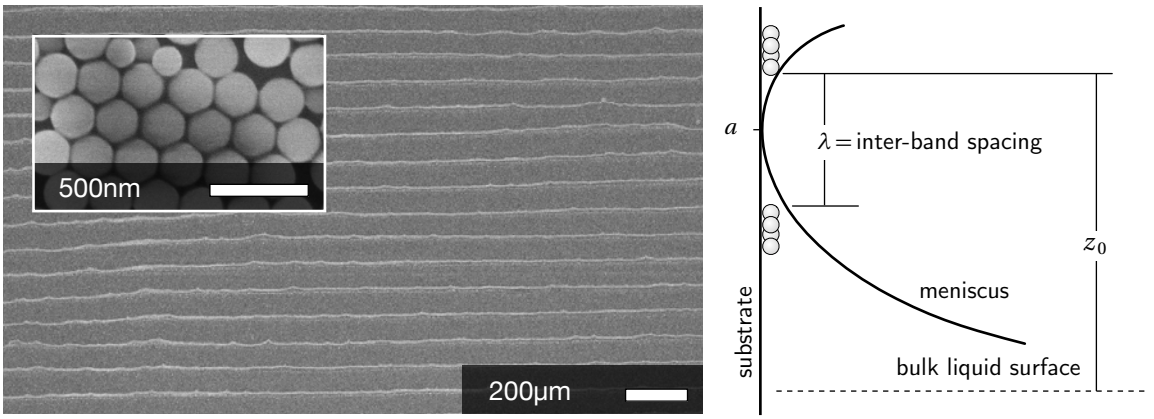

Figure 5.1: Example of a banded film with particles about 360 nm in diameter (inset). Roughly speaking, the spacings can be imagined to result from physical exclusion with respect to the liquid meniscus surface (right).

5.1 Background

As described in the previous chapters, convectively assembled [nano]particle films are prone to a regularly banded morphology (Ghosh *et al.*, 2007; Masuda *et al.*, 2004; Ray *et al.*, 2005; Watanabe *et al.*, 2009; Lee *et al.*, 2009). The case of monolayer bands was examined in Chapter 4, where it was found that the length scale of the banded pattern—that is the spacing between the bands—is a strong function of the constituent particle size (see Figure 5.1). Following the work of Ray *et al.* (2005), this dependence was attributed to the geometry of a static (equilibrium) liquid meniscus in which the assembly occurs (Lee *et al.*, 2009). While the static meniscus description is reasonably intuitive in the case of multilayered films, it is especially unsatisfying in the monolayer case because of the contrived nature of the choked meniscus configuration, which does not allow for liquid flow—certainly defining characteristic of convective assembly.

A liquid meniscus during convective assembly is pinned on the developing particle film, ostensibly on the last row of particles. Such a pinned meniscus can be defined primarily by two parameters: (1) the flow rate Q_0 that must be supported under it and (2) the extent z_0 to which the meniscus is stretched (the distance from the contact line to the bulk liquid surface; see Figure 5.1). To accommodate flow requires a finite clearance between the meniscus surface and the substrate, and we know that a meniscus generally constricts more and more as it is stretched.

Thus, in the absence of a hump in the substrate, the following complementary questions can be posed: (1) what is the maximum allowed extent of meniscus stretch z_0 for a given liquid flow Q_0 and (2) what is the maximum allowed Q_0 given some z_0. The answer to these questions defines a boundary of meniscus existence on the Q_0–z_0 plane, outside of which menisci cannot exist.

Now considering an arriving particle as a hump in the substrate, we can pose the following question: assuming a meniscus parameterized by some given pair (Q_0, z_0), how close can the hump in the substrate be placed to the pinning point? We can anticipate that this is a sensical question by considering that as the hump position approaches the pinning point, the minimum clearance between the meniscus profile (which by the way is also affected by the presence of the hump) decreases, and we further know that there should be a limiting clearance. The closest allowed position x_p of the hump can then be related to the inter-band spacing in a convectively assembled film.

The remainder of this chapter presents a thin film model for the meniscus with flow, strategies to determine the limits of (Q_0, z_0), and the closest approach x_p at the allowed (Q_0, z_0). Additionally, an attempt is made to identify regimes in this parameter space that reasonably reflect conditions relevant to a real convective assembly process. The result of this analysis will propose upper limits on the band spacings allowed for films comprising particles of a certain size.

5.2 Theory and methods

A liquid meniscus attached to the corner of an assembling particle film must support the liquid flow sucked through the film-meniscus interface by drying within the film. Ignoring the presence of particles, the film profile is related to the liquid flow through its thickness and the pressure gradient set up by the curvature gradient (additionally to any pressure difference external to the meniscus, *i.e.* suction from the film). In other words, such a meniscus must depart from its static equilibrium profile by taking on extra curvature; this can physically manifest as constriction against the substrate and an associated decrease in the apparent contact angle (negative apparent contact angles for constricted menisci; see *e.g.* Figure 5.2).

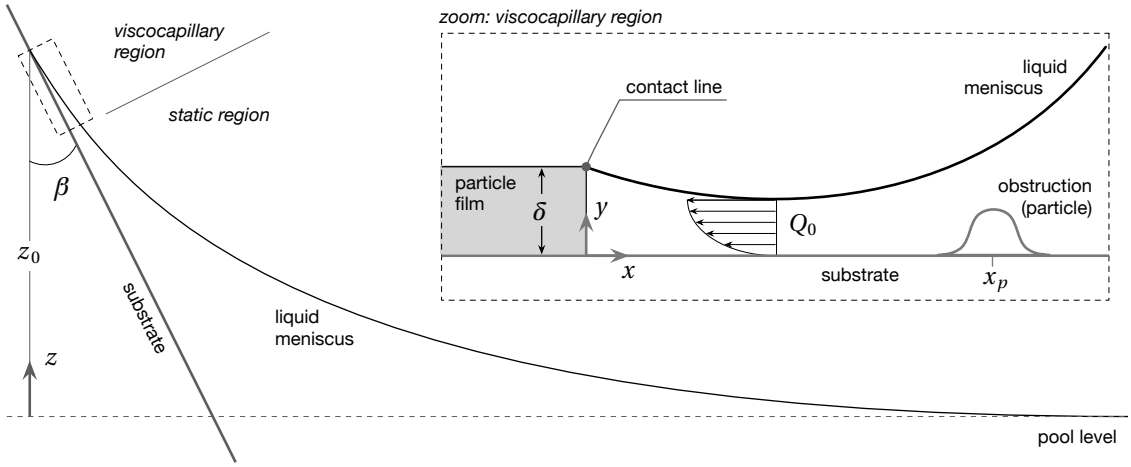

Figure 5.2: A generic meniscus supporting flow can be regarded as being mostly static. The inset shows the visco-capillary region with a schematic representation of the "particle".

The presence of a single incoming particle may be approximated as a smooth hump on the substrate, which will introduce an additional constriction to the flow and therefore further increase the curvature gradient locally. A summary schematic of the situation is presented in Figure 5.2, wherein a substrate rests in a pool of liquid at an arbitrary angle β with the vertical. Assuming that a film of finite thickness δ exists at the "contact line," the meniscus will support flow toward the film, indicated in Figure 5.2 as rectilinear (see § 5.2.1).

For convenience the coordinate system is orientated with x along the substrate and y perpendicular to it. The location of the "incoming particle" can thus be parameterized by a position x_p along the substrate direction. Additionally, the direction of gravity z will be used in formulating a boundary condition relating to the meniscus stretch (elevation of the film corner from the liquid pool) denoted z_0. A liquid flow rate Q_0 through the film of thickness δ completes the prescription; the trio of parameters z_0, x_p, and Q_0 specifies a single liquid meniscus profile assuming rectilinear flow. The problem, then, is stated as finding this profile. A summary of the symbols used in this chapter are given in Table 5.1.

Table 5.1: List of symbols

symbol		meaning
ρ		density
g		acceleration due to gravity
σ		surface tension (of liquid)
a		capillary length
θ_0 or θ		contact angle between liquid and substrate
δ		particle diameter (maximum pinning height)
β		angle of substrate from the vertical
x	(ξ)	dimension $\parallel$ substrate (dimensionless; scaled by δ)
y		dimension $\perp$ substrate
h	(η)	meniscus height in y dimension (dimensionless; scaled by δ)
K	(κ)	horizontal dimension (dimensionless; scaled by a)
S	(s)	dimension along meniscus arc (dimensionless; scaled by δ)
z	(ζ)	direction of gravity. origin is at the bulk liquid surface (infinite pool)
z_0	(ζ_0)	extent of meniscus stretch, *i.e.* separation (along z, ζ) of pinning height from infinite pool level
x_p	(ξ_p)	location (along x, ξ) of the substrate hump modeling the incoming particle
γ		length scale ratio δ/a
ϕ		inclination angle with respect to x-direction (CCW)
Q	(q)	2-D liquid flow rate (dimensionless; scaled by $\frac{\sigma\delta^2}{\mu a}$)
J_e	(j_e)	1-D liquid flow rate; evaporation per unit s (dimensionless; scaled by $\frac{\sigma\delta}{\mu a}$)

5.2.1 Film equation

In considering the relevant domain for the problem, the following informal dimensional analysis is helpful. For a film in creeping flow, velocity scales with the cube of the film thickness, and the relevant region of flow can be said to have a characteristic length scale of the particle film thickness, denoted δ. For micro- and nano-particle films, this is many orders of magnitude smaller than the capillary length scale for the entire (static) meniscus, and therefore most of the meniscus may be regarded to be static, as indicated in Figure 5.2.

As the inset in Figure 5.2 suggests, flow in the *non*-static region is approximated as rectilinear and parabolic (the thin film approximation). The exclusion of inertial terms is validated by experiment, where it is found that a typical Reynolds number based on the length scale δ is of the order of $\mathcal{O}(10^{-4})$ according to velocity tracking results: the maximum velocity of a particle in flow was estimated to be about 50 µm/s arriving to a film about 5 µm thick (10 layers of 0.5 µm diameter particles). With the appropriate simplifications, the Navier-Stokes equation is

$$\mathbf{0} = \rho\mathbf{g} - \nabla_{\text{II}} p + \mu\nabla_{\text{II}}^2\mathbf{v} \tag{5.1}$$

Further assuming rectilinear flow reduces Equation 5.1 to the scalar equations

$$0 = \rho g \cos\beta - \frac{\partial p}{\partial x} + \mu\frac{\mathrm{d}^2 v_x}{\mathrm{d}y^2} \tag{5.2}$$

$$0 = -\rho g \sin\beta - \frac{\partial p}{\partial y} \tag{5.3}$$

Applying the usual no-slip boundary conditions on Equation 5.2 gives the well-known parabolic velocity profile

$$v_x(x,y) = \left[\rho g \cos\beta - \frac{\partial p}{\partial x}\right]\frac{1}{\mu}\left(h(x)y - \frac{y^2}{2}\right) \tag{5.4}$$

and applying the Young-Laplace equation (for p_y) gives the pressure distribution in the meniscus

$$\begin{aligned} p(x,y) &= \int_0^{h(x)} \rho g \sin\beta \, \mathrm{d}y \\ &= p_{\text{atm}} - \sigma K(x) + \rho g \sin\beta \left[h(x) - y\right] \end{aligned} \tag{5.5}$$

where $K(x)$ denotes the meniscus curvature along x. Since one of the boundary conditions is given in terms of flow rate, it is convenient to integrate the velocity profile over the film thickness $h(x)$ to give the total x-wise flow rate $Q(x)$.

$$\begin{aligned} Q(x) &= \int_0^{h(x)} \left[\rho g \cos\beta - \frac{\partial p}{\partial x}\right] \frac{1}{\mu} \left(h(x)y - \frac{y^2}{2}\right) \mathrm{d}y \\ &= \frac{h^3}{3\mu} \left\{-\frac{\partial p}{\partial x} + \rho g \cos\beta\right\} \end{aligned} \tag{5.6}$$

The pressure gradient term in Equation 5.6 above represents the only mechanical potential for flow through the meniscus, and can be formulated by differentiating the pressure distribution given by Equation 5.5

$$\frac{\partial p}{\partial x} = -\sigma K(x) + \rho g \sin\beta \frac{\mathrm{d}h}{\mathrm{d}x} \tag{5.7}$$

Combining the results of Equation 5.6 and Equation 5.7 gives an expression for the flow rate in terms of the meniscus profile.

$$Q(x) = \frac{h^3}{3\mu} \left\{\sigma \frac{\mathrm{d}K}{\mathrm{d}x} - \rho g \sin\beta \frac{\mathrm{d}h}{\mathrm{d}x} + \rho g \cos\beta\right\} \tag{5.8}$$

Anticipating that Equation 5.8 will be posed in terms of arc length of meniscus surface rather than x (see § 5.2.3), the condition of liquid evaporation along the surface can be built in as a flow rate deficiency per unit arc length S.

$$\frac{\mathrm{d}Q}{\mathrm{d}S} = J_e \tag{5.9}$$

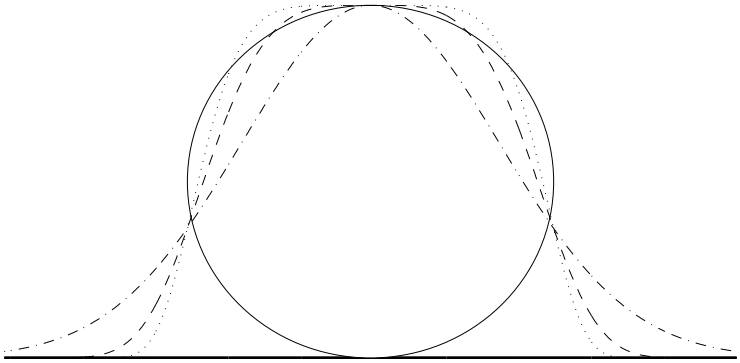

Figure 5.3: The substrate profile, which is meant to simulate an actual particle (solid line) can be represented by the shape of a bell curve. The exponent $\mathscr{P}$ can be adjusted to tighten the bounds and the factor $\mathscr{M}$ in Equation 5.10 can be reflect the girth of the particle. In the examples: $\cdots$ $(\mathscr{P},\mathscr{M})=(6,2)$, $--$ $(\mathscr{P},\mathscr{M})=(4,2)$, $\cdot-\cdot-$ $(\mathscr{P},\mathscr{M})=(2,2)$

5.2.2 Representation of incoming particle

The incoming particle can be represented as a topological feature in the substrate. The substrate profile $h_{\mathrm{B}}(x\,;x_p)$ should reasonably approximate the particle shape, but should also be differentiable at least once with respect to all of its variables (continuous). Furthermore, its derivative with respect to the x-dimension should be finite. Modified Gaussian probability distributions (Equation 5.10) are good candidates (see Figure 5.3) for avoiding piece-wise definitions.

$$h_{\mathrm{B}}(x\,;x_p)=\delta\, e^{-\mathscr{M}(x-x_p)^{\mathscr{P}}} \tag{5.10}$$

The presence of the topological feature modifies Equation 5.8 by constricting the "clearance" h in the flow term; the flow rate equation becomes

$$Q(x)=\frac{(h-h_{\mathrm{B}})^3}{3\mu}\left\{\sigma\frac{\mathrm{d}K}{\mathrm{d}x}-\rho\,g\sin\beta\frac{\mathrm{d}h}{\mathrm{d}x}+\rho\,g\cos\beta\right\} \tag{5.11}$$

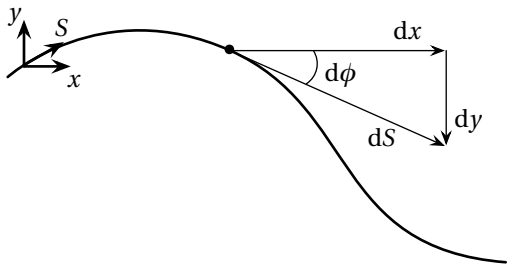

Figure 5.4: Illustration of the arc length parameterization geometry.

5.2.3 Re-parameterization from Cartesian to arc coordinates

In Equation 5.11, the curvature $K(x)$ can be expressed in terms of the first and second derivatives of the meniscus profile $h(x)$ (Equation 5.12), revealing that the overall problem is third order and nonlinear in x.

$$K = \frac{\mathrm{d}^2 h}{\mathrm{d}x^2}\left[1+\left(\frac{\mathrm{d}h}{\mathrm{d}x}\right)^2\right]^{-3/2} \tag{5.12}$$

The high order derivatives can be conveniently traded for more variables by re-parameterizing the equation in terms of arc length S along the meniscus surface, as illustrated in Figure 5.4, especially because the derivatives (or some expression involving them) are themselves physically tangible quantities. The elimination of the higher order derivatives also alleviates the issue of constructing high order finite difference equations if the problem is to be solved that way.

Briefly, the parameterization by arc length S allows a re-phrasing of the problem by eliminating the second and first derivatives of h with respect to x in favor of curvature K and inclination ϕ of the meniscus profile. First order differential equations for the spatial variables h and x can be constructed in terms of ϕ. In Figure 5.4, the inclination ϕ is defined relative to the x principle

direction, so that the parameterization can be summarized as

$$K = \frac{\mathrm{d}\phi}{\mathrm{d}S} \tag{5.13}$$

$$\tan\phi = \frac{\mathrm{d}h}{\mathrm{d}x} \tag{5.14}$$

$$\sin\phi = \frac{\mathrm{d}h}{\mathrm{d}S} \tag{5.15}$$

$$\cos\phi = \frac{\mathrm{d}x}{\mathrm{d}S} \tag{5.16}$$

In terms of these variables, Equation 5.11 becomes

$$\frac{\mathrm{d}K}{\mathrm{d}S} = \frac{3\mu}{\sigma[h - h_{\mathrm{B}}(x_p)]^3} Q\cos\phi + \frac{\rho g}{\sigma}\left(\sin\phi\sin\beta - \cos\phi\cos\beta\right) \tag{5.17}$$

The last term in Equation 5.17 can be simplified using the following trigonometric identities

$$\cos\phi\cos\beta = \frac{\cos(\phi-\beta)+\cos(\phi+\beta)}{2} \tag{5.18}$$

$$\sin\phi\sin\beta = \frac{\cos(\phi-\beta)-\cos(\phi+\beta)}{2} \tag{5.19}$$

In fact this simplification combines the two terms dealing with the gravity contribution to mechanical potential in a more physically obvious form, namely (recalling that the direction $\phi+\beta$ gives the inclination with respect to the gravitational dimension z),

$$\frac{\rho g}{\sigma}\left(\sin\phi\sin\beta - \cos\phi\cos\beta\right) = \frac{\rho g}{\sigma}\cos(\phi+\beta) \tag{5.20}$$

Thus, in terms of arc length S and allowing for the possibility for the flow rate to vary along the

substrate due to evaporation loss, Equation 5.11 can be expressed as the system

$$\frac{\mathrm{d}Q}{\mathrm{d}S} = J_e \tag{5.21}$$

$$\frac{\mathrm{d}K}{\mathrm{d}S} = \frac{3\mu}{\sigma[h - h_\mathrm{B}(x_p)]^3} Q\cos\phi - \frac{\rho g}{\sigma}\cos(\phi+\beta) \tag{5.22}$$

$$\frac{\mathrm{d}\phi}{\mathrm{d}S} = K \tag{5.23}$$

$$\frac{\mathrm{d}h}{\mathrm{d}S} = \sin\phi \tag{5.24}$$

$$\frac{\mathrm{d}x}{\mathrm{d}S} = \cos\phi \tag{5.25}$$

5.2.4 Boundary conditions

So far, the meniscus profile in the viscocapillary region has been described using the film approximation and parameterized by arc length S along the meniscus surface. The result is a system of five equations (for flow rate, curvature, inclination, and the spacial dimensions), for which five boundary conditions are required. The physical situation is illustrated in Figure 5.5, where the film and static boundaries are respectively denoted by the subscripts 0 (origin) and n.

At the origin, the pinning boundary conditions on h and x may be constructed via ϕ_0 by specifying a contact angle between the particle and the liquid.

$$\frac{\delta}{2}^2 = x_0^2 + \left(h_0 - \frac{\delta}{2}\right)^2 \tag{5.26}$$

$$x_0 = \frac{\delta}{2}\sin(\theta - \phi_0) \tag{5.27}$$

We can arbitrarily assert that $x = 0$ at the contact point between the particle and the substrate (the problem is evidently invariant to translations in x). A simplifying assumption may be made to reduce the pinning to a corner (instead of the circle shown in Figure 5.5): h_0 may be asserted as δ, the film thickness, and $x_0 = 0$. In any case, the flow rate at the origin was proposed as a parameter, and so $Q_0 = Q_0$. Summarily, there are three conditions that can be posed at the

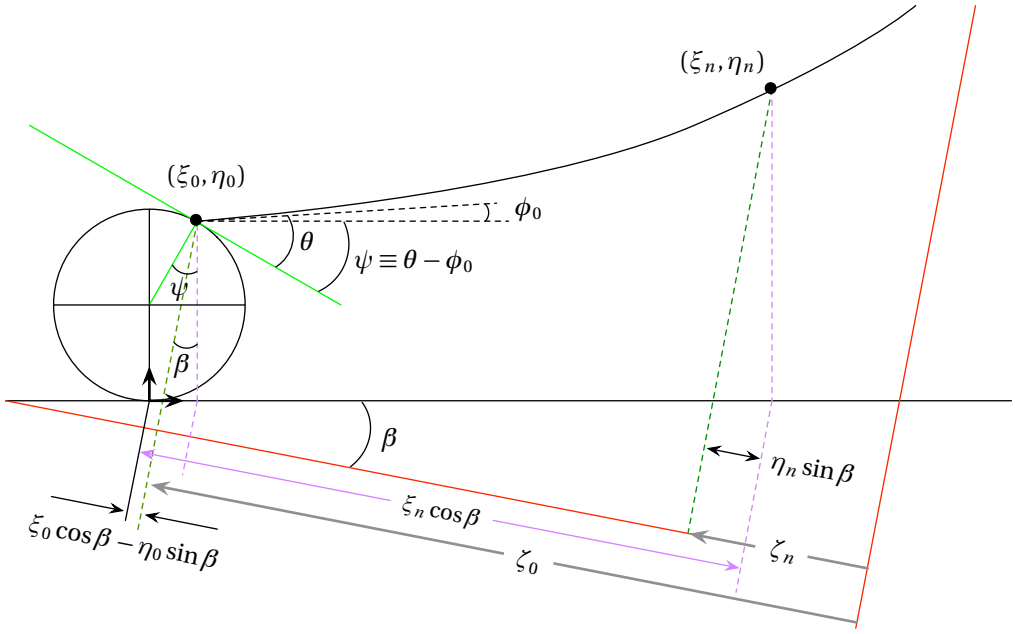

Figure 5.5: Schematic indicating the derivation of boundary conditions.

origin; in the corner pinning case they are

$$h_0 = \delta \tag{5.28}$$

$$x_0 = 0 \tag{5.29}$$

$$Q_0 = Q_0 \tag{5.30}$$

At n, the profile widens enough for the viscous terms to vanish, and the meniscus can be considered as being static. With this assertion, the remaining boundary conditions can be constructed by considering the Young-Laplace equation (to which the governing equation reduces when $Q_0 = 0$). First, the direct application of the Young-Laplace equation at n and an analysis of

Figure 5.5 gives

$$\sigma K_n = \rho g z_n$$

$$\sigma K_n = \rho g \{z_0 - (x_n - x_0)\cos\beta - (h_n - h_0)\sin\beta\}$$

or

$$\frac{\sigma}{\rho g} K_n = z_0 - (x_n - x_0)\cos\beta - (h_n - h_0)\sin\beta \tag{5.31}$$

In addition to Equation 5.31, the Young-Laplace equation can be used to derive another independent boundary condition (Ruschak, 1978) relating the curvature to inclination rather than altitude. Differentiating Equation 5.31 with respect to the arc length (omitting the subscript to emphasize that the equation holds everywhere the meniscus is "static")

$$\frac{\sigma}{\rho g}\frac{\mathrm{d}K}{\mathrm{d}S} = -\frac{\mathrm{d}x}{\mathrm{d}S}\cos\beta + \frac{\mathrm{d}h}{\mathrm{d}S}\sin\beta \tag{5.32}$$

It is recognized that Equation 5.32 is identical to Equation 5.17 without the flow term. Algebraic simplification then yields

$$0 = \frac{\sigma}{\rho g}\frac{\mathrm{d}K}{\mathrm{d}S} + \cos(\phi + \beta) \tag{5.33}$$

In anticipation of integration, we multiply the equation by twice the curvature, which can be expressed either in terms of the curvature term itself or the derivative of the inclination so that

$$0 = \frac{\sigma}{\rho g}\, 2K\frac{\mathrm{d}K}{\mathrm{d}S} + 2\frac{\mathrm{d}\phi}{\mathrm{d}S}\cos(\phi + \beta) \tag{5.34}$$

Integrating over arc length S, the equation states that the following combination of curvature and inclination is always constant along a static meniscus:

$$C = \frac{\sigma}{\rho g} K^2 + 2\sin(\phi + \beta) \tag{5.35}$$

In particular, the equation holds as $S \to \infty$, where the liquid becomes flat and level with the horizon such that according to the details in Figure 5.5, we find $\phi \to (\pi/2 - \beta)$ and so

$$C = \frac{\sigma}{\rho g}(0)^2 + 2\sin\left(\frac{\pi}{2} - \beta + \beta\right)$$

$$C = 2 \tag{5.36}$$

Thus, at S_n where the meniscus is almost static, the final boundary condition can be written

$$2 = \frac{\sigma}{\rho g} K_n^2 + 2\sin(\phi + \beta) \tag{5.37}$$

5.2.5 Nondimensionalization for computations

The natural length scale for the static meniscus, and therefore the curvature term, is the capillary length, which can be defined

$$a \equiv \sqrt{\frac{\sigma}{\rho g}} \tag{5.38}$$

The length scale of the spatial dimensions x, h, and S is most intuitively seen as being on the order of the particle film thickness δ, with the caveat that by lubrication arguments, the domain should span roughly several thousands to tens of thousands times δ to ensure that viscous effects vanish at n (in other words, scaling does not circumvent the issue of disparate length scales). Summarily, the variables can be scaled according to

$$h \equiv \delta\eta \qquad (h_\mathrm{B} \equiv \delta\eta_\mathrm{B}) \tag{5.39}$$

$$x \equiv \delta\xi \qquad (x_p \equiv \delta\xi_p) \tag{5.40}$$

$$K \equiv a^{-1}\kappa \tag{5.41}$$

$$S \equiv \delta s \tag{5.42}$$

$$z \equiv \delta\zeta \tag{5.43}$$

Then Q_0 and J_e can be scaled by the left over constants

$$Q \equiv \frac{\sigma \delta^2}{\mu a} q \tag{5.44}$$

$$J_e \equiv \frac{\sigma \delta}{\mu a} j_e \tag{5.45}$$

where it should be noted that the scaling of the flow rate may not have any physical significance, and that it is purely for the convenience of removing physical parameters from the equations. Using Equations 5.39 to 5.45 the governing equations become

$$\frac{\mathrm{d}q}{\mathrm{d}s} = j_e \tag{5.46}$$

$$\frac{\mathrm{d}\kappa}{\mathrm{d}s} = 3\frac{q}{(\eta - \eta_\mathrm{B})^3}\cos\phi - \gamma\cos(\phi + \beta) \tag{5.47}$$

$$\frac{\mathrm{d}\phi}{\mathrm{d}s} = \gamma\kappa \tag{5.48}$$

$$\frac{\mathrm{d}\eta}{\mathrm{d}s} = \sin\phi \tag{5.49}$$

$$\frac{\mathrm{d}\xi}{\mathrm{d}s} = \cos\phi \tag{5.50}$$

The boundary conditions can be scaled similarly:

$$\eta_0 = 1 \tag{5.51}$$

$$\xi_0 = 0 \tag{5.52}$$

$$q_0 = q_0 \tag{5.53}$$

$$\kappa_n = \gamma\left\{\zeta_0 - (\xi_N - \xi_0)\cos\beta + (\eta_N - \eta_0)\sin\beta\right\} \tag{5.54}$$

$$2 = \kappa_n^2 + 2\sin(\phi_n + \beta) \tag{5.55}$$

where the scaling disparity is collected into the length scale ratio defined as

$$\gamma \equiv \frac{\delta}{a} \tag{5.56}$$

For nanoparticle films, $\gamma = \delta/a$ can be quite small, possibly introducing numerical difficulties into the calculation of a meniscus surface. However, the scaling should not be used as an argument to remove terms from the equations because the basis for scaling was not for the simplification of the *physics* but rather the *mathematics*. While the $\mathcal{O}(\gamma)$ term in Equation 5.47 may probably be safely ignored, the term in Equation 5.48 is essential to the problem.

5.2.6 Solution methods

Some details of the methods are given in Appendix D, but a brief outline is given here. The set of ODE's in Equations 5.46 to 5.50 subject to boundary conditions given by Equations 5.51 to 5.55 can be solved using a finite differencing strategy and Newton's method with continuation. The derivatives are approximated as 6-th order difference equations, which are more accurate (to 5-th order with respect to mesh spacing) than the more traditional difference formulae. In fact, the common 3-node discretization causes numerical instabilities in the problem. The finite differencing scheme is described in Appendix D.I.

A balance of accuracy and efficiency can be achieved by weighting the node density of the discretized domain where they are most needed. Because the geometry of menisci are relatively predictable, the domain mesh can be tuned somewhat according to anticipated gradients. Specifically, the mesh can be constructed by splicing together a series of subdomains that monotonically increase or decrease in mesh density according to hyperbolic stretching functions (Vinokur, 1983), whose mesh density gradients are supposed to be gradual enough to limit numerical error (see Appendix D.II). Other subdomains, such as those resolving the substrate hump, can also be spliced in.

Arising from the nature of the equations is a "window of existence" of stable meniscus configurations with respect to the dimensionless parameters q_0, ζ_0, and ξ_p; the boundary of which can be considered as a locus of turning points in the respective parameter spaces. Critical points

in a solution space, such as the turning points that appear in this particular system, can in general be determined by solving the set of equations augmented by a critical condition equation (Griewank and Reddien, 1984; Bolstad and Keller, 1986; Ponisch and Schwetlick, 1981).

For this work, a less sophisticated approach suffices because of the simple nature of the critical points, namely turning points. Because these turning points can be represented as minima in the solution–parameter space, they can be approximately determined by a minimization algorithm such as Brent's method. The caveat is that to access solutions on the unstable branch of the turning point requires a pseudo-arclength continuation method (Keller, 1977), which does not allow the specification of either the solution or the physical parameter of interest, but rather only allows specification of both as a function of some pseudo-arclength parameter (see Appendix D.III); the practical consequence is that the minimization may not converge on the minimum as rapidly as it normally would.

5.3 Results and interpretation

5.3.1 Existence of stable menisci without a particle

The model equations governing the meniscus profile suggest a window on the existence of stable menisci. Parametric continuations on both the flowrate Q_0 and the extent of meniscus stretch z_0 show a turning point topography in their respective solution spaces (Figures 5.6 and 5.7). At these turning points, the steady state solution changes from stable to unstable (Christodoulou, 1990). Briefly, linear stability analysis of the steady state examines the Eigen problem

$$\mathbf{J} f_i = \lambda \mathbf{M} f_i \tag{5.57}$$

where $\mathbf{J}$ is the Jacobian of the steady state (such as calculated during the solution by Newton's method) and $\mathbf{M}$ is a so-called mass matrix arising from the analysis. The stability crossover is then given by $\lambda = 0$, *i.e.* when the leading order eigenvalue crosses the origin (or generally, the imaginary axis). At such critical points, the Jacobian $\mathbf{J}$ becomes singular; the turning point is technically just one of the many types of such singularities. Without actually carrying out the

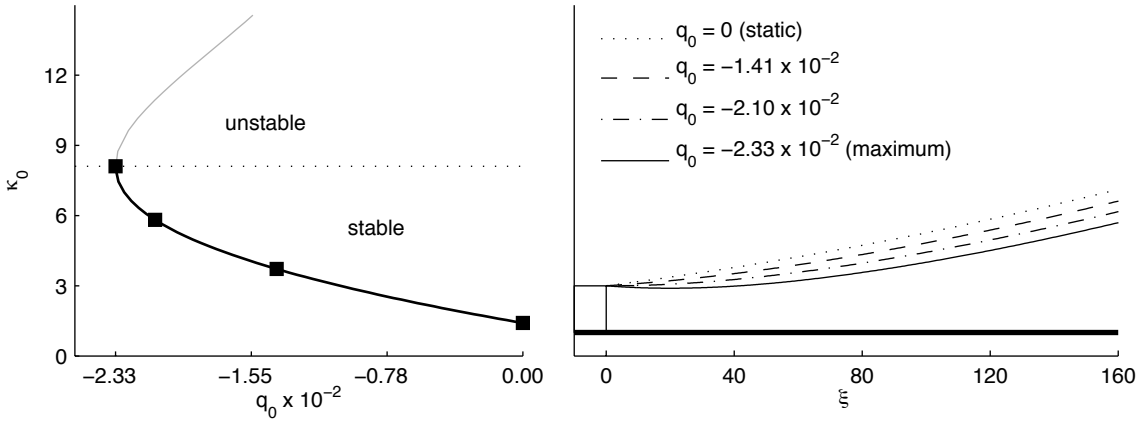

Figure 5.6: Solution path [left] characterized by κ_0 with respect to q_0 (nondimensional). The path exhibits a turning point behavior and indicates a maximum parameter value. Meniscus profiles for solutions indicated by the squares are successively more constricted with increasing flow rate [right]. The solution path is for $\delta = 100\,\mathrm{nm}$ with meniscus stretch $z_0 = 3.817\,\mathrm{mm}$.

stability analysis, we can determine the stable branch of the solution path by identifying the branch on which the static meniscus lies—because practically, the continuations must start at the static meniscus, this determination is trivial.

As the solution paths in Figures 5.6 and 5.7 indicate, the curvature at the pinning point increases with both increasing (absolute value of) flow rate and meniscus stretch; physically, this extra curvature may cause the profile to constrict against the substrate as shown. Collecting the turning points like the ones in Figures 5.6 and 5.7 yields a locus of turning points, which defines the boundary of meniscus existence on the z_0–q_0 plane, as demonstrated in Figure 5.8.

5.3.2 Experimentally relevant parameter values

Till now, we have ignored the actual values of z_0 and q_0 of interest, being satisfied that for any given q_0, a corresponding maximum value if z_0 can be calculated (and vice versa), resulting in a boundary on the z_0–q_0 plane beyond which menisci cannot exist. In fact, as the problem is formulated, we cannot determine what parameters are actually sampled in a real physical process that produces banded films. However, even in the absence of *definitive* parameters, *plausible* (z_0, q_0) pairs can still be identified and examined.

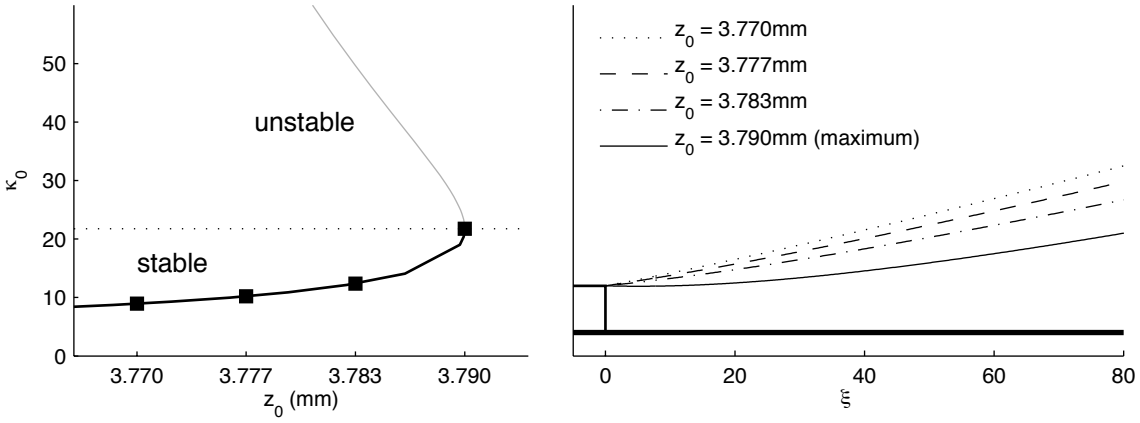

Figure 5.7: Solution path [left] characterized by κ_0 with respect to z_0 (non-dimensional). The path exhibits a turning point behavior and indicates a maximum parameter value. Meniscus profiles for solutions indicated by the squares are successively more constricted with increasing flow rate [right]. The solution path is for $\delta = 100\,\mathrm{nm}$ with a flow rate $q_0 = -0.1499$ (dimensionless), which is about 6 times stronger than the largest flow rate indicated in Figure 5.6.

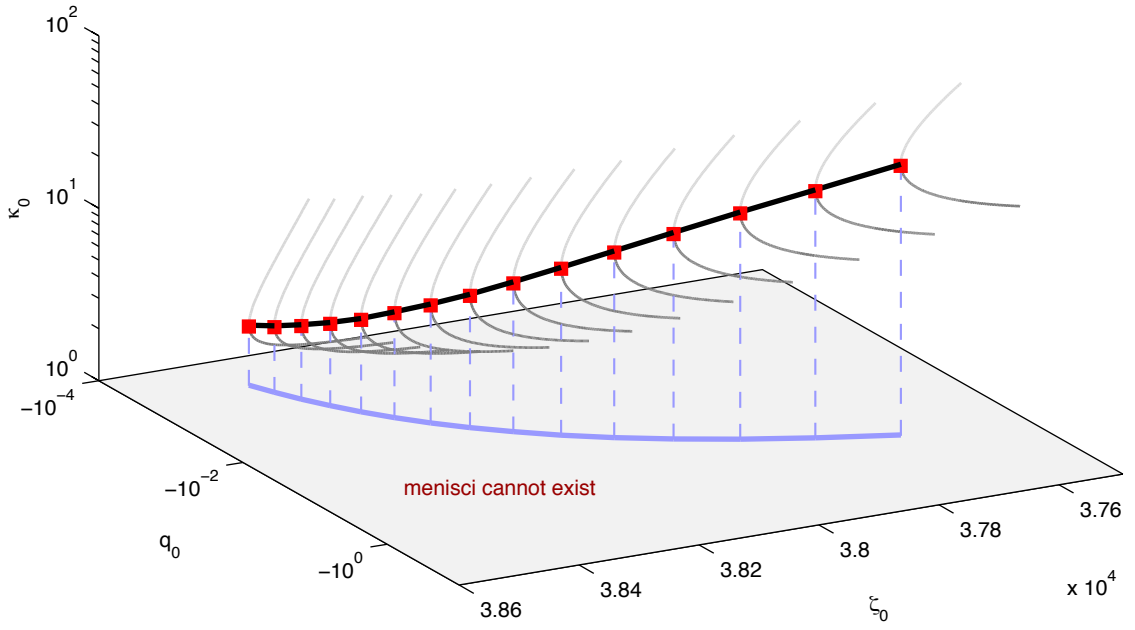

Figure 5.8: Locus of turning point meniscus profiles (characterized by the pinning curvature κ_0); a series of solution paths like that in Figure 5.7 for various q_0 (dimensionless). The locus of turning points (filled in squares, also projected onto the q_0–ζ_0 plane) defines a boundary of meniscus existence.

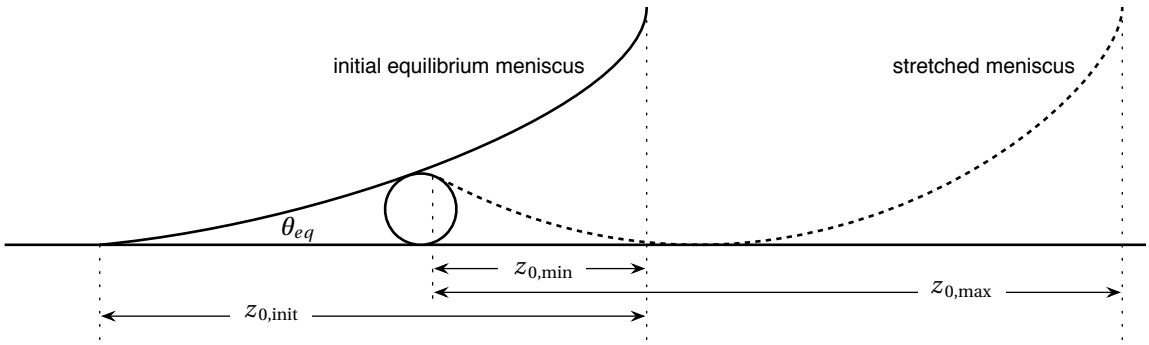

Figure 5.9: Cartoon depicting the practical limits of meniscus stretch, based on the assumption of an initial equilibrium meniscus.

Estimates of practically relevant meniscus stretch

In Figures 5.12 and 5.14, the upper limit on meniscus stretch z_0 is well-defined and corresponds to that which completely chokes the meniscus (in the limit of no flow). The lower limit of z_0 depicted in these figures were determined by making the following considerations.

There is a particle-free equilibrium configuration of the meniscus on a flat substrate forms a wedge (the details depending on the equilibrium or apparent contact angle with the substrate) into which a particle of some size can arrive. The lower limit of stretch can be asserted by determining where that first particle wedges into the otherwise equilibrium meniscus (ignoring the question of how the particle came to be wedged there in the first place). From this "initial configuration," for which the meniscus is now pinned on the particle, the practical minimum stretch can be defined as being the difference between the stretch of the equilibrium meniscus and the newly pinned meniscus, *i.e.* the distance between the original contact line and the new pinning line in the direction of gravity (see Figure 5.9).

One can argue that this is the lowest extent of stretch that the meniscus can sample during the process using the following thought experiments. From the initial configuration of a single wedged particle, there are two ways that z_0 can decrease any further. One is if the substrate is pushed back in closer to the bath (which does not happen). The other is if a new particle arrives, and the meniscus re-pins onto the new (lower) particle. However, this second situation must be examined from a dynamic point of view: the meniscus will only re-pin if the substrate has been

re-stretched to an appropriate extent. In other words, the re-pinning event only makes sense if the stretch was restored to the initial state or close to it, by action of withdrawing the substrate. (If the substrate were not moving and new particles were arriving, the film would ostensibly build outward due to the added clearance of the meniscus due to its diverging nature.)

Estimates of practically relevant flow rates

Dimitrov and Nagayama (1996) inferred the flow rates that developed in the meniscus during convective assembly by analyzing the substrate withdrawal velocity v_s required for the formation of complete monolayers according to Equation 3.1 (reproduced in relevant form below)

$$v_c = v_s = Q_0 \frac{\Theta}{\epsilon} \frac{1}{\delta} \frac{\varphi}{1-\varphi} \tag{5.58}$$

where φ is a bulk particle concentration, Θ can be thought of as a "dragging efficiency" relating the liquid flux to the particle flux, and ϵ is a packing fraction of the particles in the film. Their analysis of experiments over a range of particle sizes about $80 \sim 2000\,\text{nm}$ suggested that the flow rate that developed during the assembly was constant across particle sizes.

This analysis can be adapted for banded films by re-interpreting the packing fraction ϵ to reflect the total areal coverage fraction α_p of the bands to give

$$v_s = \Theta Q_0 \frac{1}{\delta \alpha_p} \frac{\varphi}{1-\varphi} \tag{5.59}$$

However this simplification assumes some average flux over the duration of the experiment, while in reality the flow rate must surely be periodic as with the assembly of the bands. All terms except ΘQ_0 in Equation 5.59 are available from the experiment. The results compiled from several experiments are given in Figure 5.10, from which it is evident that Q_0 is on the order of $100 \sim 1000\,\mu\text{m}^2/\text{s}$. For small particles, flow rates of such magnitude cannot be achieved when abiding the arguments that limit the extent of z_0 (see Figures 5.12 and 5.14 in the next section).

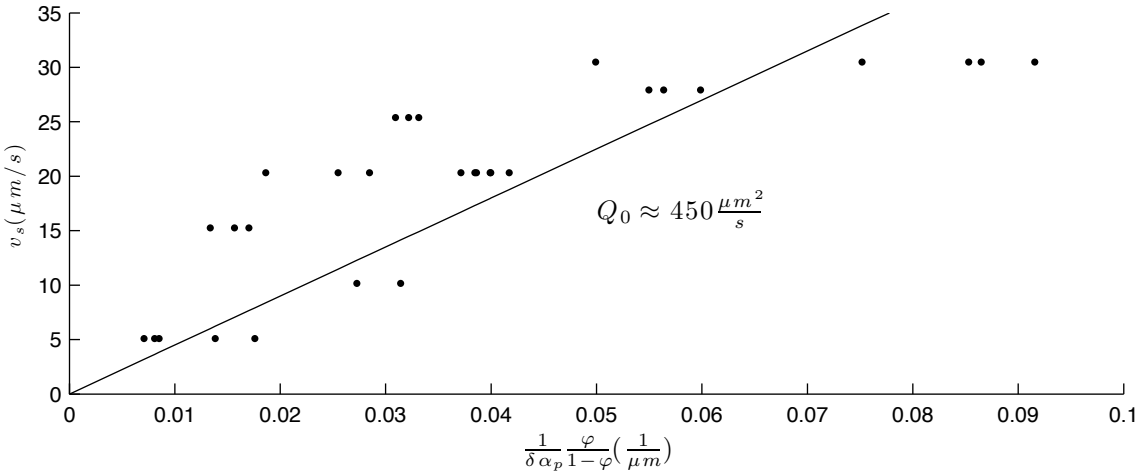

Figure 5.10: An estimate of the liquid flow rate through the meniscus during a real convective assembly experiment can be backed out from Equation 5.59.

5.3.3 Modeling band spacing

Defining the modeled band spacing in terms of ξ_p

Given reasonable bounds on meniscus stretch and corresponding flow rates, we can now consider the incoming particle (modeled as a hump in the substrate centered on $\xi = \xi_p$); specifically, we consider the closest allowed approach $\lambda \equiv \xi_{p,\min}$ of this hump to the pinning position ($\xi = 0$). The quantity ξ_p also exhibits a turning point behavior, allowing an analysis similar to that of the parameters (see Figure 5.11), and it can be considered as another dimension along which meniscus existence can be bounded.

The complete bounding surface for a given particle size δ (in monolayer) can be summarized by a plot such as that in Figure 5.12; for the purposes of this work, it can be interpreted as the predicted spacing between bands that form in a convectively assembling film, assuming that the meniscus jump occurs under conditions such that the convective flow rate and the extent of meniscus stretch is given by (ζ_0, q_0). It is important to note that these predictions reflect the situation where a meniscus becomes "unstable" at a combination of some triplet (q_0, ζ_0, ξ_p), without consideration of the actual dynamic process (how the system came to achieve these parameter values).

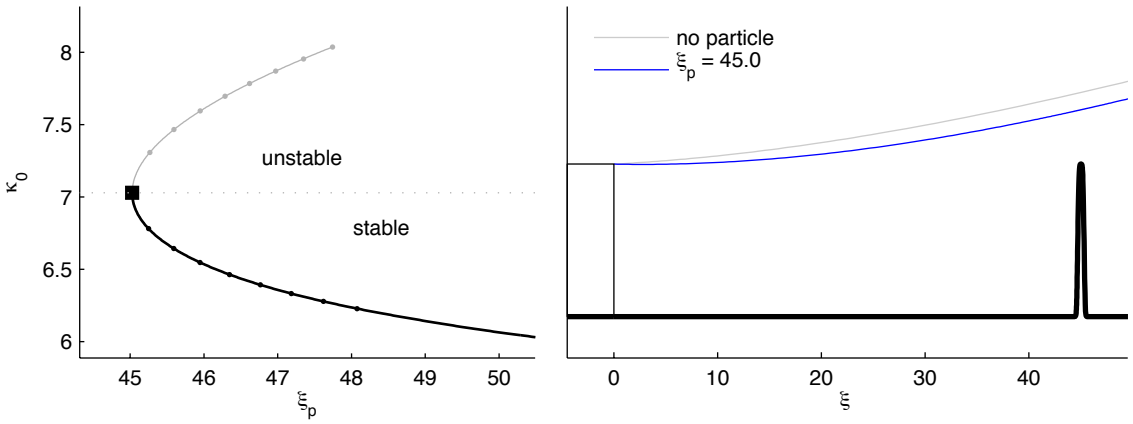

Figure 5.11: The substrate hump location (incoming particle) exhibits a turning point behavior (left) at a lower limit, indicating that an incoming particle can only come so close to the contact line before the meniscus becomes unstable. The meniscus profile and hump location are shown (right) along with the profile for a meniscus in the absence of the hump. The meniscus examined here is for $\delta = 200\,\mathrm{nm}$ and $z_0 = 3.8055$ (chosen according to the practically relevant minimum z_0; see § 5.3.2) at a fraction of the maximum flow rate at this stretch $0.8 \times q_{0,\mathrm{TP}}$.

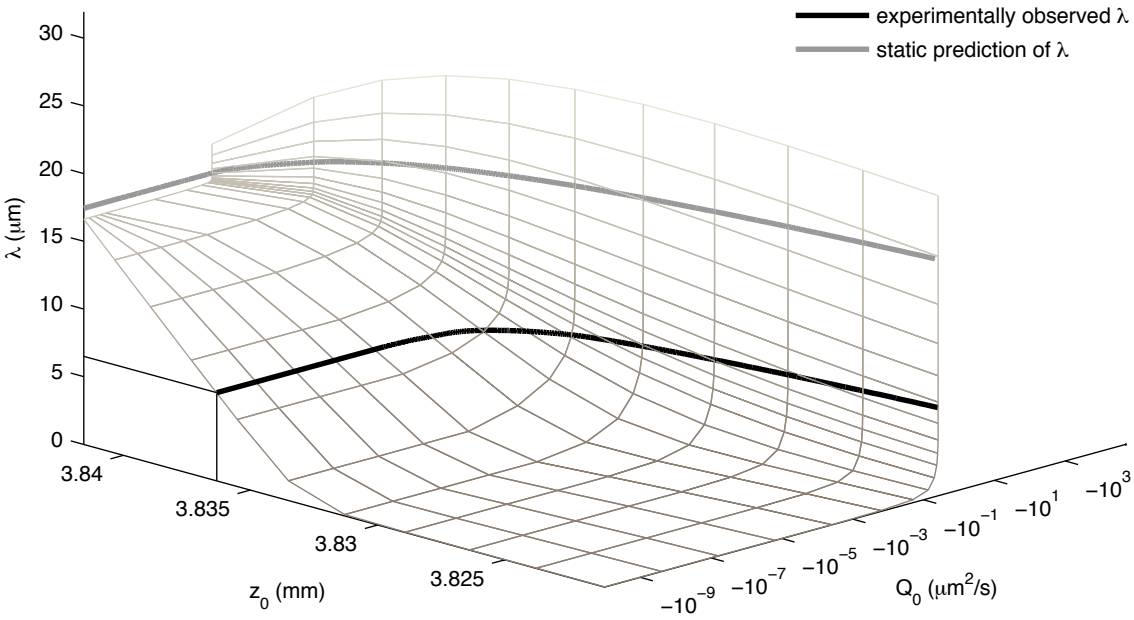

Figure 5.12: Summary behavior of band spacing λ with respect to flow rate Q_0 and stretch z_0 for a particle size of $\delta = 20\,\mathrm{nm}$. Bold curves indicate the experimentally observed λ and static model prediction of λ.

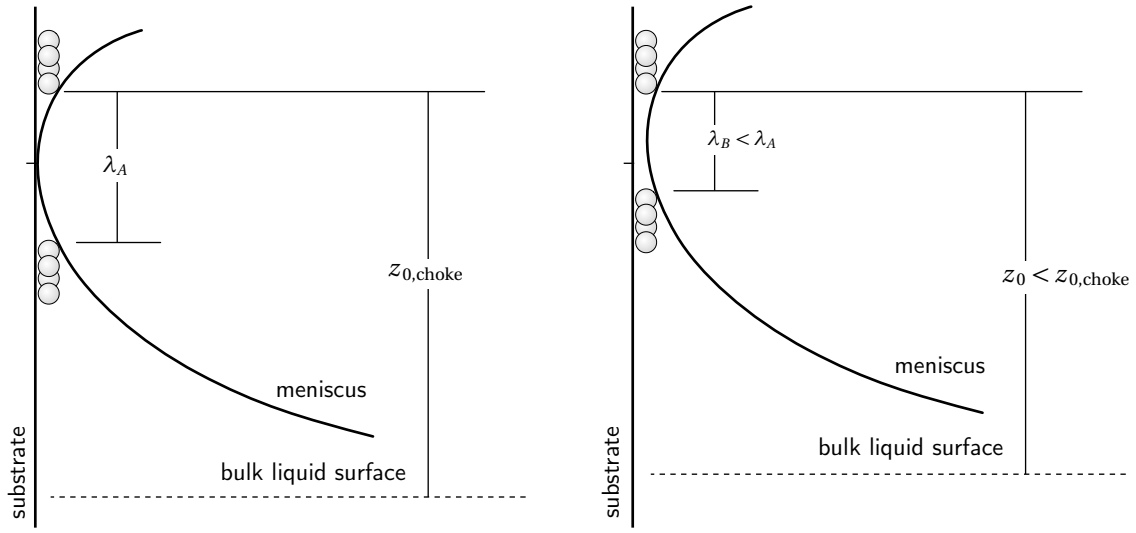

Figure 5.13: Static menisci with stretch z_0 less than the maximum value (that which completely chokes the static meniscus) allow the prediction of lower λ.

Predicted λ in terms of the static model and flow

In Figure 5.12, two curves respectively indicate the experimentally observed band spacing and spacings predicted by the static meniscus model (think of them as the intersections of the surface with planes defined by the experimental result static model prediction). From Figure 5.12, it is evident that as the stretch z_0 approaches its maximum value in the limit of $Q_0 \to 0$ (the completely choked meniscus configuration), the band spacing predicted by the current model approaches that of the static model. Thus, the left face of the plot in Figure 5.12 represents the low flow limit, and the linearly falling region of the predicted λ with decreasing z_0 represents the fact that in the static meniscus model, decreasing z_0 leads to menisci that are less constricted, therefore allowing a closer approach of the incoming particle (as in Figure 5.13; this trend was not discussed in Chapter 4).

Clearly, if the static meniscus does not constrict at all, the incoming particle can touch the assembly front, resulting in no spacing (film growth proceeds). This is reflected in the flat region of the plot in Figure 5.12. With the inclusion of flow, however, a meniscus with small z_0 can both potentially develop a constriction (due to the increase in required meniscus curvature) and impede the approach of the incoming particle by requiring a clearance with the meniscus surface

exceeding that available. In Figure 5.12, this is expressed as the increase in λ with increasing (increasingly negative) flow rate along a constant z_0.

Along such a progression, two factors contribute to the prediction of increasing λ. One is that with increasing flow rate, the meniscus curvature increases, serving to constrict the meniscus; this decreases the clearance between the meniscus and the substrate. In addition, increased flow rates also increases the clearance necessary between the meniscus surface and the substrate hump (modeling the particle).

The nature of predicted λ

One noteworthy feature of the trends expressed in Figure 5.12 is that predicted λ increase extremely sharply with increasing flow rate Q_0 (profiles viewed from the right-face of the plot). For a given z_0, λ seems to increase asymptotically with respect to Q_0 up to the maximum allowed $Q_0 = Q_{0,\mathrm{TP}}$. In fact, the plot in Figure 5.12 does not reach $Q_{0,\mathrm{TP}}$, but rather stops slightly short of it: $(1-10^{-6})\times Q_{0,\mathrm{TP}}$. The predictions of λ indeed continue to increase up to a value that far exceeds either the static limit or the experimentally observed λ, but numerical accuracy issues become problematic at high flow rates; it is also unclear whether the independent treatment of the three parameters adversely affects the analysis (the point being that perhaps simultaneously solving for the triple critical locus will give different results for the critical parameters, leading to slightly "more mild" critical parameters in each parametric dimension).

Thus, despite its purpose of providing insight into the behavior of banding, this particular model allows the prediction of almost any band spacing at an appropriate pair of (z_0, Q_0). Furthermore, over much of this parameter space, the experimentally observed λ correspond to regions where the predicted λ are rapidly changing, so that it is difficult to make any solid claims regarding the model predictions.

There is a region in Figure 5.12 (namely near z_0 where the static meniscus would be slightly constricted) where the qualitative nature of the sensitivity of λ is different from that at lower z_0. However, this region must not be "special" in any meaningful way considering that for larger δ ($\delta > 100\,\mathrm{nm}$, according to Figure 4.8), the experimentally observed λ are greater than that

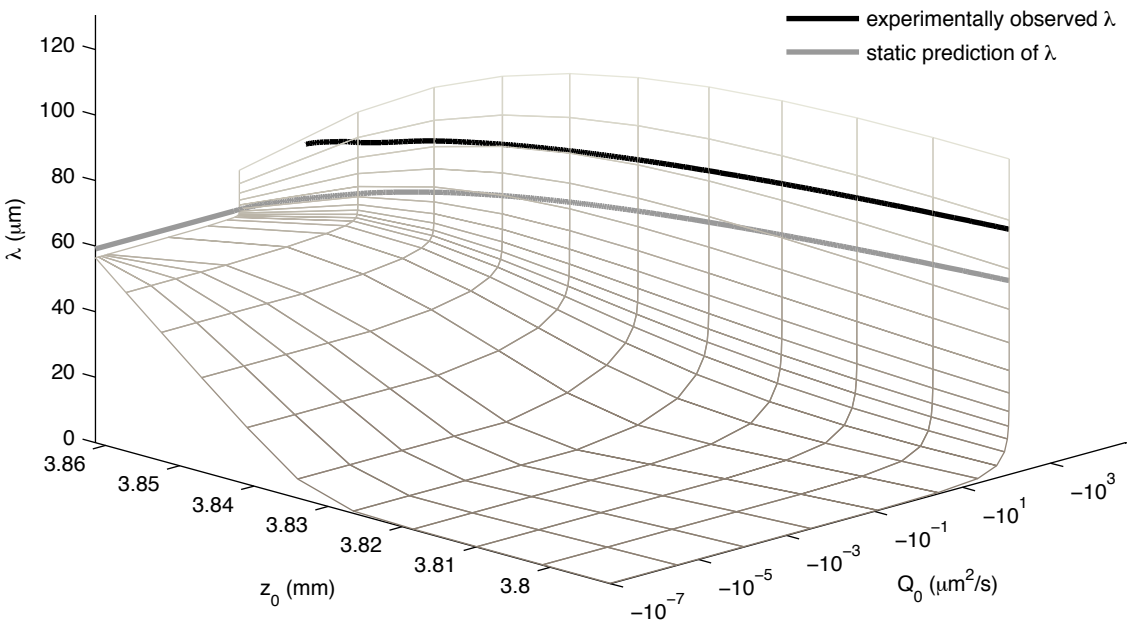

Figure 5.14: Predicted λ for a particle size of 230 nm. Although the experimentally observed λ_{exp} fall outside the range of predictions shown, extending the range of Q_0 (to arbitrarily close to the maximum values) would serve to increase the predicted λ beyond λ_{exp}.

predicted in the static limit, as shown in Figure 5.14. In other words, there is no consistent relationship between the qualitative solution topography of predicted band spacings and the experimentally observed band spacings. Alternatively, the mechanisms behind banding may be different at different particle sizes.

The qualitative behavior of λ with respect to particle size according to this model can be summarized by curves of λ along a range of z_0 at a fixed fraction of the maximum flow rate $Q_0 = (1 - 10^{-10}) \times Q_{0,\max}$ at each z_0, for several particle sizes δ (in other words, very close to the boundary of meniscus existence in the z_0–Q_0 plane; slightly beyond the ridges in the plots of Figures 5.12 and 5.12). At such a significant fraction of the maximum flow rates, the predicted λ all far exceed that of the static limit, and provides an upper bound on the prediction. Such a plot is presented in Figure 5.15. We note that although this model significantly over-predicts the actual spacings, it still recovers the qualitative trend of increasing λ with particle size at all conditions of z_0 and Q_0 considered.

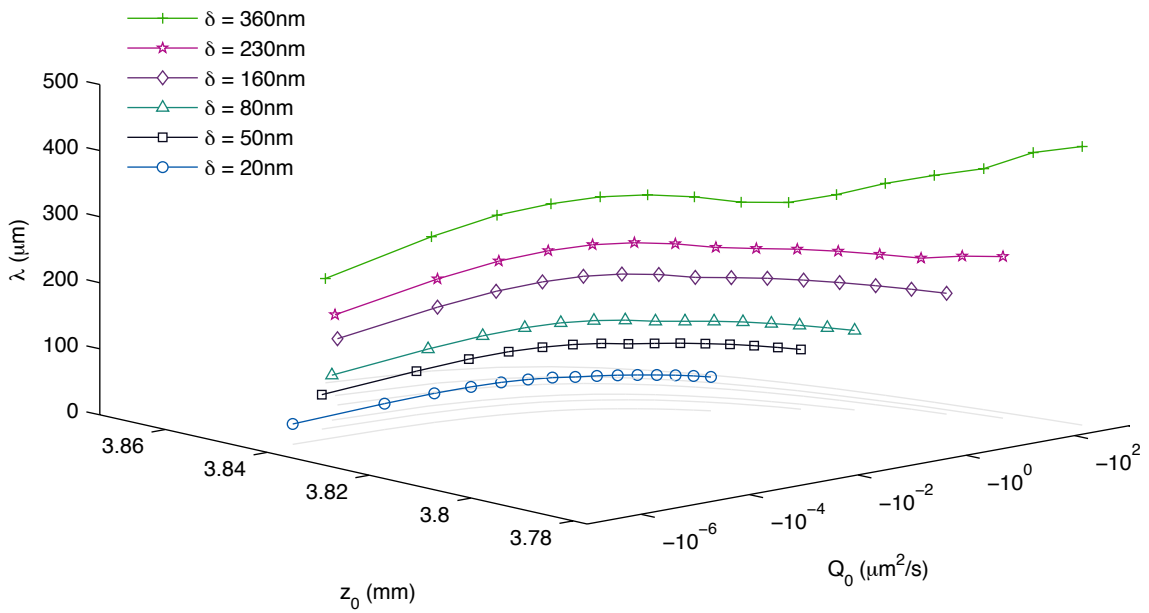

Figure 5.15: Predicted λ over a range of z_0 and a significant fraction $(1-10^{-10})$ of the maximum allowed flow rates at each z_0. The predictions should collapse to the static limits at the "left" end of the plot.

5.4 Concluding remarks

The meniscus-with-flow model was derived in an attempt to quantitatively adjust the static meniscus model for inter-band spacing in convectively assembled banded films. For this purpose, the existing band was modeled as a "shelf" onto which the meniscus was pinned, and liquid was assumed to flow under the meniscus surface in film flow. In addition to the introduction of flow, the incoming particle—that is the first particle of the next band—was modeled as a topological feature (a hump) on the substrate, characterized by its distance from the pinning point (see Figure 5.2 on p. 111).

Any meniscus so-modeled can be parameterized by the flow rate (constant throughout), the degree of its stretch (akin to capillary climb), and the position of the hump, and it has been shown that the existence of menisci are bounded in each of these dimensions. Thus, a parametric map of the minimum allowed hump-position at steady state conditions can be constructed, and we may consider these positions relative to the pinning line as representing inter-band spacings.

Qualitatively, the trends in band-spacing with respect to particle size reflect that of the static model (in fact the model is confirmed to approach the static limit with vanishing flow). Quantitative results indicate that almost any value of band spacing can be predicted at any extent of meniscus stretch, provided that the flow rate is sufficiently close to the maximum allowed flow rate (as determined in the absence of the particle). However, those values of band spacing corresponding to experimental observation are found in parameter regions where the predictions are extremely sensitive to the other parameters, with the result that the truly maximal predictions in band spacing (at the very limits of meniscus stretch and flow rate) are many times greater than either the static limit or the experimentally observed ones.

In the absence of a clear relationship between the results compiled by use of the model and the experimental data, we should conclude that there is still something missing from this model that prevents an adequate description of the banding phenomenon in convectively assembled films. Nevertheless, the model has provided a previously unavailable argument for why band spacings may *exceed* that predicted in the choked static meniscus (whereas the static model could still predict arbitrarily small band spacings by adjusting the meniscus stretch, z_0).

Any further theoretical investigation of the quantitative prediction of band spacing may augment the model with more forces, notably dispersion forces (giving rise to conjoining and disjoining pressures). However, of more importance is a dynamic description of the evolution of the meniscus that could determine the actual parameters that describe the meniscus at any given moment (especially at incipient contact-line breakage, leading to banding). In other words, it may be necessary to model the entire convective assembly process in order to adequately model the properties of the banding phenomenon.

Chapter 6

Epilogue

In this dissertation, I have described an investigation into controlling and characterizing the phenomenon of convective particle assembly at a liquid-solid-air contact line, as occurs for example on the sides of a coffee mug. Under right conditions, the convective assembly phenomenon has been shown as capable of producing continuous (close-packed) particle films. In the case of spherical particles, the films so-produced have additionally demonstrated high degrees of packing order, *viz.* colloidal crystallinity. Such "opaline" films are of both immediate and potential interest in a variety of fields, for example optically active films.

The observation of highly ordered inter-particle structure in convectively assembled opaline films suggested that the method might be adapted to produce highly ordered films of anisometric (*i.e. non*-spherical) particles. In particular, we were interested in achieving "tiled" particle films, which can serve as precursors to uniformly oriented crystalline membranes by providing a seed layer of uniformly oriented particles (see § 1.2).

For "open-framework" crystals like zeolites, such membranes can act as molecular sieves, and are attractive from the viewpoint of potentially low energy and high throughput gas separations. To date, however, fabricating these membranes is a process that can afford improvements at many stages, including at the stage of precursor seed layer [film] formation. We proposed that a simple and scalable method like convective assembly, if successful, would be superior to current methods, which are complicated and inherently resistant to scale-up.

The opening topical chapter, the actual beginnings of the project, and remarks

The dissertation opened with a proof-of-concept study (Chapter 2) for controlled evaporation convective assembly experiments, where the zeolite ZSM-2 was used in place of the usual silica spheres. The method was adapted directly from an experimental design originally intended for direct *in situ* visualization of opal formation by video microscopy (Meng, 2008), and the zeolite ZSM-2 was chosen for its hexagonal-plate shape that we deemed amenable to the desired "tiling" behavior.

We showed that although "tiling" was indeed observed in limited regions of the films, the majority of constituent particles were jumbled into a thicker film. Nevertheless, an analysis of the crystalline microstructure by x-ray diffractometry suggested that despite a jumbled appearance, the overall crystalline orientation was biased in a way that correlates with particles preferring an orientation "flat against the substrate". For application in separation membranes, this result is reasonably favorable, because according to the currently accepted view of the origins behind selectivity (molecular sieving) in zeolites, we are usually only concerned with the crystal direction (*i.e.* some given channel direction) perpendicular to the plane of the membrane.

Notwithstanding the opening chapter, my research actually started with experiments that can be more accurately characterized as dip coating, which relies on the formation and subsequent drying of an entrained liquid film laden with the particles of choice. These initial experiments yielded disordered film morphologies that can loosely be characterized as "marbly", in which regions of particle coverage were characterized by close-packing, but the interface between regions of coverage and bareness were random and swirly. Because of the seeming fundamental disparity in the mechanisms between dip coating and convective assembly, the former were not included in the scope of the dissertation. That is not to say, however, that the dip coating route should be dismissed.

In fact, one can view the two methods (convective assembly at a contact line vs. entrained liquid film coating with subsequent drying) as extremes of a spectrum, for example, that describes the "persistence" of the drying region. After all, a drying entrained liquid film laden with particles can be considered as a drawn out "contact line" at which assembly is occurring; the

drying of the liquid film in a real process will inevitably be characterized by a gradient, at the end of which must exist a "true" convective assembly front. This latter idea can be taken to the limit where the entrained film is infinitely drawn out, in which case drying occurs uniformly instead of in an "edge-in" manner that would give rise to a convective assembly front, although an assembly front will certainly still emerge in the form of "skinning" near the liquid-air interface.

Here already, we were presented with a divergence in perspective and possible routes for investigation, and I would remark that further research in this vein should consider the relationship between convective assembly and entrained liquid film coating. Especially from an industrial processing point of view, I believe the distinctions and equivalences will become important.

Carrying forth convective assembly for controlled film thickness

Following the ZSM-2 proof-of-concept, Chapter 3 described the design and application of an apparatus that combined the hitherto divorced strategies of controlled drying and controlled substrate withdrawal during convective assembly. Both are important in determining the final thickness and uniformity of the film, and we expected that the addition of controlled withdrawal would solve some problems in the discrete coverage patterns of ZSM-2 films observed by convective assembly without substrate withdrawal.

A fortuitous discovery of the facile synthesis route (lysine-hydrolysis) to stable and monodisperse silica nanoparticles led the direction of research away from zeolite films. This move was also partially a response to the persistence of discrete coverage patterns in ZSM-2 films by convective assembly despite our expectations and the new apparatus; by this point, it had become quite clear that convective assembly in the "extremely dilute regime"—that is, in pursuit of film thicknesses on the order of monolayer—generally yielded a banded monolayer pattern. Such discrete patterns leaving large regions of bare substrate are obviously problematic for membrane applications requiring continuous coverage, and so studying this phenomenon simpler model system (without anisometry) seemed an important step, especially considering that the patterns resulted for a variety of particle shapes and sizes.

On the other hand, the trends of the banded patterning with the model silica nanoparticles, for example with respect to substrate withdrawal speed, were quite regular. Owing to this regularity, we were successful to a certain extent with achieving nearly complete monolayer films with the model silica nanoparticles. These could be achieved empirically by successively tweaking the substrate withdrawal speed keeping other process conditions the same, after analyzing the degree of completeness of the resulting films: slowing down the substrate withdrawal to increase coverage and vice versa.

These results represented another fork in the road: the former suggest a more fundamental study of the process characteristics, the latter a more applied engineering study of membrane synthesis—for example in pursuit of the "tiled" films, guided by the lessons gleaned from the silica nanoparticle monolayer film assembly experiments. The brief discussions in § 3.4 concern experiments in this spirit, although this line of investigation unfortunately hit a dead-end.

Nevertheless, other efforts in the group continue to pursue facile methods for seed layer deposition for practical application to membranes. At the time of this dissertation, interest remains reasonably strong in liquid coating routes to films with varying degrees of orientational order. More importantly, these films have increasing need to be functional for testing; with regards to separations, this means the films must be formed on porous cylindrical substrates. The end of Chapter 3 briefly outlined some preliminary ideas for advancing convective assembly as an applied method for actual membrane fabrication.

Ultimately, the conclusion of my work took the other route—in the spirit of investigating fundamental process characteristics—owing to both (1) the difficulty in assembling tiled monolayers of anisometric particles and (2) the mounting evidence that even thick (multilayered) films exhibit banding in their thickness profiles. Around that time too, more reports were appearing in the literature concerning much more identifiable multilayer banding in films assembled by similar methods. Progress in this direction was also motivated by our perceived lack of a compelling explanation of, or predictive capabilities regarding, this banding phenomenon in the literature.

Attempts to describe banded films by convective assembly

In the last two chapters, I elected not to focus on the application of convective assembly to the projects characteristic in the research group, but instead discussed two successive attempts to describe the inter-band spacing in banded films in terms of the surface profile of the meniscus under which the convective assembly is occurring. The first attempt (Chapter 4) introduced the concept that inter-band spacing may arise from geometric constraints imposed by the constricting profile of a pinned and stretched liquid meniscus. While this description lacked consideration of the liquid flow it agreed qualitatively with the experimental observation that inter-band spacing is a strong function of particle size.

The final chapter (Chapter 5) described the inclusion of liquid flow in the meniscus geometry model. Incorporation of liquid flow allows for both a more accurate account of the meniscus profile, and a slightly more straightforward interpretation of the inter-band spacing. While this augmentation of the geometric meniscus model yielded predictions in the range of the observed experimental data (previously unavailable using the static model), it is evident that these predictions occurred in very narrow regions of the parameter space, suggesting that some other physics may be needed for a more complete description of band spacing.

On the other hand, I had not addressed some key issues in modeling the phenomenon, which are important not only for the band spacing aspect but for convective assembly at large. Namely, I had elected to parameterize the meniscus by constant parameters (steady state assumption) rather than to model the evolution of the meniscus and the growth of the film (in terms of all the relevant quantities including liquid flow rate, meniscus stretch, and current film thickness).

In fact, the evolution of the flow rate likely depends on the parameters of the growing film, so that the relationship is ultimately two-way. In addition to such considerations, a dynamic model would require some description of the arriving particles, and perhaps even a description of the meniscus detachment itself (see § 2.3.3).

Appendices

Appendix A

Supplementary experiments and results

A.I Chemically anchored ZSM-2 films

The chemical anchoring method for zeolite monolayer deposition introduced in § 2.1 (also see Ha *et al.*, 2000 and Choi *et al.*, 2000, *e.g.*) can be applied to ZSM-2 deposition on both the standard porous alumina support (compressed α-alumina discs) and pieces of glass microslides. The strategy follows almost exactly that laid out by Lai *et al.* (2003).

First, the substrate is functionalized with the covalent linker 3-chloropropyl tetramethoxysilane (3-CPTMS) in a moisture free environment at high temperature (carried out in refluxing toluene under continuous argon flow in glassware that was dried at high temperature). The functionalized substrates are then rinsed in toluene and dried at high temperature to prevent moisture adsorption.

The zeolite must be dispersed in toluene for the anchoring step. The aqueous suspension is dried, and the resulting powder is calcined (24 hours at 400 °C) and further dried in a desiccated jar for two days. This step is made particularly difficult for ZSM-2 (in comparison to the larger, more hydrophobic silicalite-1) because (a) the smaller ZSM-2 particles are prone to fusing during calcination, and (b) the hydrophilic ZSM-2 particles are more difficult to dry and therefore prone to agglomeration in toluene. The powder and substrate are finally immersed into toluene under stirring for the chemical anchoring step.

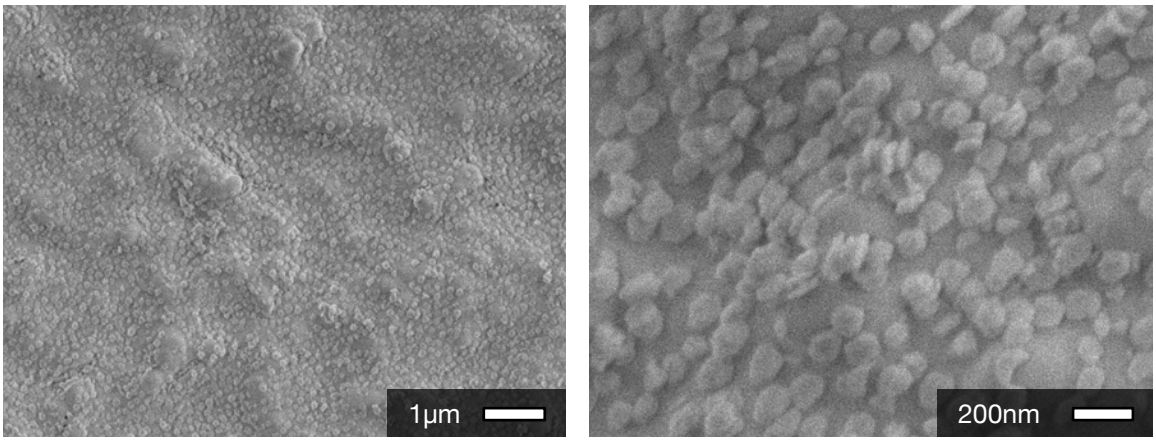

Figure A.1: Chemically anchored ZSM-2 films on a porous alumina disc. As the low magnification image on the right shows, the substrate can be rough on length scales important to particle deposition.

The "films" so produced on a porous alumina disc and a piece of glass microslide are shown respectively in Figures A.1 and A.2. In both cases, particles are apparently sparsely bonded flat against the substrate as desired, with occasional clusters (agglomerates). An XRD pattern for the film on glass is shown in Figure A.5 (next section) for comparison with films deposited by other methods; the films appear to be preferentially oriented out-of-plane.

A.II Convective assembly of ZSM-2 with adsorption

Another brief exploration was made regarding additional surface treatment of the substrate in attempts to promote adsorption by putting a positive charge on the substrate through electrostatic layer-by-layer assembly of polyelectrolyte monolayers. Because the glass substrate is already negatively charged in water at the working pH, adsorbing the positively charged polyelectrolyte poly(dodecylmethacrylamide) (PDDMA) is simply a matter of soaking the substrate (post-HF cleaning) in a PDDMA solution. Subsequent to the PDDMA monolayer adsorption, another monolayer of negatively charged polyelectrolyte poly(styrene sulfonate) (PSS) can be adsorbed by soaking in a PSS solution, and so on.

Thus, films could be convectively assembled on either a PDDMA (particle-adsorbing) surface or PSS (particle-repelling) surface covering the glass substrate. The results are shown re-

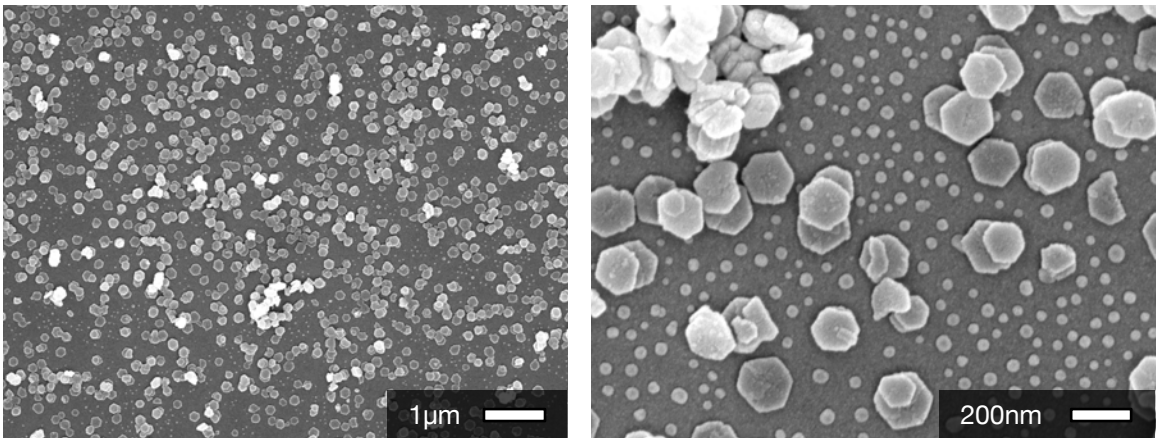

Figure A.2: Chemically anchored ZSM-2 films on a smooth flat glass microslide. Some clusters of particles are visible. Also, some amount of particle breakage is evident. This may be from the vigorous sonication treatment during re-dispersion of the particles in toluene.

spectively in Figures A.3 and A.4. In both cases, the overall banded pattern once again prevails, while in the PSS case, particles seem to be additionally adsorbed in what would otherwise be the bare regions (we expected results for the PDDMA case to closely mirror those for untreated glass surfaces inasmuch as they both presented repulsive surfaces for the particles). Moreover, some particles are able to adsorb vertically, that is, not lying flat against the substrate. Nevertheless, XRD shows that the particles are overall preferentially oriented in the flat orientation (Figure A.5).

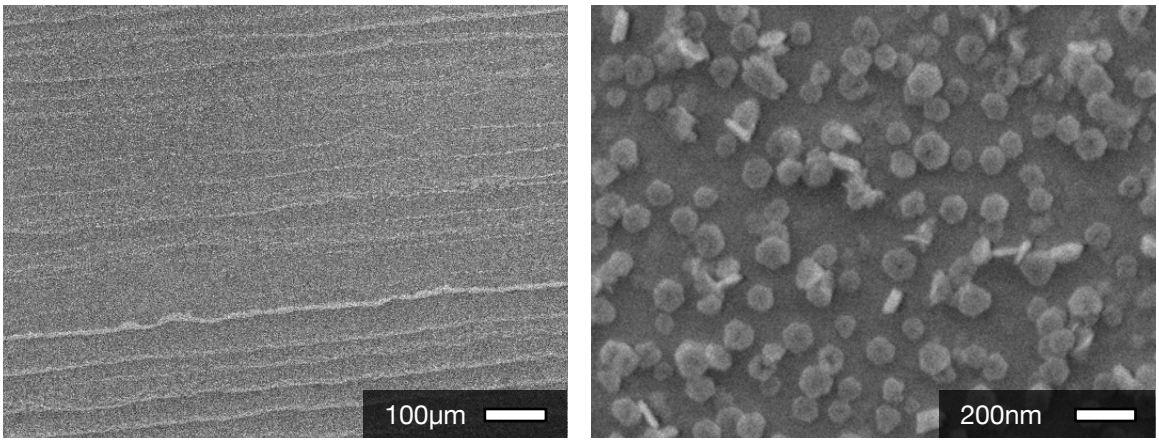

Figure A.3: Convectively assembled ZSM-2 films on a positively charged PDDMA surface. The film retains an overall banded structure, but the bare interstices are sparsely covered with adsorbed particles. Some of the particles are adsorbed on their edges so that they are standing up on the substrate.

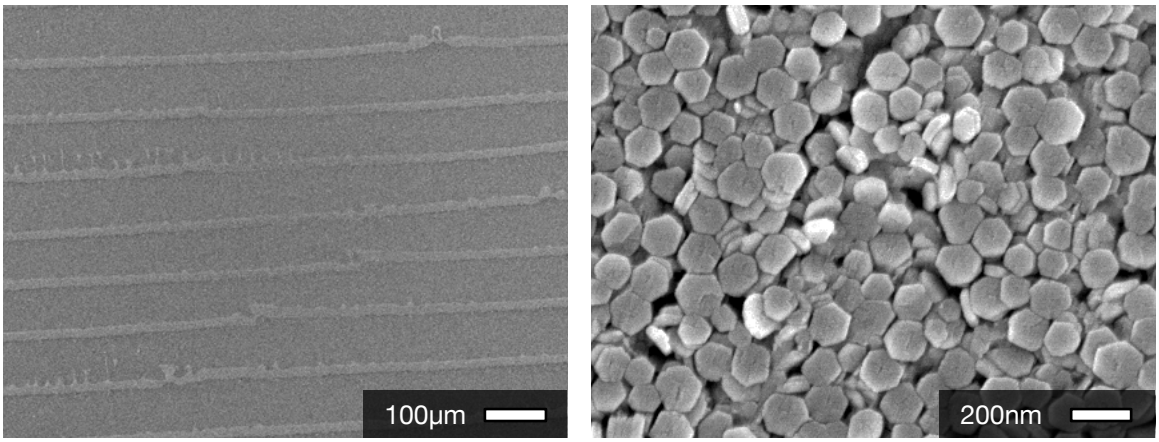

Figure A.4: Convectively assembled ZSM-2 films on a negatively charged PSS surface. These films are qualitatively identical to films assembled on clean glass substrate, as expected.

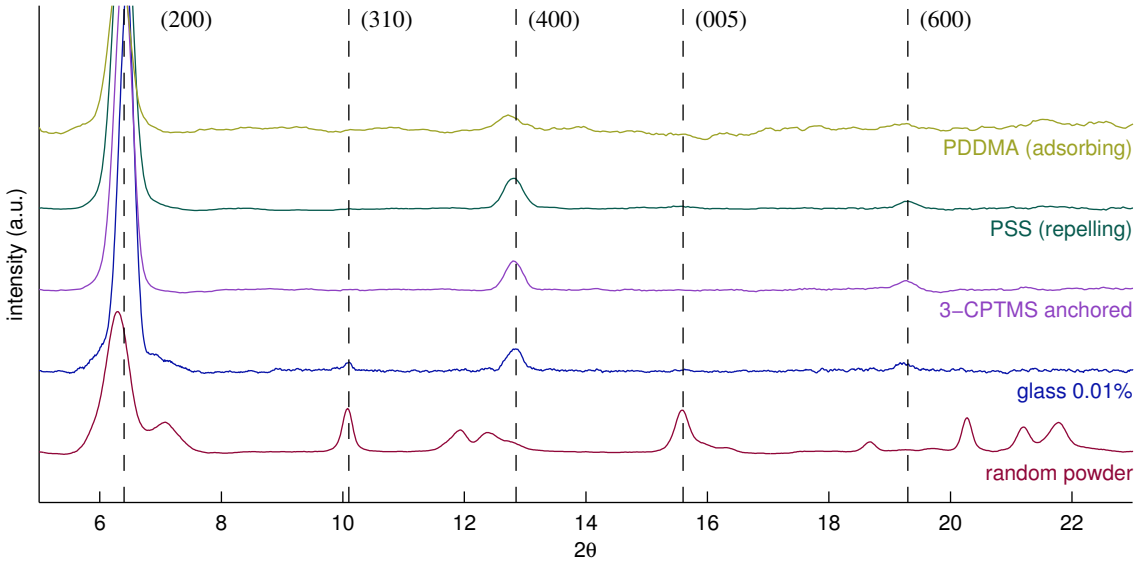

Figure A.5: XRD patterns for the films by chemical anchoring and convective assembly on polyelectrolyte layers in comparison with those taken of the powder sample and standard convectively assembled film (see § 2.3.4). The patterns are indistinguishable, indicating that they are also preferentially oriented out-of-plane of the film.

A.III Very thick multilayer LYS-SIL films

With the method of continuous convective assembly with controlled drying (Chapter 3), one can conceive of experimenting with varying drying gas flow rates in order to investigate the question of what factors affect the film crystallinity. The idea is that increased drying gas flow rate would increase the particle arrival speed, which could be hypothesized as important in the following contexts. If the crystallization mechanism is dominated by the thermodynamics of mutual repulsion, then fast-arriving particles may suppress crystallization by kinetic trapping.

On the other hand, if the convective steering mechanism (Gasperino *et al.*, 2008; Brewer *et al.*, 2008) were in effect, crystallization may be enhanced by fast-arriving particles. Unfortunately, as shown in Figure A.6, no conclusions could be drawn about the effect of drying gas flow rate in the range investigated ($1.6 \sim 14.4\,\mathrm{cm}^3/\mathrm{s/sm}$); the colloidal crystallinity at the film surface as characterized by FFT of the SEM images showed no differences.

These experiments did differ in some important respects, however, from the ones that produced the film shown in Figure 3.11 (p. 53). First, these films were coated onto a thin glass cover slide rather than a silicon substrate, and second, the substrate withdrawal speeds were reduced by about a factor of 10 to $\sim 5\,\mu\mathrm{m/s}$. While the effects of the former are unclear in principle (both have fresh silica surfaces), the latter had a clear effect of resulting in thicker films (at the same bulk suspension concentration of 1 wt%). This almost certainly contributed to the development of large cracks in the films, which were not present in the films described in § 3.3.3 (Snyder *et al.*, 2007). The question of whether the flexible glass substrates were responsible for cracking (by imparting large flexural strains in the film during handling) was not explored.

Unfortunately, the film thicknesses could not be evaluated quantitatively due to technical difficulties. At very long ranges, profilometry results are contaminated by both high frequency noise of order larger than a particle size and long-range waviness that cannot be subtracted (a lack of reference points, *i.e.*, bare substrate regions). Cross-sectional SEM images are unreliable for quantitative analysis because sharp breaks preserving the full film thickness at the edge cannot be made. Recognizing that no real argument can be made about the film thickness or cracking, the expectations and results are consistent with the heuristic observation that thicker films

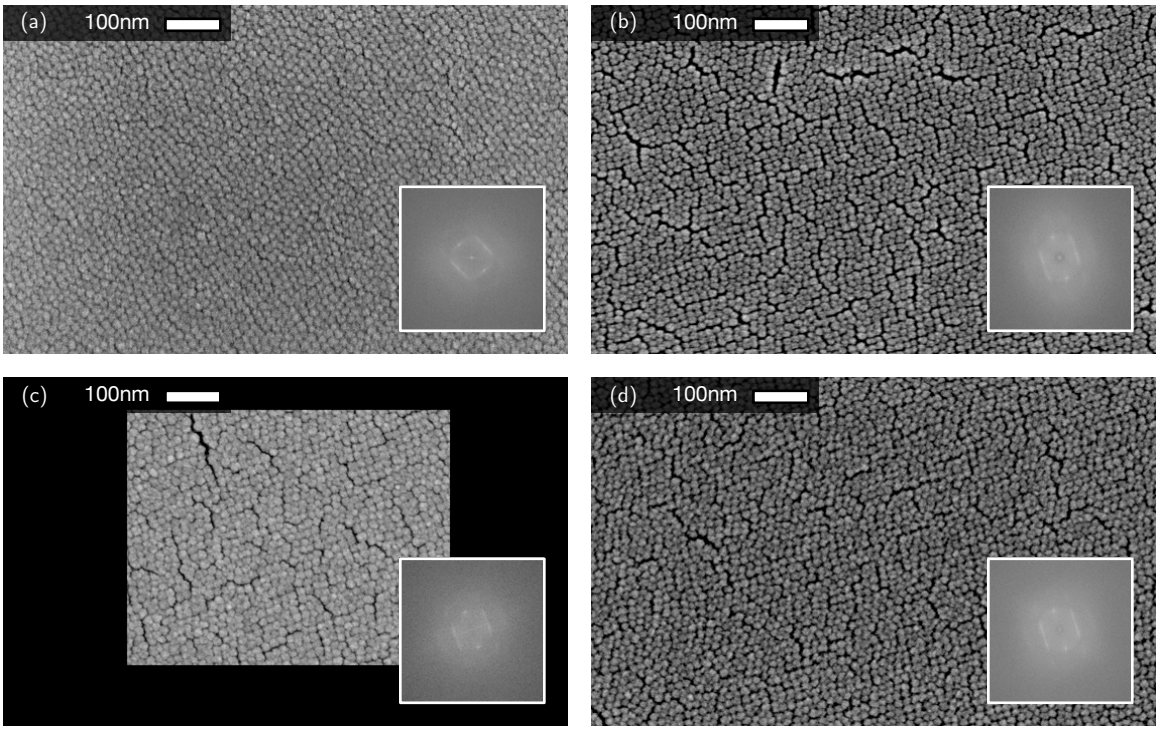

Figure A.6: Colloidal crystallinity of thick LYS-SIL films at various drying gas flow rates. Images in (a)-(d) represent experiments conducted at increasing drying gas flow rates: 1.6, 4.8, 9.6, and $14.4\,\mathrm{cm}^3/\mathrm{s}/\mathrm{sm}$. The SEM images show similar micro crevices pervading the colloidal crystal; FFT of the images show smeared primary spots and hints of higher order reflections, indicating short range colloidal crystallinity.

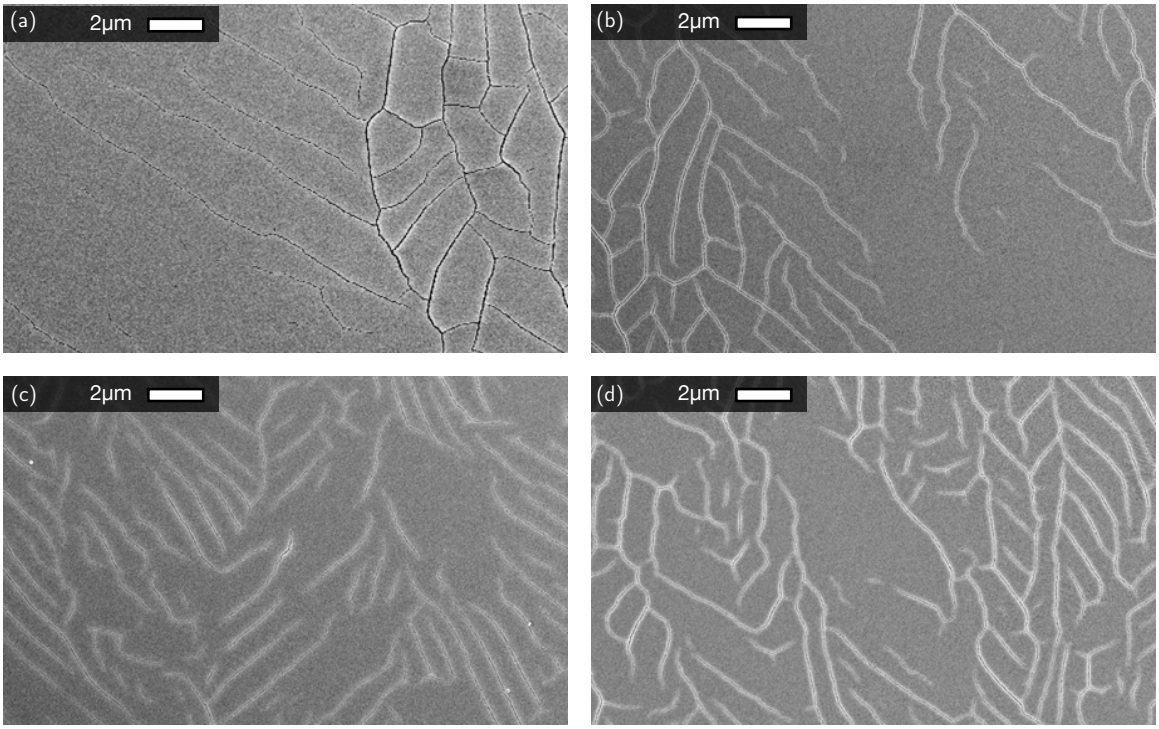

Figure A.7: Multilayer LYS-SIL films exhibit cracking at length scales much larger than the particle size. Although quantitative measurements of the film thickness could not be taken, the presence of cracks is speculated to arise due to the thickness of the multilayers. Images in (a)-(d) represent experiments conducted at increasing drying gas flow rates: 1.6, 4.8, 9.6, and $14.4\,\mathrm{cm}^3/\mathrm{s/sm}$. The results seem qualitatively insensitive to the drying gas flow rate, which should in principle increasing particle flux and increase final film thickness.

are prone to cracking. Representative images of these films are given in Figure A.7, where films were coated at varying drying gas flow rates.

Peeling of the films was observed at even higher suspension concentrations ($> 2\,\mathrm{wt\$}$) at very slow coating rates. The film appeared "furry" as the peeling strands resembled long strands of fur. These films were not imaged or further characterized.

A fortuitous observation of the interior of a thick film is given in Figure A.8. This view was probably made possible by the peeling off of a section of the multilayer.

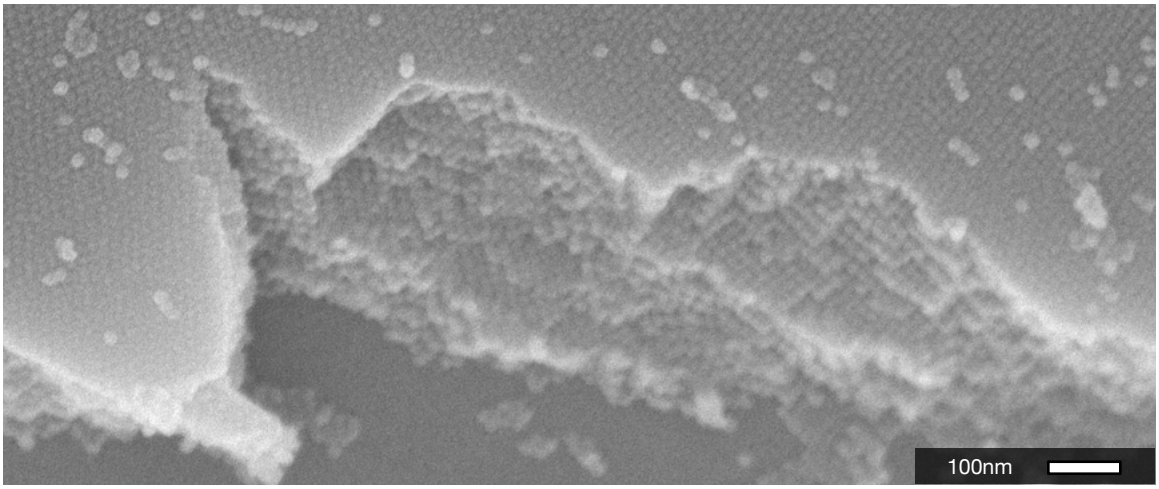

Figure A.8: Lower layers of a thick multilayer LYS-SIL film appear to be colloidally crystalline.

A.IV Multilayer LYS-SIL films with varied ionic strength

Both the micro crevices and the large cracking behavior in very thick LYS-SIL films are of interest. While the suppression of the large cracks mirrors the classic problem in solidifying [shirnking] films, the origins of the micro crevices are mysterious, especially considering their absence in the monoliths formed by evaporation.

Especially from the point of view that the micro crevices can be re-cast as disruptions in long-range colloidal crystallinity, and that it is well-known that DLVO forces play a significant role in colloidal crystallization in the liquid phase, we might expect ionic strength (or more directly the Debye length κ of the electric double layers surrounding the particles in suspension) to be an important factor. As discussed in § 2.1.2, Koh *et al.* (2008) recently showed that the Debye length indeed affected the lattice parameters of the convectively assembled colloidal crystals in the wet stage. The drying of this wet film then results in a "shrinkage" of the total film, possibly inducing the cracks.

This idea was explored very briefly by introducing simple salts into the particle suspension to increase the ionic strength (thereby decreasing the Debye length) in hopes of suppressing cracks. A suspension was prepared to have final concentrations of 1 wt% particles and 0.1 M sodium chloride salt (NaCl). In comparison to the films coated from suspensions diluted with

pure DI water, the films from the salty suspension exhibited cracking with a decidedly different qualitative nature (Figure A.9).

This line of investigation was not carried through, but some brief notes may be helpful if interest was renewed. Since the "reference" suspension was prepared by dilution of the as-synthesized suspension (filtering out only large particulates), it is important to note that lysine was still present in the suspensions. The behavior of the ionic strength of these lysine solutions is not straightforward to calculate, especially considering that there are three pKa's to consider and silicic acid also in solution.

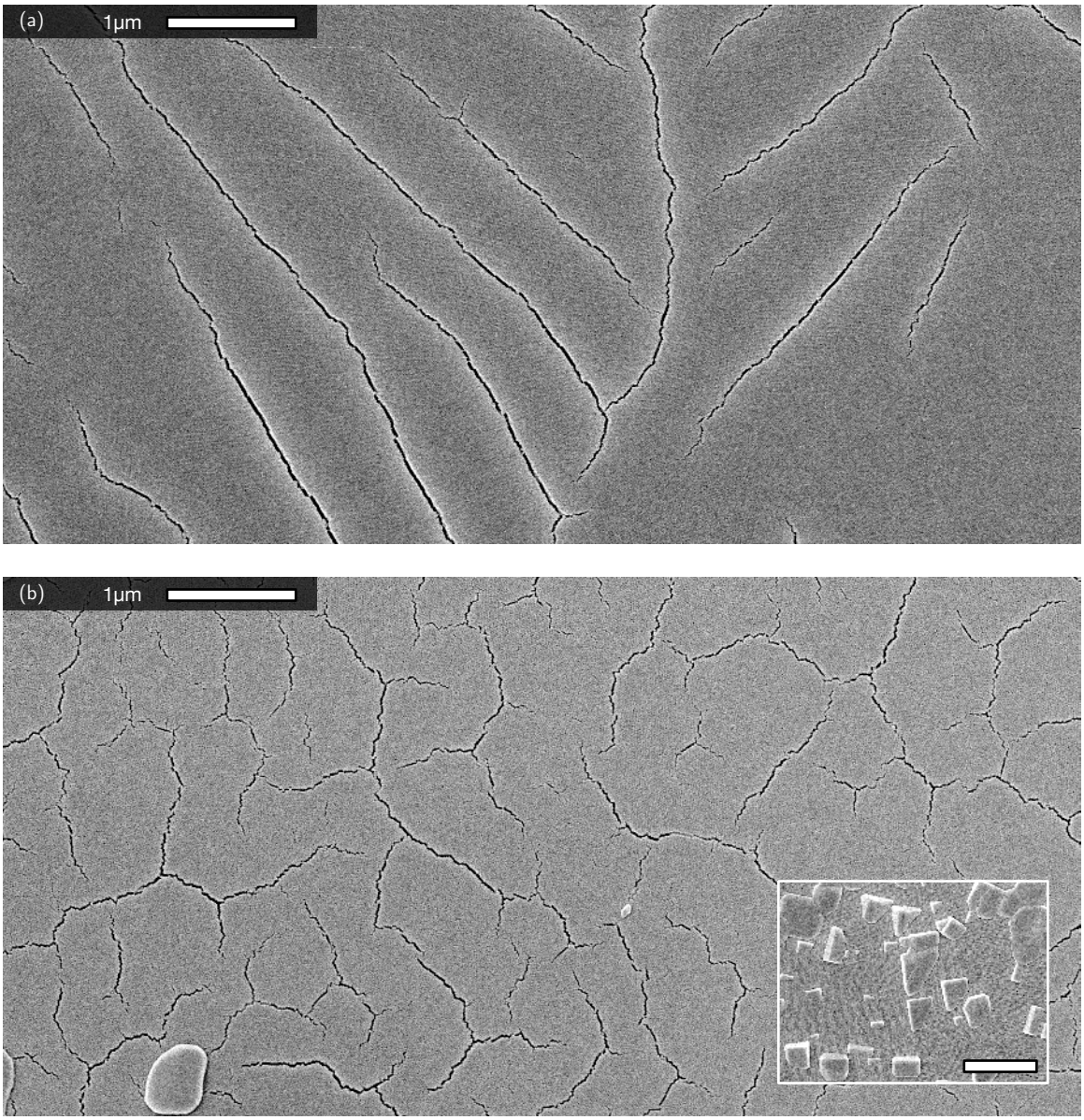

Figure A.9: Cracks in thick LYS-SIL films from "clean" solution containing only as much electrolyte (lysine) as left over from synthesis (a) compared to cracks in thick LYS-SIL films from ionically fortified suspension (b) shows qualitatively different cracking patterns. The ionic strength of the suspension for (b) was adjusted by adding NaCl (0.1 M). The glob visible in the lower left corner may be crystallized NaCl; the inset shows evidence of similar entities which are faceted (scale bar 1 µm).

A.V A menagerie of patterned films

This section showcases a menagerie of patterned LYS-SIL films. These patterns are somewhat anomalous, but display both seemingly random and strikingly regular high-order patterns. The islands and stripes shown in Figures A.10 and A.11 are relatively reproducible, and result when substrate withdrawal speeds "far exceed" the monolayer speed $v_c^{(1)}$. The remaining patterns have not been reliably reproduced, but seem to occur at similarly high substrate withdrawal speeds. The final pattern, hierarchical bands (Figure A.18), occurred at a relatively lower substrate speed.

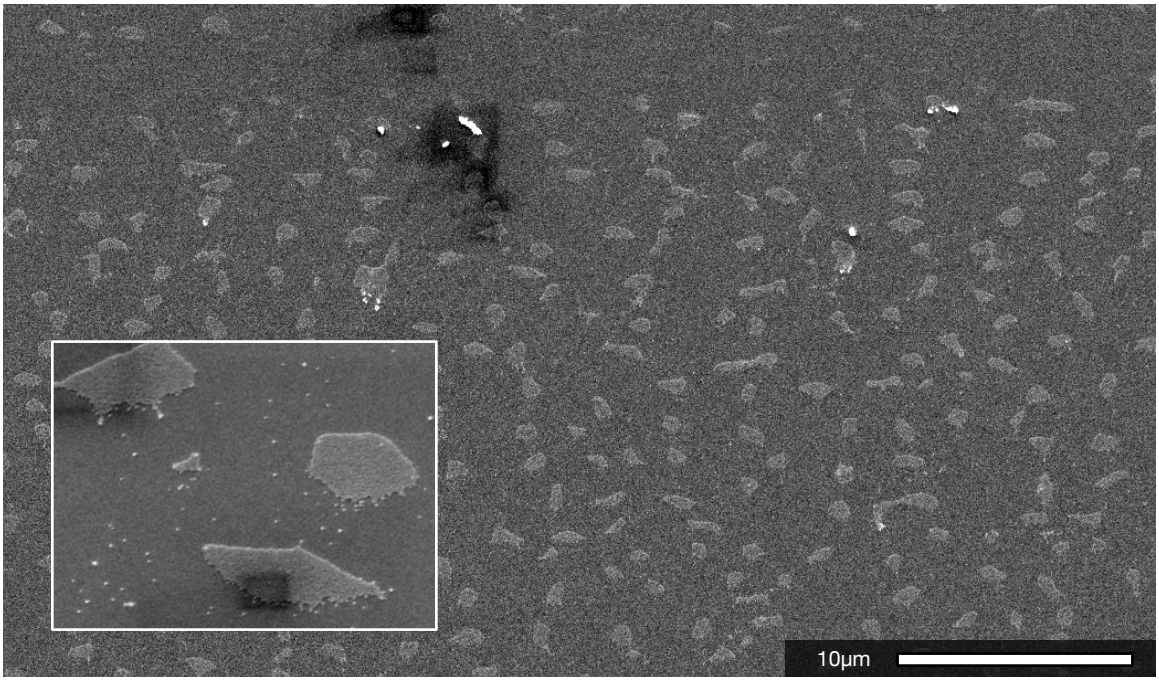

Figure A.10: Isolated islands of particles (in monolayer).

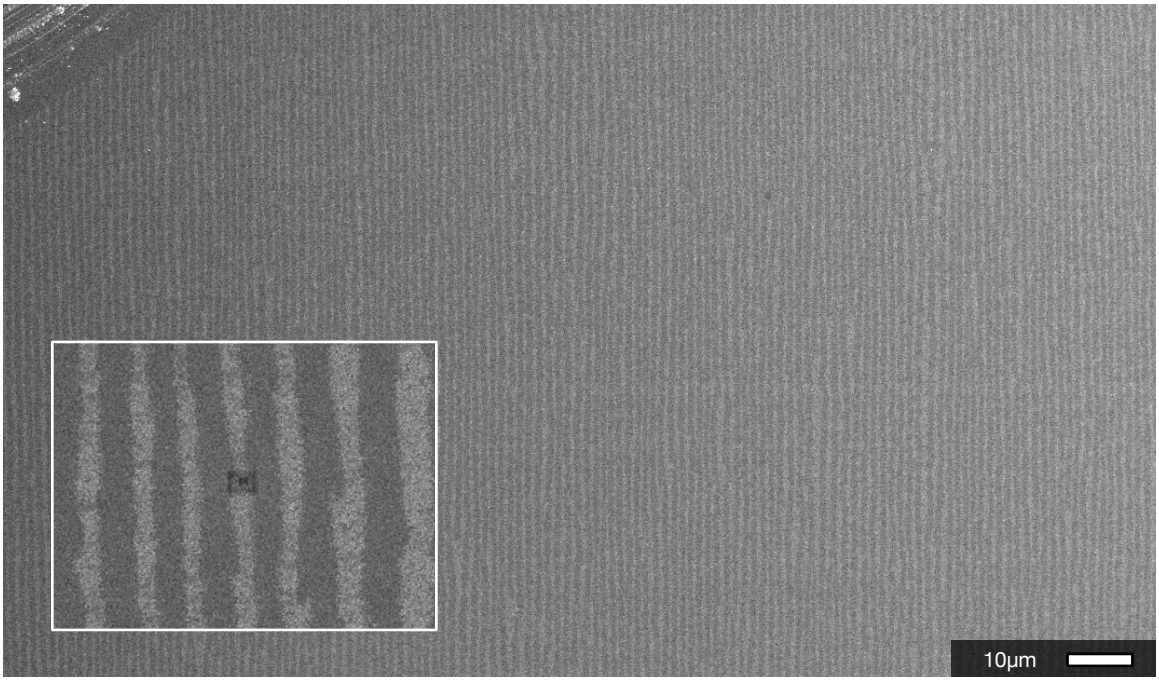

Figure A.11: Stripes (running vertical; perpendicular to "bands").

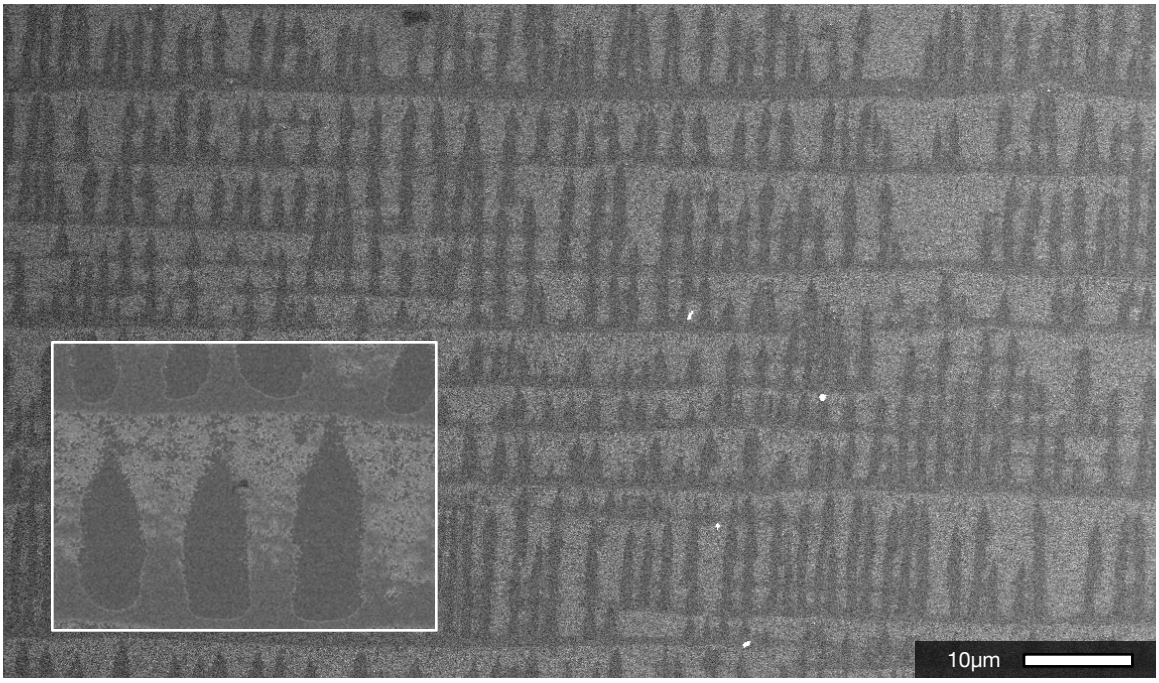

Figure A.12: Bands connected by columns of stripes.

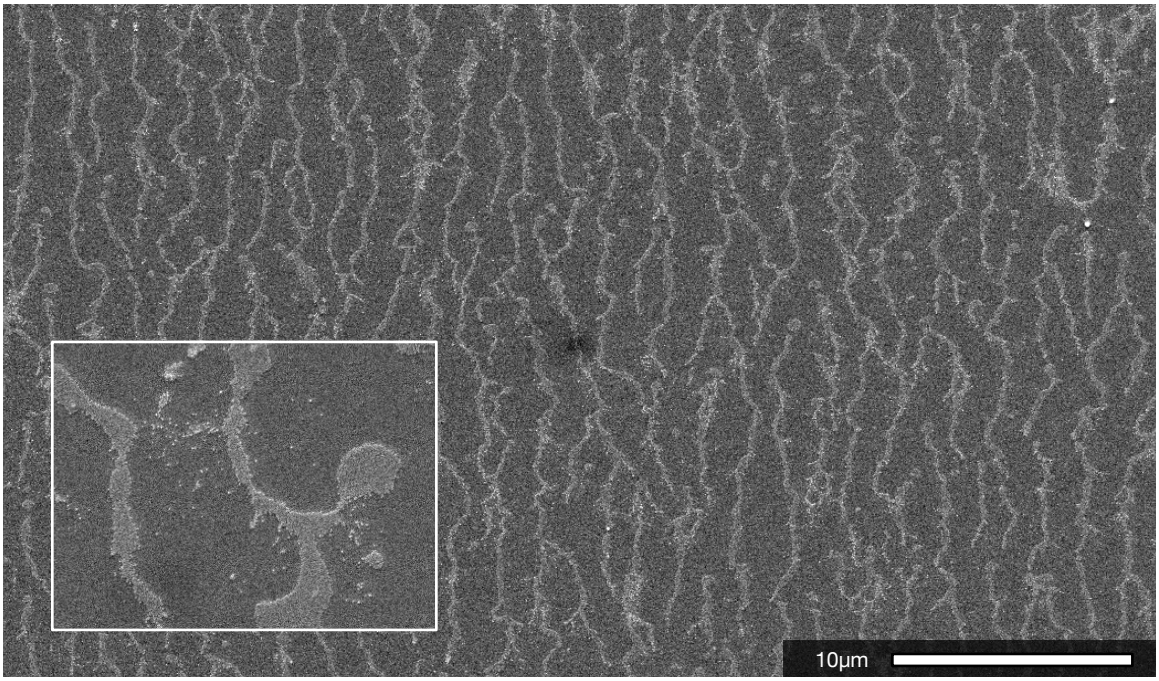

Figure A.13: Veins; somewhat less ordered version of stripes.

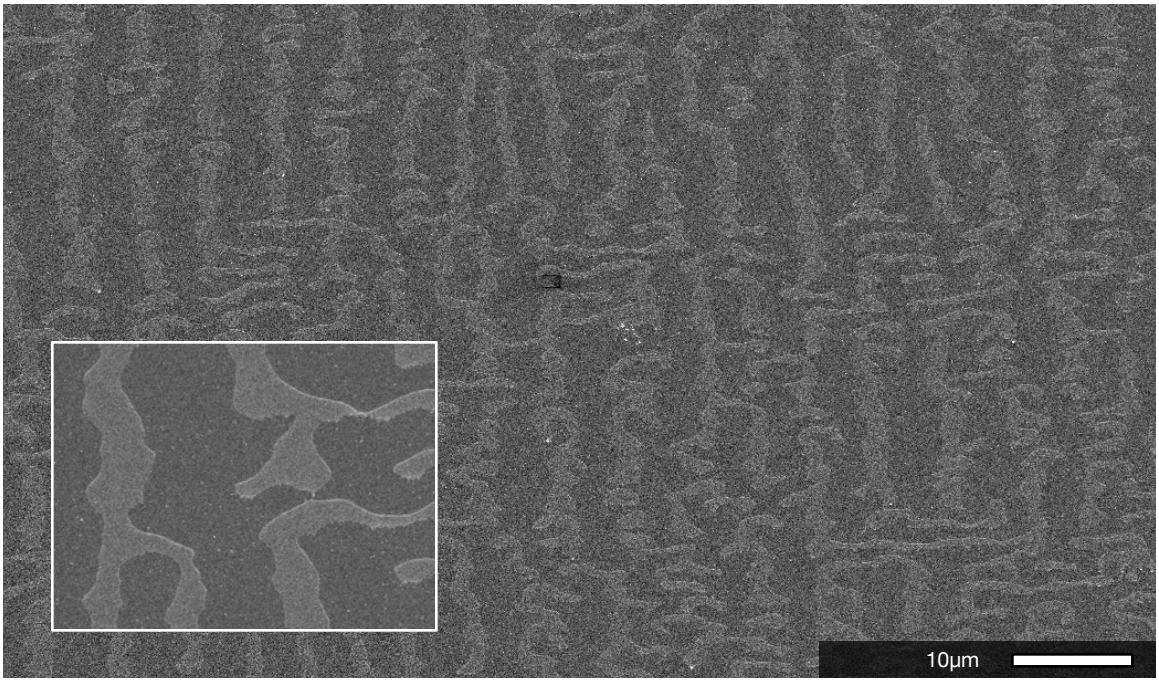

Figure A.14: Stripes mixed with islands and band segments, with a squiggly appearance.

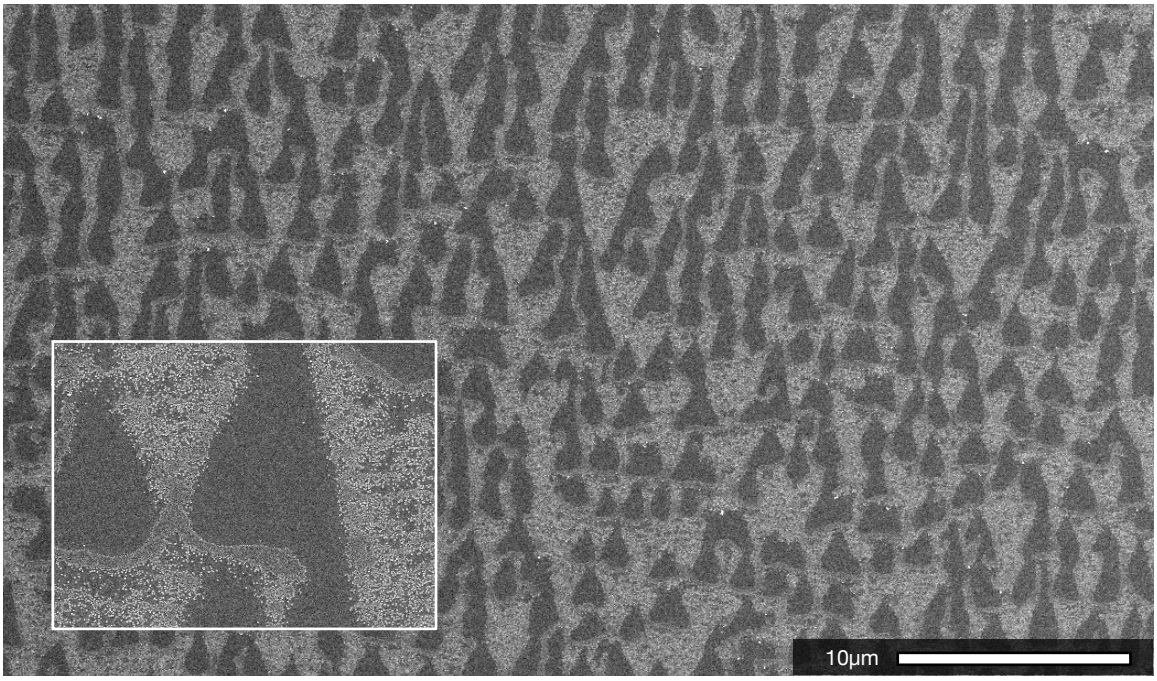

Figure A.15: Triangles with a teary appearance.

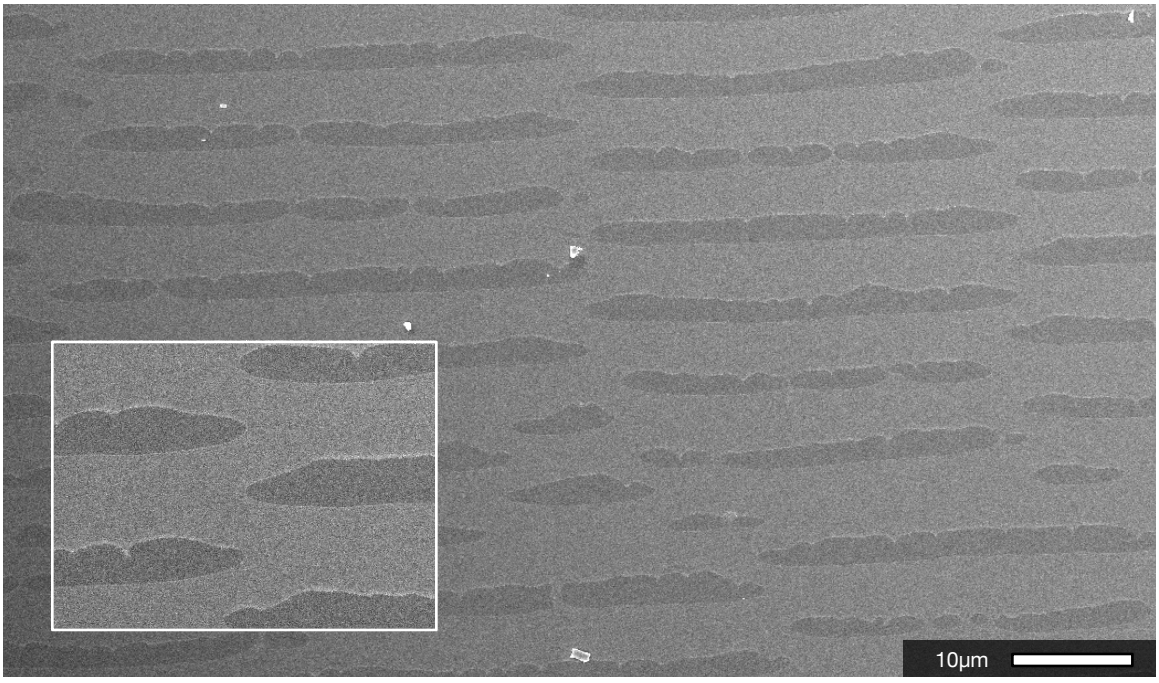

Figure A.16: Bands that are periodically shifted by half a wavelength.

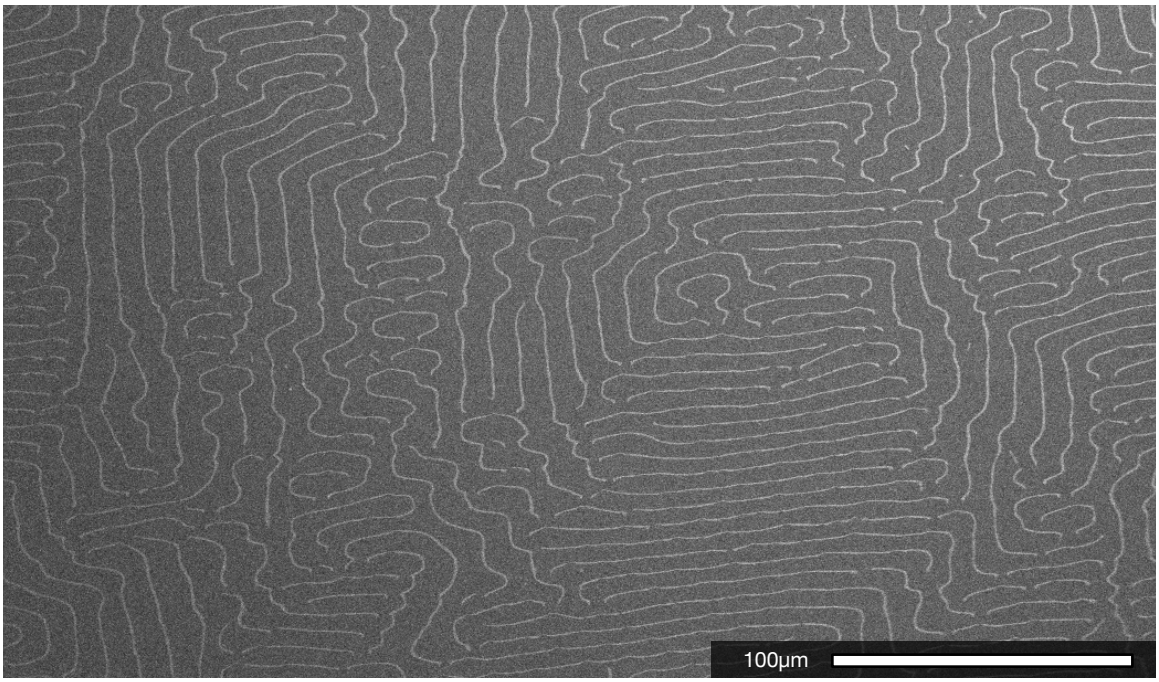

Figure A.17: Mixture of stripes and bands giving a loopy appearance.

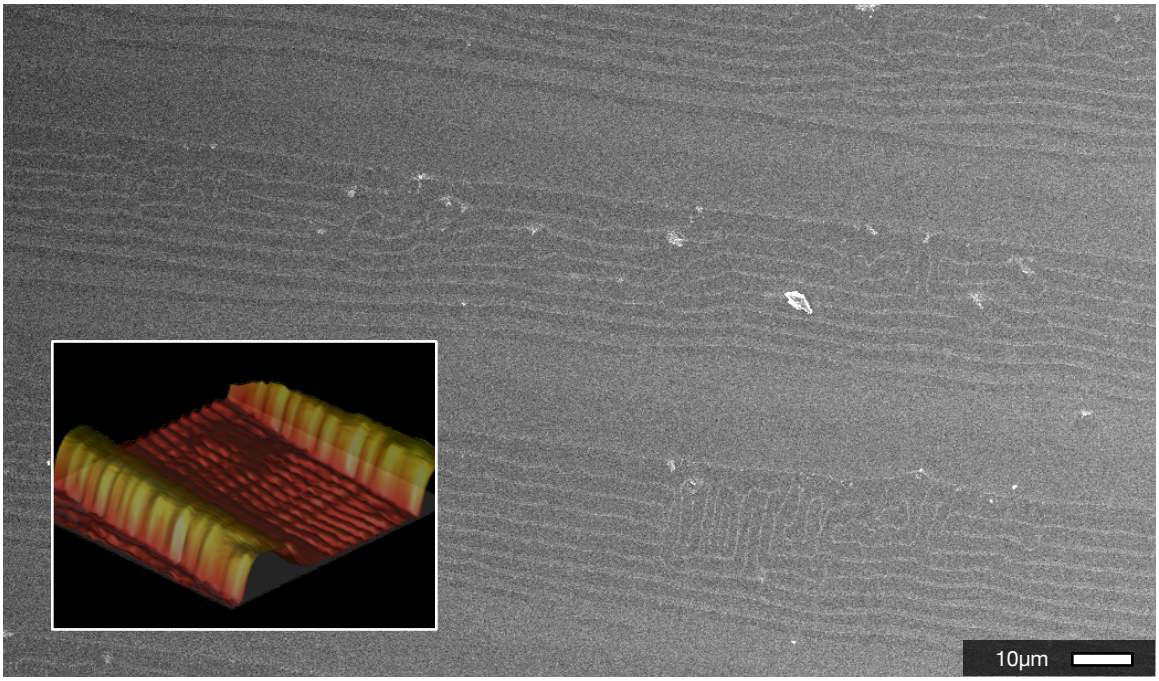

Figure A.18: Hierarchical banding; one of the few multilayer anomalies. The thin regions of the multilayered bands are themselves banded. Shown are thick multilayer bands separated by region of monolayer bands.

Appendix B

Detailed description of apparatus

B.I Technical drawings

This section contains some technical drawings for the parts of the apparatus described in § 3.2. The exploded view of the gas delivery assembly is reproduced in Figure B.1 for reference; subsequent drawings for each part follow the same nomenclature.

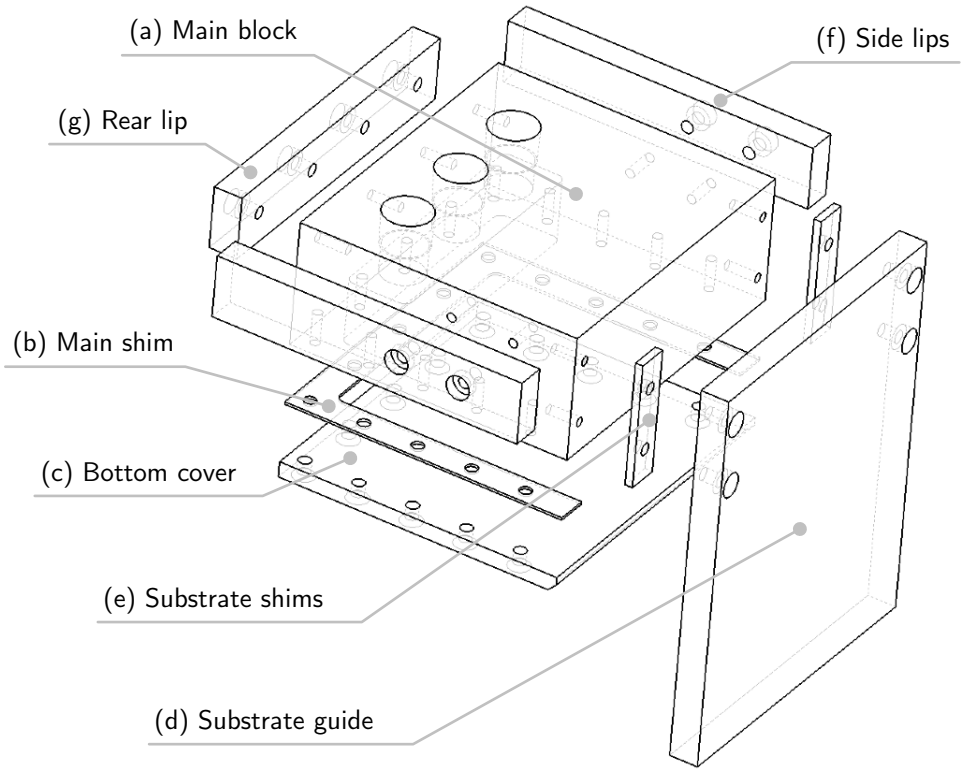

Figure B.1: Exploded view of gas delivery assembly.

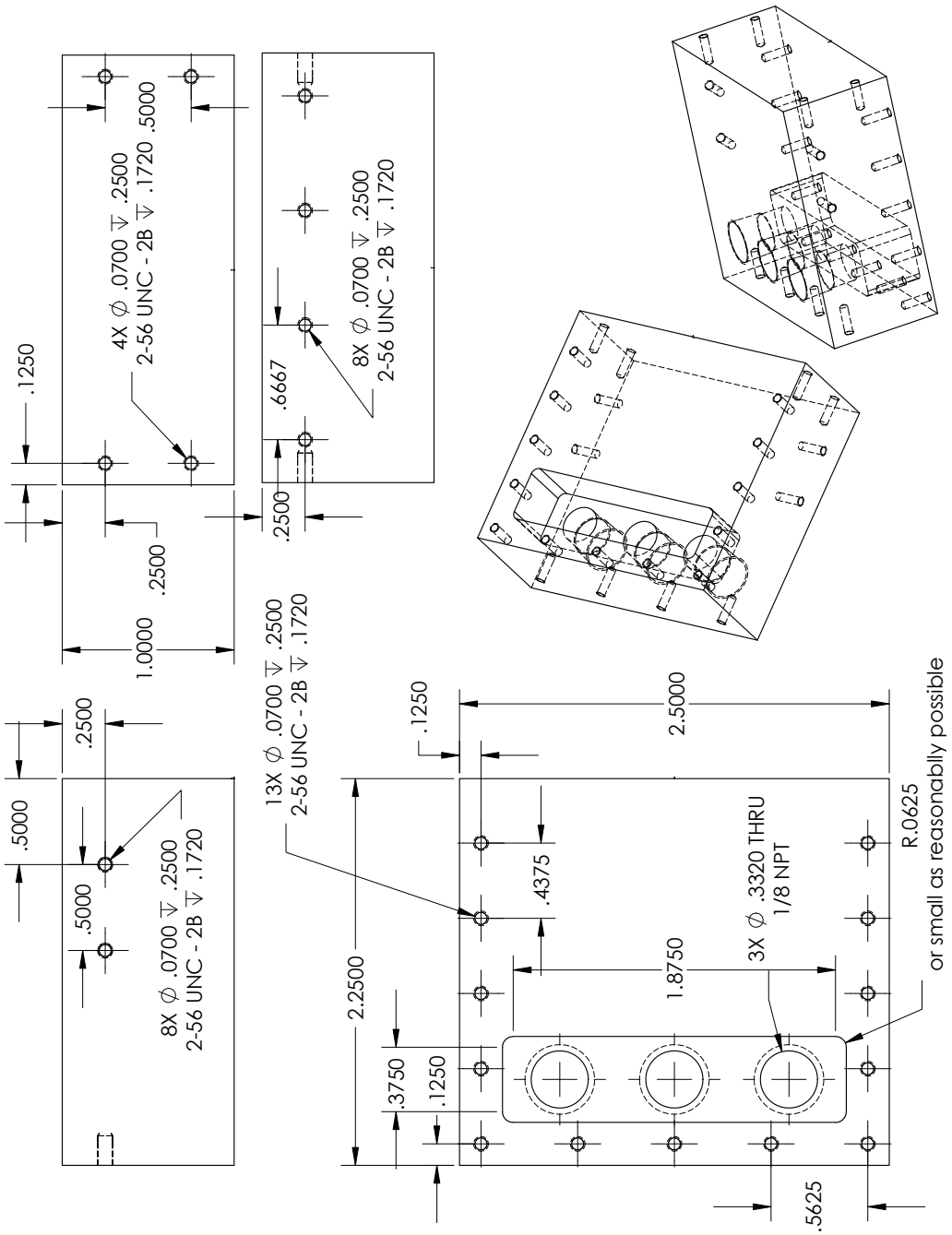

Figure B.2: Main block.

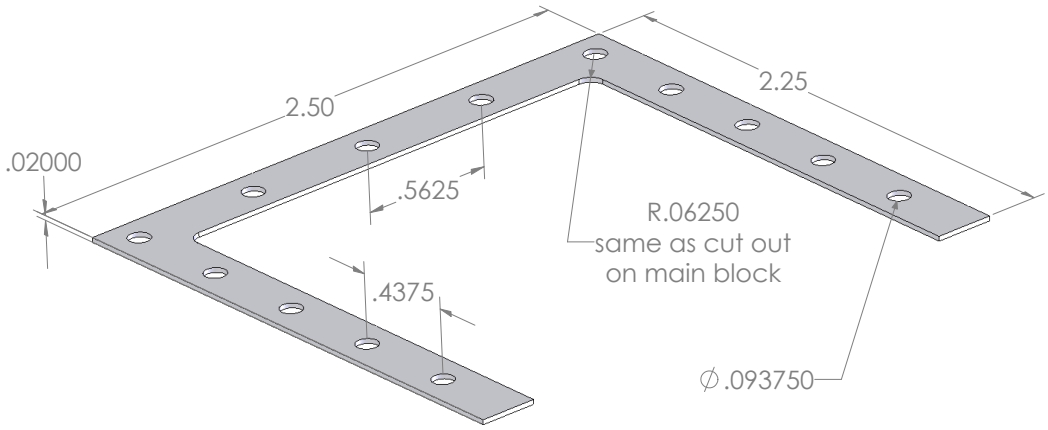

Figure B.3: Main shim.

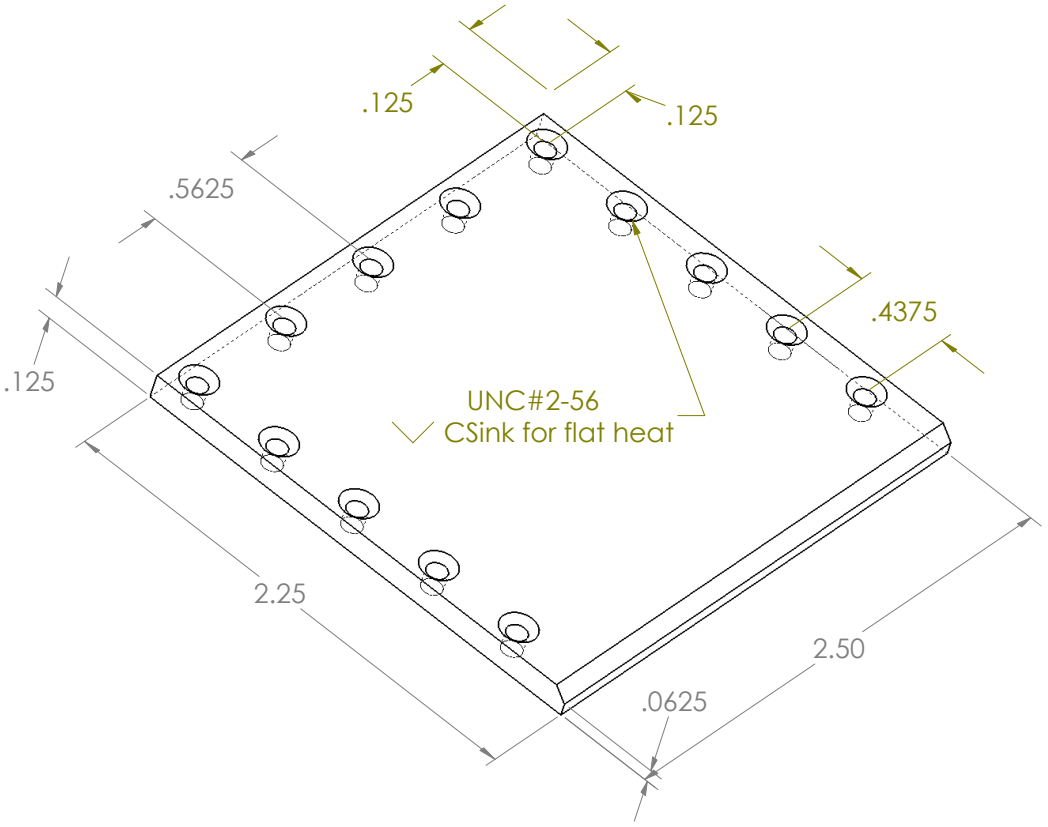

Figure B.4: Bottom cover.

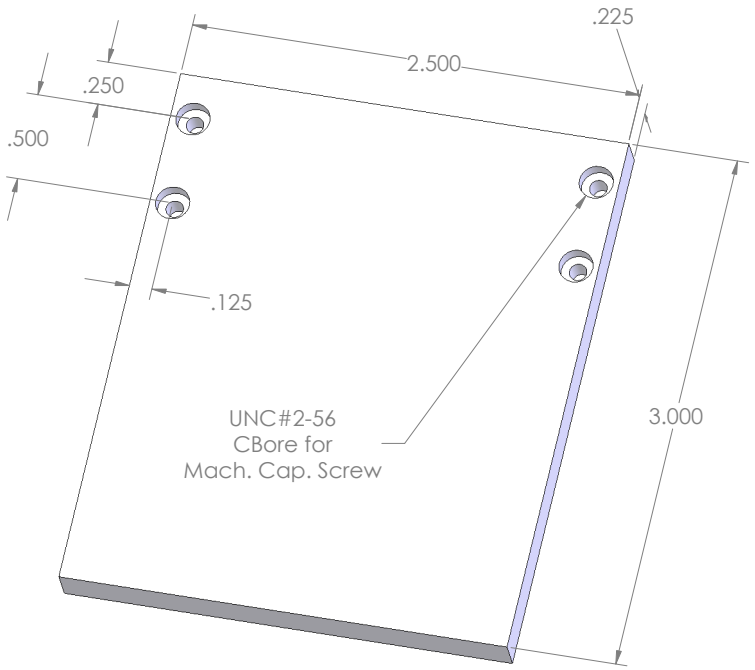

Figure B.5: Substrate guide.

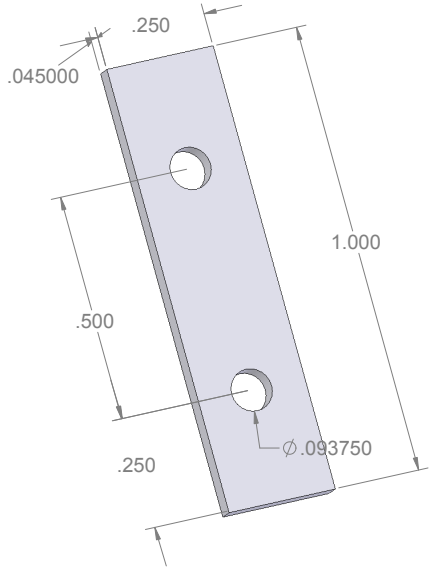

Figure B.6: Substrate shims.

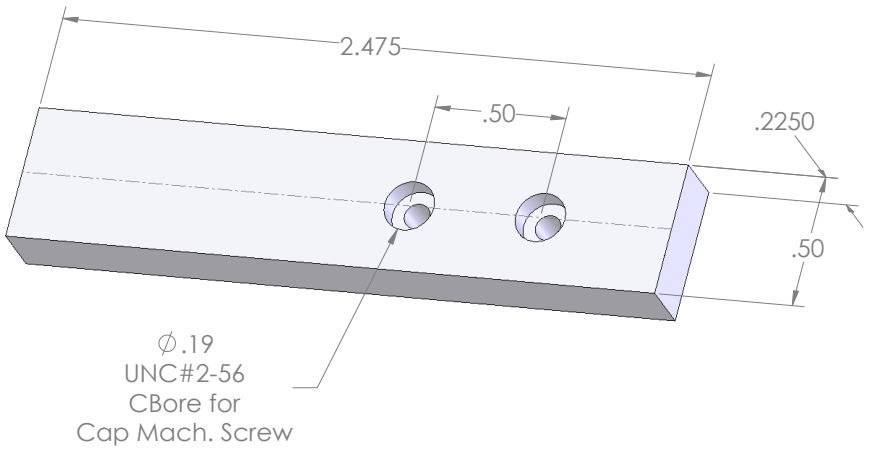

Figure B.7: Side lips.

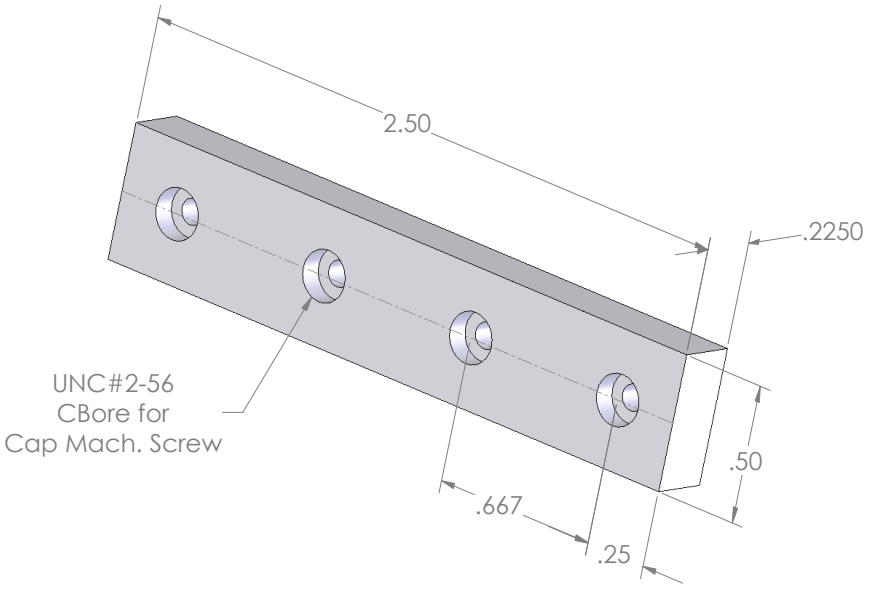

Figure B.8: Rear lip

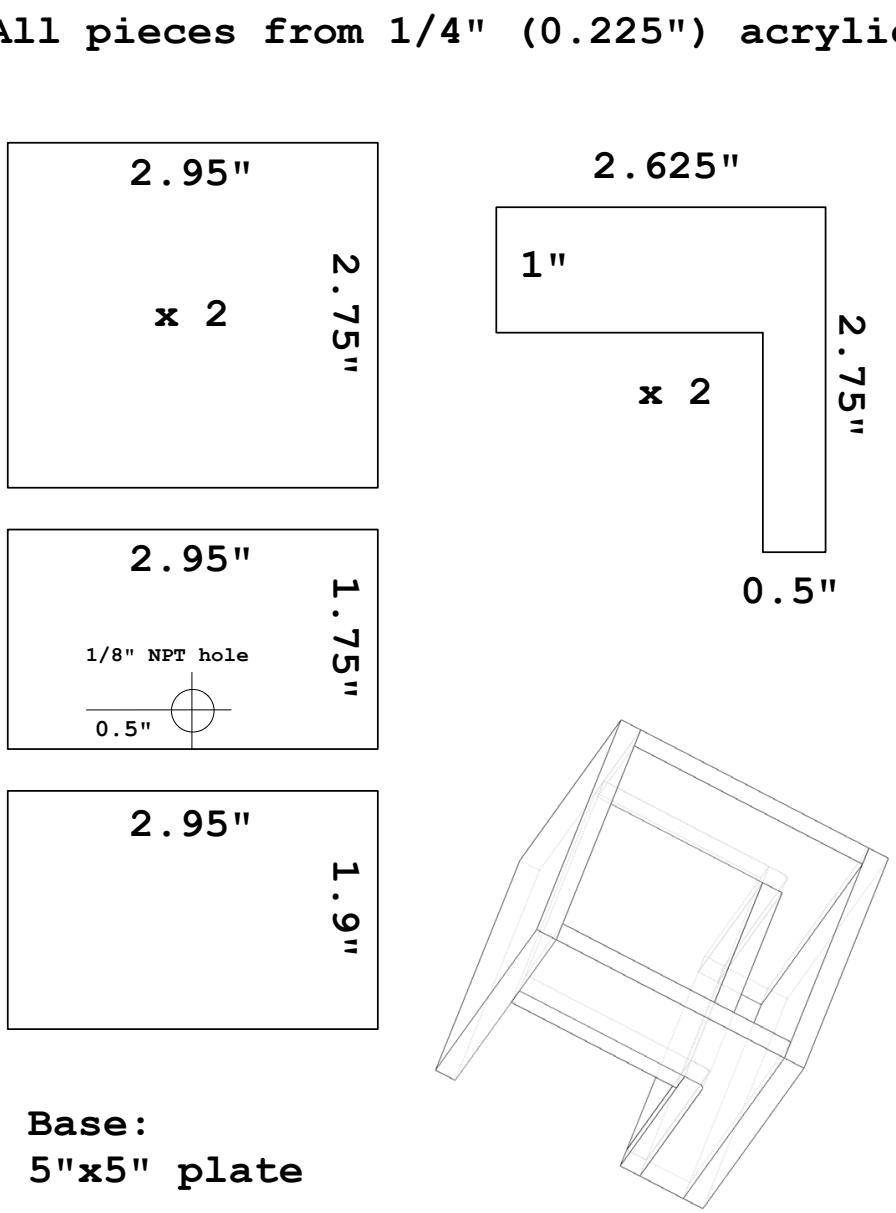

Figure B.9: Bath container. All parts are cut-outs from sheet stock. The base is not shown.

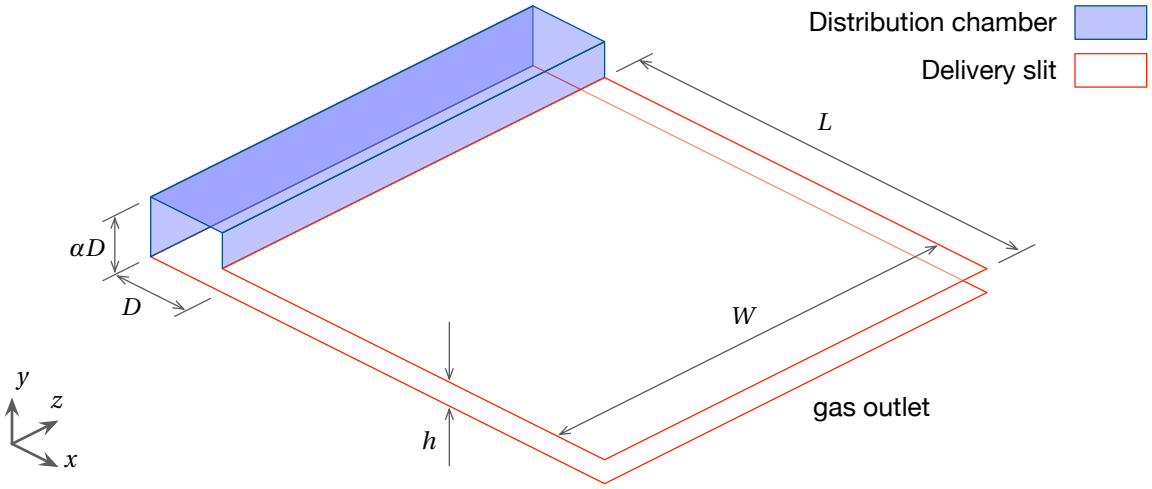

Figure B.10: Schematic of the gas distribution chamber and delivery slit. At the outlet, the z-wise flow rate distribution is proportional to the z-wise pressure distribution in the chamber (assumes uniform cross-sectional pressure distribution in the chamber and linear pressure drop along the slit length L).

B.II Distribution chamber for drying gas

Although the optimal placement of gas inlet ports to the distribution chamber may be intuitively obvious, the following analysis helps in the design of the convective assembly coating device to ensure well-characterized drying conditions.

The distribution chamber is constructed to be a rectangular duct, and the schematic in Figure B.10 provides a nomenclature. The z-wise drying gas flow rate or velocity distribution at the slit outlet of total width W is a salient factor in determining drying uniformity and consequently film coating uniformity in the cross-wise direction. Accordingly, the major design criterion for the drying gas delivery system is aimed at minimizing this variation. Specifically, the problem is to determine how the gas feed ports into the distribution chamber affect the flow rate profile at the slit outlet.

Inside the distribution chamber, flow is assumed to be unidirectional along z, *i.e.* pressure only varies with z. In the slit, flow is assumed to be unidirectional along x. Assuming that the x-wise pressure gradient in the slit is linear (slit flow approximation), the outlet gas flow rate distribution is directly proportional to the z-wise pressure gradient in the distribution chamber,

and the problem can be recast as a minimization of the z-wise pressure variation in the distribution chamber.

Flow rate analysis

In a straight duct of cross section $A = \alpha D^2$ as shown in Figure B.10, the equations for gas velocity u can be approximated as stokes flow

$$\nabla^2 u(x,y) = \frac{\partial^2 u}{\partial x^2} + \frac{\partial^2 u}{\partial y^2} = \frac{1}{\mu}\frac{\mathrm{d}p}{\mathrm{d}z} \tag{B.1}$$

Subject to no slip along all walls, the velocity profile is given by a an infinite Fourier series due to Spiga and Morino (1994) (an earlier solution was reported by Dryden *et al.*, 1932), which gives the fully developed flow rate $Q(z)$ upon integration over the cross sectional area.

$$Q(z) = -C_{\text{duct}} \frac{256A^2}{\mu\pi^4} \frac{\mathrm{d}\wp}{\mathrm{d}z} \tag{B.2a}$$

$$C_{\text{duct}} = -\sum_{n=1}^{\infty}\sum_{m=1}^{\infty} \frac{\sin^4\left(\frac{n\pi}{2}\right)\sin^4\left(\frac{m\pi}{2}\right)}{nm\left(\alpha n^2 + \frac{1}{\alpha}m^2\right)(-2n\pi + \sin(2n\pi))(-2m\pi + \sin(2m\pi))} \tag{B.2b}$$

In the delivery slit, the flow is rectilinear and laminar (parabolic velocity profile) and the flow rate is given in terms of the outlet and inlet pressure difference (for a uniform x-wise pressure gradient) by the familiar expression

$$q(z) = -\frac{h^3}{12\mu}\frac{p(z) - p_{\text{out}}}{L} \tag{B.3}$$

where the inlet pressure $p(z)$ is the z-wise pressure profile in the distribution chamber.

Pressure profile in the distribution chamber

The flow rates in the distribution chamber and slit are related by a mass balance

$$\frac{\mathrm{d}Q(z)}{\mathrm{d}z} = q(z) \tag{B.4}$$

Thus, the pressure profile in the distribution chamber can be obtained by differentiating the duct flow expression in Equation B.2 and equating to the slit flow rate via Equation B.3). The result, upon rearrangement, can be expressed as

$$0 = \frac{\mathrm{d}^2 \wp}{\mathrm{d}z^2} - \left[\frac{\pi^4}{3072 C_{\mathrm{duct}}}\right] \frac{h^3}{A^2 L} \wp \tag{B.5}$$

where for convenience, the datum pressure has been set to the slit outlet pressure, *i.e.* we are interested only in the duct pressure $\wp$ relative to ambient: $\wp(z) \equiv p(z) - p_{\mathrm{out}}$. Equation B.5 has the general form

$$0 = \wp'' - \lambda^2 \wp \tag{B.6a}$$

$$\lambda^2 \equiv \left[\frac{\pi^4}{3072 C_{\mathrm{duct}}}\right] \frac{h^3}{A^2 L} \tag{B.6b}$$

and admits the general solution

$$\wp(z) = c_1 e^{\lambda z} + c_1 e^{-\lambda z} \tag{B.7}$$

It now remains to determine how the pressure distribution $\wp(z)$ behaves with respect to placement of the feed ports. The feed ports placed at z_i are characterized by some input flow rates $Q_i = Q(z_i)$. By Equation B.2, the flow rate at each inlet port can be expressed in terms of the z-wise pressure gradient local to that port

$$\begin{aligned} \left.\frac{\mathrm{d}\wp}{\mathrm{d}z}\right|_{z_i} &= -\frac{\pi^4 \mu}{256 C_{\mathrm{duct}} A^2} Q_i \\ &= -\left[\frac{12\mu}{h^3 L}\right] \lambda^2 Q_i \end{aligned} \tag{B.8}$$

so that a port inlet flow acts like a boundary condition on $\wp'(z)$. Specifically, the distribution chamber can be split up into subdomains with internal boundaries defined by the location of the feed ports; of course the feed ports could also be exactly at the walls, so that in general, we can say given n feed ports, the domain can be split into $m = n + 1 - \epsilon$ subdomains where there

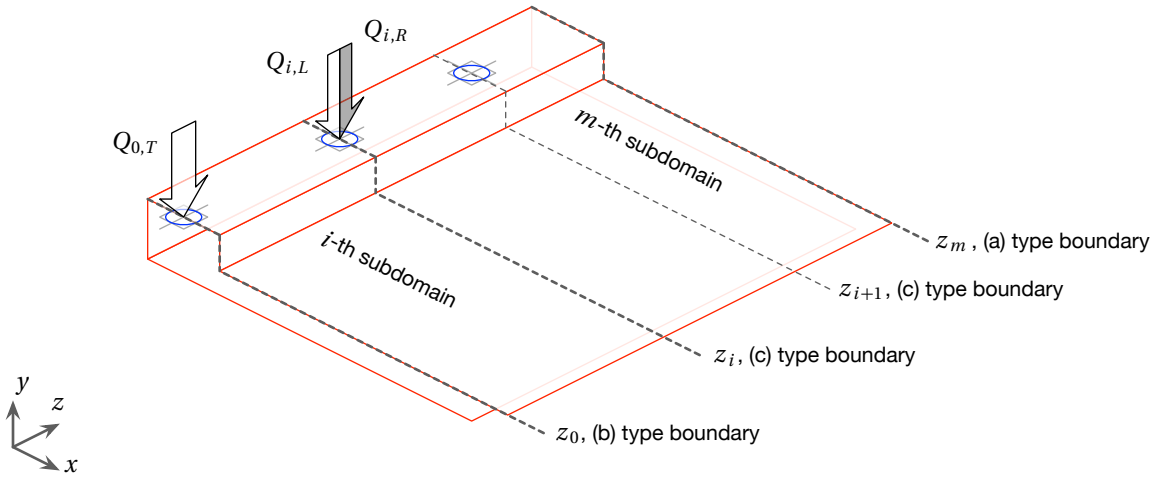

Figure B.11: A detailed analysis of the distribution chamber split up into subdomains defined by boundaries composed of either the wall or a feed port (or a feed port at a wall). The fractional feed at any given feed port boundary is specified by a pressure matching condition there.

are ϵ feed ports on the walls (up to two; one each at either $z = 0$ or $z = W$).

For each of the m subdomains, the pressure profile has the general form of Equation B.7, requiring 2 constants (2 boundary conditions) to specify, for a total of $2m$ unknown constants in the set of piece-wise pressure profile equations. In general, the boundary conditions can be posed in the form of Equation B.8 to give $2m$ boundary equations. However, the flow rates in each of these boundary equations is generally not known, so that in the end, we simply trade the $2m$ unknown constants for $2m$ unknown partial feed flow rates.

There are three kinds of boundaries: (a) boundaries that are not feed ports, and that are necessarily at the walls of the distribution chamber, (b) boundaries that *are* feed ports, *and* are at the walls, and (c) boundaries that are feed ports but not at either wall (see Figure B.11). For the boundaries of type (a), there are no unknown partial feed flow rates because $\wp' = 0$. At a boundary of type (b), there is 1 unknown partial feed flow rate. At a boundary of type (c), there are 2 unknown partial feed flow rates, 1 for each adjacent subdomain. In other words, for the arbitrary feed port arrangement, there are $2n - \epsilon$ unknown partial feed flow rates, which we must now strive to specify.

For every (b)-type boundary, *i.e.* at every internal feed port, we can assert a matching con-

dition on the pressure profile, providing $n-\epsilon$ equations. This still leaves $2n-\epsilon-(n-\epsilon)=n$ degrees of freedom.

For the special case of $n=1$, the extra equation is provided by none other than the total input flow rate. However for $n\geq 2$ feed ports, there are not enough equations to fully specify the solution because the most generally true statement we can make is that the sum of all unknown partial feed flow rates must equal the total input flow rate; this provides only a single equation and leaves $n-1$ degrees of freedom.

Evidently, as the problem is posed so far, there is not enough information to fully specify the pressure profile in the distribution chamber. The lacking information must come from the way in which the total input flow is distributed to the ports; so far we have assumed implicitly that the feed port flow rates share a single source and therefore are not independent. In practice, such a set up is probably the most logical, but generally does not guarantee the equal distribution of the feed flow into each feed port. The implication for the current analysis is that the fully specified problem requires knowledge about the details of the distribution system *before* the distribution chamber, for example the series of tubes connecting the chamber to the primary source, which would in principle provide $n-1$ equations about how the flow is split into each port.

Alternatively, the fractional flow rate to each physical feed port can be specified *a priori* to provide n equations (or $n-1$ equations plus the total input flow equation), in essence describing the hypothetical system where each feed port is fed independently. The further assumption that the total feed flow Q_T is split evenly across the feed ports is a reasonable one for feed port arrangements that are close to optimal (by definition, the optimal arrangement should distribute the flow to each feed port equally).

In summary, the pressure profile on each of the m subdomains is described in terms of the same general expression, which can be constructed from applying boundary equations with the form of Equation B.8 to the general pressure profile in Equation B.7: on the i-th subdomain bounded by the boundary locations z_i (so that $z_{i=0}=0$, $z_{i=1}$ is the location of the first internal

feed port, and so on, up to $z_{i=m} = W$; see Figure B.11):

$$\wp_i(z) = c_1 e^{\lambda z} + c_2 e^{-\lambda z} \qquad z_{i-1} \le z \le z_i \tag{B.9a}$$

$$c_1 = -\left[\frac{12\mu}{h^3 L}\right] \lambda \, \frac{Q_R e^{\lambda z_i} - Q_L e^{\lambda z_{(i-1)}}}{e^{2\lambda z_i} - e^{2\lambda z_{(i-1)}}} \tag{B.9b}$$

$$c_2 = -\left[\frac{12\mu}{h^3 L}\right] \lambda \, \frac{Q_R e^{\lambda z_i} - Q_L e^{\lambda z_{(i-1)}}}{e^{2\lambda z_i} - e^{2\lambda z_{(i-1)}}} \, e^{\lambda(z_i + z_{(i-1)})} \tag{B.9c}$$

where the Q_L and Q_R are used sloppily, and can be 0 for a wall boundary, the total flow to the 0-th or m-th [wall] port ($Q_{0,T}$ or $Q_{m,T}$), or some fraction of the flow to the i-th port at an internal feed port $Q_{i,L} + Q_{i,R} = Q_{i,T}$ (see Figure B.11), depending on which side of the subdomain under examination.

Comparison of feed port arrangements

The algebraic expression for the general piece-wise pressure profile for arbitrarily positioned feed ports is somewhat cumbersome, and are not reproduced here. The results are summarized graphically in Figure B.12. The pressures are normalized by the minimum pressures for comparison, and grouped by the number of physical feed ports in the configuration. The feed port locations are readily identified by the pressure spikes in the profile. It is apparent that the best placements result when the pressure at each feed port is equal (the darkest filled in profiles), where the maximum pressure difference is the lowest for each group.

Practically, the optimal arrangement can intuitively be reasoned as depending on symmetry; the preceding analysis could have been made more specific by considering only arrangements with the highest symmetries. Although it may be tempting to distribute the feed ports evenly along z, the results in Figure B.12 show that these are not the best placements. The the ports must be placed at positions akin to the nodes of a standing wave spanning the distribution chamber with a frequency corresponding to the number of feed ports.

In any case, the best arrangements apparently have the lowest pressure spikes, corresponding to the case where the pressure spikes to the same value at each feed port (in fact, this is the only truly self-consistent solution under the assumption of equally distributed flow to the feed

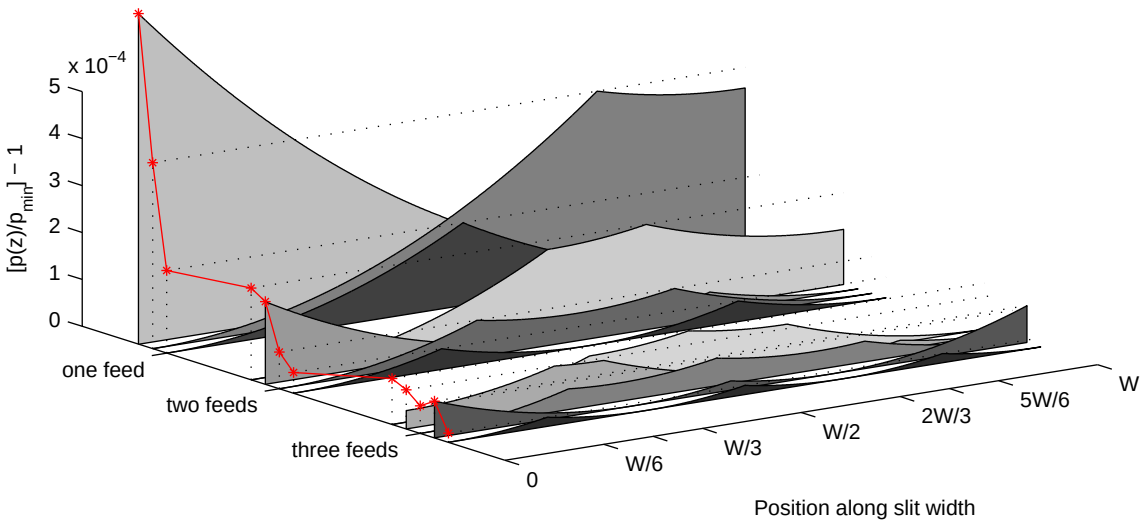

Figure B.12: Relative pressure profiles in a distribution chamber with various feed port arrangements, assuming equal distribution of total feed gas among physical feed ports. The "goodness" of the arrangement can be considered as the maximum value of the relative profile (shown as $*$ on the left face of the plot), which signifies the relative maximum pressure variation along the distribution, and consequently the flow variation at the slit outlet. Optimal placements are characterized by equal pressures at the feed ports, and evidently occur when the ports are placed at $z_i = \frac{2i-1}{2n}W$.

ports that share a common source, and therefore are not independently controlled). The optimal feed port positions can then be found easily by augmenting the pressure matching condition to ensure that the pressure is matched at *all* of the fractional-feed ports, not just the adjacent ones. Without presenting the algebraic details, the result can be given as

$$z_i = \frac{2i-1}{2n}W \tag{B.10}$$

The optimal feed port arrangement for the 3-feed design is therefore at $[W/6, 3W/6, 5W/6]$.

Final remarks about drying gas feed distribution

Assuming that the placement of the feed ports is made optimal for a given geometry, it remains to optimize the rest of the gas distribution system geometry. Intuitively, the ideal geometry is characterized by an infinitely thin slit, an infinitely long slit, an infinitely big (cross-sectionally) distribution chamber, and/or an infinitesimally short distribution chamber. A quantity that con-

firms these intuitions is evident from the preceding analysis:

$$\lambda W = \sqrt{\left[\frac{\pi^4}{3072\, C_{\text{duct}}}\right] \frac{h^3 W^2}{A^2 L}} \tag{B.11}$$

which additionally includes information about the aspect ratio of the distribution chamber duct, embodied in C_{duct}. In particular, this quantity must be minimized, according to the form of Equation B.9, to minimize the pressure variation along the slit width. Although there cannot be a true minimum λ, this quantity provides the guideline for constraining the device geometry. The distribution chamber duct aspect ratio, however, can be optimized. The parameter C_{duct} given in Equation B.2b must be maximized according to Equation B.11. Since the series is converging, only the leading order term needs to be examined. It is apparent that to maximize C_{duct}, the quantity $\alpha + 1/\alpha$ appearing in the denominator should be minimized. It is easy to show that this quantity is minimized when $\alpha = 1$, that is when the duct is square in cross section.

Appendix C

Inter-band spacing measurements

C.I Algorithm overview

Inter-band spacings are experimentally measured using a custom algorithm. Given a typical SEM image (as taken by a JEOL-6500 or JEOL-6700; see Figure C.1), the following basic pre-processing steps are taken. The images are black and white, and the gray value (luminance) is taken to be the topography.

1. Crop the bottom information bar
2. subtract a best-fit plane (of luminance values)
3. Gaussian smooth of a user-defined width (adjustable)
4. Binary threshold; convert to black and white for "particle", "no-particle"

The resulting image (Figures C.2 and C.3) is analyzed by compiling several profile line scans and measuring the "trough" lengths. An average trough length for many such line scans is taken to be the mean inter-band spacing λ. However, since the measured λ depends on the orientation of the line scans with respect to the image, several sets of line scans are taken at many angles, and the "true" mean λ is taken to be the minimum value (see Figure C.4).

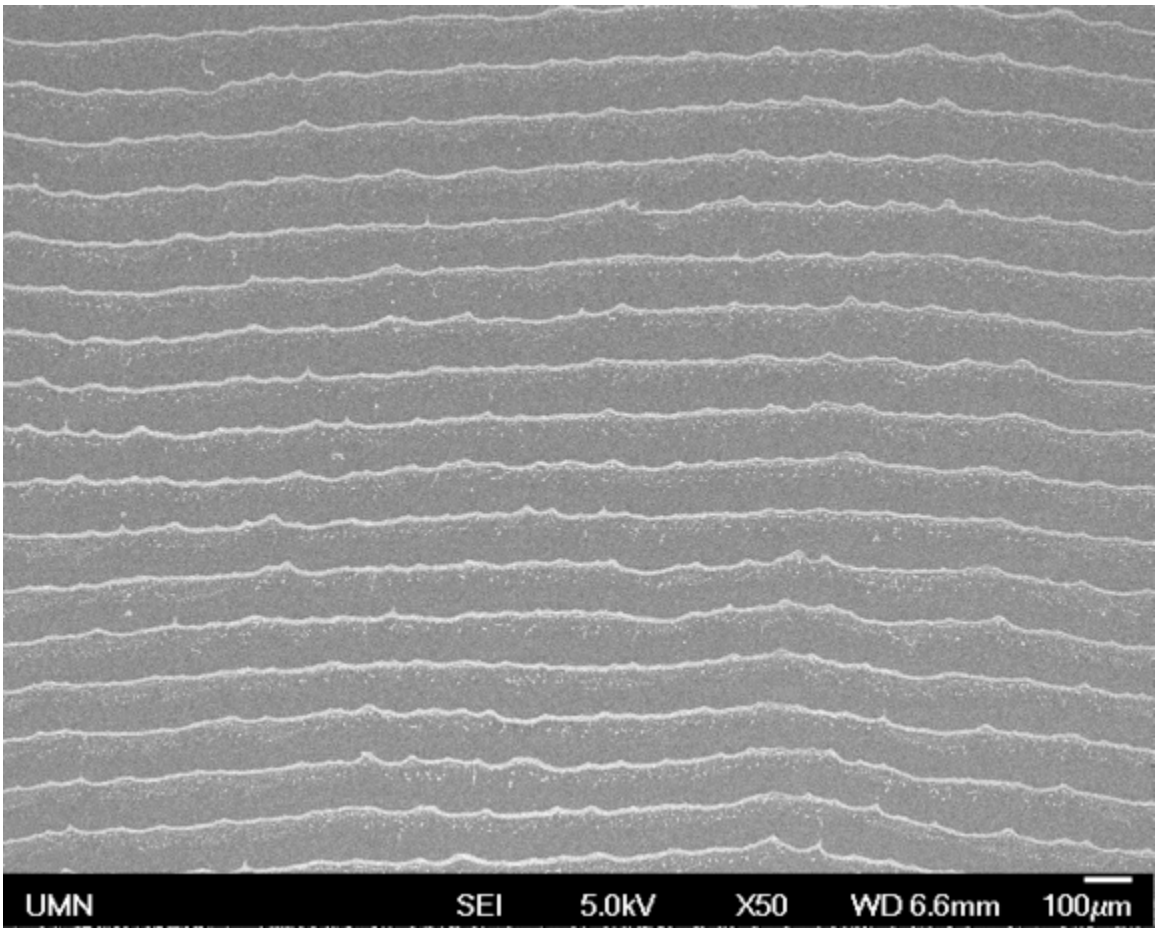

Figure C.1: Typical SEM image produced by a JEOL instrument. The image has 1280×960, pixels including the information bar at the bottom.

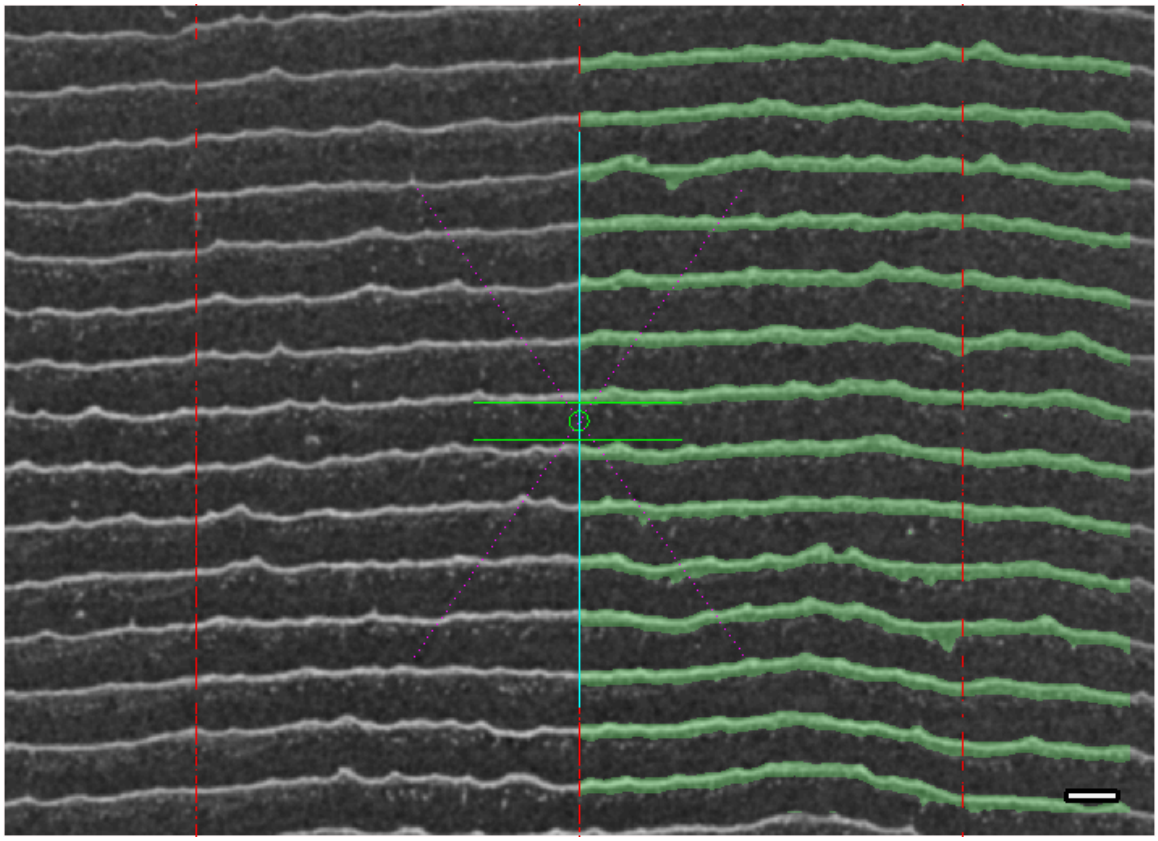

Figure C.2: Top view of pre-processed thresholded SEM image. The band regions are highlighted in green.

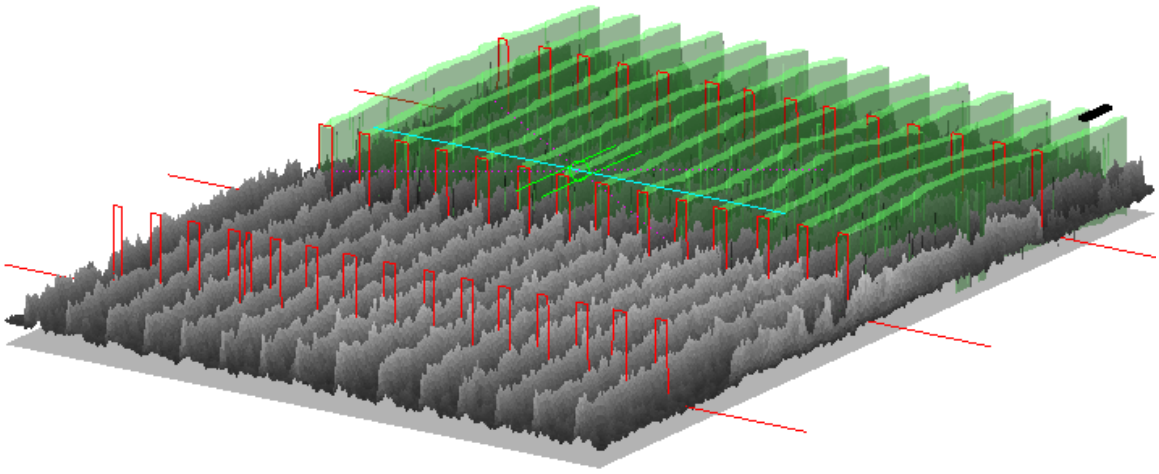

Figure C.3: Angled view of pre-processed thresholded SEM image. The band regions are highlighted in green. The superimposed lines represent the orientation of the profile line scans.

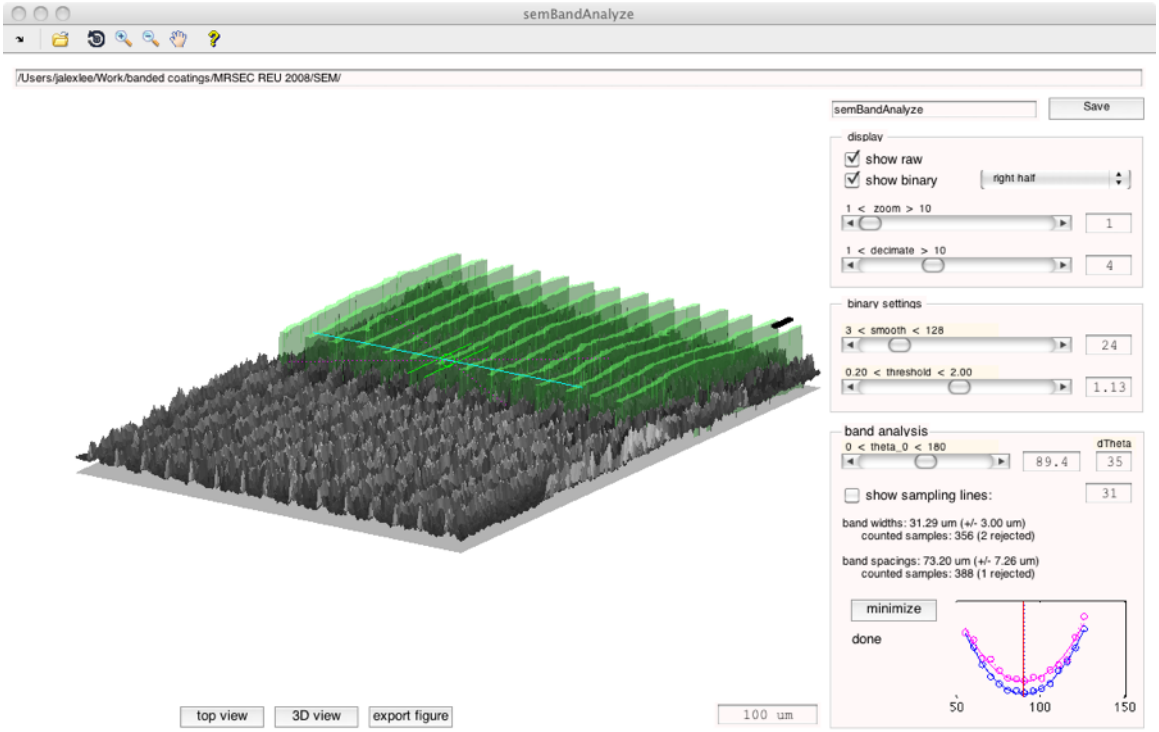

Figure C.4: Interface for inter-band spacing measurement algorithm. The control elements on the right are used for the smoothing and thresholding operations, as well as interface display options. The best orientation of the scan lines is determined by a fitting a parabola through a λ vs. θ_{scan} plot as shown in the bottom right corner.

C.II Algorithm details

Best-fit plane background subtraction

The SEM image is considered as a luminance values on a uniform grid of dimensions corresponding to the image pixel resolution. A best-fit plane through the luminance is obtained by a linear least squares fit. The resulting image is shifted by adding a constant (the minimum resulting luminance) in order to remove negative values, and subsequently normalized.

Gaussian smoothing

This plane-subtracted image is smoothed by convolution with a Gaussian kernel. The width of the kernel is determined interactively by visually observing how well the thresholded image corresponds with the original image. Because of the smoothing method, a finite width around the image must be discarded. Of particular importance is to have a sufficiently smooth image that no artificial "pocks" or "specks" can pollute the image (such features would cause problems in the profile analysis).

Binary thresholding

The smoothed image is thresholded by a simple absolute cut-off method. The cut-off value is determined interactively by visually observing how well the thresholded image corresponds with the original image. As in the case of smoothing, it is important to choose values of the thresholding cut-off that result in the fewest "pocks" and "specks".

Profile scan and analysis

The profiles at arbitrary angles are generated by 2D interpolation of the image luminance along pre-defined lines in the dimension of the image plane (see Figure C.3). The troughs and crests can be identified by first identifying the transition points and then determining their direction. Only full troughs (surrounded on both sides by crests) are considered, to avoid counting partial

troughs. All of the trough lengths (inter-band spacings) from each line scane are then averaged. The same method can be used to measure the crest lengths (band widths).

Determination of the perpendicular to the bands

The λ measured by this averaged trough length method clearly depends on the orientation of the line scans with respect to the image; as the line scans are taken in an orientation farther away from the direction perpendicular to the bands, the measured apparent λ become larger. Thus, the "best" line scan orientation (most perpendicular to the bands) can be determined by collecting the mean λ at a series of angular orientations θ_{scan}, and taking the minimum λ. Specifically, a λ vs. θ_{scan} plot is fit with a parabola, which can be easily be minimized (see Figure C.4).

Appendix D

Numerical methods

This appendix documents some of the details behind the computations of the liquid meniscus profiles described in Chapter 5. Many of the techniques are textbook techniques or straightforward extensions. A resource I have found extremely useful is the series of textbooks *Numerical Recipes*, for example the particular edition by Press *et al.* (1993).

D.I Finite difference equations

Solution of an ODE by finite differencing means that the differential equations are approximated by difference equations at discrete positions (nodes) along the domain. Accuracy of a difference equation obviously depends on the spacing between these nodes, but also on how many nearest nodes are used in the approximation of the differential expression.

The trivial case is the 2-node difference where the difference equation at a particular node is the slope of the line connecting that node to either the node before or after it. In a 3-node difference scheme, the center node's derivative is traditionally approximated by the slope between its flanking nodes; this is correct only when the nodes are equally spaced. It can be shown that a 3-node approximation is accurate to second-order while the 2-node approximation is accurate to first-order, and using more nodes can further increase accuracy, while preserving the problem size (see Figure D.1). More generally, a 3-node approximation can be formulated to accommo-

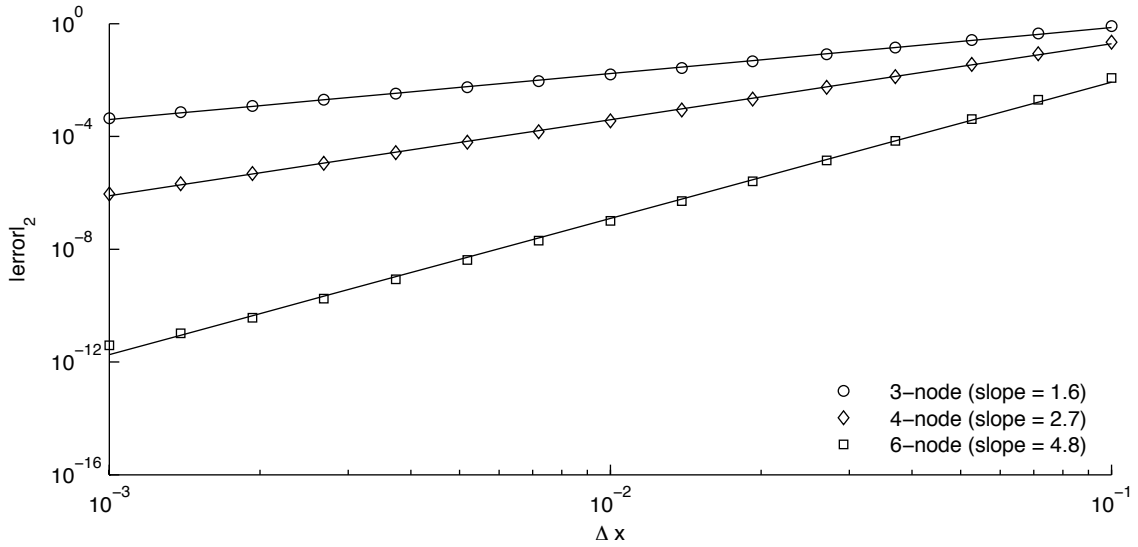

Figure D.1: Error of finite difference approximations with respect to node spacing for differentiating the function x^7. The slope of the relation (in log space) reflects the order of accuracy.

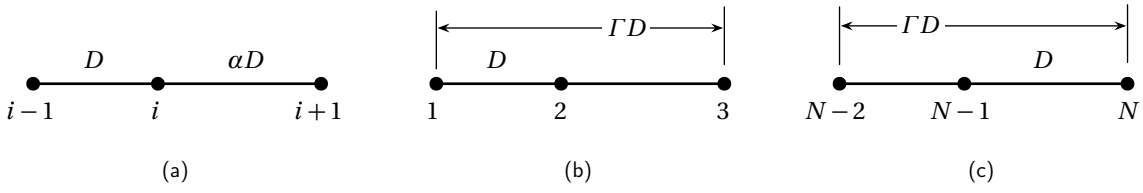

Figure D.2: Three consecutive nodes for use in formulating a finite difference approximation to $\mathrm{d}y/\mathrm{d}x$ at node i. Three distinct treatments: (a) internal, (b) first, and (c) last node.

date the possibility of uneven node spacing. The formulation can be thought of as the solution for the first order term in a set of Taylor series representations of the variable at the surrounding nodes, about the node at which the derivative is to be approximated. The Taylor series is truncated at an appropriate term to ensure accuracy to desired order. For the 3-node second order case, the derivative at y_i at node i (see Figure D.2a) can be obtained by writing the Taylor series expansion of y_{i-1} and y_{i+1} (using the prime notation for derivatives):

$$\begin{aligned} y_{i-1} &= y_i + (-D)y_i' + \frac{(-D)^2}{2}y_i'' + \text{H.O.T.} \\ y_{i+1} &= y_i + (\alpha D)y_i' + \frac{\alpha^2 D^2}{2}y_i'' + \text{H.O.T.} \end{aligned} \tag{D.1}$$

where α and αD represent the real spacings between the nodes. Ignoring the higher order terms denoted H.O.T. and writing the linear combination of the equations (such that the second order terms are eliminated) gives an approximation to the derivative at i accurate to second order:

$$y_{i+1} - \alpha^2 y_{i-1} \approx (1-\alpha^2)y_i + (\alpha^2 D + \alpha D)y_i'$$

or

$$y_i' \approx \frac{y_{i+1} - (1-\alpha^2)y_i - \alpha^2 y_{i-1}}{\alpha D(1+\alpha)} \tag{D.2}$$

Similarly, non-central difference equations can be formulated with the two consecutive nodes before or after the node of interest, as in the case of boundary nodes for which there are no "outside" nodes to use (see Figure D.2b,c); however these difference approximations seem to have a reduced accuracy. This process can presumably be continued for successively higher order accuracies by including more nodes, but the extension is not straightforward.

An equivalent but more generalizable approach is to recognize that this method is actually the same as differentiating the interpolating polynomial of degree $n-1$ (where n is the number of nodes used in the local approximation), and evaluating the derivative at the node of interest. For example, the Lagrange form the polynomial (in this case the most useful representation) can

be written

$$P(x) = \sum_{j=1}^{n} \left(y_j \prod_{l=1}^{n} \frac{x - x_l}{x_j - x_l} \right) \tag{D.3}$$

or, explicitly for the case of 3 nodes:

$$P(x) = \frac{x - x_2}{x_1 - x_2} \frac{x - x_3}{x_1 - x_3} y_1 + \frac{x - x_1}{x_2 - x_1} \frac{x - x_3}{x_2 - x_3} y_2 + \frac{x - x_1}{x_3 - x_1} \frac{x - x_2}{x_3 - x_2} y_3 \tag{D.4}$$

Then the finite differences at x_i can be obtained by evaluating the derivative $P'(x)$ at x_i. Just as the polynomial itself, the approximate derivatives can be expressed as a weighted sum, which is convenient for constructing the Jacobian in Newton's method.

$$y_i' \approx \sum_{j=i-k+1}^{i+n-k} a_j y_j \tag{D.5}$$

where $1 \leq k < n$ represents the local node at which the derivative is to be taken (for example in 3-node central differencing, $k = 2$ so that, $j = [i-1, i+1]$). The weighting coefficients a_j can take a general form for arbitrary j, k, and n in terms of x_j; the expression involves products, summations, and combinatorial terms. In practice, the conversion of these expressions into algorithms would be less efficient during computation than if the coefficients were computed explicitly on a case-by-case basis, namely for each of $k = \{1, 2, ..., n\}$ at each node i. For example, using 6-node differences ($n = 6$) and computing a "central-forward" difference ($k = 3$) at some internal node i (*i.e.* the i-th global node corresponds to the k-th local node):

$$a_{i-2} = \frac{(x_{i-1}-x_i)(x_i-x_{i+1})(x_i-x_{i+2})(x_i-x_{i+3})}{(x_{i-2}-x_{i-1})(x_{i-2}-x_i)(x_{i-2}-x_{i+1})(x_{i-2}-x_{i+2})(x_{i-2}-x_{i+3})} \tag{D.6}$$

$$a_{i-1} = \frac{(x_{i-2}-x_i)(x_i-x_{i+1})(x_i-x_{i+2})(x_i-x_{i+3})}{(x_{i-2}-x_{i-1})(x_{i-1}-x_i)(x_{i-1}-x_{i+1})(x_{i-1}-x_{i+2})(x_{i-1}-x_{i+3})} \tag{D.7}$$

$$a_i = \left(\frac{1}{x_{i-2}-x_i} + \frac{1}{x_{i-1}-x_i} - \frac{1}{x_i-x_{i+1}} - \frac{1}{x_i-x_{i+2}} + \frac{1}{x_i-x_{i+3}}\right) \tag{D.8}$$

$$a_{i+1} = \frac{(x_{i-2}-x_i)(x_{i-1}-x_i)(x_i-x_{i+2})(x_i-x_{i+3})}{(x_{i-2}-x_{i+1})(x_{i-1}-x_{i+1})(x_i-x_{i+1})(x_{i+1}-x_{i+2})(x_{i+1}-x_{i+3})} \tag{D.9}$$

$$a_{i+2} = \frac{(x_{i-2}-x_i)(x_{i-1}-x_i)(x_i-x_{i+1})(x_i-x_{i+3})}{(x_{i-2}-x_{i+2})(x_{i-1}-x_{i+2})(x_i-x_{i+2})(x_{i+1}-x_{i+2})(x_{i+2}-x_{i+3})} \tag{D.10}$$

$$a_{i+3} = -\frac{(x_{i-2}-x_i)(x_{i-1}-x_i)(x_i-x_{i+1})(x_i-x_{i+2})}{(x_{i-2}-x_{i+3})(x_{i-1}-x_{i+3})(x_i-x_{i+3})(x_{i+1}-x_{i+3})(x_{i+2}-x_{i+3})} \tag{D.11}$$

Usually, k will take a value central to the span of local nodes, *i.e. the* central local node for odd number of nodes. However, at the boundary nodes and those nodes close to the boundaries, the non-central k's must be used. It seems that the accuracy of finite differencing at non-central k's diminishes somewhat.

Thus, using 6-node differencing, the Equations 5.46 to 5.50 can be written for each node i after replacing the derivative terms by approximate difference terms (which in turn are a weighted summation of the variable at consecutive nodes)

$$0 = \left(\sum_{j=i-k+1}^{i+n-k} a_j q_j \right) - j_e \tag{D.12}$$

$$0 = \left(\sum_{j=i-k+1}^{i+n-k} a_j \kappa_j \right) - 3\frac{q_i}{\eta^3}\cos\phi_i + \gamma\cos(\phi_i + \beta) \tag{D.13}$$

$$0 = \left(\sum_{j=i-k+1}^{i+n-k} a_j \phi_j \right) - \gamma\kappa_i \tag{D.14}$$

$$0 = \left(\sum_{j=i-k+1}^{i+n-k} a_j \eta_j \right) - \sin\phi_i \tag{D.15}$$

$$0 = \left(\sum_{j=i-k+1}^{i+n-k} a_j \xi_j \right) - \cos\phi_i \qquad \text{for } i = 1,2,...,N-1,N \text{ and } k = 1,2,3,4,5,6 \tag{D.16}$$

where the values of a_j depend on i and k, *i.e.* exactly which points to use to locally approximate the derivative. For nodes 1, 2, and 3 it makes sense to use $k = 1,2,3$, and similarly for nodes $N-2$, $N-1$, and N, we use $k = 4,5,6$, respectively. For all other interior nodes, a choice may be made for using either $k = 3$ or $k = 4$; the choice may be made based on which end its boundary condition (the boundary condition containing at least the variable) is applied. For example the boundary condition $\eta_0 = 1$ is applied at s_0, so we may choose $k = 4$ to compute the difference equations for the i-th internal nodes for the terms containing $\frac{\mathrm{d}\eta}{\mathrm{d}s}$ to avoid over-emphasizing the value at s_0. This might not be important. The boundary conditions are applied by replacing some of the difference equations at the boundary to avoid over-specifying the problem. In discrete form, they are:

$$0 = q_1 - q_0 \tag{D.17}$$

$$0 = \kappa_N - \zeta_0 + \gamma \xi_N \cos\beta - \gamma(\eta_N - 1)\sin\beta \tag{D.18}$$

$$0 = 2 - \kappa_N - 2\sin(\phi_N + \beta) \tag{D.19}$$

$$0 = \eta_1 - 1 \tag{D.20}$$

$$0 = \xi_1 \tag{D.21}$$

A final note about this 6-node finite differencing formula is that it implicitly assumes the solution is very smooth across any 6 consecutive nodes; the interpolating polynomial must not oscillate, otherwise the interpolated slope may not reflect the actual slope. For the meniscus problem, this does not appear to be a problem, and the gain in accuracy (efficiency) is well worth the risk.

D.II Mesh density / node allocation

Overall accuracy and efficiency of the finite differences can be improved by selectively increasing and decreasing mesh density near regions of high and low gradients, respectively. By its nature, the static meniscus monotonically decreases in curvature, and its inclination (gradients in the profile) have well defined bounds. The inclusion of the rectilinear flow terms can only exacerbate the gradients.

Therefore, a straightforward lower limit on mesh density can be determined by a simple and fast accuracy sensitivity study on the strictly static meniscus. This limiting mesh density is appropriate for regions of the meniscus where flow terms are negligible compared to the hydrostatic terms, *i.e.* at large s. The accuracy can be characterized in terms of the change in the pinning point curvature κ_0 at the converged solution, with respect to mesh density (uniform density), as shown in Figure D.3 for various length scale ratios γ and inclination angles β. As suggested in Figure D.3, there is no additional gain in accuracy beyond about $\gamma\Delta s < 2.5 \times 10^{-3}$; for the solution of any meniscus profile, the minimum mesh density can be prescribed as such.

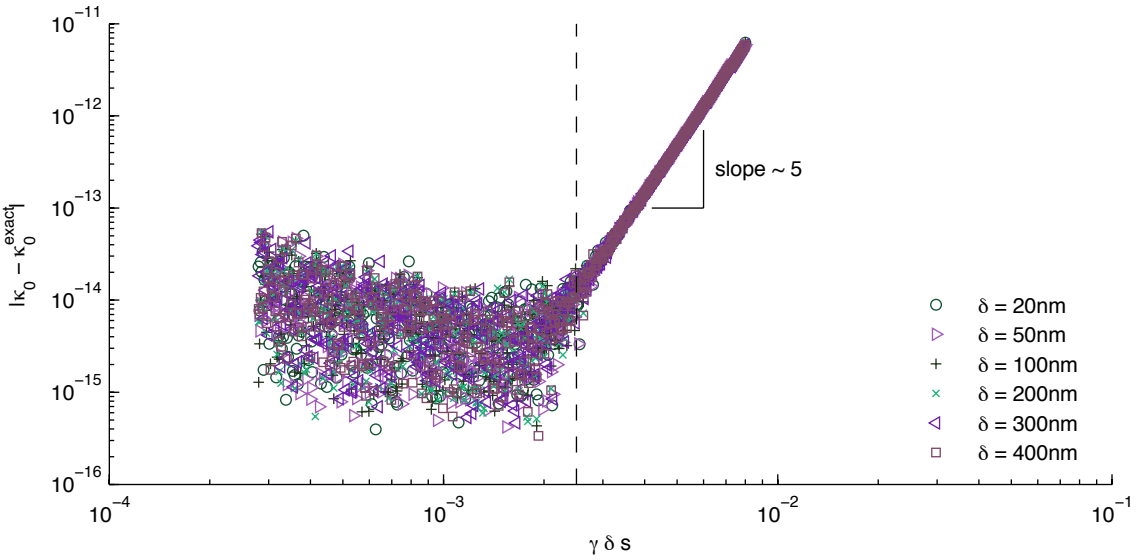

Figure D.3: Accuracy of the finite difference solution to the static meniscus profile with respect to mesh density on a uniform mesh. For low mesh densities, the slope of the error in log space is approximately 5, affirming the order of accuracy of 6-node finite differences. Beyond a mesh density of $\gamma \Delta s \approx 2.5 \times 10^{-3}$ (dashed line), no added accuracy is gained.

When the problem involves flow terms, the gradients will become stronger, particularly near the pinning point (high curvature) and constrictions (high curvature gradients), so that the mesh density should be increased there. Without quantitatively optimizing the mesh density (which requires *a priori* knowledge of the solution), accuracy can still be improved by prescribing either a monotonically decreasing mesh density from $s = 0$ to $s = s_n$ (in the case of non-constricting menisci) or prescribing a two-region mesh in which the mesh density of the first region increases from $s = 0$ to the constriction and that of the second region decreases from the constriction to $s = s_n$. Such meshes can be generated algebraically using the hyperbolic tangent function (see Equations D.22 and D.23), as described by Vinokur (1983).

$$\frac{s(i/N)}{s_n} = 1 + \frac{\tanh\left[\mathscr{A}\left(\frac{i}{N} - 1\right)\right]}{\tanh \mathscr{A}} \qquad i = 0, 1, \cdots, N \qquad \text{(left-accumulated)} \qquad \text{(D.22)}$$

$$\frac{s(i/N)}{s_n} = \frac{\tanh\left[\mathscr{A}\left(\frac{i}{N}\right)\right]}{\tanh \mathscr{A}} \qquad i = 0, 1, \cdots, N \qquad \text{(right-accumulated)} \qquad \text{(D.23)}$$

In fact, in resolving the substrate hump, a reasonably good mesh can be constructed by splicing together a series of left- and right- accumulated mesh fragments according to Equations D.22 and D.23. This scheme has several caveats, including the first obvious one, which is that the mesh density profile is not optimal because it is prescribed without regard for the actual gradient profiles in the solution. Second, the high mesh densities necessary to resolve the substrate hump may be overkill, unnecessarily introducing high *mesh density gradients*, which may adversely affect numerical accuracy despite better resolution. Third, whether or not the previous is the case, the act of subdomain splicing itself destroys the smoothness of the stretching functions, possibly affecting the numerical accuracy. In general, the mesh can be smoothed after splicing.

While the lower limit on mesh density can safely be assumed as $\gamma\Delta s < 2.5\times10^{-3}$ as in the case of a static meniscus, an estimate of the mesh density in high-curvature regions can be obtained by a rough sensitivity study at a variety of conditions on meniscus stretch and flow rates. One such study would be to set up two-part spliced meshes based on the constriction of static meniscus, varying the mesh density at the constriction. This can be done at various z_0 to sample a range of degrees of constriction, and at the turning point flow rate for the "worst case". Such a sensitivity study is summarized in Figure D.4, where the accuracy dependency is separated to clarify the "kink" in sensitivity. The results for several values of δ (*i.e.* γ) are in Figure D.5, each grouping representing a non-separated version of Figure D.4.

Resolving the substrate hump presents some practical challenges. Because the problem is solved on the arclength dimension s rather than the spatial dimension along the substrate x, the domain mesh must anticipate the solution $x(s)$ in order to correctly capture the topology (because the h_B is defined in terms of x).

Specifically, the problem is solved twice during the continuation on ξ_p; the first solution is based on a mesh that anticipates the location of the particle based on the previous solution (the first order predictor solution), and the second solution is determined using the mesh generated based on the first solution. This two-step solution does not guarantee that the mesh is based on the exact location of the converged solution of ξ_p because the mesh may affect its converged value (so that ξ_p from the first solution may not be strictly accurate). Nevertheless, the solutions

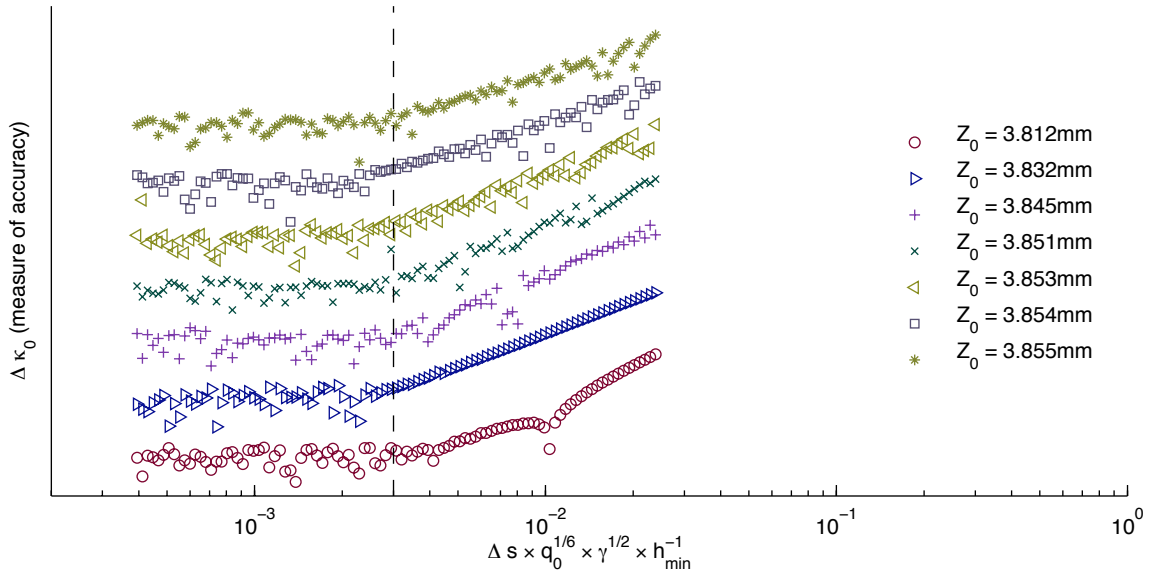

Figure D.4: Accuracy of finite difference solutions for menisci with flow.

should be practically acceptable after the second solution.

The refined meshes discussed above are generated by the following steps. First, the meniscus profile is inverted to obtain the position of the particle s_p in s-space. The position of the particle s_p is then used to refine the mesh on an interval of $[s_p - 1, s_p + 1]$, using a mesh density sufficient to capture the shape of the particle, *viz.* η_B as given by Figure 5.3. This refined portion of the domain is then spliced into the original domain by the following. On the splicing region to the left of the particle, a buffer interval of a length some fraction of s_p, for example 10 %, is used to gradually expand the spacing from the refined density to the original density; this is necessary to avoid a step change in mesh density from the "particle" interval to the original mesh. On the right of the particle, the mesh can simply be redefined to expand in spacing gradually from the refined density to the maximum spacing as determined from Figure D.3.

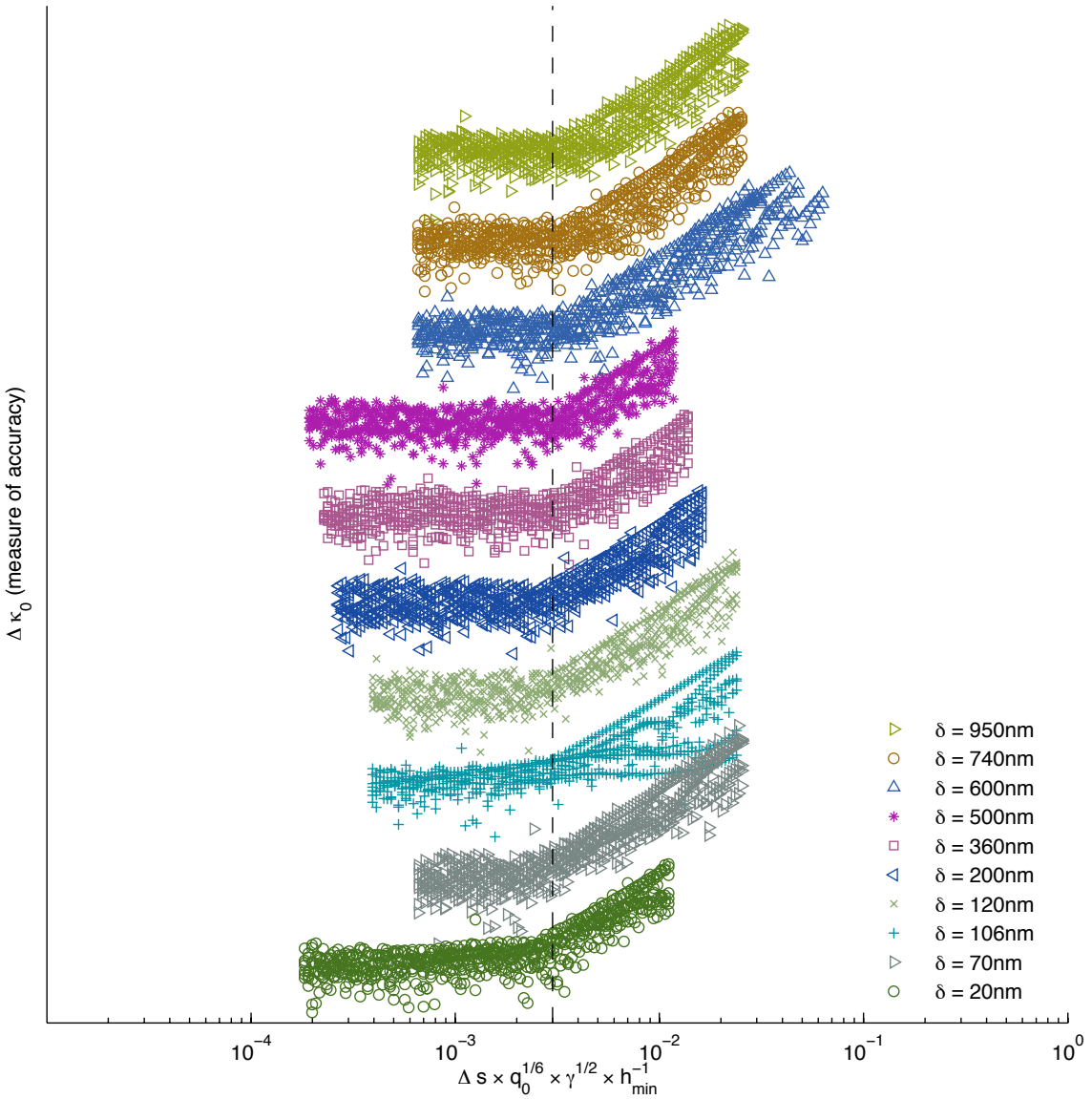

Figure D.5: Accuracy of finite difference solutions for menisci with flow.

D.III Newton's method with continuation

The governing equations in § 5.2.5 (Equations D.12 to D.21) represent $5N$ nonlinear algebraic equations, which are composed of finite difference approximations to the governing equations at most of the nodes, and boundary conditions at the rest. They must be solved simultaneously, and because they are nonlinear, they must be solved iteratively. The well-known Newton's method for solving nonlinear equations is based upon the successive zeroing of the Taylor series approximation to the equation(s) at the current iterate (guess), and is quite efficient for guesses sufficiently near the true solution. Briefly, if the system is represented as the vector equation

$$\mathbf{r}(\mathbf{u}, s\ ;\ \zeta_0, q_0, \xi_p) = \mathbf{0} \tag{D.24}$$

the equation can be solved by starting at some initial guess solution $\mathbf{u}^k$ and successively solving

$$\mathbf{J}^{(k)} \cdot (\mathbf{u}^{(k+1)} - \mathbf{u}^{(k)}) = -\mathbf{r}(\mathbf{u}^k, s\ ;\ \zeta_0, q_0, \xi_p) \tag{D.25}$$

which gives $\mathbf{u}^{(k)}$ as a root of the linearized (Taylor series) approximation of $\mathbf{r}$ about the current iterate $\mathbf{u}^{(k)}$, so that the Jacobian $\mathbf{J}^{(k)}$ represents the gradient of the residual function along the solution $\mathbf{u}^{(k)}$, *i.e.* the coefficient of the first order term in the Taylor series:

$$\mathbf{J}^{(k)} \equiv \left.\frac{\partial \mathbf{r}}{\partial \mathbf{u}}\right|_{\mathbf{u}^{(k)}} \tag{D.26}$$

The solution has converged when the final solution, $\mathbf{u}^{(f)}$, satisfies either or both of the criteria

$$\left|\left|\mathbf{u}^{(f)} - \mathbf{u}^{(f-1)}\right|\right|_2 \leq \text{tolerance} \tag{D.27}$$

$$\left|\left|\mathbf{r}(\mathbf{u}^{(f)}\ ;\ \zeta_0, q_0, \xi_p)\right|\right|_2 \leq \text{tolerance} \tag{D.28}$$

For efficient solution of the problem along the entire range of parameters, continuation methods can be employed to provide successive initial guesses of solutions at extrapolated parameter values; in the simplest case, the solution for the desired parameter (generically λ) value can be

seeded by the solution at a parameter value reasonably close to the desired one,

$$\mathbf{u}^{(0)}(s\ ;\ (\lambda+\delta\lambda)) = \mathbf{u}^{(f)}(s\ ;\ \lambda) \tag{D.29}$$

The preceding scheme is commonly designated the zeroth order continuation, but a much better scheme is to use a so-called first order continuation, in which a better guess can be made by extrapolating the solution using local information about how the solution changes with the parameter

$$\mathbf{u}^{(0)}(s\ ;\ (\lambda+\delta\lambda)) = \mathbf{u}^{(f)}(s\ ;\ \lambda) + \left.\frac{\partial \mathbf{u}}{\partial \lambda}\right|_{\mathbf{u}^{(f)},\lambda} \cdot \delta\lambda \tag{D.30}$$

This solution sensitivity with respect to the parameter can be obtained essentially for free based on the Jacobian at the final solution at the previous λ, *viz.*

$$\left.\frac{\partial \mathbf{r}}{\partial \mathbf{u}}\right|_{\mathbf{u}^{(f)},\lambda} \left.\frac{\partial \mathbf{u}}{\partial \lambda}\right|_{\mathbf{u}^{(f)},\lambda} = -\left.\frac{\partial \mathbf{r}}{\partial \lambda}\right|_{\lambda} \tag{D.31}$$

where the residual's gradient with respect to the parameter (right hand side) is usually trivial to determine, especially in the case of the meniscus problem as posed here. On the other hand, as alluded to in the results, a solution is not guaranteed to exist over all λ, in which case it is desirable to determine the limiting value of the parameter, $\lambda_{\text{critical}}$. More generally, the solution path may be afflicted by critical points (as for the parameters Q_0 and z_0), at which the Jacobian is singular (near to the critical points, the Jacobian is ill-conditioned), precluding the applicability of Newton's method and the first order continuation scheme. To circumvent this issue, the system of equations can be modified by treating the parameter in question as part of the unknown solution; the set of unknowns becomes augmented according to

$$\mathbf{U} \equiv \begin{bmatrix} \mathbf{u} \\ \lambda \end{bmatrix} \tag{D.32}$$

Thus, the residual equations will need to be augmented with an additional equation, and introducing a new independent variable v, or arclength along the solution path (hence such methods are called pseudo arclength continuation methods):

$$\mathbf{R}(\mathbf{U}\ ;\ \mathrm{v}) \equiv \begin{bmatrix} \mathbf{r}(\mathbf{U}) \\ f(\mathbf{U}\ ;\ \mathrm{v}) \end{bmatrix} \tag{D.33}$$

where the augmenting equation $f(\mathbf{U}\ ;\ \mathrm{v})$ is a scalar equation relating the step length along v (instead of along λ) to estimates of the corresponding step lengths in the λ and $\mathbf{u}$ dimensions. The augmented system is robust to the presence of critical points in the solution path because the augmenting equation prevents the Jacobian from becoming singular at the critical points in λ; the augmented Jacobian is

$$\frac{\partial \mathbf{R}}{\partial \mathbf{U}} = \begin{bmatrix} \frac{\partial \mathbf{r}}{\partial \mathbf{u}} & \frac{\partial \mathbf{r}}{\partial \lambda} \\ \frac{\partial f}{\partial \mathbf{u}}^{\mathrm{T}} & \frac{\partial f}{\partial \lambda} \end{bmatrix} \tag{D.34}$$

Several kinds of augmenting equations f can be chosen; perhaps the most intuitive version states that $\mathbf{U}_2 = [\mathbf{u}_2\ ;\ \lambda_2]$ lies on a circle centered about the previous solution (subscripts denoting successive solutions in the continuation, not the index isolating the nodal value of the solution vector)

$$f_{\text{circle}} = \left|\left|\mathbf{u}_2^{(k)} - \mathbf{u}_1\right|\right|^2 + \left|\lambda_2^{(k)} - \lambda_1\right|^2 - |\Delta \mathrm{v}|^2 \tag{D.35}$$

Although easy to imagine, this condition is not as convenient as the following, in which the next solution intersects the solution path with the tangent of the previously considered circle at the initial guess according to the first order predictor (see Figure D.6)

$$\begin{aligned} f_{\text{linear}} &= \left.\frac{\partial \mathbf{u}}{\partial \mathrm{v}}\right|_1^{\mathrm{T}} \cdot \left(\mathbf{u}_2^{(k)} - \mathbf{u}_1\right) + \left.\frac{\partial \lambda}{\partial \mathrm{v}}\right|_1 \cdot \left(\lambda_2^{(k)} - \lambda_1\right) - \Delta \mathrm{v} \\ &= \left.\frac{\partial \mathbf{U}}{\partial \mathrm{v}}\right|_1^{\mathrm{T}} \cdot \left(\mathbf{U}_2^{(k)} - \mathbf{U}_1\right) - \Delta \mathrm{v} \end{aligned} \tag{D.36}$$

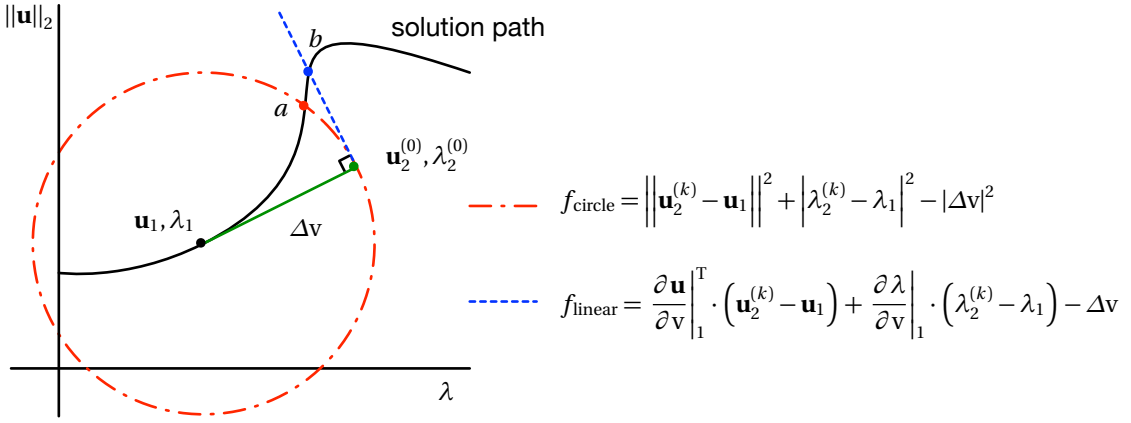

Figure D.6: Graphical representation of pseudo arclength continuation. The solution path is in the $||\mathbf{u}||_2$-λ plane, but the continuation proceeds in the v-direction *on* the solution path. Two possible augmenting conditions are shown, which converge to different solutions a and b on the path.

the utility of which is apparent when the derivatives $\frac{\partial f}{\partial \mathbf{u}}$ and $\frac{\partial f}{\partial \lambda}$ are computed for the augmented Jacobian. Specifically, it can be seen easily that the respective derivatives are simply

$$\frac{\partial f}{\partial \mathbf{u}} = \left.\frac{\partial \mathbf{u}}{\partial \mathrm{v}}\right|_1 \tag{D.37}$$

$$\frac{\partial f}{\partial \lambda} = \left.\frac{\partial \lambda}{\partial \mathrm{v}}\right|_1 \tag{D.38}$$

The right hand sides of the above equations can be evaluated from the solution's sensitivity to the parameter, which was evaluated from the Jacobian when constructing the first order predictor:

$$\left.\frac{\partial \lambda}{\partial \mathrm{v}}\right|_1 = \pm \left(1 + \left|\left|\left.\frac{\partial \mathbf{u}}{\partial \lambda}\right|_1\right|\right|^2\right)^{-1/2} \tag{D.39}$$

$$\left.\frac{\partial \mathbf{u}}{\partial \mathrm{v}}\right|_1 = \left.\frac{\partial \lambda}{\partial \mathrm{v}}\right|_1 \left.\frac{\partial \mathbf{u}}{\partial \lambda}\right|_1 \tag{D.40}$$

where the sign is chosen to ensure the continuation occurs always in increasing $\mathbf{r}$, namely so that

given two prior solutions

$$\left.\frac{\partial \mathbf{u}}{\partial \mathrm{v}}\right|_1 \cdot (\mathbf{u}_1 - \mathbf{u}_0) + \left.\frac{\partial \lambda}{\partial \mathrm{v}}\right|_1 \cdot (\lambda_1 - \lambda_0) > 0 \tag{D.41}$$

One computational issue is that of destroying the sparse structure of the Jacobian (banded intrinsically due to the finite differencing and ensured by a practical book-keeping scheme) with the augmenting equation, which generally involves all of the nodal solutions so that the Jacobian takes on an arrowhead structure. Whether or not this is problematic for robust or non-optimized linear solvers, the issue can be circumvented (*i.e.* the inversion may be restricted to that of a banded Jacobian) using a bordering algorithm (Keller, 1977), which is basically a block elimination method and can be summarized as:
Solve for $\mathbf{Z}$ and $\mathbf{w}$ in

$$\frac{\partial \mathbf{r}}{\partial \mathbf{u}} \cdot \mathbf{Z} = \frac{\partial \mathbf{r}}{\lambda} \tag{D.42}$$

$$\frac{\partial \mathbf{r}}{\partial \mathbf{u}} \cdot \mathbf{w} = -\mathbf{r} \tag{D.43}$$

Solve for $\delta\lambda$ in

$$\left(\frac{\partial f}{\partial \lambda} - \frac{\partial f}{\partial \mathbf{u}^{\mathrm{T}} \cdot \mathbf{Z}}\right) \cdot \delta\lambda = \left(-f - \frac{\partial f}{\partial \mathbf{u}}^{\mathrm{T}} \cdot \mathbf{w}\right) \tag{D.44}$$

And finally compute $\delta\mathbf{u}$ as

$$\delta\mathbf{u} = \mathbf{w} - \delta\lambda\mathbf{Z} \tag{D.45}$$

D.IV Determining the turning point

As discussed in the results, the solution shows a turning point with respect to at least the parameters ζ_0 and q_0. While the pseudo arclength continuation method allows uninterrupted solution along the solution path, it is not enough to determine the turning point solution itself. Although

an additional augmentation of the equations can be constructed (from considering characteristics of the solution there) to determine the turning point solution, a simpler approach based on the simple nature of a turning point (relative to other kinds of critical points) is used here. Specifically, the turning point topology is amenable to treating the problem as a minimization problem, and since the turning point solution must always be approached from some previous solution anyway, we can be guaranteed to bracket the turning point by pseudo arclength continuation.

Although the discussion in Appendix D.III remained fairly general, we now ground the discussion by characterizing the solution $\mathbf{u}$ by some metric. In general, the solution can be represented by the 2-norm $||\mathbf{u}||_2$, but when considering the turning points on ζ_0 and q_0, an intuitive choice is to select the pinning point curvature because it seems to represent both the strength of flow and the stretch at a physically intuitive location. In other words, we abandon consideration of the entire solution $\mathbf{u}$ in favor of one component of it, specifically the pinning point curvature κ_0. This allows us to pose the problem as a minimization of λ with respect to κ_0.

Posed as a minimization problem with the availability of at least 3 solutions (obtained by pseudo arclength continuation) that bracket the turning point, a simple choice of method is that of Brent, which combines the robustness of a golden section search and the high convergence properties of inverse parabolic interpolation to successively shrink the bracket and close in on the turning point solution.

An important caveat is that we do not have control over the *actual* step size in κ_0, but rather only a *rough* idea of it based on a step size δv that we do control in the solution path arclength $\mathbf{r}$. Consequently, the minimization cannot converge as rapidly because our actual steps in κ_0 are neither optimal (in the case of a golden section bisection) nor exactly at the minimum of the interpolating parabola. In fact, the solution after the continuation step, although target to be within the bracketing triplet, is not guaranteed to be so, probably because of the numerical error in the solution sensitivity obtained during Newton's method (namely the vector $\frac{\partial \mathbf{u}}{\partial c}$).

D.V Determining the critical approach of the next particle

For the turning point in the solution path ξ_p, the problem is exacerbated by the requirement of adjusting the mesh to sufficiently resolve both the gradients in the equations *and* the shape of the substrate topology (the hump), although in the cases where the hump is sufficiently close to the meniscus surface, both requirements are equivalent. The issue is a practical one, since it can be circumvented by fixing a uniform mesh with the lowest required mesh spacing, but for these problems, such a mesh is prohibitive for solution on a personal computer.

When meshes are adjusted between continuation steps, the pseudo arclength continuation method, which requires information about solution sensitivity at every node (in this case $\frac{\partial \mathbf{u}}{\partial \xi_p}$), must be extended to interpolate the necessary information across disparate meshes, as it is relevant to each task within the method.

Bibliography

Abkarian M., Nunes J., and Stone H. A. (2004) Colloidal crystallization and banding in a cylindrical geometry. *Journal of the American Chemical Society* **126** [No. 19] 5978–5979.

Adachi E., Dimitrov A. S., and Nagayama K. (1995) Stripe patterns formed on glass surface during droplet evaporation. *Langmuir* **11** [No. 4] 1057–1060.

Adachi E., Dimitrov A. S., and Nagayama K. (2006) Stripe patterns formed in particle films: Cause and remedy. *Film Formation in Waterborne Coatings* **648** 418–428.

Adamczyk Z. (2003) Particle adsorption and deposition: role of electrostatic interactions. *Advances in Colloid and Interface Science* **100–102** 267–347.

Barrer R. M. and Sieber W. (1977) Hydrothermal chemistry of silicates. part 21. zeolites from reaction of lithium and caesium ions with tetramethylammonium aluminosilicate solutions. *Journal of the Chemical Society Dalton Transactions* **10** 1020–1025.

Bein T. (1996) Synthesis and applications of molecular sieve layers and membranes. *Chemistry of Materials* **8** [No. 8] 1636–1653.

Bertrand P., Jonas A., Laschewsky A., and Legras R. (2000) Ultrathin polymer coatings by complexation of polyelectrolytes at interfaces: suitable materials, structure and properties. *Macromolecular Rapid Communications* **21** [No. 7] 319–348.

Bolstad J. H. and Keller H. B. (1986) A multigrid continuation method for elliptic problems with folds. *SIAM Journal of Scientific Statistical Computing* **7** 1081–1104.

Boudreau L. and Tsapatsis M. (1997) A highly oriented thin film of zeolite a. *Chemistry of Materials* **9** 1705.

Boudreau L., Kuck J., and Tsapatsis M. (1999) Deposition of oriented zeolite a films: in situ and secondary growth. *Journal of Membrane Science* **152** 41–59.

Brewer D. D., Allen J., Miller M. R., Santos J. M. D., Kumar S., Norris D. J., Tsapatsis M., and Scriven L. E. (2008) Mechanistic principles of colloidal crystal growth by evaporation-induced convective steering. *Langmuir* **24** [No. 23] 13683–13693.

Bruce W. M. Process of making zeolites. Patent Permutit Company New York (1933).

Caro J. and Noack M. (2008) Zeolite membranes - recent developments and progress. *Microporous and Mesoporous Materials* **115** 215–233.

Choi J., Jeong H.-K., Snyder M. A., Stoeger J. A., Masel R. I., and Tsapatsis M. (2009) Grain boundary defect elimination in a zeolite membrane by rapid thermal processing. *Science* **325** 590–593.

Choi S. Y., Lee Y. J., Park Y. S., Ha K., and Yoon K. B. (2000) Monolayer assembly of zeolite crystals and glass with fullerene as the covalent linker. *Journal of the American Chemical Society* **122** [No. 21] 5201–5209.

Christodoulou K. N. *Computational physics of slide coating flow*. PhD thesis University of Minnesota (1990).

Chun Y. S., Ha K., Lee Y.-J., Kim H. S., Park Y. S., and Yoon K. B. (2002) Diisocyanates as novel molecular binders for monolayer assembly of zeolite crystals on glass. *Chemical Communications* pages 1846–1847.

Ciric J. Zsm-2 zeolite and preparation thereof. Patent Mobil Oil Corporation Glassoboro, NJ (1968).

Corma A., Fornés V., Martínez-Triguero J., and Pergher S. B. (1999) Delaminated zeolites: Combining the benefits of zeolites and mesoporous materials for catalytic uses. *Journal of Catalysis* **186** [No. 1] 57–63.

Covarrubias C., Garcia R., Arriagada R., Yanez J., Ramanan H., Lai Z., and Tsapatsis M. (2008) Removal of trivalent chromium contaminant from aqueous media using FAU-type zeolite membranes. *Journal of Membrane Science* **312** [No. 1-2] 163–173.

Davis T. M., Snyder M. A., Krohn J. E., and Tsapatsis M. (2006) Nanoparticles in lysine-silica sols. *Chemistry of Materials* **18** [No. 25] 5814–5816.

Denkov N. D., Velev O. D., Kralchevsky P. A., Ivanov I. B., Yoshimura H., and Nagayama K. (1992) Mechanism of formation of two-dimensional crystals from latex particles on substrates. *Langmuir* **8** [No. 12] 3183–3190.

Dimitrov A. S. and Nagayama K. (1995) Steady-state unidirectional convective assembling of fine particles into two-dimensional arrays. *Chemical Physics Letters* **243** 462–468.

Dimitrov A. S. and Nagayama K. (1996) Continuous convective assembling of fine particles into two-dimensional arrays on solid surfaces. *Langmuir* **12** [No. 5] 1303–1311.

Dryden H. L., Murnaghan F. D., and Bateman H. (1932). *Comm. Hydrodyn. Bull.* **84** 197–201.

Fan F. and Stebe K. (2004) Assembly of colloidal particles by evaporation on surfaces with patterned hydrophobicity. *Langmuir* **20** [No. 8] 3062–3067.

Fowles G. R. *Introduction to Modern Optics*. Dover Publications New York 2 edition (1989).

Fukada Y., Nagarjan N., Mekky W., Bao Y., and Kim H. (2004) Electrophoretic deposition–mechanisms, myths and materials. *Journal of Materials Science* **39** 787–801.

Gasperino D., Meng L., Norris D. J., and Derby J. J. (2008) The role of fluid flow and convective steering during the assembly of colloidal crystals. *Journal of Crystal Growth* **310** [No. 1] 131–139.

Geus E. R., van Bekkum H., Bakker W. J. W., and Moulijn J. A. (1993) High-temperature stainless steel supported zeolite (mfi) membranes: Preparation, module construction, and permeation experiments. *Microporous Materials* **1** 131–147.

Ghosh M., Fan F., and Stebe K. J. (2007) Spontaneous pattern formation by dip coating of colloidal suspensions on homogeneous surfaces. *Langmuir* **23** [No. 4] 2180–2183.

Gleiche M., Chi L., and Fuchs H. (2000) Nanoscopic channel lattices with controlled anisotropic wetting. *Nature* **403** 173–175.

Griewank A. and Reddien G. W. (1984) Characterization and computation of generalized turning points. *SIAM Journal on Numerical Analysis* **21** [No. 1] 176–185.

Gu Z.-Z., Fujishima A., and Sato O. (2002) Fabrication of high-quality opal films with controllable thickness. *Chemistry of Materials* **14** [No. 2] 760–765.

Ha K., Lee Y.-J., Lee H. J., and Yoon K. B. (2000) Facile assembly of zeolite monolayers on glass, silica, alumina, and other zeolites using 3-halopropylsilyl reagents and covalent linkers. *Advanced Materials* **12** [No. 15] 1114–1117.

Ha K., Seonpark J., Sunoh K., Zhou Y., Sungchun Y., Lee Y., and Yoon K. (2004) Aligned monolayer assembly of zeolite crystals on platinum, gold, and indium–tin oxide surfaces with molecular linkages. *Microporous and Mesoporous Materials* **72** [No. 1-3] 91–98.

Hartlen K. D., Athanasopoulos A. P. T., and Kitaev V. (2008) Facile preparation of highly monodisperse small silica spheres (15 to >200 nm) suitable for colloidal templating and formation of ordered arrays. *Langmuir* **24** [No. 5] 1714–1720.

Hattori H. (2001) Anti-reflection surface with particle coating deposited by electrostatic attraction. *Advanced Materials* **13** [No. 1] 51–54.

Hosein I. D. and Liddell C. M. (2007a) Convectively assembled nonspherical mushroom cap-based colloidal crystals. *Langmuir* **23** 8810–8814.

Hosein I. D. and Liddell C. M. (2007b) Convectively assembled asymmetric dimer-based colloidal crystals. *Langmuir* **23** [No. 21] 10479–10485.

Huang J., Kim F., Tao A. R., Connor S., and Yang P. (2005) Spontaneous formation of nanoparticle stripe patterns through dewetting. *Nature Materials* **4** 896–900.

Jiang P., Bertone J. F., Hwang K. S., and Colvin V. L. (1999) Single-crystal colloidal multilayers of controlled thickness. *Chemistry of Materials* **11** [No. 8] 2132–2140.

Karakurt I., Leiderer P., and Boneberg J. (2006) Size-dependent self-organization of colloidal particles on chemically patterned surfaces. *Langmuir* **22** [No. 6] 2415–2417.

Ke C., Yang W. L., Ni Z., Wang Y. J., Tang Y., Gu Y., and Gao Z. (2001) Electrophoretic assembly of nanozeolites: zeolite coated fibers and hollow zeolite fibers. *Chemical Communications* **2001** [No. 8] 783–784.

Keller H. B. *Numerical solution of bifurcation and nonlinear eigenvalue problems* pages 45–52. Dekker New York (1977).

Kistler S. F. and Schweizer P. M. *Liquid Film Coating* chapter Free-meniscus coating processes. Chapman Hall London (1997).

Koh Y., Yip C., Chiang Y., and Wong C. (2008) Kinetic stages of single-component colloidal crystallization. *Langmuir* **24** [No. 10] 5245–5248.

Kralchevsky P., Denkov N., and Danov K. (2001) Particles with an undulated contact line at a fluid interface: Interaction between capillary quadrupoles and rheology of particulate monolayers. *Langmuir* **17** [No. 24] 7694–7705.

Kralchevsky P. A. and Nagayama K. (1994) Capillary forces between colloidal particles. *Langmuir* **10** [No. 1] 23–36.

Kulak A., Lee Y.-J., Park Y. S., and Yoon K. B. (2000a) Orientation-controlled monolayer assembly of zeolite crystals on glass and mica by covalent linkage of surface-bound epoxide and amine groups. *Angewandte Chemie International Edition* **39** [No. 5] 950–953.

Kulak A., Park Y. S., Lee Y.-J., Chun Y. S., Ha K., and Yoon K. B. (2000b) Polyamines as strong molecular linkers for monolayer assembly of zeolite crystals on flat and curved glass. *Journal of the American Chemical Society* **122** [No. 38] 9308–9309.

Lai Z., Bonilla G., Diaz I., Nery J. G., Sujaoti K., Amat M. A., Kokkoli E., Trasaki O., Thompson R. W., Tsapatsis M., and Vlachos D. G. (2003) Microstructural optimization of a zeolite membrane for organic vapor separation. *Science* **300** 456–460.

Lallet F. and Olivi-Tran N. (2006) Micrometer-sized particles in a two-dimensional self-assembly during drying of liquid film. *Physical Review E* **74** [No. 6] 061401.

Landau L. and Levich L. (1942) Dragging of a liquid by a moving plate. *Acta Physicochemica U.R.S.S* **XVII** [No. 1-2] 42–54.

Lee G. S., Lee Y.-J., Ha K., and Yoon K. B. (2000) Orientation-controlled monolayer assembly of zeolite crystals on glass using terephthaldicarboxaldehyde as a covalent linker. *Tetrahedron* **56** 6965–6968.

Lee J. A., Meng L., Norris D. J., Scriven L. E., and Tsapatsis M. (2006) Colloidal crystal layers of hexagonal nanoplates by convective assembly. *Langmuir* **22** [No. 12] 5217–5219.

Lee J. A., Reibel K., Snyder M. A., Scriven L. E., and Tsapatsis M. (2009) Geometric model describing the banded morphology of particle films formed by convective assembly. *Chemphyschem* **10** [No. 12] 2116–2122.

Lee Y., Lee J., and Yoon K. (2005) Synthesis of long zeolite-L crystals with flat facets. *Microporous and Mesoporous Materials* **80** [No. 1-3] 237–246.

Loudet J., Alsayed A., Zhang J., and Yodh A. (2005) Capillary interactions between anisotropic colloidal particles. *Physical Review Letters* **94** [No. 1] 018301.

Lovallo M. C. and Tsapatsis M. (1996a) Preparation of an asymmetric zeolite L film. *Chemistry of Materials* **8** [No. 8] 1579–1583.

Lovallo M. C. and Tsapatsis M. (1996b) Preferentially oriented submicron silicalite membranes. *AIChE Journal* **42** [No. 11] 3020–3029.

Maheshwari S., Gettel M., lee J. A., Sanchez C.-M., Bates F. S., Corma A., Koros W. J., and Tsapatsis M. (2010) Highly crystalline zeolite nanosheets and their coatings for various applications. *(in preparation)*.

Malaquin L., Kraus T., Schmid H., Delamarche E., and Wolf H. (2007) Controlled particle placement through convective and capillary assembly. *Langmuir* **23** [No. 23] 11513–11521.

Masuda Y., Itoh T., Itoh M., and Koumoto K. (2004) Self-assembly patterning of colloidal crystals constructed from opal structure of NaCl structure. *Langmuir* **20** [No. 13] 5588–5592.

Meng L. *Microscopic examination of the growth of thin silica colloidal crystals formed by convective assembly*. PhD thesis University of Minnesota (2008).

Meng L., Wei H., Nagel A., Wiley B. J., Scriven L. E., and Norris D. J. (2006) The role of thickness transitions in convective assembly. *Nano Letters* **6** [No. 10] 2249–2253.

Nikolakis V., Xomeritakis G., Abibi A., Dickson M., Tsapatsis M., and Vlachos D. G. (2001) Growth of a faujasite-type zeolite membrane and its application in the separation of saturate/unsaturated hydrocarbon mixtures. *Journal of Membrane Science* **184** 209–219.

Norris D. J., Arlinghaus E. G., Meng L., Heiny R., and Scriven L. E. (2004) Opaline photonic crystals: How does self-assembly work? *Advanced Materials* **16** [No. 16] 1393–1399.

Picard G. (1998) Fine particle monolayers made by a mobile dynamic think laminar flow (DTLF) device. *Langmuir* **14** [No. 13] 3710–3715.

Pieranski P. (1983) Colloidal crystals. *Contemporary Physiscs* **24** [No. 1] 25–73.

Ponisch G. and Schwetlick H. (1981) Computing turning points of curves implicitly defined by nonlinear equations depending on a parameter. *Computing* **26** 107–121.

Press W. H., Teukolsky S. A., Vetterling W. T., and Flannery B. P. *Numerical Recipes in C*. Cambridge University Press New York 3 edition (1993).

Prevo B., Kuncicky D., and Velev O. (2007) Engineered deposition of coatings from nano-and micro-particles: A brief review of convective assembly at high volume fraction. *Colloids and Surfaces A* **311** 2–10.

Prevo B. G. and Velev O. D. (2004) Controlled, rapid deposition of structured coatings from micro- and nanoparticle suspensions. *Langmuir* **20** [No. 6] 2099–2107.

Prevo B. G., a Yeon Hwang , and Velev O. D. (2005a) Convective assembly of antireflective silica coatings with controlled thickness and refractive index. *Chemistry of Materials* **17** [No. 14] 3642–3651.

Prevo B. G., Fuller J. C., and Velev O. D. (2005b) Rapid deposition of gold nanoparticle films with controlled thickness and structure by convective assembly. *Chemistry of Materials* **17** [No. 1] 28–35.

Ray M. A., Kim H., and Jia L. (2005) Dynamic self-assembly of polymer colloids to form linear patterns. *Langmuir* **21** [No. 11] 4786–4789.

Ruschak K. J. (1978) Flow of a falling film into a pool. *AIChE Journal* **24** [No. 4] 705–708.

Schoeman B. J., Sterte J., and Otterstedt J.-E. (1995) Synthesis of colloidal suspensions of zeolite ZSM-2. *Journal of Colloid and Interface Science* **170** 449–456.

Shan W., Zhang Y., Yang W., Ke C., Gao Z., Ye Y., and Tang Y. (2004) Electrophoretic deposition of nanosized zeolites in non-aqueous medium and its application in fabricating thin zeolite membranes. *Microporous and Mesoporous Materials* **69** [No. 1–2] 35–42.

Snyder M. A., Lee J. A., Davis T. M., Scriven L. E., and Tsapatsis M. (2007) Silica nanoparticle crystals and ordered coatings using Lys-Sil and a novel coating device. *Langmuir* **23** [No. 20] 9924–9928.

Spiga M. and Morino G. L. (1994) A symmetric solution for velocity profile in laminar flow through rectangular ducts. *International Communications in Heat and Mass Transfer* **21** [No. 4] 469–475.

Stöber W. and Fink A. (1968) Controlled growth of monodisperse silica spheres in the mircon size range. *Journal of Colloid and Interface Science* **26** 62–69.

Treacy M. M. J., Vaughan D. E. W., Strohmaier K. G., and Newsam J. M. (1996) Intergrowth segregation in FAU-EMT zeolite materials. *Proceedings: Mathematical, Physical and Engineering Sciences* **452** [No. 1947] 813–840.

Vinokur M. (1983) On one-dimensional stretching functions for finite-difference calculations. *Journal of Computational Physics* **50** 215–234.

Watanabe S., Inukai K., Mizuta S., and Miyahara M. T. (2009) Mechanism for stripe pattern formation on hydrophilic surfaces by using convective self-assembly. *Langmuir* **25** [No. 13] 7287–7295.

Xia D., Li D., Ku Z., Luo Y., and Brueck S. R. J. (2007) Top-down approaches to the formation of silica nanoparticle patterns. *Langmuir* **23** [No. 10] 5377–5385.

Yokoi T., Sakamoto Y., Terasaki O., Kubota Y., Okubo T., and Tatsumi T. (2006) Periodic arrangement of silica nanospheres assisted by amino acids. *Journal of the American Chemical Society* **128** 13664–13665.

Yoo W. C., Kumar S., Wang Z., Ergang N. S., Fan W., Karanikolos G. N., McCormick A. V., Penn R. L., Tsapatsis M., and Stein A. (2008) Nanoscale reactor engineering: Hydrothermal synthesis of uniform zeolite particles in massively parallel reaction chambers. *Angewandte Chemie International Edition* **47** 9096–9099.

Yoo W. C., Kumar S., Penn R. L., Tsapatsis M., and Stein A. (2009) Growth patterns and shape development of zeolite nanocrystals in confined syntheses. *Journal of the American Chemical Society* **131** [No. 34] 12377–12383.

Zheng H., Rubner M., and Hammond P. (2002) Particle assembly on patterned "plus/minus" polyelectrolyte surfaces via polymer-on-polymer stamping. *Langmuir* **18** [No. 11] 4505–4510.

Zhou Z. and Zhao X. S. (2004) Flow-controlled vertical deposition method for the fabrication of photonic crystals. *Langmuir* **20** [No. 4] 1524–1526.